



Mehran Ghafouri

**THERMOMECHANICAL FINITE ELEMENT  
SIMULATION OF WELDING, AND ELEVATED-  
TEMPERATURE MECHANICAL BEHAVIOUR OF  
HIGH AND ULTRA-HIGH STRENGTH STEELS**



Mehran Ghafouri

# **THERMOMECHANICAL FINITE ELEMENT SIMULATION OF WELDING, AND ELEVATED- TEMPERATURE MECHANICAL BEHAVIOUR OF HIGH AND ULTRA-HIGH STRENGTH STEELS**

Dissertation for the degree of Doctor of Science (Technology) to be presented with due permission for public examination and criticism in the Auditorium 1318 at Lappeenranta-Lahti University of Technology LUT, Lappeenranta, Finland on the 23<sup>rd</sup> of November, 2023, at noon.

Acta Universitatis  
Lappeenrantaensis 1101

Supervisors Professor Timo Björk  
LUT School of Energy Systems  
Lappeenranta-Lahti University of Technology LUT  
Finland

PhD Antti Ahola  
LUT School of Energy Systems  
Lappeenranta-Lahti University of Technology LUT  
Finland

Reviewers Professor Zuheir Barsoum  
Department of Engineering Mechanics  
KTH Royal Institute of Technology  
Sweden

Professor Martin Leitner  
Institute of Structural Durability and Railway Technology  
Graz University of Technology  
Austria

Opponent Associate Professor Andreas Lundbäck  
Department of Engineering Sciences and Mathematics  
Luleå University of Technology  
Sweden

ISBN 978-952-335-995-6  
ISBN 978-952-335-996-3 (PDF)  
ISSN 1456-4491 (Print)  
ISSN 2814-5518 (Online)

Lappeenranta-Lahti University of Technology LUT  
LUT University Press 2023

# Abstract

**Mehran Ghafouri**

**Thermomechanical finite element simulation of welding, and elevated-temperature mechanical behaviour of high and ultra-high strength steels**

Lappeenranta 2023

95 pages

Acta Universitatis Lappeenrantaensis 1101

Diss. Lappeenranta-Lahti University of Technology LUT

ISBN 978-952-335-995-6, ISBN 978-952-335-996-3 (PDF), ISSN 1456-4491 (Print),

ISSN 2814-5518 (Online)

The development of high and ultra-high strength steels (HSSs/UHSSs) emerged as an engineering approach to enable lightweight structural applications and an environmental solution to reduce the steel production-related carbon footprint. There is increasing use of HSSs/UHSSs in a diverse range of industrial applications due to their excellent strength-to-weight ratio, weldability, and toughness. Fusion welding techniques and in-between, arc welding processes are indispensable as efficient methods to make permanent joints between components and structural members made from HSSs/UHSSs. Ensuring the safe application of assemblies made from these materials and exploiting their maximum load-bearing capacities require extensive research on the behaviour of such materials due to welding heat and elevated temperatures that cause welding residual stresses, different welding deformations, and strength degradation.

Consequently, the development of welding residual stresses and distortions in different HSSs/UHSSs was investigated by means of finite element (FE) simulation of welding. Sequentially coupled thermomechanical formulation was adopted in all the cases considered, and mathematical modelling of the heat source was based on a double ellipsoidal heat source model. In this regard, welding distortions due to bead-on-plate welding of a specimen made of S960MC were simulated incorporating solid-state phase transformation models. Comparison of the simulated results and experimental measurements showed that a more accurate prediction of angular and out-of-plane bending distortions is possible when the effect of phase transformation is considered.

Development of welding residual stresses and distortions in T-joints made of S700MC under different external restraints and welding sequences for continuous and short non-continuous fillet welds were numerically and experimentally investigated in separate studies. Thermo-elastic-plastic FE models were developed considering material and geometrical nonlinearities. The results showed that for both continuous and short fillet welds, the effects of mechanical boundary conditions on sequential and cumulative welding distortions and welding residual stresses are more significant than the welding sequence. While angular distortion and transverse residual stresses were highly affected by the configuration of external constraints, longitudinal residual stresses were found to be less affected. Comparing the results of the two studies showed that localized transverse stress fields with higher peak magnitudes resulted from short fillet welds.



The strength degradation of two grades of UHSSs, namely, S960MC and S1100, due to elevated temperatures in as-received and as-welded conditions was investigated experimentally. Standard specimens were manufactured, and steady-state hot tensile tests from room temperature to 900 °C were carried out. The reduction factors of the constitutive mechanical properties of the two steels were determined and compared with several leading standard predictive models and datasets from the literature. Finally, predictive equations were proposed to estimate those reduction factors for the tested UHSSs at elevated temperatures.

**Keywords:** finite element simulation, welding simulation, welding distortion, residual stress, high strength steel, ultra-high strength steel, elevated temperature, gas metal arc welding

## Acknowledgements

First and foremost I would like to express my profound gratitude towards my supervisor, Professor Timo Björk, for his invaluable support, guidance and supervision during the research and work in the Laboratory of Steel Structures. PhD Antti Ahola is highly thanked for his help, valuable comments and co-supervising the doctoral thesis.

The research respecting this dissertation was carried out in the Laboratory of Steel Structures at Lappeenranta-Lahti University of Technology LUT, Finland. My warm appreciation is extended to all my research colleagues and friends for their fruitful discussions and providing a professional work atmosphere. Special thanks to my colleague PhD Shahriar Afkhami for his assistance and comments to improve the quality of my work. I wish to thank Mr Matti Koskimäki and all the personnel in the laboratories of Steel Structure and Welding Technology for their excellent work in management and carrying out experiments, mechanical tests and measurements.

I wish to thank all my co-authors, PhD Joseph Ahn, PhD Mohsen Amraei and Professor Jari Larkiola for their contribution in enhancing the content quality of the papers presented in this dissertation. Mr Aki-Petteri Pokka and Mr Juho Mourujärvi are warmly acknowledged for their patience in meticulously carrying out mechanical tests and measurements at the University of Oulu.

I would also like to offer my gratitude to Professor Zuheir Barsoum and Professor Martin Leitner for reviewing and commenting on this dissertation. Associate Professor Andreas Lundbäck is gratefully acknowledged for accepting to act as the opponent.

The financial support for this research from “Finnish Foundation for Technology Promotion”, and “Business Finland” (BF) through the ISALUT and DigRob projects is highly appreciated. The support of SSAB Europe in providing the steel materials for this research is acknowledged.

Last and most importantly, my everlasting thankfulness towards my beloved parents and sister for their unconditional support and encouragement, to whom this dissertation with love is dedicated.

Mehran Ghafouri  
October 2023  
Lappeenranta, Finland



# Contents

**Abstract**

**Acknowledgements**

**Contents**

**List of publications** 9

**Nomenclature** 11

**1 Introduction** 15

- 1.1 Background and motivation ..... 15
- 1.2 Objectives of the research ..... 18
- 1.3 Scope and limitations ..... 19
- 1.4 Scientific contribution ..... 19
- 1.5 Structure of the dissertation ..... 21

**2 Materials and experimental setup** 23

- 2.1 Materials ..... 23
- 2.2 Test specimens ..... 24
- 2.3 Welding procedures and experimental setups ..... 25
- 2.4 Temperature measurement ..... 28
- 2.5 Deformation measurements ..... 30
- 2.6 Residual stress measurement ..... 30

**3 Finite element modelling** 33

- 3.1 Finite element geometry and mesh ..... 33
- 3.2 Material modelling ..... 35
  - 3.2.1 Temperature-dependent thermo-physical properties ..... 35
  - 3.2.2 Temperature-dependent mechanical properties ..... 36
- 3.3 Thermal analysis ..... 37
  - 3.3.1 Heat source modelling ..... 38
  - 3.3.2 Heat loss modelling (thermal boundary conditions) ..... 42
- 3.4 Solid-state phase transformation ..... 44
- 3.5 Mechanical analysis ..... 46
  - 3.5.1 Strain decomposition ..... 46
  - 3.5.2 Mechanical boundary conditions ..... 48

**4 Results and discussion** 51

- 4.1 Thermal fields ..... 51
- 4.2 Microstructure prediction ..... 54
- 4.3 Welding deformation ..... 56
- 4.4 Welding residual stress ..... 62
- 4.5 Elevated-temperature mechanical properties ..... 72

4.5.1	Elastic modulus .....	77
4.5.2	Yield strength .....	79
4.5.3	Ultimate tensile strength .....	80
4.5.4	Predictive equations .....	81
<b>5</b>	<b>Conclusions</b>	<b>87</b>
<b>6</b>	<b>References</b>	<b>89</b>
	<b>Publications</b>	

## List of publications

This dissertation is based on material taken from the following publications. The rights to include the published papers in the dissertation have been granted by the publishers.

- I. Ghafouri, M., Ahn, J., Mourujärvi, J., Björk, T., and Larkiola, J. (2020). Finite element simulation of welding distortions in ultra-high strength steel S960 MC including comprehensive thermal and solid-state phase transformation models. *Engineering Structures*, 219, 110804.
- II. Ghafouri, M., Ahola, A., Ahn, J., and Björk, T. (2022). Welding-induced stresses and distortion in high-strength steel T-joints: Numerical and experimental study. *Journal of Constructional Steel Research*, 189, 107088.
- III. Ghafouri, M., Ahola, A., Ahn, J., and Björk, T. (2022). Numerical and experimental investigations on the welding residual stresses and distortions of the short fillet welds in high strength steel plates. *Engineering Structures*, 260, 114269.
- IV. Ghafouri, M., Amraei, M., Pokka, A., Björk, T., and Larkiola, J. (2022). Mechanical properties of butt-welded ultra-high strength steels at elevated temperatures. *Journal of Constructional Steel Research*, 198, 107499.

## Author's contribution

Mehran Ghafouri is the principal investigator in all the above-mentioned publications and responsible for designing the experiments, conducting finite element simulations, and preparing the manuscripts. Dr Joseph Ahn contributed to commenting the numerical simulations and revising the manuscripts in **Publications I, II and III**. Dr Antti Ahola contributed to assisting the management of experiments and revising the manuscripts in **Publications II and III**. Dr Mohsen Amraei was the corresponding author and contributed to assisting in analysing the data, providing the literature review, commenting on, and revising the manuscript in **Publication IV**. Mr Juho Mourujärvi contributed to performing the elevated-temperature tensile tests and dilatometric tests and preparing the CCT diagram in **Publication I**. Tensile tests at elevated temperatures in **Publication IV** were performed by Mr Aki-Petteri Pokka. Prof. Jari Larkiola contributed to commenting on the manuscripts in **Publications I and IV**. Dr Heidi Piili and Prof. Xiao-Lin Zhao contributed to providing guidelines and commenting on the manuscript in **Publication IV**. The entire research was conducted under the supervision of Prof. Timo Björk.

**Other publications by the author and related to this research:**

Ghafouri, M., Amraei, M., Gopaluni, A., Piili, H., Björk, T., Hämäläinen, J. (2023). Simulation and Its Use in Additive Manufacturing, in: Impact of Scientific Computing on Science and Society. *Springer Cham*, pp. 111-126.

Neuvonen, R., Peltoniemi, T., Skriko, T., Ghafouri, M., Amraei, M., Ahola, A., Björk, T. (2023). The effects of geometric and metallurgical constraints on ultra-high strength steel weldments. *Structures*, 56, 104900.

## Nomenclature

### List of symbols

$\nabla$	divergence operator	—
$\nabla T$	temperature gradient	$^{\circ}\text{C}/\text{m}$
$a$	semi-axis of the double-ellipsoid in $x$ -coordinate	$\text{mm}$
$A_1$	lower critical temperature	$^{\circ}\text{C}$
$A_3$	upper critical temperature	$^{\circ}\text{C}$
$b_f$	semi-axis in front half of the double-ellipsoid in $y$ -coordinate	$\text{mm}$
$B_f$	bainite finish temperature	$^{\circ}\text{C}$
$b_r$	semi-axis in rear half of the double-ellipsoid in $y$ -coordinate	$\text{mm}$
$B_s$	bainite start temperature	$^{\circ}\text{C}$
$c$	specific heat	$(\text{J}/\text{kg}^{\circ}\text{C})$
$c_g$	semi-axis of the double-ellipsoid in $z$ -coordinate	$\text{mm}$
$C_{th}$	thermal stiffness matrix	—
$D^e$	elastic stiffness matrix	—
$D^p$	plastic stiffness matrix	—
$E$	modulus of elasticity	$\text{MPa}$
$f_b^{\circ}$	final volume fraction of bainite during transformation	—
$f_m^{\circ}$	final volume fraction of martensite during transformation	—
$f_{0.2}$	strength at 0.2% total strain	$\text{MPa}$
$f_{0.5}$	strength at 0.5% total strain	$\text{MPa}$
$f_{1.5}$	strength at 1.5% total strain	$\text{MPa}$
$f_2$	strength at 2% total strain	$\text{MPa}$
$f_a$	volume fraction of austenite	—
$f_b$	volume fraction of bainite at temperature $T$	—
$\mathbf{F}_b$	vector of body force per unit volume	$\text{N}/\text{mm}^3$
$f_f$	fraction of the heat deposited in the front half of the heat source	—
$f_m$	volume fraction of martensite at temperature $T$	—
$f_r$	fraction of the heat deposited in the rear half of the heat source	—
$f_u$	ultimate tensile strength	$\text{MPa}$
$h$	temperature-dependent heat transfer coefficient	$(\text{W}/\text{m}^2^{\circ}\text{C})$
$h_{conv}$	convective heat transfer coefficient	$(\text{W}/\text{m}^2^{\circ}\text{C})$
$I$	welding electric current	$\text{A}$
$k$	thermal conductivity	$\text{W}/\text{m}^{\circ}\text{C}$
$k_a$	characteristic factor	—
$k_m$	transformation characterizing parameter	—
$M_f$	martensite finish temperature	$^{\circ}\text{C}$
$M_s$	martensite start temperature	$^{\circ}\text{C}$
$\mathbf{q}$	heat flux density vector	$\text{W}/\text{m}^2$
$Q$	welding power (heat input)	$\text{W}$
$q$	volumetric heat source density	$\text{W}/\text{m}^3$
$q_{conv}$	convective heat transfer per unit area	$\text{W}/\text{m}^2$



$q_{rad}$	radiative heat transfer per unit area	W/m <sup>2</sup>
$q_f$	heat flux distribution in the front half of the heat source	W/m <sup>3</sup>
$q_r$	heat flux distribution in the rear half of the heat source	W/m <sup>3</sup>
$t$	time	s
$T$	temperature	°C
$T_0$	ambient temperature	°C
$T_{max}$	maximum temperature of a material point in austenitic transformation	°C
$U$	welding voltage	V
$v$	welding travel speed	mm/s
$v_{8/5}$	cooling rate in the range 500 °C–800 °C	°C/s
$x$	x-coordinate	mm
$y$	y-coordinate	mm
$z$	z-coordinate	mm
$\alpha$	linear thermal expansion coefficient	1/°C
$\alpha_a$	linear thermal expansion coefficient of austenite	1/°C
$\alpha_b$	linear thermal expansion coefficient of bainite	1/°C
$\alpha_i$	linear thermal expansion coefficient of phase i	1/°C
$\alpha_m$	linear thermal expansion coefficient of martensite	1/°C
$\varepsilon^*$	emissivity	—
$\varepsilon^e$	elastic strain rate	—
$\varepsilon^p$	plastic strain rate	—
$\varepsilon^{th}$	thermal strain rate	—
$\varepsilon^{total}$	total strain rate	—
$\varepsilon^{\Delta V}$	volumetric change strain rate	—
$\varepsilon^{\Delta V^*}_a$	full volumetric change strain of austenite	—
$\varepsilon^{\Delta V^*}_b$	full volumetric change strain of bainite	—
$\varepsilon^{\Delta V^*}_i$	full volumetric change strain of phase i	—
$\varepsilon^{\Delta V^*}_m$	full volumetric change strain of martensite	—
$\eta$	welding efficiency coefficient	—
$\nu$	Poisson's ratio	—
$\rho$	density	(kg/m <sup>3</sup> )
$\sigma$	Cauchy stress tensor	MPa
$\sigma^*$	Stefan–Boltzmann constant	(W/m <sup>2</sup> K <sup>4</sup> )
$\sigma_y$	yield strength	MPa

### Abbreviations

2D	two-dimensional	—
3D	three-dimensional	—
AISC	American Institute of Steel Construction	—
ASTM	American Society for Testing and Materials	—
CCT	continuous cooling transformation	—
CEV	carbon equivalent value	—
CWM	computational weld mechanics	—
DQ	direct quenching	—

---

EC3	Eurocode 3	-
FE	finite element	-
FZ	fusion zone	-
GMAW	gas metal arc welding	-
HAZ	heat-affected zone	-
HSS	high strength steel	-
RT	room temperature	-
SD	standard deviation	-
SDV	solution-dependent state variable	-
SEM	scanning electron microscopy	-
SSPT	solid-state phase transformation	-
TMM	thermo-metallurgical-mechanical	-
UHSS	ultra-high strength steel	-
WPS	welding procedure specification	-
XRD	X-ray diffraction	-



# 1 Introduction

## 1.1 Background and motivation

In the world of manufacturing and construction, steel has become one of the main construction materials worldwide. Due to high demand and its importance in industrial economic infrastructure, steel consumption per capita of population is often called a progress and industrialization index (Kumar and Kumar, 2015). Steel production is a highly energy-intensive process, and the iron and steel industry is thus spoken of as the most energy-consuming industrial sector. In addition to the energy demands attributed to steel production, the process has significant environmental impacts through generating considerable amounts of perilous waste and emitting toxic pollutants into the air. Indeed, the iron and steel industry is the main contributor to CO<sub>2</sub> emissions, being responsible for almost 7% of the globally produced CO<sub>2</sub> (Conejo et al., 2020; Kumar and Kumar, 2015; Rosenfeld and Feng, 2011). It is therefore of particular importance to maintain a balance between the increasing global demand for steel, on the one hand, and the list of hazards and environmental consequences attached to steel production on the other. One practical and energy-efficient solution to improve sustainability is an engineering approach to increase the strength grade of steels. This insight has triggered the advent and development of light weight and high-performance steels, that is, high- and ultra-high strength steels (HSSs/UHSSs). Increasing the strength of the steel proportionally reduces the weight, which accordingly helps to reduce the energy required for exploitation, processing, transportation, etc. and subsequently the associated carbon footprint. High load-bearing capacity and good weldability, toughness, and strength-to-weight ratio are among the remarkable features of these materials that have made them highly applicable in a broad spectrum of industrial applications (Guo et al., 2017). The production of fossil-free steels as a further step towards sustainability will highlight their use as green construction materials in the near future.

Fusion welding techniques have been extensively used to make permanent joints between mechanical components due to their advantages over mechanical joining methods. Different features, such as high flexibility in design, cost-effectiveness, reliability, and productivity, have made this technology indispensable method in the manufacturing and construction of a wide variety of assemblies and structures made from HSSs/UHSSs (Liang and Deng, 2018; Sun et al., 2014). In general, this technology, is operated upon transferring a huge amount of heat input into the joint. This nonlinear temperature field, comprising a high heating rate followed by an uneven cooling in the weld region, can cause serious problems in welded joints made up of HSSs/UHSSs. Heat-affected zone (HAZ) softening is frequently reported for a series of UHSSs in the literature (Amraei et al., 2019; Skriko et al., 2017). The effects of the elevated temperatures on the strength reduction and impairment of the constitutive mechanical behaviour of the welded joints made from HSSs/UHSSs have been investigated (Neuenschwander et al., 2017; Qiang et al., 2016; Shakil et al., 2020). In addition, a transient thermal field in the weld area causes thermal strains that give rise to welding residual stresses and distortions.

Stresses developed upon the application of arc welding processes are among the main concerns in welded structures loaded dynamically or supposed to operate in adverse conditions (Heinze et al., 2012a; Ueda et al., 2012). Localized heating due to a moving heat source during welding causes a sharp temperature gradient in the weld area followed by a non-uniform thermal expansion. This thermal expansion is opposed by the surrounding colder zone and causes the rise of thermal stresses. The thermal contraction that occurs upon cooling varies across zones due to differences in their cooling rates. As a result of this inhomogeneous expansion and contraction, welding residual stresses develop. The formation of the welding residual stresses is governed by temperature-dependent material properties.

Depending on their signs, magnitudes, and distributions, residual stresses can be detrimental or beneficial (Barsoum and Lundbäck, 2009). The acceleration of a diverse range of degradation phenomena is directly attributed to the tensile residual stresses in the fusion zone (FZ) and HAZ of the welded joints. Tensile residual stresses negatively affect the structural integrity, service performance and fatigue life of welded connections (Cui et al., 2019; Jiang et al., 2021), and their adverse influence may be extended to deterioration of buckling strength (Deng, 2009), increased incidence of stress corrosion cracking (Yan and Yang, 2019), and promotion of brittle fracture (Moshayedi and Sattari-Far, 2015).

Evaluation of detrimental residual stresses is thus inevitable to alleviate or negate their impacts, increase design reliability, and ensure the safe application of welded structures. Residual stresses can be assessed through experimental measurements post welding. However, experimental methods might have their own limitations and challenges. Hole drilling, for example, is a destructive method and is thus impracticable for real components and assemblies. Non-destructive methods, while applicable to real structures, have their own restrictions. X-ray diffraction (XRD) is only applicable to capture surface residual stresses, and, as it pertains to fillet welded joints, contingent upon the height of the vertical attachment (stiffener); moreover, it can have limitations in terms of reaching the regions near the weld toe, and the neutron diffraction method may be costly.

As mentioned earlier, non-uniform heating and the uneven ensuing cooling during welding cause welding stress. If the generated stress exceeds the material's yield strength, the material may deform plastically. This localized plastic deformation may lead to permanent change in the dimensions or shape of the welded members and is generally called welding deformation. Whereas welding residual stress might be noticeable in a region close to the weldment, welding distortion can often extend to the entire welded structure (Chao, 2005). Welding distortion is a serious challenge, as it adversely affects the dimensional accuracy and quality of welded joints. This might lead to performance degradation of the joint and loss in structural integrity, and, in extreme cases, to the inapplicability or failure of the joint. Additionally, welding distortion can impair productivity by imposing delays in the assembly process due to additional corrections, which itself imposes further financial costs (Lee et al., 2018; Liang et al., 2020).

In view of the deleterious consequences of welding-induced stresses and deformations in HSSs/UHSSs, accurate prediction and assessment of such stresses and distortions is imperative to have a safe and robust design that uses the maximum potential of such materials. In this regard, the finite element (FE) method has shown its power to give solutions to a wide variety of scientific and engineering problems. In the field of heat transfer and simulation of welding processes, introducing computational methods mainly based on the FE method has led to the development of computational welding mechanics (CWM). The aim of CWM is to predict and analyse the temperature field, welding residual stresses and distortions and microstructural evolution (Goldak and Akhlaghi, 2005; Lindgren, 2007).

The superiority of numerical simulations over experimental methods lies in the ability of computational methods to predict the evolution of welding imperfections prior to the application of the welding process. Although complete prevention of the development of residual stresses and distortions might not be possible, accurate prediction makes it feasible to take countermeasures to largely control or alleviate such unfavourable effects. For HSSs and UHSSs, whose high load-bearing capacity may negatively be impacted by welding heat, accurate prediction of the development of residual stresses and distortions is of paramount importance.

Fillet weld is one of the most commonly applied weld types. Due to the low costs and simplicity of the joint, fillet welds have been extensively used to fabricate a wide range of steel structures (Hicks, 1999). Plate girders are widely used in steel bridges and offshore structures, and stiffened panels, frequently used in the shipbuilding industries, are among the structures in which fillet welds are most notably used. Angular distortion and longitudinal and transverse shrinkages are among the welding distortions from which fillet welded joints may suffer (Deng et al., 2007a). In fillet welded joints, depending on the applied load and design code guidelines, short fillet welds, also known as intermittent or non-continuous fillet welds, are applied as alternatives to continuous fillet welds to reduce costs, save weight, and reduce distortion in the long run (Carvill, 1993; Khedmati et al., 2007). Tack welding is another type of non-continuous short fillet welding used to attach structural members temporarily before the final weld is applied. It is important to investigate the formation of residual stress fields and welding distortions of the short fillet welds that are subject to different welding sequences and external restraints. From a manufacturing standpoint, deformations, even small in magnitude, might be important, for example, in robotized welding where precision is concerned. Although numerous welding simulation studies have been carried out, FE simulation of welding residual stresses and distortions in HSSs/UHSSs has not been extensively investigated. In this regard, there is still a lack of knowledge about the effect of different welding fixtures and welding sequences on the residual stress fields and welding distortions of the welded joints made from these materials.

As mentioned above, HAZ softening and strength degeneration in HSSs/UHSSs are important issues resulting from the application of fusion welding methods. Fire is undoubtedly among the most frequent and calamitous incidents threatening structures and

buildings. High conductivity and elevated-temperature degradation of mechanical properties make steel structures highly vulnerable to fire. Structural failure and collapse, financial loss, human fatalities, and air pollution are among the ramifications of such undesirable occurrences (Garlock et al., 2012; Li and Song, 2020; Li et al., 2021). Obtaining a profound understanding of the constitutive mechanical response of steels from which structures are made is a major requirement in having fire resistance designs.

Existing models in the leading design standards to predict the constitutive mechanical properties of steels, namely, elastic modulus, 0.2% proof, and ultimate tensile strengths at elevated temperatures, are mainly developed for mild steels. Therefore, their application to predict the elevated-temperature mechanical properties reduction factors of UHSSs is questionable. Increased application of UHSSs in the construction of structures due to their excellent strength-to-weight ratio, on the one hand, and the potential of fire to degrade such characteristics, on the other, alongside the lack of recommendations from design standards makes it a meaningful task to conduct research in this context.

## 1.2 Objectives of the research

Exploitation of the maximum load-bearing capacity of the welded members made from HSSs and UHSSs and ensuring the safety of their applications necessitate research on the effects of the detrimental phenomena attributed to the welding heat and elevated temperatures. In this regard, the primary aims of this research are as follows.

First, this research aims to predict the welding residual stresses and distortions in HSSs and UHSSs through developing thermomechanical FE models. To meet this aim, several case studies were developed including different materials, joints, external restraints and welding pass arrangements. All the developed FE simulations were verified by experimental measurements. **Publication I** investigates the FE simulation of welding-induced angular and out-of-plane bending distortions of a bead-on-plate welded specimen made of S960MC in free deformation condition with and without incorporation of solid-state phase transformation. **Publications II** and **III**, by means of the FE method, study the effect of external constraint and welding sequence on the development of residual stress fields and distortions in T-fillet joints made from S700MC welded in continuous and non-continuous manners, respectively.

Second, this research aims to study the constitutive mechanical behaviour of butt-welded UHSSs at elevated temperatures. In this respect, **Publication IV** investigates the elevated-temperature strength degeneration of two types of UHSSs, S960MC and S1100, in as-built and as-welded conditions. The applicability of design models from the leading standards such as Eurocode 3 (EC3), AS4100, and AISC, to estimate the elevated-temperature mechanical properties reduction factors of the investigated steels are thus discussed. Further, predictive equations to safely predict the reduction factors related to constitutive mechanical properties are established.

### 1.3 Scope and limitations

As it pertains to welding of HSSs/UHSSs, gas metal arc welding (GMAW) is a widely used process to make permanent joints and, is therefore the only welding process applied in the experiments conducted for this research. The main part of this research focuses on developing FE-based computational models to predict the welding-induced residual stresses and deformations in bead-on-plate welded specimens made from S960MC (**Publication I**) and T-fillet welded specimens made from S700MC (**Publications II** and **III**). In terms of the required properties for conducting the simulations, due to the laborious nature of the tests, the temperature-dependent mechanical properties to perform simulation were obtained experimentally in **Publication I** only. In **Publications II** and **III**, the temperature-dependent mechanical properties of the investigated material were obtained from the literature. For the same reason, the parameters required to include phase transformation in the computational model, were experimentally obtained for S960MC only, and that study was excluded from **Publications II** and **III**.

The XRD method was used to measure residual stresses in **Publications II** and **III**; thus, surface stresses were measured. In terms of external restraints and welding sequences in **Publications II** and **III**, due to time limitations, only two different welding fixtures and two welding pass orders were selected among possible arrangements for each study.

In **Publication IV**, steady-state elevated temperature tensile tests in the temperature range room temperature (RT)–900 °C were carried out to study the mechanical properties of two types of UHSSs in as-built and as-welded conditions. In this regard, quasi-static tests with a constant strain rate of  $0.0001 \text{ s}^{-1}$  were conducted, and the effect of different strain rates on elevated-temperature tensile properties of the materials was not investigated.

### 1.4 Scientific contribution

The entire research investigates the effect of elevated temperatures on welding stresses, distortions, and strength degradation of novel HSSs/UHSSs with nominal yield strength levels of 700, 960, and 1100 MPa, to which far less research has been devoted than to investigating mild steels.

As it pertains to FE simulation of welding processes, there is plentiful research on structural steels. However, welding simulation and numerical evaluation of residual stresses and strains in HSSs/UHSSs have not extensively been covered in the literature. In this context, there is a lack of knowledge about different grades of these materials designed with different joint types subject to different welding procedures and external constraints.

The publications in this thesis overall contribute to extending knowledge of such materials and fill some of the gaps in the literature.



Phase transformation incorporated welding simulation of a bead-on-plate welded joint made from an UHSS with nominal yield strength of 960 MPa (i.e., S960MC) to evaluate the developed welding distortions is included in **Publication I**. With a focus on welding distortion, this study attempts to investigate the effect of solid-state phase transformation (SSPT) on this welding imperfection as a scientific contribution.

Regarding the importance of fillet welds in steel structures, **Publication II** investigates the evolution of residual stress field and angular distortion in fillet welded joints made from S700MC by means of the FE method. Although few researchers have attempted welding simulation studies on S700, the present study investigates welding-induced residual stresses and distortions under different boundary conditions and welding pass arrangements. The results of this study, through comparisons, highlight the effects of the applied welding fixtures and sequences on residual stresses and strains in T-fillet welded joints made up of HSSs. **Publication III** extends the findings of **Publication II** for short fillet welds on T-joints made from S700MC with similar welding pass orders and external restraints on which research has rarely been conducted. The result of this investigation highlights the developed mechanical field due to short fillet welds. Through comparisons with the findings in **Publication II**, **Publication III** scientifically contributes to drawing attention to the differences in the developed mechanical field when the length of a fillet weld is shortened and welds are applied in a non-continuous manner. From an engineering point of view, the results of the two studies are important as they highlight the importance of welding fixture stiffness on the mechanical field and the need to take countermeasures to reduce the induced distortions. This matter is particularly notable in automated welding, where accuracy is a concern, and even small deformations need to be controlled in order to achieve the desired accuracy.

The matter of structural collapse due to the strength degeneration of structural steels under fire conditions has become increasingly important. As data are lacking regarding the elevated-temperature mechanical properties of UHSSs in the leading design standards, research in this field is necessary to improve the current design code models and make them applicable for UHSSs. Little research has been conducted on the mechanical properties of UHSSs at elevated temperatures, and further research on different types of steels categorised as UHSSs is required to improve knowledge in this field. **Publication IV**, as an experimental investigation, focuses on the strength degradation of two types of UHSSs, namely, quenched and tempered (S1100) and direct quenched (S960MC) at elevated temperatures (fire conditions), which is not covered in the literature. This research contributes to providing further data for comparisons and filling the knowledge gap in this field for the mentioned materials. In addition, as-welded specimens were tested to enhance understanding of the performance of welded joints made from the tested steels under fire conditions. The temperature-dependent mechanical properties obtained experimentally in this study can also be used as an input for the welding simulation of the tested steels by researchers interested in that field.

## 1.5 Structure of the dissertation

This dissertation comprises five chapters. In Chapter 1, the background, aims, scope, limitations, and scientific contribution are introduced. Chapter 2 provides information regarding the investigated materials, specimens, experimental procedures, and measurement plans. The sequentially coupled thermomechanical FE simulation method (implemented in **Publications I–III**) is described in Chapter 3 and the results are reflected in Chapter 4. It should be noted that the results are accompanied by the relevant discussions. Finally, a summary of the thesis, the main conclusions and future research proposals are presented in Chapter 5.



## 2 Materials and experimental setup

This research is based on several case studies of welded specimens made up of different HSSs/UHSSs. In addition to several materials, different geometries, joint designs, welding procedures, and various experimental measurements were incorporated. This chapter reviews the materials and experimental procedures for testing and measurements used in each publication.

### 2.1 Materials

The base materials used in this research were S700MC (**Publications II and III**), S960MC (**Publications I and IV**), and S1100 (**Publication IV**). S700MC and S960MC are manufactured by a modern thermo-mechanical hot rolling process integrated with direct quenching (DQ). In the DQ process, water quenching occurs immediately after hot rolling (Siltanen et al., 2015; Suikkanen and Kömi, 2014). S1100, however, is manufactured by a quenching and tempering process. The filler materials used in the welding procedures were Esab OK AristoRod 13.29 to weld S700MC and Böhler Union X96 to weld S960MC and S1100. Both welding wires were solid wires with a 1 mm diameter, and their strength level practically matched that of their base materials. The chemical compositions of the base and corresponding filler materials used in this research, based on the manufacturer's certificates, are listed in Table 2.1, Table 2.2, and Table 2.3.

Table 2.1: Nominal chemical compositions (in wt%) of S960MC and Union Böhler X96 in **Publication I**.

Material	C	Si	Mn	P	S	Al	Ti	Cu	Cr	Ni	Mo
S960MC	0.097	0.2	1.09	0.008	0.001	0.034	0.02	0.033	1.13	0.38	0.191
Union X96	0.12	0.8	1.90	-	-	-	-	-	0.45	2.35	0.55

Table 2.2: Nominal chemical compositions (in wt%) of S700MC and Esab OK AristoRod 13.29 in **Publications II and III**.

Material	C	Si	Mn	P	S	Al	Ti	Cr	Ni	Mo	V
S700MC	0.12	0.25	2.1	0.02	0.01	0.015	0.15	-	-	-	0.2
Esab 13.29	0.089	0.53	1.54	-	-	-	-	0.26	1.23	0.24	-

Table 2.3: Nominal chemical compositions (in wt%) of S960MC and S1100 in **Publication IV**.

Material	C	Si	Mn	P	S	V	Cu	Cr	Ni	Mo	CEV
S960MC	0.088	0.20	1.11	0.008	-	0.01	0.009	1.09	0.06	0.125	0.52
S1100	0.129	0.18	1.48	0.006	0.002	-	0.439	1.29	0.99	0.371	0.83

The slight difference in the chemical compositions of S960MC in **Publications I and IV** was due to different material batches being used.

## 2.2 Test specimens

The specimen in **Publication I** was a rectangular plate from S960MC that was laser cut to reach the dimensions of  $300 \times 300 \times 8$  mm, as shown schematically in Figure 2.1

Specimens in **Publications II** and **III** were T-joint specimens fabricated from laser-cut hot rolled strips of S700MC. The dimensions of the base plates and stiffeners from a 6-mm thick material were  $460 \times 130$  mm and  $130 \times 25$  mm, respectively. The schematic of the T-joint specimens in **Publication II** and **Publication III** is shown in Figure 2.2.

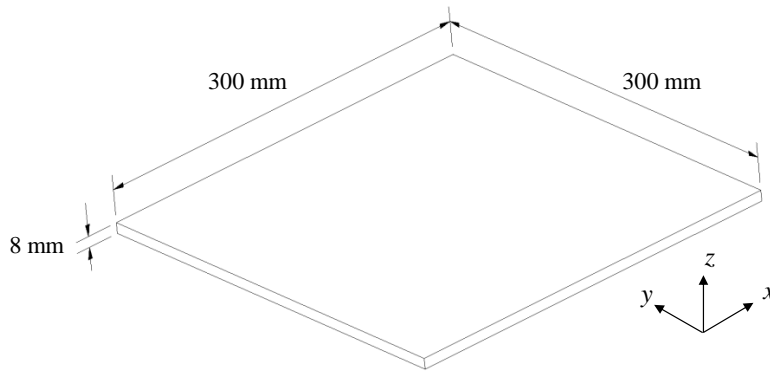


Figure 2.1: Schematic of the test specimen used in **Publication I**.

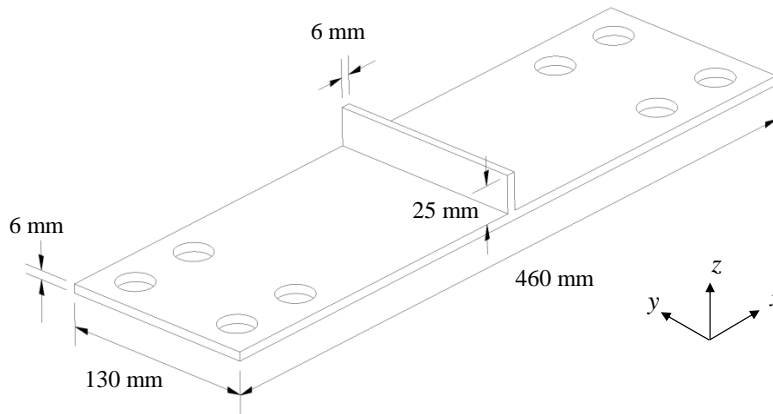


Figure 2.2: Schematic of the test specimen used in **Publication II** and **Publication III**.

The elevated-temperature tensile samples in **Publication IV** were fabricated in as-received and as-welded forms for each material (i.e., S960MC and S1100). As-received specimens were laser cut from 8-mm thick plates. Then, they were machined to form

cylindrical specimens in accordance with the specifications of ASTM E8M (ASTM, 2022), as shown in Figure 2.3. In order to fabricate as-welded specimens, two laser-cut plates were machined to form a double-V groove. After welding, specimens were laser cut from the welded block perpendicular to the welding direction and machined to produce cylindrical specimens identical to as-received specimens, according to the requirements of ASTM E8M.

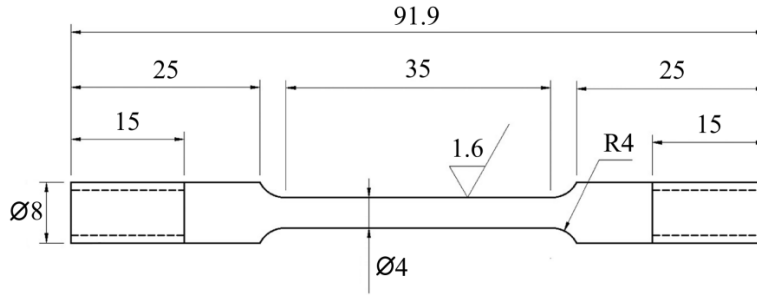


Figure 2.3: Schematic presentation of the cylindrical specimen used in **Publication IV** (Dimensions are in mm).

## 2.3 Welding procedures and experimental setups

The welding process for the entire research was GMAW applied with a robot arm. For welding processes in **Publications I–III**, where simulation was involved, an identical convention was considered. The welding direction was assumed to be along the  $+y$ -axis, while the  $+z$ -axis was normal to the top surface of the specimens. Welding in all the cases was carried out in an ambient temperature of 20 °C without the application of preheat, based on the recommendations of the manufacturer. For each case, welding parameters were set to reach the designed weld in terms of quality and size considering heat input limitations. That is, where HAZ softening is involved, the heat input should be kept optimized; hence, welding parameters were set to meet the heat input requirements (Björk et al., 2012). Welding process parameters for the welding processes used in this research are summarized in Table 2.4.

Table 2.4: Welding process parameters used in this research in the different publications (shielding gas for all the cases was Ar + 8% CO<sub>2</sub>).

Publication	Voltage (V)	Current (A)	Travel speed (mm/s)	Wire diameter (mm)	Wire feed rate (m/min)	Tip distance (mm)	Heat input (J/mm)
<b>I</b>	28	200	7	1.0	10	18	640
<b>II</b>	25	260	7	1.0	12.5	16	790
<b>III</b>	25	260	7	1.0	12.5	16	790
<b>IV</b>	25.1	216	6.2	1.0	10	18	700

In **Publication I**, the welding procedure consisted of the deposition of the filler material to produce a single-pass bead-on-plate weld. The specimen was positioned on the working table without the use of any external restraints (clamps) so that the specimen can deform freely, as schematically shown in Figure 2.4.

In **Publication II**, the fillet welding procedure included producing the designed leg size of 6 mm along the entire joint on both sides of the stiffeners (vertical attachments) to make double-sided fillet welds (one pass per side). In order to investigate the effect of the welding pass arrangement, in one case, the filler material was deposited on both sides in the same welding direction, denoted by S1. In another scenario, the two welding passes were applied in the opposite directions, named S2, as shown in Figure 2.5. The effect of external restraints was studied by applying two different mechanical boundary conditions. In one setup, a clamping configuration was applied to rigidly clamp the specimens at one end, while the other configuration rigidly clamped the specimens at both ends to satisfy the designed mechanical boundary conditions. In total, four specimens were used in the experiments in **Publication II**.

The fillet welding procedure in **Publication III** included the deposition of the filler material to produce short fillet welds. Two welds per side, each with an approximate length of 20 mm, were deposited. The mechanical boundary conditions in **Publication III** were identical to those in **Publication II**. The effect of the welding pass arrangement on the development of residual stresses and strains was investigated by considering two different arrangements for short fillet welds, as shown in Figure 2.6. It should be noted that the specimens in **Publications II** and **III** remained in their defined mechanical boundary conditions throughout the welding process, and the clamps were removed only when the welding process ended and specimens reached the ambient temperature.

In order to facilitate the discussion of and drawing of conclusions for the different cases in **Publications II** and **III**, a label was assigned to each specimen, as summarized in Table 2.5.

Table 2.5: The labels assigned to the specimens in **Publications II** and **III**.

Publication	Label	Condition
II	II-FS1	One free end, arrangement S1 (Figure 2.5)
II	II-FS2	One free end, arrangement S2 (Figure 2.5)
II	II-CS1	Two clamped ends, arrangement S1 (Figure 2.5)
II	II-CS2	Two clamped ends, arrangement S2 (Figure 2.5)
III	III-FS1	One free end, arrangement S1 (Figure 2.6)
III	III-FS2	One free end, arrangement S2 (Figure 2.6)
III	III-CS1	Two clamped ends, arrangement S1 (Figure 2.6)
III	III-CS2	Two clamped ends, arrangement S2 (Figure 2.6)

The experimental setup in **Publication IV** consisted of performing elevated-temperature tensile tests using a Zwick/Roell Z100 testing machine with a maximum load capacity of 100 kN. The tensile test machine was equipped with two separate chambers: one high-temperature furnace for tests above 300 °C and one environmental chamber for temperatures below 300 °C. Continuous temperature monitoring was carried out using three N-type thermocouples in the high-temperature furnace and one K-type thermocouple in the environmental chamber. Strain measurement in the high-temperature furnace was facilitated using a high-temperature MayTec extensometer with ceramic sensor arms, while a Zwick's 'makroXtens' extensometer with extended arms was used in the environmental chamber. Ten target temperatures between RT and 900 °C were determined. The tensile testing procedure consisted of heating the specimen with a heating rate of 20 °C/min to the target temperature and holding the specimen at that temperature for almost 5 min before loading. Keeping the specimen at target temperature prior to loading ensures uniform temperature distribution. A constant strain rate of 0.0001 s<sup>-1</sup> was applied for all the specimens up to rupture in strain-controlled tensile tests. Similar procedures can be found in the literature (Li and Song, 2020; Qiang et al., 2016).



## 2.4 Temperature measurement

In general, to verify the results of the thermal analysis in terms of temperature histories, the welding thermal cycles during welding are monitored by thermocouples. In each welding experiment in **Publications I–III**, several K-type thermocouples were attached to the top and bottom surfaces of the welded specimens. The location of the thermocouples in all the experiments was selected to include both high-temperature HAZ and regions with lower temperatures. The positions in which thermocouples were mounted in each specimen are schematically shown in Figure 2.4, Figure 2.5, and Figure 2.6.

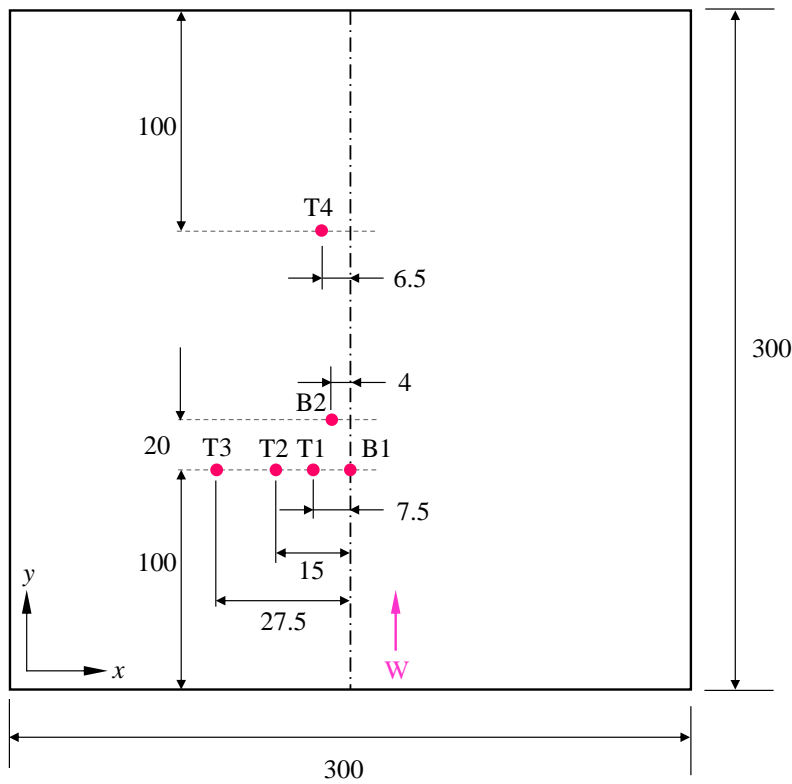


Figure 2.4: The location of thermocouples attached to the top and bottom sides of the bead-on-plate welded specimen in **Publication I**. The welding direction was in +y direction and all the dimensions are nominal ones in mm. B1 and B2 are thermocouples on the bottom side, and T1–T4 are thermocouples on the top side.

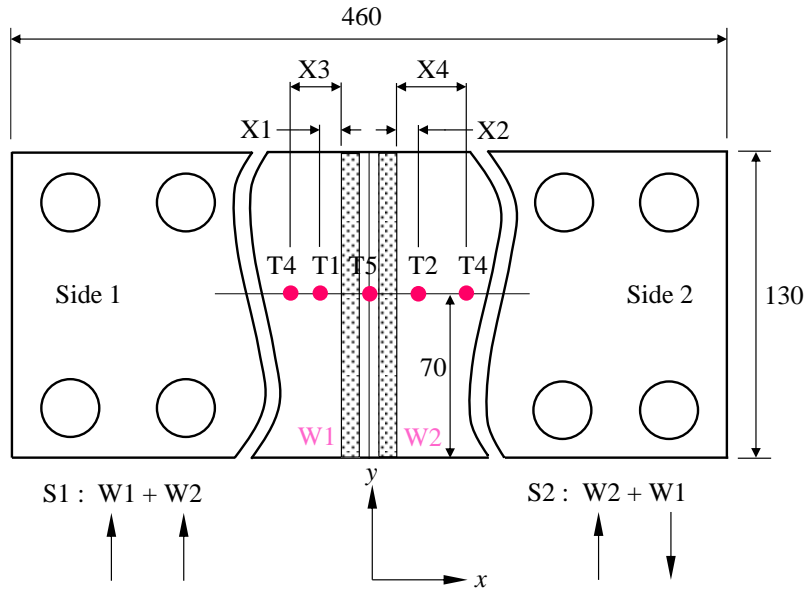


Figure 2.5: The location of the thermocouples attached to the top and bottom sides of the fillet welded specimens in **Publication II**. The welding direction was in +y direction, and all the dimensions are in mm. T1–T4 are thermocouples on the top side, and T5 was attached to the bottom side. X1–X4 are the distances of the thermocouples from the weld toe, which were measured post welding, and will be discussed in the results and discussion section. S1 and S2 show the order of the welding passes.

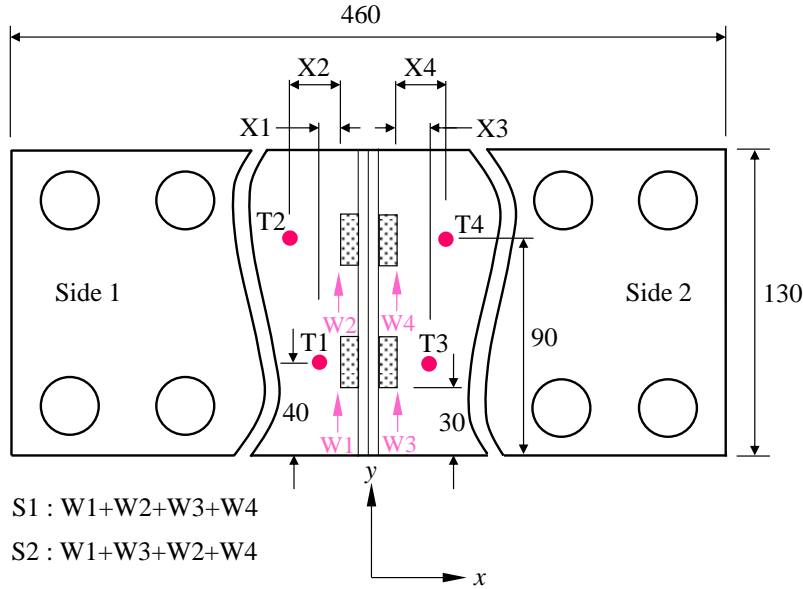


Figure 2.6: The location of the thermocouples attached to the top side of the intermittently fillet welded specimens in **Publication III**. The welding direction was in +y direction, and all the dimensions are in mm. T1–T4 are thermocouples on the top side. X1–X4 are the distances of the thermocouples from the weld toe, which were measured post welding. S1 and S2 show the order of the welding passes.

## 2.5 Deformation measurements

For the bead-on-plate case in **Publication I**, the angular and out-of-plane bending distortions were measured using a two-dimensional (2D) laser profile scanner Micro-Epsilon optoNCDT 1700–20. Measurements were carried out before welding and post welding, after the ambient temperature was reached on the top surface of the specimen along the specified paths, as shown in Figure 2.7. For the T-fillet welded specimens in **Publications II**, angular distortion was measured on the bottom side of the specimens in the mid-section in transverse (perpendicular to welding) direction using a Hexagon ROMER Absolute Arm 3D Scanner (resolution up to 63  $\mu\text{m}$ ), as shown in Figure 2.8. The measurement path for angular distortion of the intermittently fillet welded specimen in **Publication III** was identical to that of the specimen in **Publication II**. In **Publications II** and **III**, each specimen was measured prior to welding, after each welding pass and reaching the ambient temperature, and, finally, after release from the external restraints.

## 2.6 Residual stress measurement

The transverse residual stresses that developed due to welding in each specimen in **Publications II** and **III** were measured by means of the XRD method using a Stresstech

X3000 G3 device with a collimator diameter of 1 mm. In each set of specimens, residual stress was measured along specified paths, as schematically shown in Figure 2.8 and Figure 2.9, for continuous fillet weld case and short fillet welds, respectively. It should be noted that measurements were carried out after the entire welding procedure had been completed, the ambient temperature had been reached, and the external constraints had been released. However, for the fully clamped specimens, residual stress measurement was also performed after welding and after the ambient temperature was reached prior to releasing the clamps.

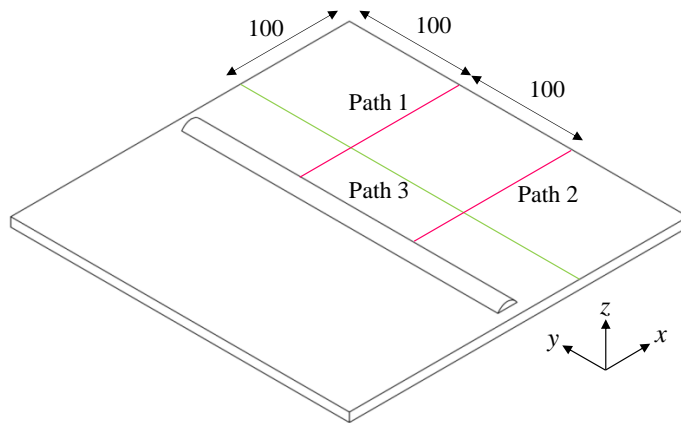


Figure 2.7: The measurement paths for angular and out-of-plane bending distortions of the bead-on-plate specimen in **Publication I**. Angular distortion was measured along Path 1 and Path 2, whereas out-of-plane bending distortion was measured along Path 3 (units in mm).

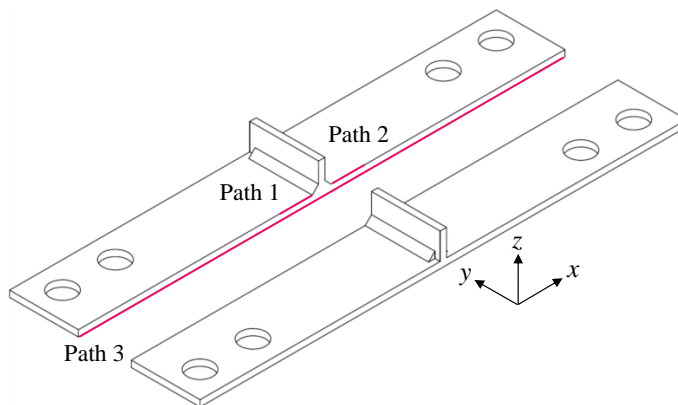


Figure 2.8: The measurement paths for transverse residual stresses (Path 1 and Path 2 on the top surface) and angular distortion (Path 3 on the bottom side) of the fillet welded specimens in **Publication II**. Path 1 and Path 2 start 1 mm from the weld toe and have an approximate length of 25 mm each.

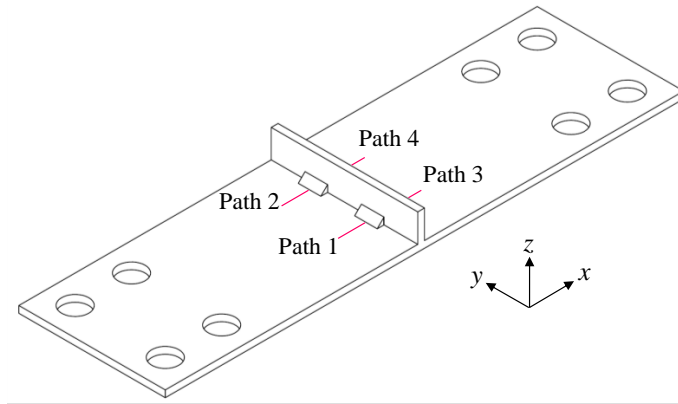


Figure 2.9: Schematic representation of the four paths used in the evaluation of the residual stresses of the fillet welded specimens in **Publication III**. Experimental measurements were carried out along Path 1 and Path 4 only. The measurement path for angular distortion was exactly the same as that shown in Figure 2.8.

### 3 Finite element modelling

In this research, temperature fields and the evolution of the welding-induced residual stresses and strains were investigated by means of the FE method in **Publications I–III**. To do so, three-dimensional (3D) thermo-elastic–plastic FE models were developed in **Publications II** and **III**, and a thermo-metallurgical-mechanical (TMM) model was developed in **Publication I**. All the simulation cases were accomplished in ABAQUS FE code (ABAQUS, 2020, 2017), and sequentially coupled analysis was adopted. It is claimed that this formulation performs well inasmuch as the structural response has an insignificant effect on the temperature field or, in other words, that the mechanical work is inconsequential compared to the thermal energy of the welding arc (Deng and Murakawa, 2006; Lee and Chang, 2009; Shen and Chen, 2014). In this formulation, the heat conduction equation is solved independent of the mechanical field equations. In general, the solution procedure consists of two steps. In the first step, the temperature distribution due to a moving heat source is captured by solving the heat conduction equation. The nodal temperatures captured in the thermal analysis are then transferred into a mechanical analysis and applied as a thermal load to obtain the mechanical response and, accordingly, calculate the developed residual stresses and strains. This chapter provides a detailed review of the FE geometries, element selection, material properties, equations, and modelling considerations in each publication included in this research.

#### 3.1 Finite element geometry and mesh

In **Publication I**, the weld bead geometry was modelled based on the bead curvature of the as-welded specimen. The weld bead was layered in the centreline of the specimen, and no external restraint was employed; thus, only half of the specimen was modelled and considered as the analysis domain in order to reduce the computation time. In **Publications II** and **III**, the geometries of the fillet welds were modelled based on the measured leg size and throat of the weld with the idealized curvatures. In each study, in order to facilitate the data mapping (transfer of nodal temperature histories) from the thermal to the mechanical model, 3D FE models with the identical mesh structure and density, albeit with different element types, were developed. In terms of element types in sequentially coupled welding simulations, application of both the linear and quadratic elements in thermal and mechanical analyses have been reported in the literature (Ahn et al., 2017; Bhatti et al., 2014; Chen et al., 2020; Danis et al., 2010; Shan et al., 2009). In this research, in the thermal analysis 8-node linear 3D solid (continuum) diffusive heat transfer brick (hexahedral) elements (DC3D8 in ABAQUS) were used. In the mechanical analysis, 8-node linear reduced integration 3D solid brick elements (C3D8R in ABAQUS) were used. This element type has three translational degrees of freedom at each node and owns only one integration point. Application of the reduced integration scheme prohibits shear locking, reduces computation time, and facilitates convergence (Lee and Chang, 2011). In order to eliminate hourglassing, which is attributed to linear reduced integration elements, hourglass control should be activated for such elements. The application of linear elements requires fine mesh grids to be provided in regions with

high stress gradients. In this regard, in all the simulation cases, fine mesh grids were defined in FZ and HAZ and become coarser as the distance from the fusion line increased in the transverse direction. Fine mesh grids ensured the accurate capture of the heat flux distribution due to a moving heat source in the regions with dramatic temperature change and the ensuing significant stress gradient. Mesh sensitivity analysis was performed to check the effect of mesh density on the accuracy of the results. In each case, convergence was achieved when an insignificant change in the results was observed due to further refinement of the mesh. Taking the accuracy of the results and computational costs into account, the mesh densities for the simulation cases in this research are summarized in Table 3.1. Mesh details of the bead-on-plate specimen in **Publication I** are shown in Figure 3.1 as an example of the mesh grids produced for the specimens in this research.

Table 3.1: The number and minimum size of the elements in each publication.

Publication	Number of elements	Minimum elements size		
		x-axis (mm)	y-axis (mm)	z-axis (mm)
<b>I</b>	64808	0.5	2.8	0.5
<b>II</b>	30738	0.5	3	1
<b>III</b>	28988	0.5	2.5	1

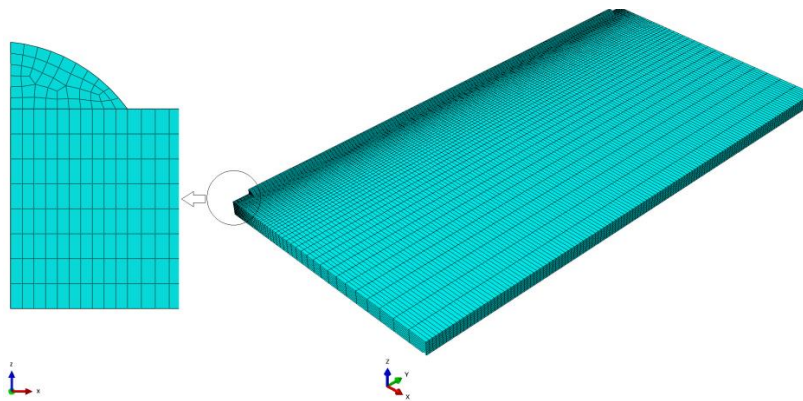


Figure 3.1: Mesh details of the bead-on-plate specimen.

The gradual addition of weld metal in all the simulation cases was considered using the element birth and death technique which is known as model change in ABAQUS (Seleš et al., 2018). In this technique, the part that represents the weld metal is generally divided into several segments. Prior to welding, all the elements representing weld metal are inactivated. When a heat source approaches specific elements based on the assigned time step, and the elements are heated up, their status is changed from inactivated to activated. Then, temperature-dependent thermo-physical properties, in the thermal analysis, and temperature-dependent mechanical properties, in the mechanical analysis, are allocated to activated elements.

## 3.2 Material modelling

In CWM, material modelling is defined as the application of the thermo-physical, mechanical, and, where related, metallurgical properties of a material. Fundamentally, material properties govern different coupled phenomena involved in a welding process and material modelling thus becomes an indispensable and prominent task in this context. In welding simulation problems, material properties are basically used as a function of temperature (Zhu and Chao, 2002).

### 3.2.1 Temperature-dependent thermo-physical properties

Thermal analysis, in general, is contingent upon specifying the temperature-dependent thermal and physical properties of a material. The influence of these parameters on welding simulation accuracy, whether taken as temperature-dependent or constant values, has been extensively investigated in the literature (Bhatti et al., 2015; Heinze et al., 2012b; Little and Kamtekar, 1998; Zhu and Chao, 2002). These parameters are density ( $\rho$ ), specific heat ( $c$ ), and thermal conductivity ( $k$ ). In this research, all the thermo-physical properties are taken as temperature-dependent. In **Publication I**, the temperature-dependent thermo-physical properties were obtained from JMatPro software (JMatPro Ver.8.0, 2014) using chemical compositions of S960MC, as shown in Figure 3.2. These properties for S700MC in **Publications II** and **III** were taken from the literature (Bhatti et al., 2015), and are shown in Figure 3.3. It should be noted that in all the simulation cases, the base and related filler materials were defined as identical materials, and the thermo-physical properties of the filler materials were considered identical to those of their base materials. It should also be noted that the units were arranged in such a way that all the properties could be shown in one graph.

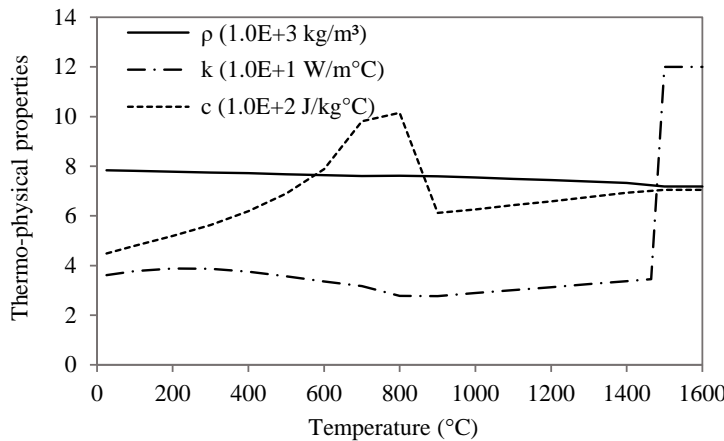


Figure 3.2: Temperature-dependent thermo-physical properties of S960MC used in **Publication I** (modified from **Publication I**).



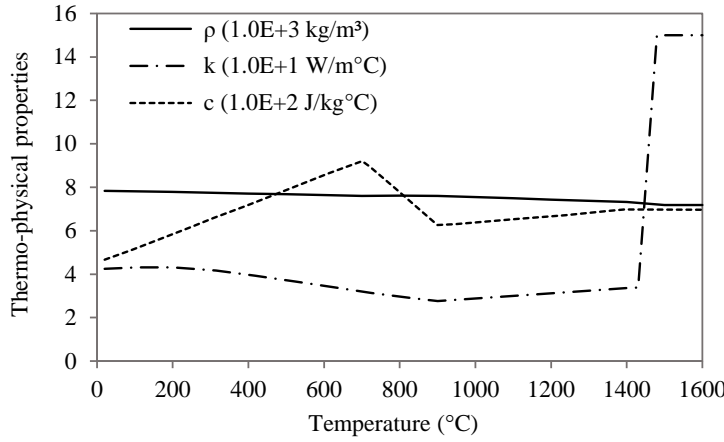


Figure 3.3: Temperature-dependent thermo-physical properties of S700MC used in **Publications II** and **III** (modified from **Publication II**).

### 3.2.2 Temperature-dependent mechanical properties

The mechanical properties of a material are of paramount importance in the evaluation of the developed residual stresses and distortions due to welding. Welding thermal cycles, which include rapid heating and cooling, are highly nonlinear. Under the influence of such nonlinearity, the mechanical characteristics of material change dramatically, mainly owing to microstructure changes, which makes them highly dependent on temperature. The mechanical properties of a material that are principally used in mechanical analysis related to the evaluation of welding residual stresses and strains are the modulus of elasticity or the Young's modulus ( $E$ ), yield strength ( $\sigma_y$ ), Poisson's ratio ( $\nu$ ), and thermal expansion coefficient ( $\alpha$ ). The temperature-dependent modulus of elasticity and yield strength of S960MC used in **Publication I** were obtained by conducting hot tensile tests in the temperature range RT–1200 °C. Poisson's ratio was obtained as a function of temperature using JMatPro (JMatPro Ver.8.0, 2014). The thermal expansion coefficient in **Publication I** was applied using a user subroutine in ABAQUS, which will be explained in detail in section 3.5. Since obtaining temperature-dependent mechanical properties by conducting experiments is time-consuming, it was decided to take the mechanical properties from a reliable study (Bhatti et al., 2015) for the case studies in **Publications II** and **III** due to time limitation issues. In terms of the mechanical properties of filler materials, since making specimens from the pure weld metal is an expensive and time-intensive process, in each case study in **Publications I–III**, the temperature-dependent mechanical properties for the filler materials were considered identical to those of the relevant base materials. The temperature-dependent properties used in the mechanical analyses for S960 (in **Publication I**), and S700MC (in **Publications II** and **III**) are shown in Figure 3.4 and Figure 3.5, respectively. It should be noted that all the units were arranged to be able to show all the properties in a single graph for each material.

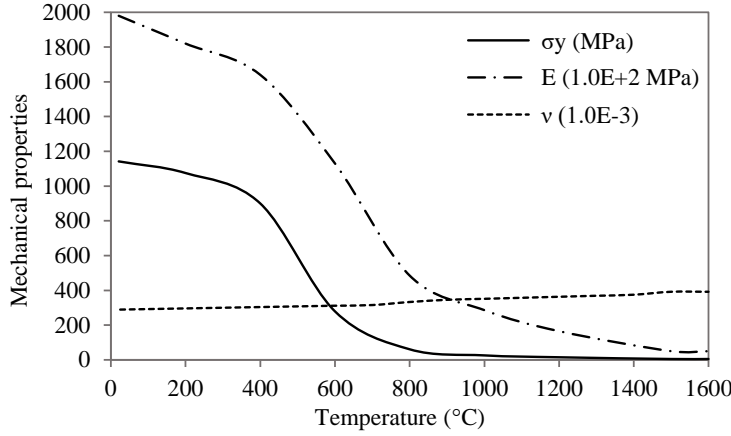


Figure 3.4: Temperature-dependent mechanical properties of S960MC used in **Publication I**. (modified from **Publication I**).

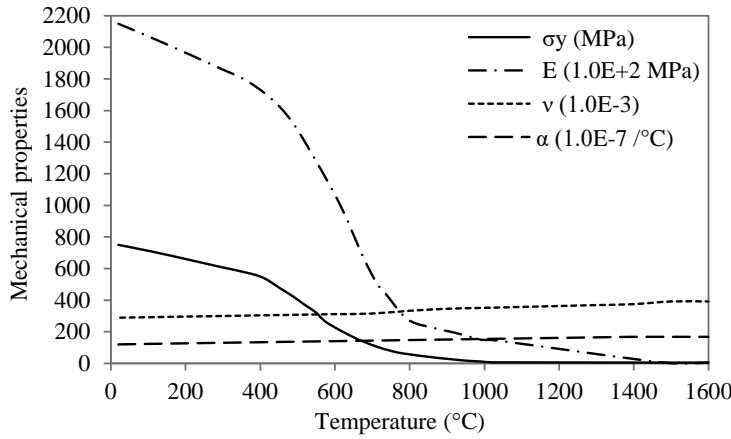


Figure 3.5: Temperature-dependent mechanical properties of S700MC used in **Publications II** and **III** (modified from **Publication II**).

### 3.3 Thermal analysis

Heat conduction, which was formulated by Fourier, states that heat flux density (heat transfer rate per unit area) from a surface is proportional to the negative gradient in the temperature (Serth and Lestina, 2014), as stated by the following equation in differential form:

$$\vec{q} = -k\nabla T \quad (3.1)$$

where  $\vec{q}$  is heat flux density vector (W/m<sup>2</sup>),  $k$  is the thermal conductivity of the material (W/m°C), and  $\nabla T$  is temperature gradient (°C/m). In welding simulation problems, thermal analysis is performed to capture the nonlinear transient thermal fields and obtain nodal temperature histories. In **Publications I–III**, thermal analyses were performed based on the 3D constitutive heat conduction equation, which is derived from Fourier's law of heat conduction, and law of energy conservation:

$$\rho(T)c(T)\frac{\partial T}{\partial t} = \frac{\partial}{\partial x}\left(k(T)\frac{\partial T}{\partial x}\right) + \frac{\partial}{\partial y}\left(k(T)\frac{\partial T}{\partial y}\right) + \frac{\partial}{\partial z}\left(k(T)\frac{\partial T}{\partial z}\right) + \dot{q} \quad (3.2)$$

where  $\rho(T)$  (kg/m<sup>3</sup>) is the temperature-dependent density,  $c(T)$  (J/kg°C) is the temperature-dependent specific heat, and  $k(T)$  (W/m°C) is the temperature-dependent thermal conductivity.  $t$  (s) is time, and  $T$  (°C) represents the temperature.  $x$ ,  $y$ , and  $z$  are axes in the Cartesian coordinate system.  $\dot{q}$  (W/m<sup>3</sup>) is the volumetric heat source density or internal heat generation rate.

### 3.3.1 Heat source modelling

The main task in thermal analysis and welding simulation is modelling a transient heat source. The heat sources in **Publications I, II, and III** were modelled based on a volumetric heat source with double ellipsoidal distribution proposed by (Goldak et al., 1984), which has been used extensively in welding simulation research in the literature (Li et al., 2022; Rikken et al., 2018; Zhang et al., 2022). Modelling of the arc energy transferred from a welding torch to the base and filler materials by this model is performed through defining two heat flux distributions, one for the front half of the heat source, and one for the rear half, as expressed by Equation 3.3 and Equation 3.4, respectively, and shown schematically in Figure 3.6.

$$q_f(x, y, z, t) = \frac{6\sqrt{3}f_f Q}{ab_f c_g \pi \sqrt{\pi}} e^{-3\left(\frac{x^2}{a^2} + \frac{[y-vt-y_0]^2}{b_f^2} + \frac{z^2}{c_g^2}\right)}, \quad y \geq 0 \quad (3.3)$$

$$q_r(x, y, z, t) = \frac{6\sqrt{3}f_r Q}{ab_r c_g \pi \sqrt{\pi}} e^{-3\left(\frac{x^2}{a^2} + \frac{[y-vt-y_0]^2}{b_r^2} + \frac{z^2}{c_g^2}\right)}, \quad y < 0 \quad (3.4)$$

where  $x$ ,  $y$ , and  $z$  are nodal coordinates in the local coordinate system, and  $t$  is time.  $q_f$  and  $q_r$  are heat flux distributions in the front and rear half of the heat source, respectively.  $v$  is the travel speed of the welding heat source, as introduced earlier in Table 2.4 for each publication. As mentioned earlier, the +y-axis was selected as the convention for the welding direction in the entire research.

$Q$  is the welding arc power (transferred energy per unit time), which is also known as heat input, and was calculated in **Publications I–III** by the following equation:

$$Q = UI\eta \quad (3.5)$$

where  $U$  is the voltage of the welding arc, and  $I$  is the welding current, as used in the welding procedure specifications (WPS) and introduced in Table 2.4 for each publication.  $\eta$  is the dimensionless welding efficiency coefficient. For the GMAW process, the efficiency of the heat source has been proposed to be in the range of 0.65–0.93 (Grong and Institute of Metals, 2006; Radaj, 1992). However, in many research papers, the value of  $\eta$  is considered in the range 0.8–0.85 for the GMAW process (Deng et al., 2007b; Deng and Murakawa, 2008). The adjusted values for  $\eta$  and the calculated  $Q$  based on Equation 3.5 in **Publications I, II, and III** are summarized in Table 3.2.

Table 3.2: Welding efficiency coefficients and net heat inputs used in **Publications I–III**.

Publication	$\eta$	$Q$ (J/s)
<b>I</b>	0.80	4480
<b>II</b>	0.85	5525
<b>III</b>	0.85	5525

$a$ ,  $b_f$ ,  $b_r$ , and  $c_g$  in Equation 3.3 and Equation 3.4 are the Goldak's weld pool characteristics. These weld pool parameters can initially be set based on the dimensions of the weld pool from the weld cross section photomicrograph (Goldak and Akhlaghi, 2005). Since these parameters play important roles in the accuracy of thermal analysis, their precise values can be adjusted via iteration and matching the nodal temperature histories from thermal analysis as well as by experimental measurements.  $f_f$  and  $f_r$  are dimensionless fractions of heat deposited in the front and rear half of the heat source. The following expressions are observable by taking the continuity of the heat source into account:

$$\frac{f_r}{b_r} = \frac{f_f}{b_f} \quad (3.6)$$

$$f_f + f_r = 2 \quad (3.7)$$

Provided that Equation 3.6 and Equation 3.7 are combined,  $f_f$  and  $f_r$  can be calculated by the following mathematical relationships:

$$f_f = \frac{2b_f}{b_f + b_r} \quad (3.8)$$

$$f_r = \frac{2b_r}{b_f + b_r} \quad (3.9)$$

Table 3.3 summarizes the heat source parameters adjusted for the simulated case studies after iteration.

Table 3.3: Adjusted heat source parameters used in the simulations (from **Publications I, II, and III**).

Publication	$a$ (mm)	$b_f$ (mm)	$b_r$ (mm)	$c_g$ (mm)	$f_f$	$f_r$
<b>I</b>	4.6	5	14	4	0.53	1.47
<b>II</b>	7	4	10	10	0.57	1.43
<b>III</b>	7	3	10	7	0.46	1.54

It should be noted that the values for the weld pool characteristics and welding efficiency coefficient in each FE simulation were established by fitting the thermal analysis results to experimental measurements through several iterations. The fitting process included matching the simulated FZ and boundaries of HAZ in terms of the shape and dimensions of the transverse cross section to the experimental weld macrograph. Further calibration involved matching the simulated welding thermal cycles for a specific node in terms of the heating rate, cooling rate and peak temperature to the temperature histories captured by thermocouples during the real welding experiment at the corresponding location.

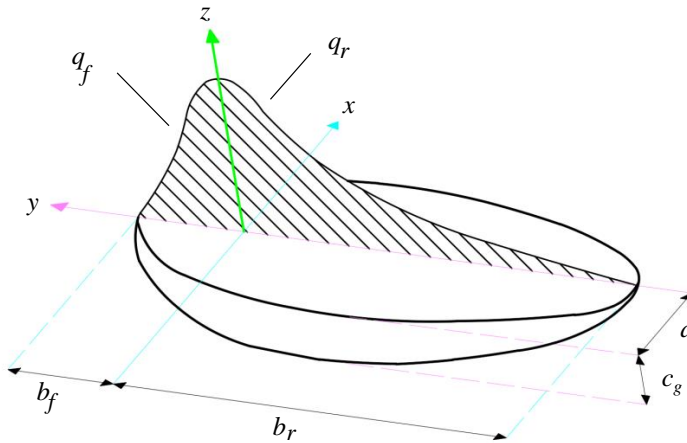


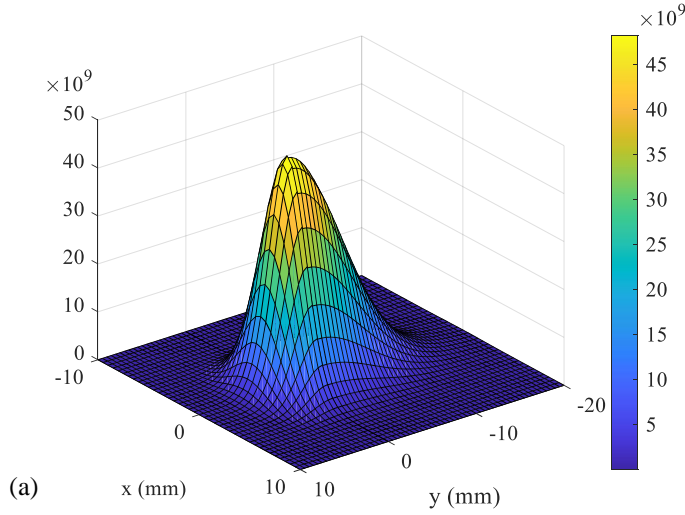
Figure 3.6: Schematic representation of Goldak's double ellipsoidal heat source model (modified from **Publication III**).

To simulate the heat source in each case, related mathematical equations were implemented in the ABAQUS user subroutine DFLUX programmed in FORTRAN. In the bead-on-plate case (**Publication I**), the welding torch was perpendicular to the welding plane; hence, no translation matrix was used. In the case of T-fillet welds (**Publications II and III**), the work angle of the welding torch was either  $45^\circ$  or  $-45^\circ$ . Simulation of the position of the heat source at any specified angle required the points in the global coordinate system to be transformed into a local coordinate system. To do so, two rotation and translation matrices were defined for the work angles of  $-45^\circ$  and  $45^\circ$  for side 1 and side 2, respectively, as described by the following expressions:

$$\begin{bmatrix} x \\ y \\ z \end{bmatrix} = \begin{bmatrix} \cos 45 & 0 & \sin 45 \\ 0 & 1 & 0 \\ -\sin 45 & 0 & \cos 45 \end{bmatrix} \begin{bmatrix} X - X_0 \\ Y - Y_0 \\ Z - Z_0 \end{bmatrix} \quad (3.10)$$

$$\begin{bmatrix} x \\ y \\ z \end{bmatrix} = \begin{bmatrix} \cos 45 & 0 & -\sin 45 \\ 0 & 1 & 0 \\ \sin 45 & 0 & \cos 45 \end{bmatrix} \begin{bmatrix} X - X_0 \\ Y - Y_0 \\ Z - Z_0 \end{bmatrix} \quad (3.11)$$

where  $X$ ,  $Y$ , and  $Z$  are nodal coordinates in the global coordinate system,  $x$ ,  $y$ , and  $z$  are nodal coordinates in a local coordinate system, and  $X_0$ ,  $Y_0$ , and  $Z_0$  are initial points in the global coordinate system. In each simulation case, the position of the heat source was calculated with respect to welding travel speed, time, and nodal coordinates. Based on the implemented mathematical equations, the heat flux distribution at each integration point was calculated as a function of time, nodal coordinates, and welding power. Figure 3.7 graphically shows the volumetric heat source distribution on the top surfaces of the simulated cases.



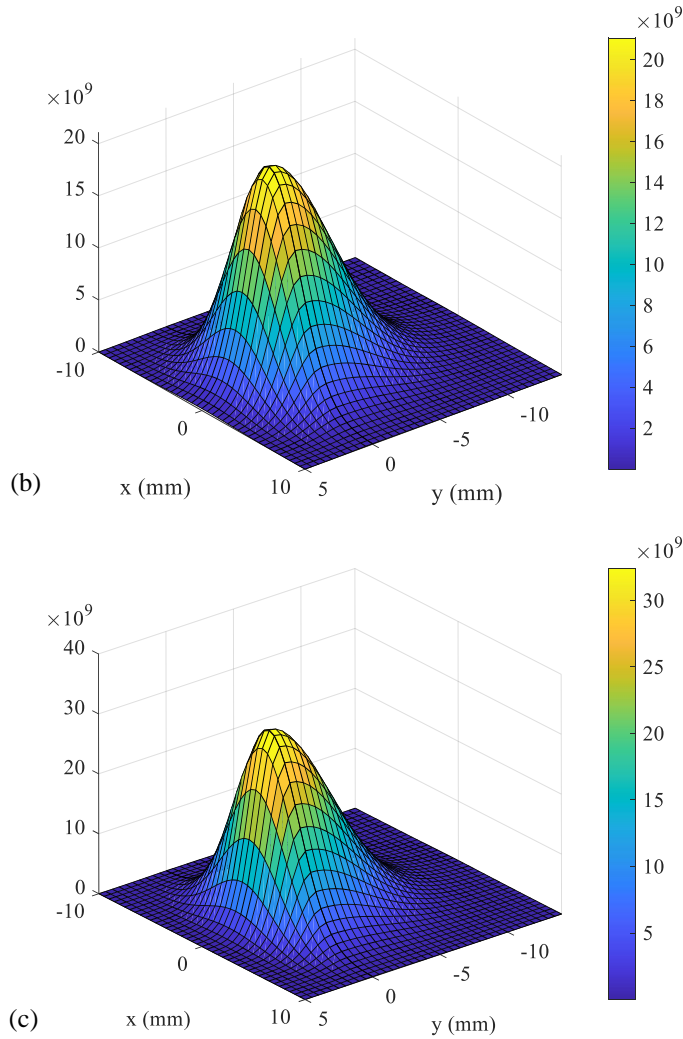


Figure 3.7: Graphical presentation of the heat intensity based on the calibrated Goldak's double ellipsoidal heat source model on the top surface for (a) the bead-on-plate specimen in **Publication I**, (b) the specimen with continuous fillet welds in **Publication II**, and (c) the specimen with non-continuous fillet welds in **Publication III**. For each case, the units on the  $x$  and  $y$  axes are in mm, and the unit of volumetric heat source density on the vertical axis is  $\text{W/m}^3$ .

### 3.3.2 Heat loss modelling (thermal boundary conditions)

To obtain a unique response, every differential equation should be solved subject to unique boundary conditions. Equation 3.2 was solved in each FE simulation under specific boundary conditions to obtain nodal temperature histories. These boundary conditions in thermal analysis are called thermal boundary conditions. In welding simulation problems, thermal boundary conditions are generally referred to as modelling

the heat loss due to convection or radiation or a combination of the two from the free surfaces of the welded specimen.

Heat loss due to convection is generally modelled using Newton's law of cooling. Based on this law, the rate of heat transfer per unit area is proportional to the temperature difference between the body and surrounding area:

$$\dot{q}_{conv} = h_{conv}(T - T_0) \quad (3.12)$$

where  $\dot{q}_{conv}$  (W/m<sup>2</sup>) is the heat loss due to convection from the free surfaces of the body per unit area, and  $h_{conv}$  (W/m<sup>2</sup>°C) is the convective heat transfer coefficient.  $T$  (°C) and  $T_0$  (°C) are the current and ambient temperatures, respectively. Heat loss due to convection dominates in regions with lower temperatures, that is, the areas far from the weld seam (Deng and Murakawa, 2006).

Heat transfer due to radiation is another source of heat loss in welding. Thermal radiation is governed by the Stefan–Boltzmann law, based on which heat transfer rate per unit area is proportional to the fourth power of the difference in the body and the ambient temperature:

$$\dot{q}_{rad} = \varepsilon^* \sigma^* (T^4 - T_0^4) \quad (3.13)$$

where  $\dot{q}_{rad}$  (W/m<sup>2</sup>) is heat loss due to radiation per unit area.  $\varepsilon^* < 1$  is emissivity, which is a dimensionless parameter, and  $\sigma^* = 5.67 \times 10^{-8}$  (W/m<sup>2</sup>K<sup>4</sup>) is the Stefan–Boltzmann constant. Radiation prevails at higher temperatures, that is, regions close to the weld, and is insignificant for low temperature areas (Ahn et al., 2018).

Modelling of the heat loss necessitates calibration of  $h_{conv}$  and  $\varepsilon^*$ . In this research, the combined effect of convection and radiation was considered in the modelling of the heat loss. The combined effect takes into account a temperature-dependent heat transfer coefficient that has been frequently used by different studies in this area (Brickstad and Josefson, 1998; Yaghi et al., 2006) and is defined by the following mathematical expressions:

$$h = \begin{cases} 0.0668 \times T \left( \frac{W}{m^2 \text{ } ^\circ\text{C}} \right) & 0 \leq T \leq 500 \\ 0.231 \times T - 82.1 \left( \frac{W}{m^2 \text{ } ^\circ\text{C}} \right) & T \geq 500 \end{cases} \quad (3.14)$$

where  $h$  is the temperature-dependent heat transfer coefficient. The above equation was performed using the ABAQUS user subroutine FILM and was applied to all the free surfaces that were expected to exchange heat with the surrounding environment. It should be noted that in **Publication I**, only the half of the specimen was considered as the modelling domain; hence, the symmetry plane was excluded as there was no contact



between it and the air. The initial, sink, and ambient temperatures in all the FE simulation cases in **Publications I, II, and III** were set to 20 °C.

### 3.4 Solid-state phase transformation

The effect of phase transformation was investigated for the bead-on-plate specimen in **Publication I**. SSPT kinetics were defined based on the available mathematical models for the present phases during heating and cooling. The dilatometric data, transformation temperatures, linear thermal expansion coefficients, and full volumetric change strains were obtained experimentally for S960 MC. Based on the scanning electron microscopy (SEM) image, the microstructure of the base material is a mixture of bainite and martensite, as shown in Figure 3.8.

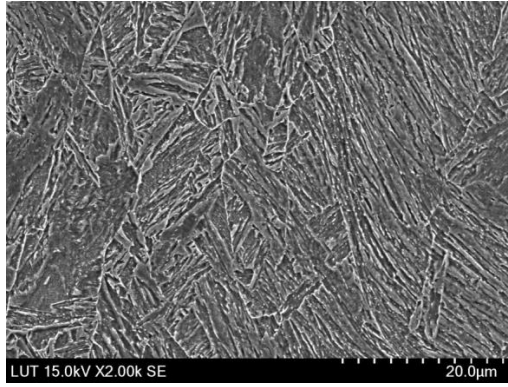


Figure 3.8: Scanning electron microscopy image of S960 MC with bainite and martensite as microstructure constituents (*from Publication I*).

During welding, as the material is heated up, until  $A_1$ , which is the lower critical temperature, no phase transformation occurs. When the material reaches  $A_1$ , the bainitic–martensitic microstructure starts to transform to austenite, and such transformation is called austenitic transformation. Transformation to austenite depends on temperature and is completed when the material reaches  $A_3$ , the upper critical temperature. It was assumed that an increase in the volume fraction of austenite during heating follows a simple linear rule between  $A_1$  and  $A_3$  (Kubiak and Piekarska, 2016), as expressed by the following equation:

$$f_a = \frac{T_{max} - A_1}{A_3 - A_1} \quad (3.15)$$

$$A_1 \leq T_{max} \leq A_3$$

where  $f_a$  is the volume fraction of austenite,  $T_{max}$  is the maximum temperature a material point reaches during austenitic transformation, and  $A_1$  and  $A_3$  are the lower and upper

critical temperatures, respectively.  $A_1$  and  $A_3$  were obtained based on the experimental dilatometric data during heating by using the tangent-intersection method following (Li et al., 2016). In this regard, 775 °C and 863 °C were assigned to  $A_1$  and  $A_3$ , respectively.

In diffusional transformation, the chemical compositions of nascent phases that arise during the transformation of austenite might be different from the composition of the parent phase. Transformation of austenite to bainite is considered a diffusional transformation. For the investigated material, that is, S960 MC, it was assumed that bainite transformation is the only diffusional transformation based on the prevalent HAZ cooling rate from the experimentally determined CCT diagram. The diffusional transformation was simulated based on the Machnienko model, following (Piekarska et al., 2012) and is expressed by the following equation:

$$f_b(T, t) = f_b^{\%} f_a \left[ 1 - \exp \left( -k_a \frac{B_s - T}{B_s - B_f} \right) \right] \quad (3.16)$$

$$B_f \leq T \leq B_s$$

where  $f_b(T, t)$  is the volume fraction of bainite during transformation from austenite.  $f_b^{\%}$  implies the maximum fraction of the bainite forms during the transformation, which was determined based on the CCT diagram and depends on the cooling rate in the range 500 °C–800 °C ( $v_{8/5}$ ).  $f_a$  is the volume fraction of the austenite during heating.  $B_s$  and  $B_f$  are the bainite start and finish temperature, respectively. The values of 520 °C and 460 °C were experimentally obtained and assigned to  $B_s$  and  $B_f$ , respectively.  $k_a$  is a factor whose value is generally accepted to be in the range 2.5–3.

In contrast to diffusional transformation, in diffusionless transformation the nascent phase directly inherits the chemical composition of its parent phase. Martensite transformation in steels occurs in a diffusionless manner in which martensite directly inherits its chemical composition from austenite (Deng, 2009). Transformation of austenite to martensite is accompanied by an increase in the net volume, similar to the transformation of austenite to bainite. Martensite transformation is time-independent and strongly depends on the martensite start temperature ( $M_s$ ). Martensite transformation is assumed to be completed when the martensite finish temperature ( $M_f$ ) is reached. In this situation, further cooling has no effect on the volume fraction of martensite, as no more austenite transforms to martensite. Based on the experimental data, 460 °C and 355 °C were assigned to  $M_s$  and  $M_f$ , respectively. The Koistinen-Marburger kinetics (Koistinen and Marburger, 1959) was employed to mathematically track the volume fraction of the martensite for temperatures below  $M_s$ , as expressed by the following equation:

$$f_m(T) = f_m^{\%} f_a [1 - \exp(-k_m(M_s - T))] \quad (3.17)$$

$$M_f \leq T \leq M_s$$

where  $f_m(T)$  denotes the volume fraction of the formed martensite at temperature  $T$ .  $f_m^{\%}$  is the final fraction of the martensite based on the CCT diagram.  $k_m$  is a parameter to characterize the transformation evolution and was set to 0.05 based on the recommendation of (Li et al., 2015).

### 3.5 Mechanical analysis

In a sequentially coupled welding simulation, the predicted transient temperature histories obtained based on solving the heat conduction equation in thermal analysis, are generally used as an input (thermal load) in mechanical analysis. Structural analysis which is a nonlinear elastic-plastic analysis is performed to evaluate the stress field and material straining based on solving a set of governing partial differential equations. These governing relationships are:

- Equilibrium equation (balance of momentum equation)  
In static problems, the equilibrium equation can be written as follows:

$$\nabla \sigma + F_b = 0 \quad (3.18)$$

where  $\nabla$  is the divergence operator,  $\sigma$  is the Cauchy stress tensor, and  $F_b$  denotes the vector of the body force per unit volume.

- Thermal-elastic-plastic constitutive equation  
The relationship between strain and stress is expressed via a constitutive equation, which in incremental form, can be given by:

$$\{d\sigma\} = [D]\{d\varepsilon\} - [C_{th}]\{dT\} \quad (3.19)$$

And  $[D] = [D^e] + [D^p]$

where  $d\sigma$ ,  $d\varepsilon$ , and  $dT$  are incremental forms of stress, strain, and temperature, respectively.  $D^e$  and  $D^p$  are stiffness matrices in the elastic range and plastic range, respectively, and  $C_{th}$  denotes the thermal stiffness matrix.

#### 3.5.1 Strain decomposition

Calculation of residual stress and distortion in welding simulation requires the total strain component to be determined. In a nonlinear FE analysis, the total incremental strain is determined from incremental displacements. In general, the total strain in incremental form can be calculated as the summation of elastic, plastic, and thermal strain rates, as expressed by the following equation:

$$\dot{\varepsilon}^{total} = \dot{\varepsilon}^e + \dot{\varepsilon}^p + \dot{\varepsilon}^{th} \quad (3.20)$$

where  $\dot{\varepsilon}^{total}$  implies the total strain rate of the material.  $\dot{\varepsilon}^e$ ,  $\dot{\varepsilon}^p$ ,  $\dot{\varepsilon}^{th}$ , and  $\dot{\varepsilon}^{AV}$  are elastic, plastic, thermal, and volumetric change strain rates, respectively. It should be noted that a thermomechanical analysis must take account of elastic, plastic, and thermal strain components. Where the SSPT effect is incorporated in the simulation, the volumetric change strain is also considered. In this regard, the above equation was used for the fillet welded cases in **Publications II** and **III**, where the effect of SSPT was excluded from the calculations. For the bead-on-plate case in **Publication I**, however, the effect of SSPT was considered, and the following equation was applied to calculate the total strain rate:

$$\dot{\varepsilon}^{total} = \dot{\varepsilon}^e + \dot{\varepsilon}^p + \dot{\varepsilon}^{th} + \dot{\varepsilon}^{AV} \quad (3.21)$$

In all the simulations, the elastic strain rate was calculated using the temperature-dependent modulus of elasticity, Poisson's ratio, and generalized Hooke's law. The plastic strain rate was modelled using the temperature-dependent yield strength and isotropic hardening features. The thermal strain increment is originated by thermal expansion and is generally calculated using the temperature-dependent thermal expansion coefficient, as was done in **Publications II** and **III** in this research. When the volumetric change strain component is included to calculate the total strain component, the summation of strain rates due to thermal expansion and volumetric change can be calculated by the following equation, following (Piekarska et al., 2012):

$$\begin{aligned} d\varepsilon^{th+AV} &= d\varepsilon^{th} + d\varepsilon^{AV} \\ &= \sum_i \alpha_i f_i dT - \text{sign}(dT) \sum_i \varepsilon_i^{AV*} df_i \end{aligned} \quad (3.22)$$

where  $\alpha_i$  is the linear thermal expansion coefficient of phase  $i$ . For austenite, bainite, and martensite, the corresponding thermal expansion coefficients  $\alpha_a$ ,  $\alpha_b$  and  $\alpha_m$  were used. The values were calculated based on the experimental dilatometric tests, as presented in Table 3.4. The full volumetric change strain of phase  $i$  ( $\varepsilon_i^{AV*}$ ) during austenite, bainite, and martensite transformations was determined based on the dilatometric tests, as demonstrated in Table 3.4.  $f_i$  is the volume fraction of phase  $i$  calculated using Equations 3.15, 3.16, and 3.17.  $df_i$  is the derivative of these equations for phase  $i$ . The *Sign* in Equation 3.22 is a function which depends on temperature difference; that is, during heating, when the temperature difference is positive, the value of +1 is assigned to *Sign*, and during cooling, when the temperature difference has a negative value, *Sign* is assigned the value of -1.

SSPT kinetics in ABAQUS to modify the strain rates due to thermal expansion and volumetric change was implemented using USDFLD and UEXPAN subroutines. It is possible to define the material properties at each integration point in USDFLD as a function of field variables. In this regard, based on the temperature difference sign (plus during heating and minus during cooling) and the maximum temperature reached by a material point, different scenarios were defined, and the decision was made whether or

not a material point experienced transformation. Equations 3.15, 3.16, and 3.17 were implemented in USDFLD to obtain the nodal volume fractions at each time increment. When a material point underwent transformation, the corresponding equation to calculate the volume fraction of the formed phase was used, and the results were saved inside solution-dependent state variables (SDVs). Once the calculations had been made in USDFLD, they were passed into UEXPAN through SDVs, where Equation 3.22 was implemented to modify the incremental strains.

Table 3.4: The thermal expansion coefficients and full volumetric change strains of austenite, bainite, and martensite related to S960MC.

Constituent	Thermal expansion coefficient ( $\alpha_i$ )	Full volumetric change strain ( $\varepsilon_i^{\Delta V*}$ )		
Austenite ( $\alpha$ )	$\alpha_a$	$2.44 \times 10^{-5}$	$\varepsilon_a^{\Delta V*}$	$0.51 \times 10^{-3}$
Bainite ( $b$ )	$\alpha_b$	$1.15 \times 10^{-5}$	$\varepsilon_b^{\Delta V*}$	$4.10 \times 10^{-3}$
Martensite ( $m$ )	$\alpha_m$	$1.37 \times 10^{-5}$	$\varepsilon_m^{\Delta V*}$	$5.75 \times 10^{-3}$

### 3.5.2 Mechanical boundary conditions

In general, the mechanical boundary conditions in FE simulation problems correspond to the application of external restraints. Welding-induced distortions can be controlled to a large extent by using appropriate welding fixtures. In a welding process, careful design of the welding fixture is an important and yet complex task, as the stiffness of an external constraint is a determining factor in the development of residual stress fields and distortions. In general, lower distortion results when higher restraints are applied, which also causes higher residual stress field and vice versa. An over-constraint condition gives rise to residual stresses while reducing the distortions by increasing the plastic deformation as well as the elastic strains that are responsible for distortions after unclamping (Ahn et al., 2018). Such condition signifies that residual stresses can accumulate and cause welding cracks. On the other hand, in an under-constraint condition, excessive distortion can cause dimensional inaccuracy and instability problems. Therefore, a successful design of the welding fixtures can efficiently minimize laborious and expensive post-weld dimensional corrections and increase the in-service life of the welded structures.

In **Publication I**, welding-induced distortions were studied in free deformation condition, which implies that no external constraint was used in the experiment. In modelling, no mechanical boundary conditions were applied apart from those used merely to prevent rigid body motion, as shown in Figure 3.9. The applied mechanical boundary conditions are valid for this condition in which only half of the specimen is considered as the analysis domain.

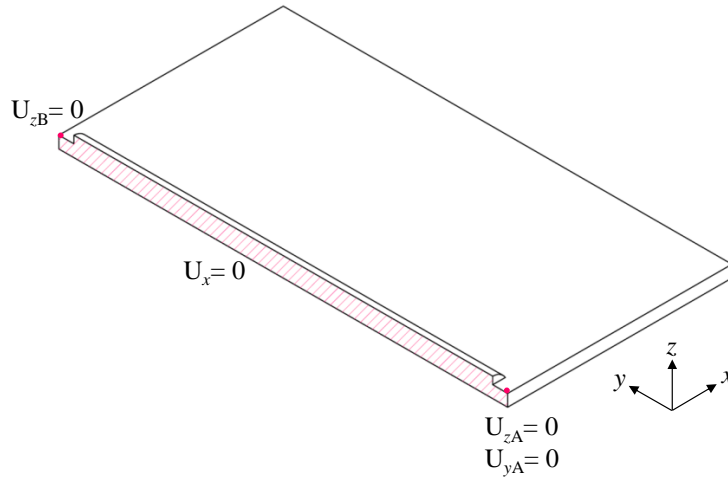


Figure 3.9: The free deformation mechanical boundary conditions for the bead-on-plate welded specimen. At node A, movements in the  $y$ -direction and  $z$ -direction are prevented. At point B, motion of the body in the  $z$ -axis is restricted, and all the nodes in the symmetry plane (red hatch) are prevented from moving in the  $x$ -direction (*modified from Publication I*).

In **Publication II**, two different restraining conditions were applied in the experimental part of the study to investigate the effect of external restraints on the developed welding distortions and residual stress field. In one constraint setup, fixtures were used to clamp the specimen rigidly at one end in a specified area, enabling angular distortion to develop at the free end of the specimen. In the corresponding FE model, all the nodes in the clamped area were restricted translationally and rotationally, as shown in Figure 3.10. In the other constraining condition, welding fixtures were applied at both ends of the specimen in specified areas to rigidly clamp the specimen. The corresponding mechanical boundary conditions in the FE model were set to prevent nodal translation and rotation at the two specified areas, as shown in Figure 3.10. The mechanical boundary conditions to simulate the removal of the clamp at the end of the welding process after the ambient temperature was reached were set only to prevent rigid body motion, as shown in Figure 3.10. It should be noted that in **Publication III**, the mechanical boundary conditions were identical to those applied in **Publication II**.

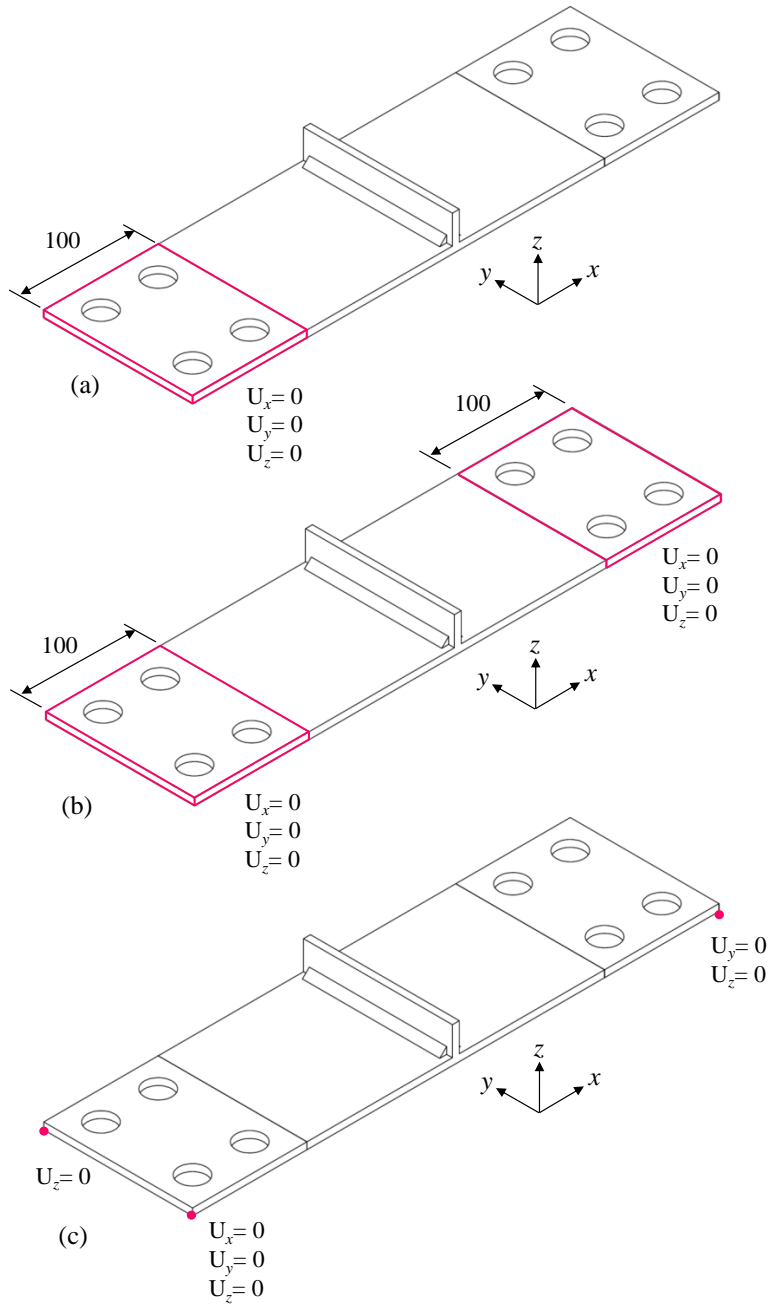


Figure 3.10: Schematic presentation of the mechanical boundary conditions for: (a) specimens FS1 and FS2, (b) specimens CS1 and CS2, and (c) removal of the welding fixtures after the ambient temperature was reached (*modified from Publication II*).

## 4 Results and discussion

The results of this research in terms of the simulated temperature fields, welding-induced distortions, and residual stresses (investigated in **Publications I, II, and III**) and the results of the elevated-temperature constitutive mechanical behaviour of UHSSs (investigated in **Publication IV**) are summarized and discussed in separate sections.

### 4.1 Thermal fields

Correct prediction of mechanical response necessitates accurate prediction of temperature distribution during welding. An accurately predicted weld pool geometry is one of the indicators that temperature fields have been correctly simulated. For each case study, the size and shape of the simulated weld pool were matched against the experimentally observed FZ from the polished weld cross section. Figure 4.1(a) shows a comparison between the length and width of the weld pool on the top surface and the corresponding simulation for the bead-on-plate case from **Publication I**. The depth of penetration from the simulation versus the experimental macrograph of the welded specimen at mid-section in a longitudinal direction are depicted in Figure 4.1(b). In a similar manner, the simulated weld pool geometry for the T-fillet welded specimen in **Publication II** in the mid-section of the specimen against the experimental macrograph is shown in Figure 4.2. Regarding the non-continuous fillet weld case in **Publication III**, the simulated weld pool geometry at 5 mm from the start of the weld segment is compared with the corresponding weld macrograph, as shown in Figure 4.3.

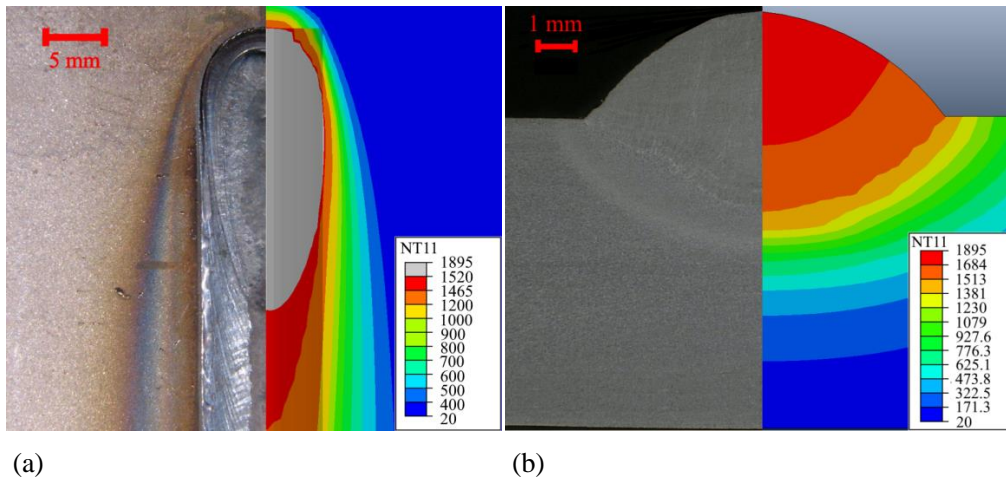


Figure 4.1: The simulated welding temperatures (NT11) and the boundaries of the FZ for the bead-on-plate specimen: (a) top surface and (b) through thickness (*modified from Publication I*).



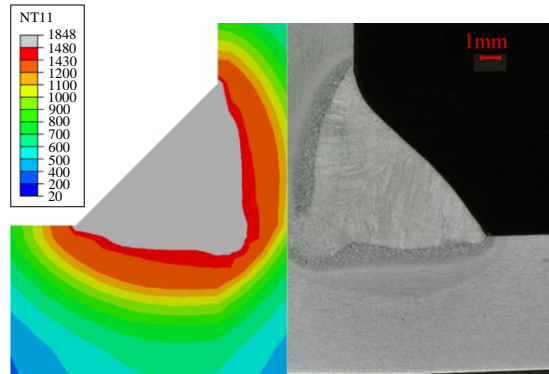


Figure 4.2: The simulated welding temperatures (NT11) and the boundaries of the FZ for the fillet welded specimen in **Publication II** in the thickness direction (*modified from Publication II*).

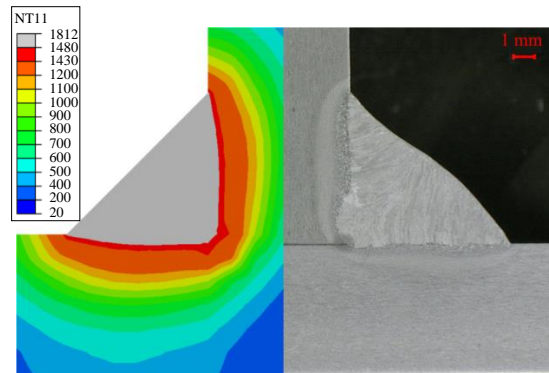


Figure 4.3: The simulated welding temperatures (NT11) and the boundaries of the FZ for the fillet welded specimen in **Publication III** in the thickness direction (*modified from Publication III*).

As can be seen in Figure 4.1, the width and depth of the weld pool for the bead-on-plate specimen are in close agreement with the corresponding experimental weld macrograph. For the continuous and non-continuous fillet welded specimens, in each case, the depth of penetration is well-captured by simulation, and the boundaries of FZ reasonably match the corresponding weld macrographs, as shown in Figure 4.2 and Figure 4.3, respectively.

It should be noted that the four welded cases in **Publications II** and four in **Publication III** were simulated, and the results of thermal analyses were verified against the thermocouple measurement. As the welding parameters and, accordingly, heat inputs were identical in each publication, only one specimen was chosen from each study for the sake of comparison with the experimental measurement in terms of temperature

distribution. In this regard, II-FS2 from **Publication II** and III-FS1 were chosen for the mentioned comparisons.

A close match between the thermal cycles recorded by thermocouples and the corresponding simulated nodal temperatures is another indicator of the accuracy of a thermal analysis. In this respect, the time-temperature curves recorded by thermocouples versus the simulation results for the corresponding nodes in the bead-on-plate, continuous fillet weld (II-FS2), and short fillet weld (III-FS1) cases are shown in Figure 4.4, Figure 4.5 and Figure 4.6, respectively.

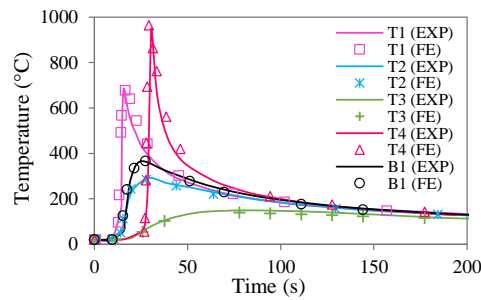


Figure 4.4: The simulated time-temperature curves versus the experimental thermal cycles obtained by thermocouple measurement at different distances from the weld seam on the top and bottom surfaces of the bead-on-plate specimen (*modified from Publication I*).

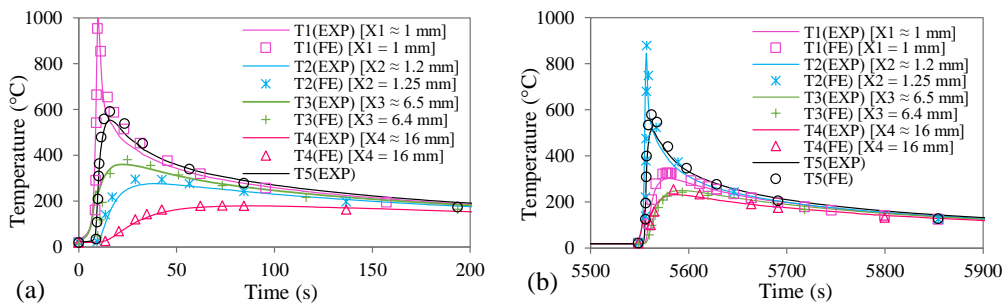


Figure 4.5: The simulated temperature histories versus the experimental thermal cycles obtained by thermocouple measurement for the continuous fillet weld case (II-FS2): (a) the first welding pass, and (b) the second welding pass. X1–X4 are the distances from the weld toes, measured post welding, and the corresponding nodes in simulation (*modified from Publication II*).

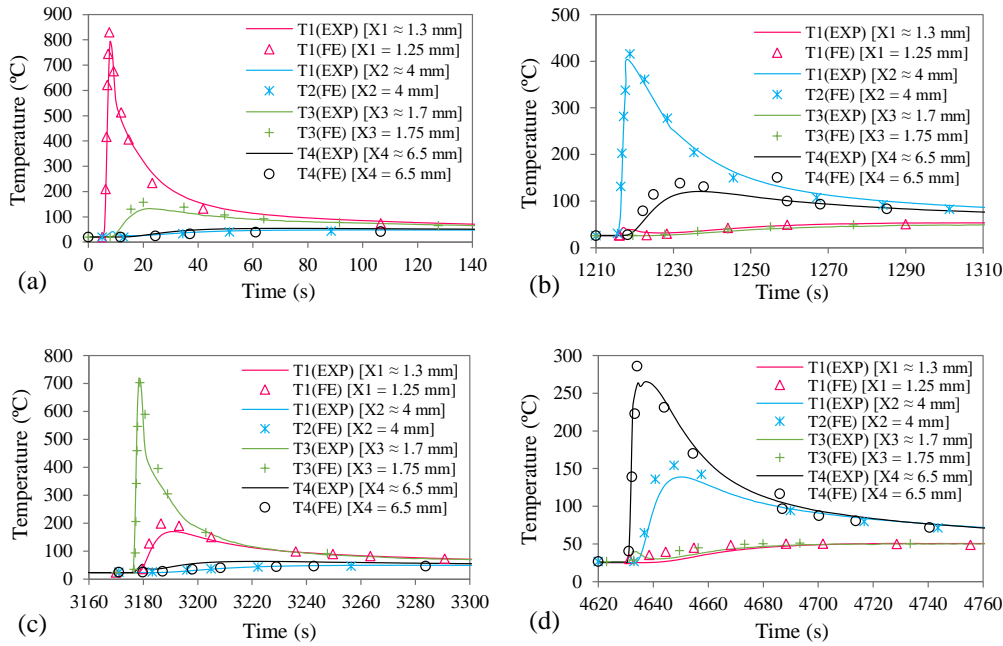


Figure 4.6: The simulated temperature histories versus the experimentally obtained thermal cycles for the non-continuous fillet weld case (III-FS1): (a) W1, (b) W2, (c) W3, and (d) W4. X1–X4 are the experimentally measured and corresponding nodal distances from the weld toe (*modified from Publication III*).

## 4.2 Microstructure prediction

Metallurgical analysis for the bead-on-plate welded case in **Publication I** was performed. Phase transformation kinetics during heating and cooling were involved, and the microstructure of all the nodes whose temperatures exceeded  $A_1$  was predicted. Figure 4.7 shows the graphical presentation of the calculated fractions of bainite and martensite transformed from austenite during cooling in the mid-section of the specimen in a longitudinal direction.

As mentioned earlier, based on the implemented transformation kinetics, the volume fraction of the phases arising during cooling upon austenite decomposition was calculated. The material at each node is either transformed or untransformed. As shown in Figure 4.7(a), the red-coloured region (volume fraction equal to 1 in the contour bar) is the region with no transformation, that is, temperatures below  $A_1$ . The blue-coloured region, where the volume fraction is zero, represents the region fully transformed to austenite, that is, temperature above  $A_3$ . The area between these two regions has undergone an incomplete transformation. During cooling, the regions that partially or fully transformed to austenite underwent either bainitic or martensitic transformation. The

simulated volume fractions of bainite and martensite are shown in Figure 4.7(b) and Figure 4.7(c), respectively.

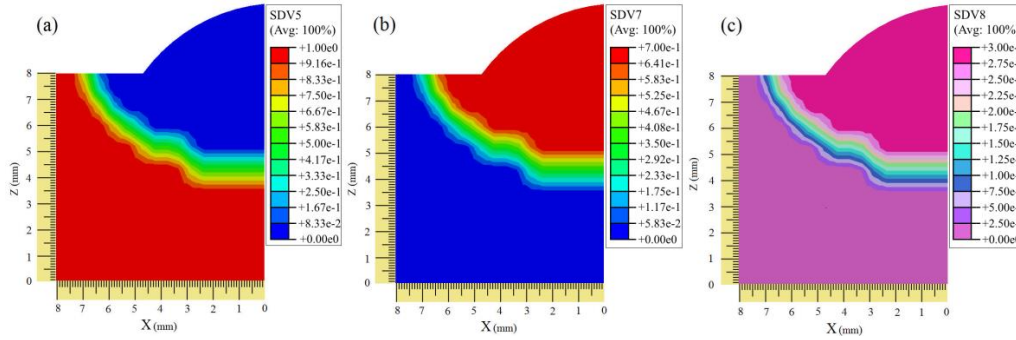


Figure 4.7: The simulated volume fractions: (a) untransformed base material, (b) bainite, and (c) martensite (*modified from Publication I*).

Transformation of the base material to austenite and subsequent austenite decomposition to bainite and martensite during a thermal cycle as a function of time for an arbitrary node are shown in Figure 4.8. The node was located 6.2 mm from the weld centre line in the mid-section of the specimen in a longitudinal direction on the top surface.

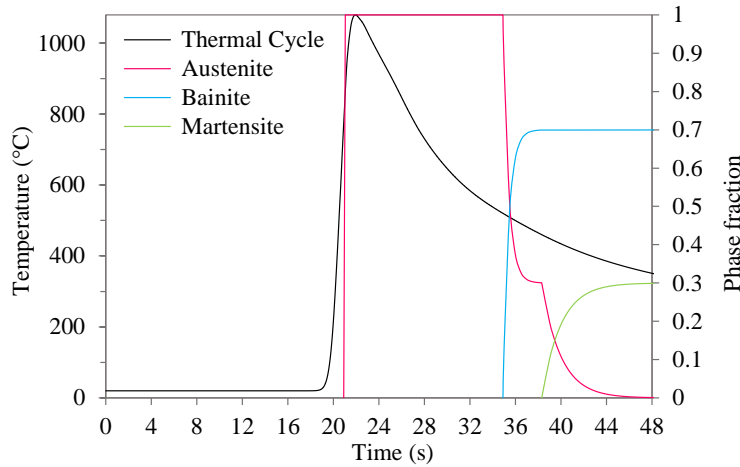


Figure 4.8: Welding thermal cycle for a node in the HAZ (6.2 mm from the weld centre line) and formation of microstructural constituents during heating and cooling (*modified from Publication I*).

### 4.3 Welding deformation

Welding deformations in **Publication I**, that is, angular and out-of-plane bending distortions were simulated with and without considering the effect of SSPT and compared with experimental measurements, as shown in Figure 4.9 and Figure 4.10 , respectively.

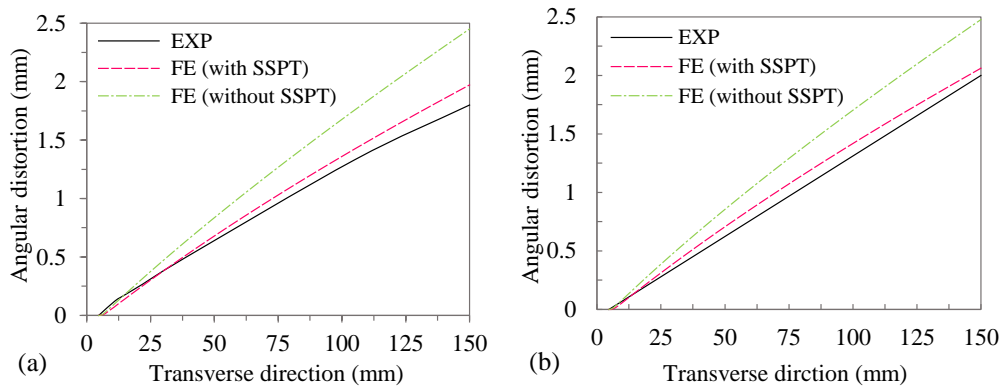


Figure 4.9: The simulated angular distortion with and without considering the effect of SSPT versus the experimental measurement: (a) Path 1 and (b) Path 2 (*modified from Publication I*).

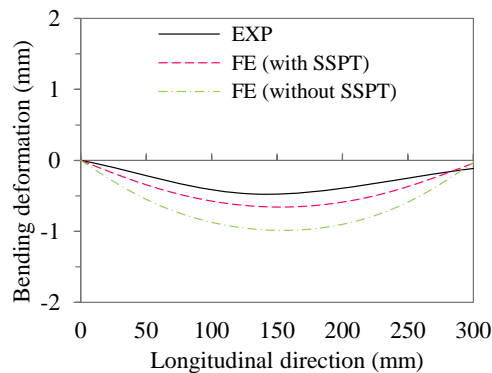


Figure 4.10: The simulated out-of-plane bending distortion with and without considering the effect of SSPT versus the experimental measurement along Path 3 (*modified from Publication I*).

As shown in Figure 4.9, the simulation results reasonably agree with the experimental measurements. However, the model in which the SSPT effect was incorporated more accurately predicted the angular distortion along the two measurement paths. As can be seen in Figure 4.10, bending distortion in this case is smaller than angular distortion and limited to a fraction of a millimetre. The predictions of both models are in acceptable agreement with the experimental measurements. The estimations provided by the model

considering SSPT effect maintain a smaller deviation from the experimental values, which shows the relative superiority of this model to the other. The deformation values predicted by the model in which SSPT was incorporated are always smaller than those predicted by that which neglected SSPT. The volume increase during bainitic and, mainly, martensitic transformations results in smaller distortion, as was also studied by (Deng, 2009).

With respect to welding distortion for the welded cases in **Publication II**, the contours of the final angular distortion for II-FS1 and II-FS2 are shown in Figure 4.11. As is observable, the pattern of angular distortion for both cases, fixed at one end and welded with different welding sequences, is similar with a small difference in the magnitude of the maximum angular distortion. The patterns of angular distortion for specimens II-CS1 and II-CS2 before and after removal of the clamps are shown in Figure 4.12 and Figure 4.13, respectively. As can be seen in Figure 4.12(a) and Figure 4.13(a), before removal of the external restraints both specimens experienced very small deformation, which increased to slightly less than 4 mm at each end after the clamps were removed, as shown in Figure 4.12(b) and Figure 4.13(b).

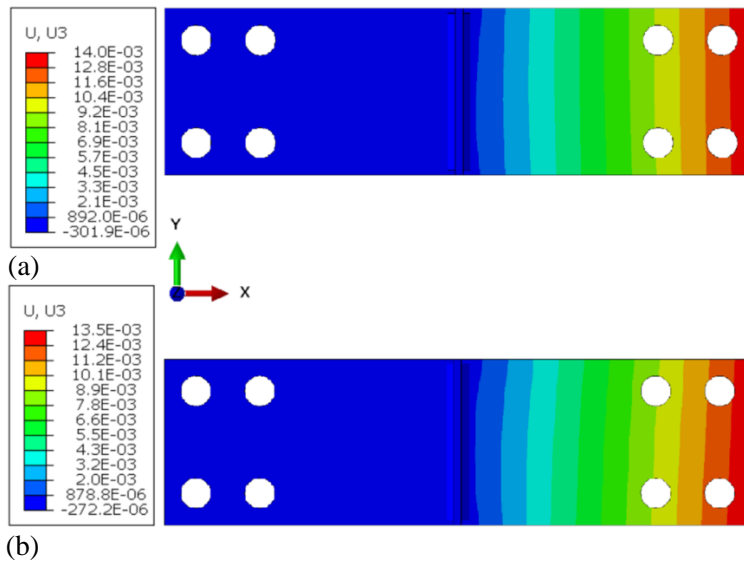


Figure 4.11: The simulated contours of final angular distortion for (a) II-FS1 and (b) II-FS2. The units are in mm (*modified from Publication II*).

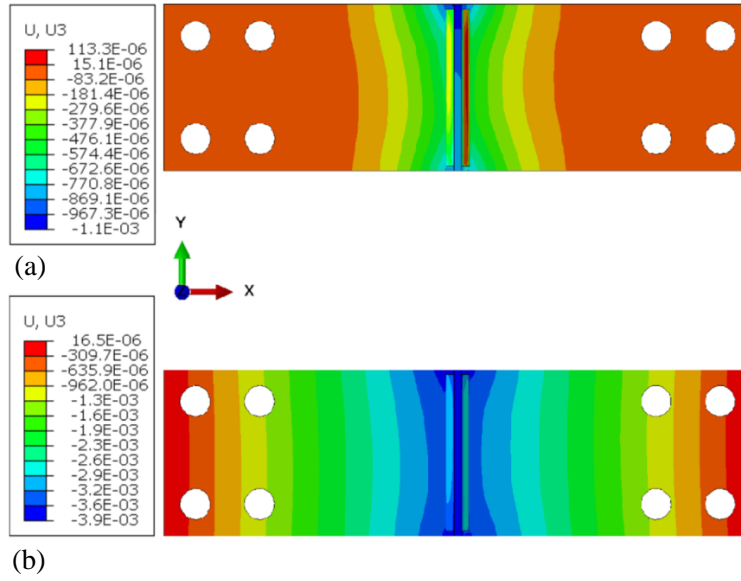


Figure 4.12: The simulated contours of final angular distortion for II-CS1 (a) before the release of the specimen from the fixtures, and (b) after the clamps were removed. The units are in mm (modified from **Publication II**).

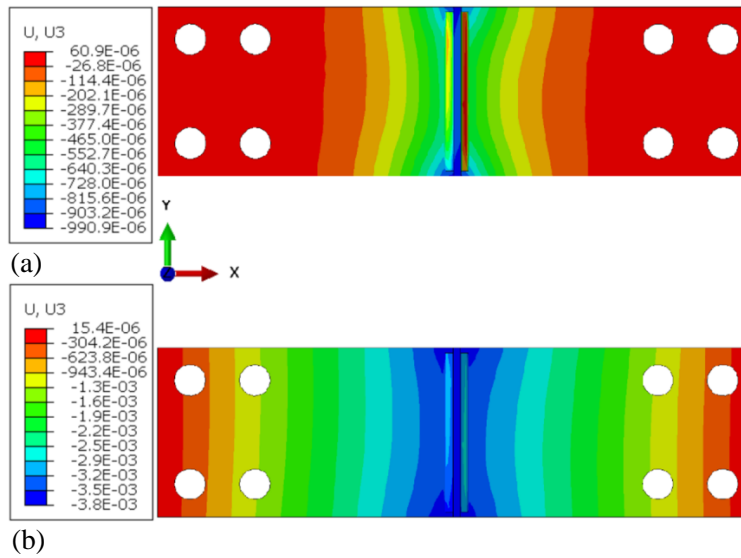


Figure 4.13: The simulated contours of final angular distortion for II-CS2 (a) before the release of the specimen from the fixtures, and (b) after the clamps were removed. The units are in mm (modified from **Publication II**).

The accuracy of the developed FE model in terms of angular distortion prediction was evaluated by comparing the results of the simulation and experimental measurement for all the welded specimens. Figure 4.14 compares the simulated angular distortion for each case versus the corresponding experimentally measured deflection.

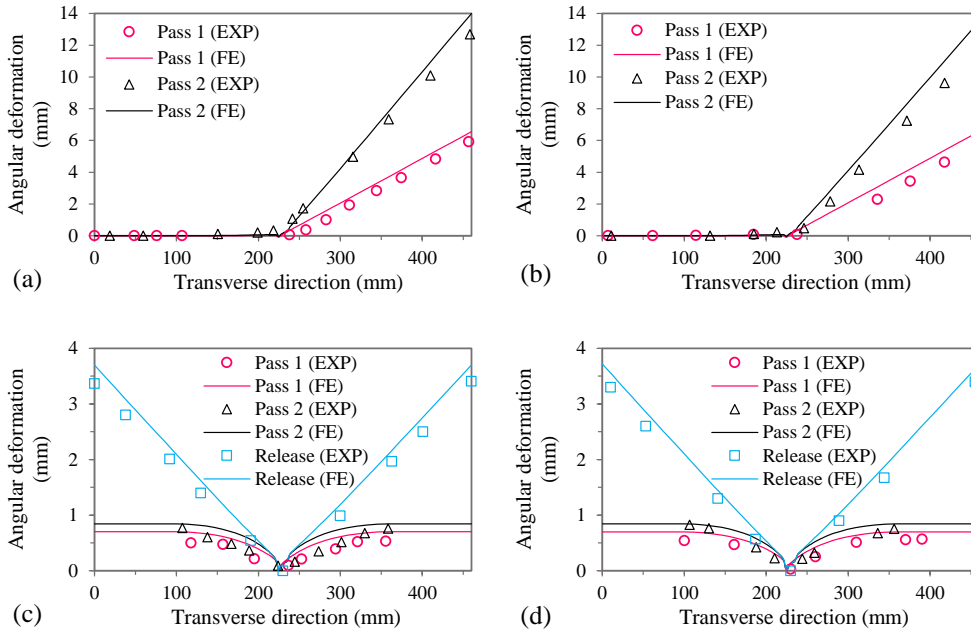


Figure 4.14: The simulated results versus the experimentally measured sequential and cumulative angular distortions for (a) II-FS1, (b) II-FS2, (c) II-CS1, and (d) II-CS2 (*modified from Publication II*).

As can be seen in Figure 4.14, in general, the FE model was able to predict the developed angular distortion in all cases with reasonable accuracy. The percent errors regarding the maximum deflection in specimens II-FS1 and II-FS2 after cooling are almost 9% and 11%, respectively. As is observed, the maximum angular distortion in II-FS2 is slightly smaller than that in II-FS1. This implies that when T-fillet joints are welded with one welding pass per side and clamped at one end, the resulting angular distortion is smaller if the two passes are applied in the opposite directions than in the same direction. Although the difference in this study compared to the maximum resulted deflection is negligible, this matters in real applications, where the weld length and dimension of the specimen in transverse direction are larger and can be important and adopting the opposite directions for welding passes can lead to smaller deformation than that resulting from applying the welding passes in same direction.

For II-CS1 and II-CS2, to compare the results of the simulation with the experimental data, the simulated angular distortion values were moved along the vertical axis to set the minimum distortion value to zero, as shown in Figure 4.14(c) and Figure 4.14(d). As



expected, when the specimens were still clamped rigidly at both ends, after welding and after the ambient temperature was reached, the resulting angular distortions were small. As can be seen, the change in the welding direction had a minor impact on the final deflection of II-CS1 and II-CS2. For both specimens, the measured and simulated values of the maximum angular distortion before the release from the welding fixtures were 0.75 mm and 0.84 mm, respectively, which makes a percent error of 10.7%. Although the final deflection was quite small when the specimens were still clamped, the share of pass 1 from the simulation is 0.70 mm in contrast to 0.14 mm for pass 2. Understanding the difference between the magnitudes of sequential angular distortions may be important during the welding of real structures such as large plate girders. Correctly pre-aligning welded joint members might be helpful to control the sequential distortions. Releasing the residual stresses after the external restraints were removed caused angular distortion in II-CS1 and II-CS2. The simulated results in this context are in acceptable agreement with experimental measurements with an approximate percent error of 8.4% for both cases. As can be seen, the values of the final angular distortion after release from the restraints for the specimens clamped at both ends are considerably smaller than those for the specimens clamped at one end. In this regard, as plotted in Figure 4.14(a), the simulated cumulative angular distortion in II-FS1 is approximately 14 mm, which is almost twice as large as the final angular distortion in II-CS1, which is 7.20 mm, plotted in Figure 4.14(c). This indicates the importance of external constraints to control the distortion in welded joints.

The accuracy of the developed FE model in predicting the sequential and cumulative angular distortions of the welded specimens in **Publication III** under different boundary conditions and welding sequences was quantitatively evaluated. In this regard, the simulated and experimentally measured angular distortions for III-FS1 and III-FS2 are plotted in Figure 4.15. As the sequential angular distortion due to each short fillet weld (W1–W4) for the welded cases III-CS1 and III-CS2 during welding was very small, only the simulated results in terms of angular distortion before the clamps were removed are presented, as shown in Figure 4.16.

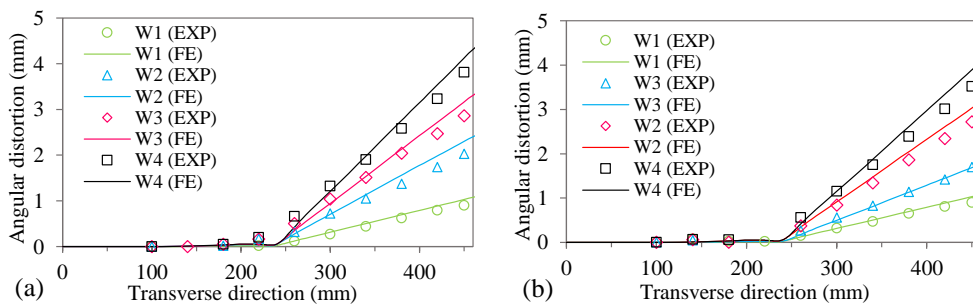


Figure 4.15: The simulated results versus the experimentally measured sequential angular distortion for (a) III-FS1 and (b) III-FS2 (*modified from Publication III*).

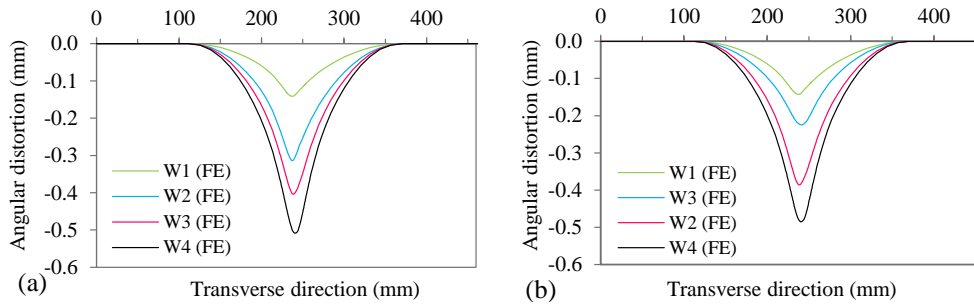


Figure 4.16: The simulated sequential angular distortion before removal of the external restraints for (a) III-CS1 and (b) III-CS2 (*modified from Publication III*).

As can be seen in Figure 4.15, the predictions of the developed FE model in terms of angular distortion in III-FS1 and III-FS2 are in reasonable agreement with the measurement data. The final angular distortion magnitudes for III-FS1 are 3.95 mm and 4.61 mm, based on experimental measurement and simulation, respectively, with a percent error of 16.7%. The final angular distortion values for III-FS2 from measurement and simulation are 3.76 mm and 4.34 mm, respectively, which makes a percent error of 15.4%. The results of the simulation and measurement data both indicate that slightly larger angular distortion is developed in III-FS1 than in III-FS2. In real structures where the design requires that short welds or several tack welds prior to the final weld pass are applied, the correct welding sequence can minimize the considerable distortion that results from a large number of short welds. The final angular distortion for III-CS1 and III-CS2 before release from the welding fixtures, based on the plots in Figure 4.16, are 0.50 mm and 0.48 mm, respectively.

The influence of the external restraints on the induced cumulative angular distortion was numerically investigated by plotting the results of the FE simulation for all the cases after the external constraints were removed, as shown in Figure 4.17.

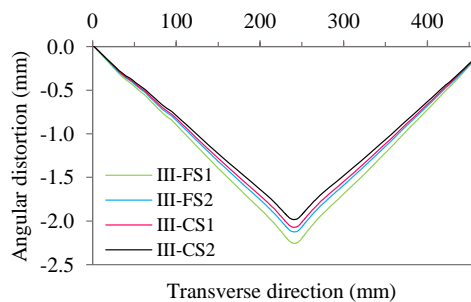


Figure 4.17: The simulated final angular distortion after the external restraints were removed for the welded cases in **Publication III** (*modified from Publication III*).

As expected, in III-FS1 and III-FS2, which were clamped at one end and free deformation was thus permitted in the transverse direction, release from the external restraints after reaching the ambient temperature had no effect on the final angular distortion magnitudes. Clamping at both ends of the specimens with a higher degree of geometrical constraints, as was applied in III-CS1 and III-CS2, prevented angular distortion during welding. In general, external constraints with great stiffness cause low distortion and a high residual stress field, as plastic strains are increased and the remaining elastic strains reduced. The release of elastic strains after the clamps are removed causes distortion (Ahn et al., 2018). As can be seen in Figure 4.17, the smallest distortion was obtained for III-CS2, and the largest distortion occurred in III-FS1. It is observable that external restraint had larger effects than welding sequence on the final angular distortion of the welded cases in this study.

A comparison was drawn between the welded cases II-FS1 and II-CS1 from **Publication II** and III-FS1 and III-CS1 from **Publication III**, as plotted in Figure 4.18.

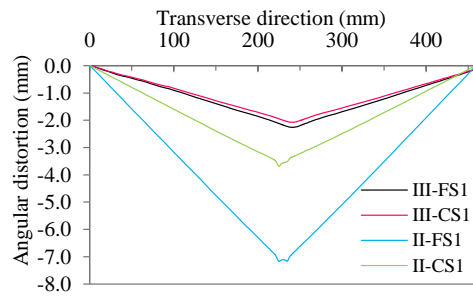


Figure 4.18: The simulated final angular distortion after removal of the external restraints for the welded cases III-FS1, III-CS1, II-FS1 and II-CS1 (*modified from Publication III*).

Comparison between II-FS1 and II-CS1 shows that in a fillet joint being welded continuously over the length of the joint, using external constraints with higher stiffness can considerably reduce the final angular distortion. However, comparison between III-FS1 and III-CS1 demonstrates that in the case of short non-continuous welds, final distortion was only slightly better prevented by using high restraints. Therefore, in the case of tack welds or short intermittent fillet welds, other distortion control techniques, such as applying pre-deformation may be considered.

#### 4.4 Welding residual stress

Study of the welding-induced residual stresses in this research was conducted in **Publications II** and **III**. In order to validate the simulation results, experimental measurements were carried out, as explained in Chapter 2.

In **Publication II**, along the specified paths on the top surfaces of the specimens (see Figure 2.8) transverse residual stresses were experimentally measured. Measurements started approximately 1 mm from the weld toes for an approximate length of 25 mm towards the outer edges. The results of the welding simulation in terms of transverse residual stress for the welded specimens II-FS1, II-FS2, II-CS1, and II-CS2 were compared against the measurement results, as shown in Figure 4.19, Figure 4.20, Figure 4.21, and Figure 4.22, respectively.

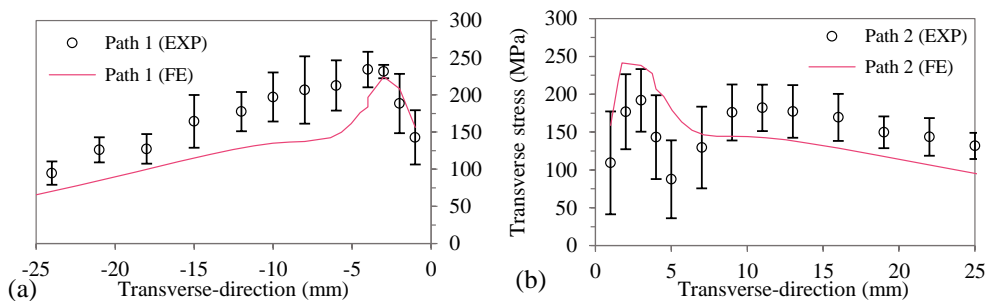


Figure 4.19: The simulated transverse residual stresses versus the measurement for II-FS1: (a) path 1 and (b) path 2 (*modified from Publication II*).

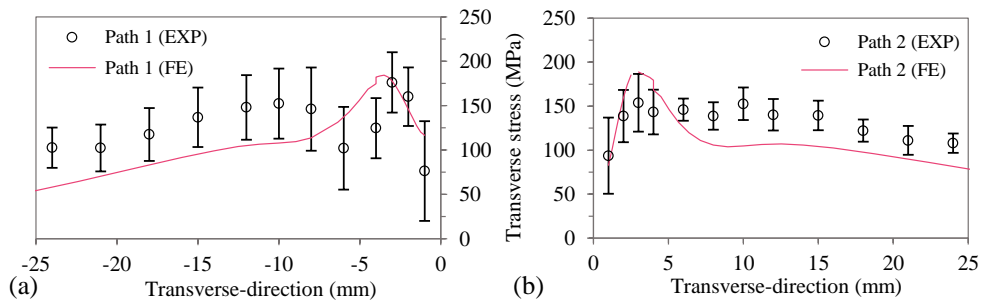


Figure 4.20: The simulated transverse residual stresses versus the measurement for II-FS2: (a) path 1 and (b) path 2 (*modified from Publication II*).

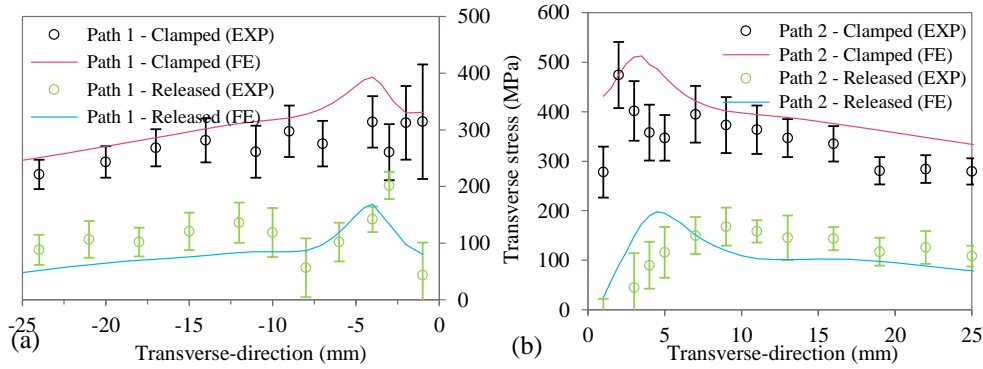


Figure 4.21: The simulated transverse residual stresses versus the measurement for II-CS1 before and after removal of the clamps: (a) path 1 and (b) path 2 (*modified from Publication II*).

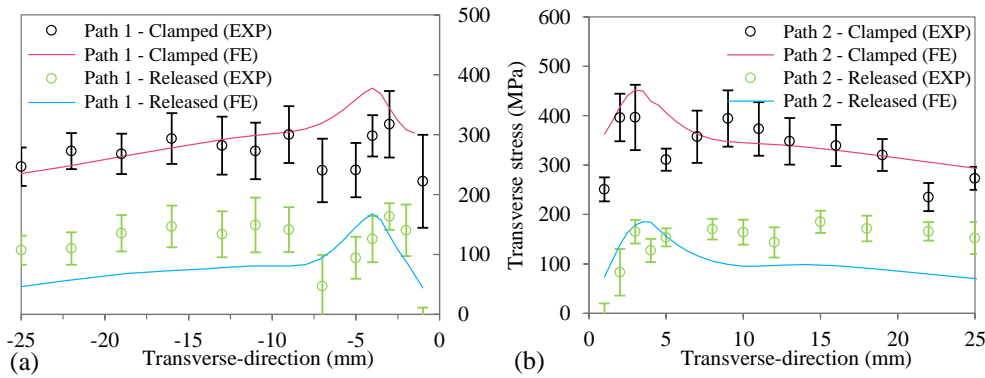


Figure 4.22: The simulated transverse residual stresses versus the measurement for II-CS2 before and after removal of the clamps: (a) path 1 and (b) path 2 (*modified from Publication II*).

As can be seen in Figure 4.19 and Figure 4.20, the patterns of transverse residual stress distribution for both II-FS1 and II-FS2 are similar with peak magnitudes in the HAZ with approximate distances of 3–4 mm from the weld toes. The results of the simulation are in reasonable agreement with the XRD measurements in terms of the peak magnitude and approximate location of the maximum stress value in the HAZ. It should be noted that an error band is always involved in XRD measurements, which should be considered when comparing them with FE results. The simulated maximum stress values along Path 1 and Path 2 for II-FS1 are 224 MPa and 241 MPa, respectively. The peak magnitudes of transverse stress for II-FS2 are 174 MPa and 189 MPa, along Path 1 and Path 2, respectively. As is observable, the maximum transverse stress values of II-FS2 are slightly smaller than those of II-FS1, which shows the effect of weld pass arrangement.

As shown in Figure 4.21 and Figure 4.22, the results of the simulation in terms of transverse residual stress for both II-CS1 and II-CS2 are in acceptable agreement with the measurement data. Using external constraints with a higher geometrical constraint (i.e., rigid clamping at both ends of the specimens) prevented angular distortion to a large extent while giving rise to residual stress, as anticipated. The patterns of stress distribution before and after release from the welding fixtures are similar, albeit with different magnitudes. In the clamped condition, the simulated tensile residual stress in II-CS1 reaches a maximum value of 393 MPa and 512 MPa on Path 1 and Path 2, respectively. The peak magnitudes in II-CS2 are 378 MPa and 452 MPa, along Path 1 and Path 2, respectively. After release from the clamps, residual stresses in both II-CS1 and II-CS2 ease and fall in magnitude, and the distribution patterns become comparable to those of II-FS1 and II-FS2, although the peak magnitudes for II-FS1 and II-FS2 are slightly greater.

Comparison between the simulated longitudinal residual stresses developed in II-FS1 and II-FS2 is shown in Figure 4.23. In a similar manner, comparison between the longitudinal stresses of II-CS1 and II-CS2 before and after unclamping is shown in Figure 4.24.

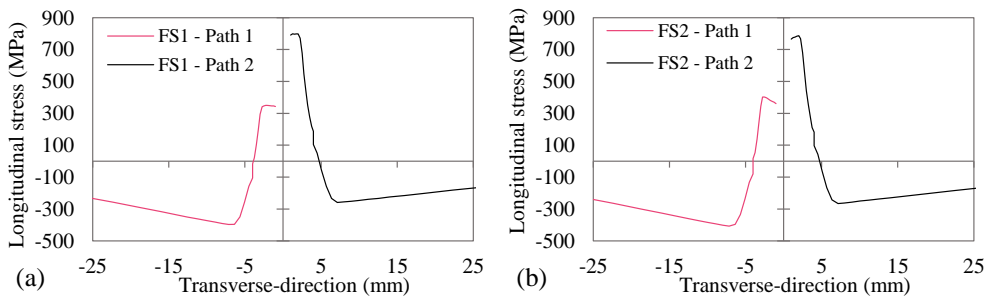


Figure 4.23: The simulated longitudinal residual stresses along Path 1 and Path 2 for (a) II-FS1, and (b) II-FS2 (*modified from Publication II*).

As can be seen in Figure 4.23, change in the weld pass arrangement did not have a significant effect on longitudinal stress, as the general stress distribution pattern and peak magnitudes (tensile and compressive) in both welding cases remain almost unchanged. Moving far from the weld toe, tensile stress falls in magnitude and reaches a peak compressive value at approximately 7 mm from the weld toe. In both cases, the magnitude of tensile stress in Path 2 was greater than that of Path 1. A possible reason for this phenomenon can be thermal effects: the heat of weld from the second welding pass may be responsible for modifying and redistributing stresses in the first welding pass. A similar matter was reported by (Ahn et al., 2018).

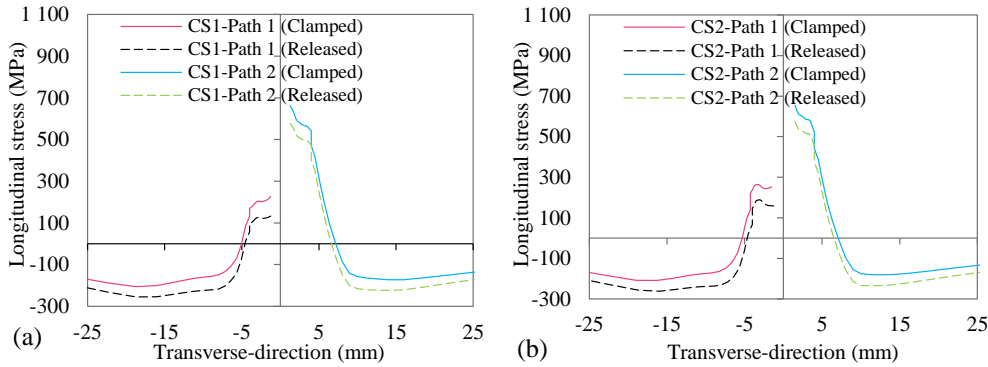


Figure 4.24: The simulated longitudinal residual stresses along Path 1 and Path 2 before and after unclamping for (a) II-CS1 and (b) II-CS2 (*modified from Publication II*).

The pattern of stress distribution for II-CS1 and II-CS2, as shown in Figure 4.24, is quite similar to that reported for II-FS1 and II-FS2. The maximum stress values for II-CS1 and II-CS2 are comparable to, although smaller than, those for II-FS1 and II-FS2. As can be seen, the pattern of stress distribution in both cases experienced no changes after unclamping. Removal of the external constraints only slightly affected the level of longitudinal residual stress by reducing the tensile and increasing the compressive stresses through a shift towards the compressive side compared to the clamped condition. Unclamping had a greater effect on transverse stresses, as shown in Figure 4.21 and Figure 4.22. The sensitivity of transverse and longitudinal residual stresses to the stiffness of external constraints was investigated numerically for II-FS1 and II-CS1. In this regard, an arbitrary node in the mid-section of each case in the welding direction located 1 mm from the weld toe was chosen, and the evolution of residual stresses by completion of the thermal cycles against time was plotted, as shown in Figure 4.25.

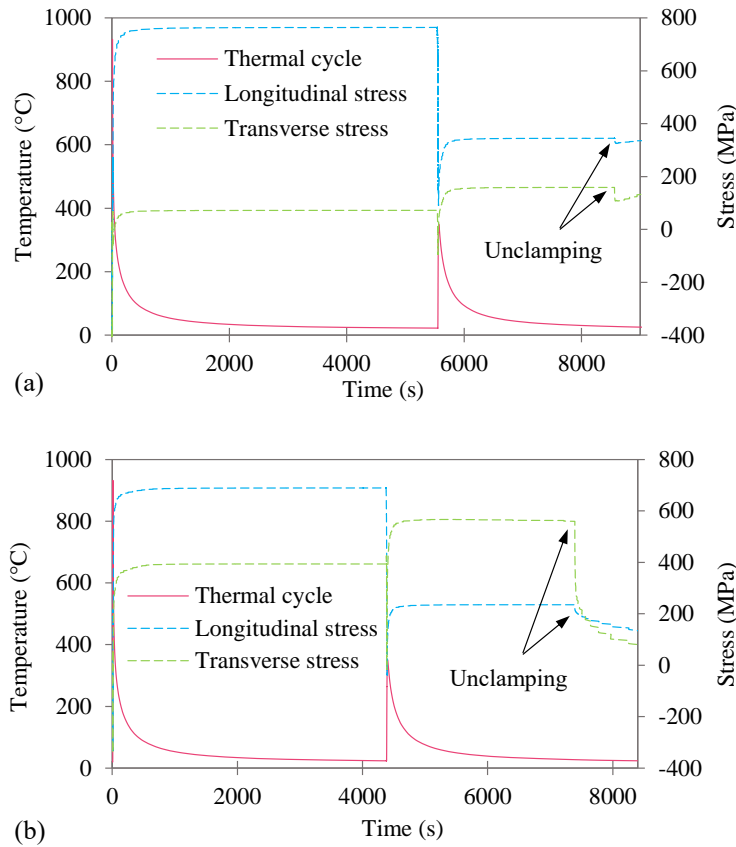


Figure 4.25: Simulation of the evolution of transverse and longitudinal residual stresses for an arbitrary node at 1 mm from the weld toe for (a) II-FS1 and (b) II-CS1 (*modified from Publication II*).

As can be seen in Figure 4.25(a), at the beginning of the first welding pass and when a high temperature of approximately 900 °C had been reached for the selected node, both longitudinal and transverse stresses are compressive due to expansion in the near-weld regions. As the specimen starts to cool down, the residual stresses start to rise and reach their maximum values. The maximum values for the tensile longitudinal and transverse stresses remain constant during the cooling and while the ambient temperature is reached. As the welding of the second pass starts, the residual stresses start to decline due to the welding heat and expansion of the heated areas. This fall, however, due to the higher distance of the heat source from the selected node, is lower than that seen in the first welding pass. The subsequent cooling stage causes the residual stresses to rise and assume their final states while they are still in their related welding fixtures. It is observable that unclamping had almost no effect on the stress state in II-FS1. The scenario for II-CS1 is different, as removal of the welding fixtures caused both longitudinal and transverse



stresses to fall. The decrease in the magnitude of the tensile transverse stress is more remarkable than that in the longitudinal stress, implying that transverse stress is more sensitive to the stiffness of the clamps than longitudinal stress. Transverse stress can be released if the stiffness of external restraint decreases, as was also reported by (Fu et al., 2014).

Residual stresses in **Publication III** along the specified paths (see Figure 2.9) for two specimens, that is, III-FS1 and III-CS1, were measured to verify the simulation results. It should be noted that the rest of the comparisons were drawn based on the validated FE models. The starting point of the transverse stress measurement was approximately 1 mm from the weld toe and continued along a line of almost 25 mm in length in the transverse direction ( $x$ -axis). In all the related graphs, Path 1 and Path 2 are located on the negative side of the  $x$ -axis, while Path 3 and Path 4 are shown on the positive side of the  $x$ -axis. In order to evaluate the accuracy of the FE model, the results of the simulation in terms of the transverse stresses for III-FS1 along the two mentioned paths are plotted in Figure 4.26. The effect of external constraints on the development of residual stress fields was investigated by plotting the results of the simulation before and after the removal of the welding fixtures against the measurements, as shown in Figure 4.27.

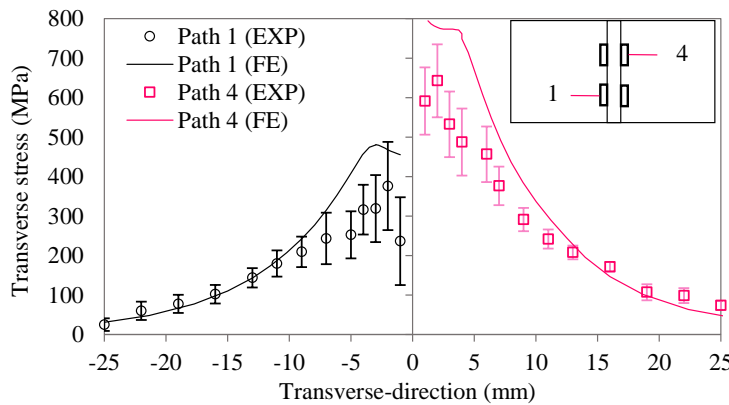


Figure 4.26: The simulated transverse residual stresses along Path 1 and Path 4 for III-FS1 (modified from **Publication III**).

As can be seen in Figure 4.26, the simulation results are in relatively good agreement with the measurement data. Both the simulation and measurement show that the maximum tensile stress along Path 4 is considerably greater than that of Path 1. The maximum transverse stress along Path 1 is approximately 65% of the yield strength of the base material, and that of Path 4 exceeds the yield strength of the base material.

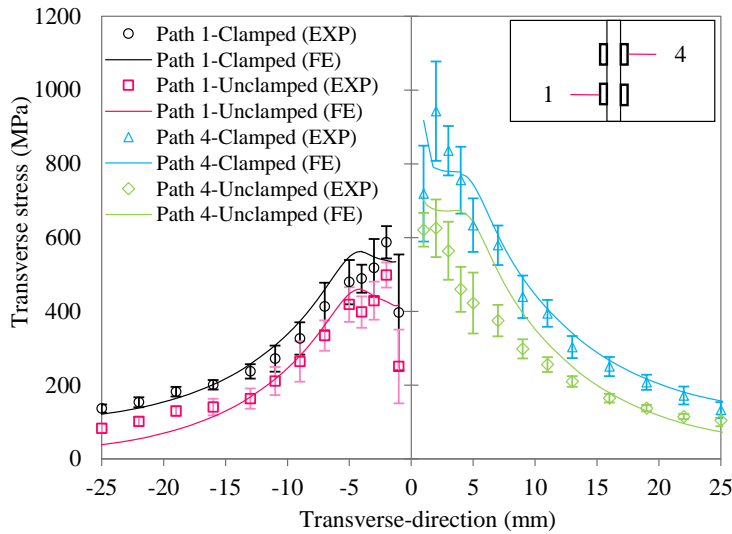


Figure 4.27: The simulated transverse residual stresses along Path 1 and Path 4 in clamped and unclamped conditions for III-CS1 (*modified from Publication III*).

For III-CS1, as shown in Figure 4.27, predictions of simulation before and after removal of the external restraints are in acceptable agreement with the measurement data. Along Path 4, in the clamped condition, the maximum transverse stress reaches 1000 MPa, which is greater than the yield strength of the material. This can be important when, in practice, a T-fillet specimen needs to be welded intermittently and then perform its service in high geometrical constraints. Unclamping, however, lowered the level of residual stresses along both paths. As seen in III-FS1, the transverse stresses along Path 4 are considerably larger than those of Path 1 in both clamped and unclamped conditions.

The effect of external restraints on the development of longitudinal stress was investigated numerically for III-FS1 and III-CS1, as shown in Figure 4.28. As can be seen, the maximum tensile stress along Path 4 is greater than that along Path 1 for both cases, which is similar to the transverse stress trend albeit with a smaller difference. Peak tensile stresses along Path 1 and Path 2 for both cases in the clamped condition are approximately identical. The peak values along Path 3 and Path 4 are slightly greater in III-FS1. However, when the specimens are unclamped, the final tensile residual stresses in III-CS1 along all paths are smaller than those in III-FS1.

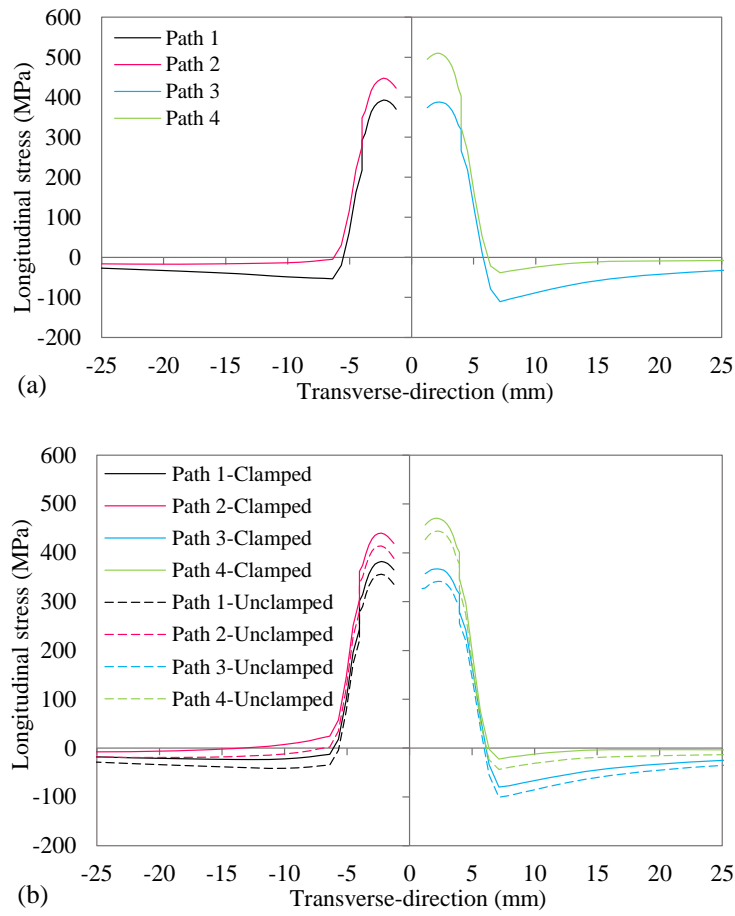


Figure 4.28: The simulated longitudinal residual stresses along Paths 1–4 for (a) III-FS1 and (b) III-CS1 (*modified from Publication III*).

A comparison was drawn between the residual stress state between II-CS1 from **Publication II** and III-CS1 from **Publication III**. The former was continuously welded along the joint, and the latter was welded in a non-continuous manner with short fillet welds; both were clamped at both ends, as plotted in Figure 4.29.

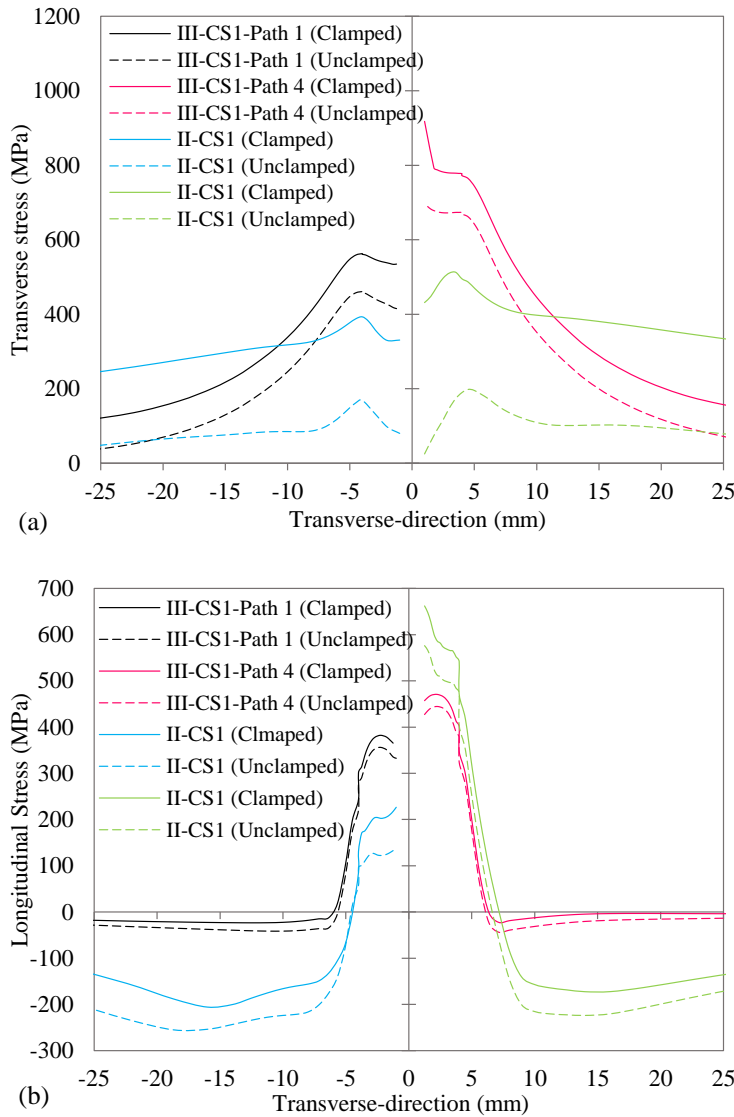


Figure 4.29: Comparison between II-CS1 and III-CS1 in terms of the simulated stress state in both clamped and unclamped conditions: (a) transverse residual stress, and (b) longitudinal residual stress. For III-CS1, Path 1 and Path 4 are selected for the sake of comparison (*modified from Publication III*).

As is observable, the peak tensile transverse stress magnitudes in both the clamped and unclamped conditions developed in II-CS1 with longer weld length (over the entire joint length) are considerably smaller than those in III-CS1, especially after unclamping. The transverse stress in II-CS1, however, is more sensitive to the removal of the external

restraints than that in III-CS1. The tensile transverse stress in III-CS1 decreased remarkably more quickly than in II-CS1.

Longitudinal stress is sensitive to unclamping at a considerably lower level than transverse stress. This sensitivity is slightly greater in II-CS1 than in III-CS1. The fall of longitudinal stresses for both cases occurred with almost the same gradient as moving from the HAZ towards the outer edges; however, the compressive longitudinal stresses in II-CS1 reached greater peak values than those in III-CS1.

#### 4.5 Elevated-temperature mechanical properties

In order to study the elevated-temperature constitutive mechanical properties of UHSSs in this research, elastic modulus, proof stress at different strain levels and ultimate tensile strength were determined from the stress-strain curves of the tested specimens. Since a conspicuous yield point is not present in stress-strain graphs, yield strength is generally evaluated at various strain levels especially for elevated temperatures. In this respect, the strength at 0.2% total strain ( $f_{0.2}$ ) is defined as the effective yield strength by (Eurocode 3, 2005). Effective yield strength may also be determined as the proof stress at 0.5%, 1.5% and 2% of total strain level, as practised by other researchers (Azhari et al., 2017; Qiang et al., 2012; Ranawaka and Mahendran, 2009). The stress-strain curves of the as-received and as-welded specimens made from S960MC and S1100 at different temperatures are shown in Figure 4.30 and Figure 4.31.

The strain and stress characteristics of the as-received and as-welded specimens made of S960 MC and S1100 are presented in Table 4.1 and Table 4.2, respectively. It should be noted that in the labelling of the specimens in this study, BM and W denote as-received base material and as-welded joint, respectively. The numbers 96 and 11 indicate steel grades 960 and 1100, respectively. The latter term is the temperature at which the tensile test was performed. In this regard, W-96-400, for example, corresponds to the tensile test of the welded joint made of S960MC tested at 400 °C.

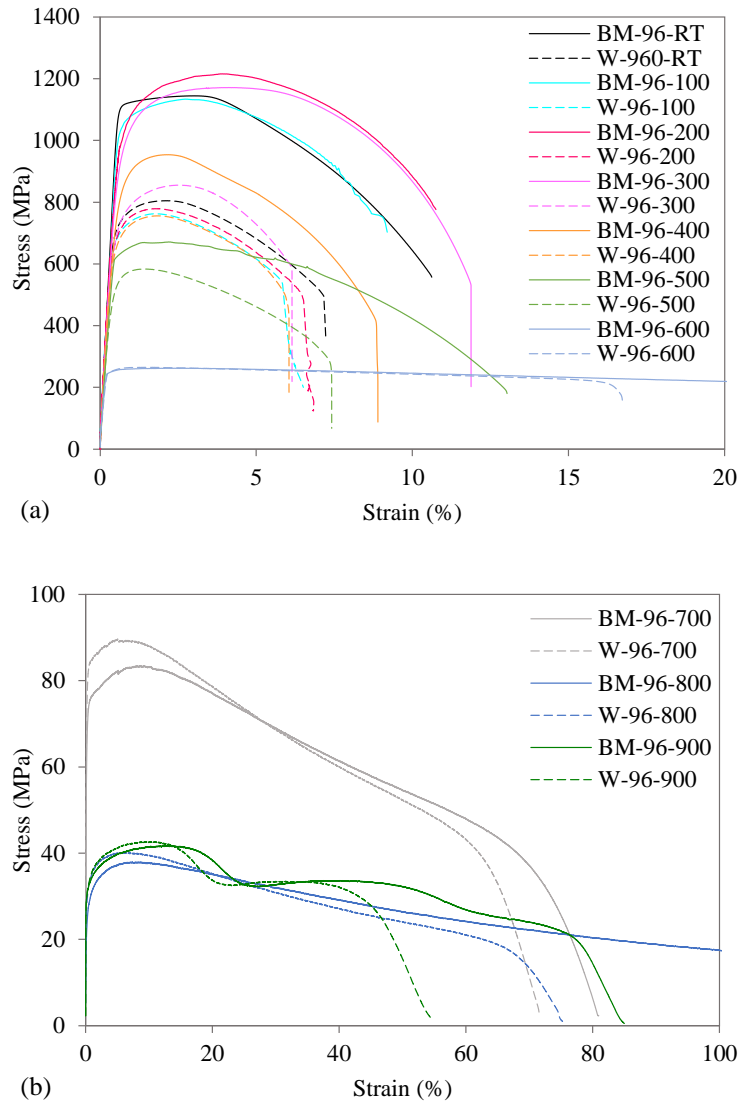


Figure 4.30: The engineering stress-strain curves for the specimens made from S960MC at different temperatures: (a) RT–600 °C and (b) 700 °C–900 °C (*modified from Publication IV*).

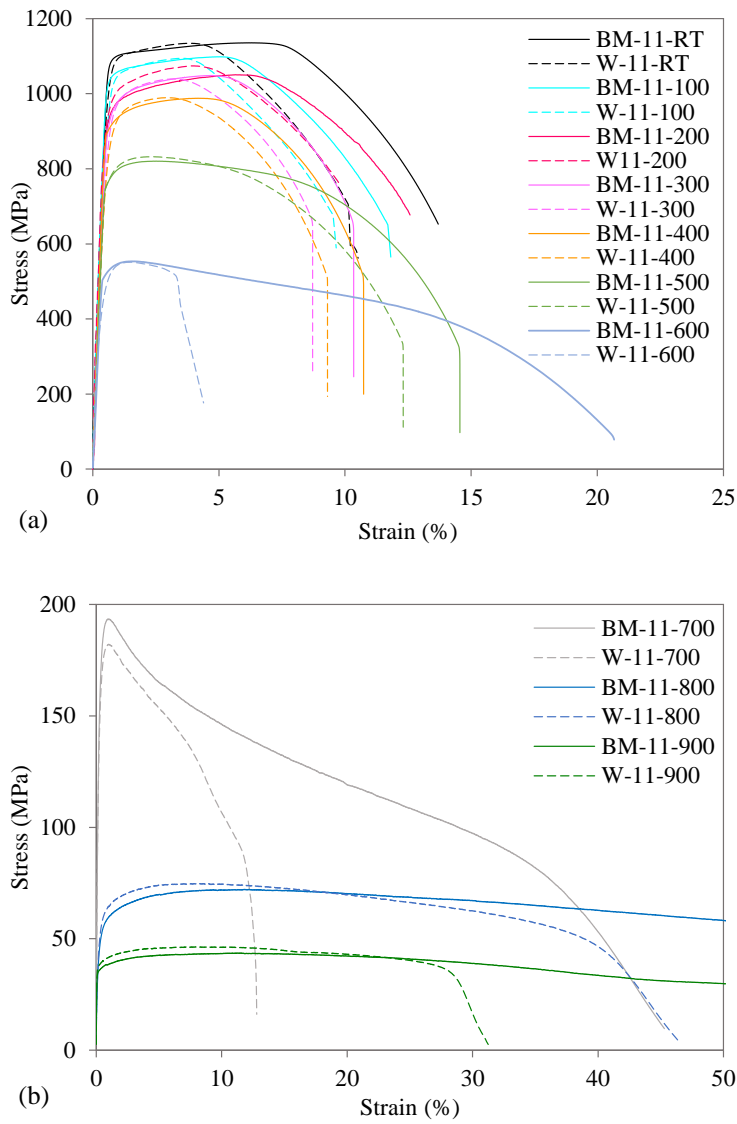


Figure 4.31: The engineering stress-strain curves for the specimens made from S1100 at different temperatures: (a) RT–600 °C and (b) 700 °C–900 °C (*modified from Publication IV*).

Table 4.1: Elevated-temperature mechanical properties of S960 in as-received and as-welded conditions (*from Publication IV*).

$T$ (°C)	$Label$	$E$ (GPa)	$f_{0.2}$ (MPa)	$f_{0.5}$ (MPa)	$f_{1.5}$ (MPa)	$f_2$ (MPa)	$f_u$ (MPa)	$\varepsilon_{0.2}$	$\varepsilon_u$
RT	BM	200	1115	1127	1133	1139	1145	0.75	3.03
	W	195	722	765	797	805	805	0.57	2.08
100	BM	190 (0.95)	1053 (0.94)	1083 (0.96)	1106 (0.97)	1121 (0.98)	1134 (0.99)	0.75	2.73
	W	184 (0.94)	688 (0.95)	729 (0.95)	760 (0.95)	761 (0.94)	762 (0.95)	0.57	1.77
200	BM	182 (0.91)	985 (0.88)	1076 (0.95)	1143 (1.008)	1177 (1.033)	1216 (1.062)	0.66	3.92
	W	176 (0.88)	703 (0.97)	747 (0.98)	776 (0.97)	777 (0.97)	779 (0.97)	0.60	1.83
300	BM	176 (0.88)	949 (0.85)	1041 (0.92)	1109 (0.98)	1140 (1.00)	1171 (1.02)	0.69	4.13
	W	160 (0.82)	722 (1.00)	781 (1.02)	831 (1.04)	849 (1.06)	855 (1.06)	0.61	2.56
400	BM	164 (0.82)	829 (0.74)	899 (0.80)	941 (0.83)	953 (0.84)	954 (0.83)	0.69	2.18
	W	153 (0.78)	655 (0.91)	713 (0.93)	752 (0.94)	755 (0.94)	756 (0.94)	0.53	1.85
500	BM	145 (0.73)	614 (0.55)	642 (0.57)	668 (0.59)	670 (0.59)	671 (0.59)	0.46	2.20
	W	144 (0.73)	524 (0.73)	568 (0.74)	583 (0.73)	578 (0.72)	584 (0.73)	0.52	1.43
600	BM	114 (0.57)	244 (0.22)	255 (0.23)	261 (0.23)	262 (0.23)	262 (0.23)	0.22	2.63
	W	107 (0.55)	248 (0.34)	260 (0.34)	265 (0.33)	265 (0.33)	265 (0.33)	0.26	2.60
700	BM	80 (0.4)	69 (0.06)	83 (0.07)	86 (0.08)	86 (0.08)	90 (0.08)	0.27	9.17
	W	80 (0.41)	78 (0.11)	83 (0.11)	86 (0.11)	86 (0.11)	90 (0.11)	0.28	5.06
800	BM	42 (0.21)	24 (0.02)	28 (0.03)	33 (0.03)	34 (0.03)	38 (0.03)	0.25	7.32
	W	42 (0.22)	29 (0.04)	33 (0.04)	37 (0.05)	38 (0.05)	40 (0.05)	0.25	6.08
900	BM	62 (0.31)	30 (0.03)	32.5 (0.03)	36 (0.03)	37 (0.03)	42 (0.04)	0.22	12.16
	W	63 (0.32)	31 (0.04)	33 (0.04)	37 (0.05)	38 (0.05)	43 (0.05)	0.24	9.58



Table 4.2: Elevated-temperature mechanical properties of S1100 in as-received and as-welded conditions (*from Publication IV*).

$T$ (°C)	$Label$	$E$ (GPa)	$f_{0.2}$ (MPa)	$f_{0.5}$ (MPa)	$f_{1.5}$ (MPa)	$f_2$ (MPa)	$f_u$ (MPa)	$\epsilon_{0.2}$	$\epsilon_u$
RT	BM	193	1089	1103	1109	1113	1135	0.76	6.28
	W	193	1036	1093	1109	1117	1134	0.67	3.83
100	BM	193 (1.00)	1035 (0.95)	1057 (0.96)	1070 (0.96)	1076 (0.97)	1098 (0.97)	0.67	5.08
	W	187 (0.97)	986 (0.95)	1048 (0.96)	1067 (0.96)	1078 (0.96)	1094 (0.96)	0.69	3.55
200	BM	189 (0.98)	947 (0.87)	980 (0.89)	999 (0.90)	1011 (0.91)	1050 (0.93)	0.71	5.64
	W	182 (0.94)	937 (0.90)	998 (0.91)	1032 (0.93)	1048 (0.94)	1074 (0.95)	0.60	3.89
300	BM	169 (0.88)	943 (0.87)	983 (0.89)	1007 (0.91)	1021 (0.92)	1048 (0.92)	0.74	4.74
	W	163 (0.85)	899 (0.87)	971 (0.89)	1009 (0.91)	1024 (0.92)	1039 (0.92)	0.68	3.21
400	BM	162 (0.84)	889 (0.82)	924 (0.84)	958 (0.86)	970 (0.87)	988 (0.87)	0.52	4.14
	W	159 (0.83)	866 (0.84)	937 (0.86)	967 (0.87)	980 (0.88)	989 (0.87)	0.70	3.00
500	BM	161 (0.83)	746 (0.69)	784 (0.71)	814 (0.73)	819 (0.74)	820 (0.72)	0.49	2.47
	W	155 (0.80)	742 (0.72)	788 (0.72)	825 (0.74)	831 (0.74)	832 (0.73)	0.48	2.36
600	BM	144 (0.74)	503 (0.46)	532 (0.48)	553 (0.50)	552 (0.50)	553 (0.49)	0.38	1.59
	W	142 (0.74)	468 (0.45)	529 (0.48)	551 (0.50)	545 (0.49)	551 (0.49)	0.47	1.49
700	BM	122 (0.63)	165 (0.15)	183 (0.17)	190 (0.17)	186 (0.17)	193 (0.17)	0.32	0.92
	W	133 (0.69)	152 (0.15)	172 (0.16)	179 (0.16)	174 (0.16)	182 (0.16)	0.30	0.97
800	BM	44 (0.23)	47 (0.04)	54 (0.05)	62 (0.06)	64 (0.06)	72 (0.06)	0.29	12.15
	W	44 (0.23)	52 (0.05)	59 (0.05)	67 (0.06)	69 (0.06)	75 (0.07)	0.30	8.05
900	BM	66 (0.34)	36 (0.03)	37 (0.03)	40 (0.04)	40 (0.04)	44 (0.04)	0.26	11.21
	W	73 (0.38)	38 (0.04)	40 (0.04)	43 (0.04)	44 (0.04)	46 (0.04)	0.25	7.92

As can be seen in Figure 4.30 and Figure 4.31, for all of the tested specimens, the ductility of the as-welded joint decreased compared to the as-received material at an identical testing temperature. As presented in Table 4.1 and Table 4.2, as-received S960MC and S1100 demonstrate comparably similar strength characteristics ( $E$ ,  $f_{0.2}$ , and  $f_u$ ) at RT, whereas the scenario for the as-welded joints at RT is significantly different. That is, while the S1100 welded joint reveals no strength deterioration compared to the as-received material, the welded joint made of S960MC shows significant strength reduction (approximately 35%) compared to the as-received specimen. The difference is attributed to the softening effect or hardness decline that occurs in the HAZ of welded joints made of S960MC. This hardness reduction results from the formation of a softer microstructure than that of the base material during the cooling stage of welding (Amraei et al., 2019).

#### 4.5.1 Elastic modulus

Exposure to elevated temperatures can consequentially impact the service life and load-bearing capacity of steels by decreasing the elastic modulus. Obtaining a fire-resistance design including UHSS structural members requires a detailed evaluation of elastic modulus deterioration at elevated temperatures. Deterioration of strength characteristics of steels at elevated temperatures is generally discussed through defining reduction factors. The elastic modulus reduction factor at an elevated temperature is defined as the ratio of elastic modulus at the given temperature to the reference elastic modulus at RT. It should be noted that elastic modulus reduction factors for BM-960/1100 and W-960/1100 were calculated as  $(E_{BM_T}/E_{BM_{RT}})$  and  $(E_{W_T}/E_{W_{RT}})$ , respectively, from their stress–strain curves, as presented in Table 4.1 and Table 4.2. It is worth noting that the strength characteristic reduction factors in Table 4.1 and Table 4.2 are the values between parentheses. The elastic modulus reduction factors of the tested UHSSs in this study were evaluated through comparisons with predictive models from the leading design standards, namely, EC3, (AISC, 2005), and (AS4100, 1998), in addition to several datasets of HSSs/UHSSs from the literature, as shown in Figure 4.32 (Neuenschwander et al., 2017; Qiang et al., 2016, 2013; Shakil et al., 2020).

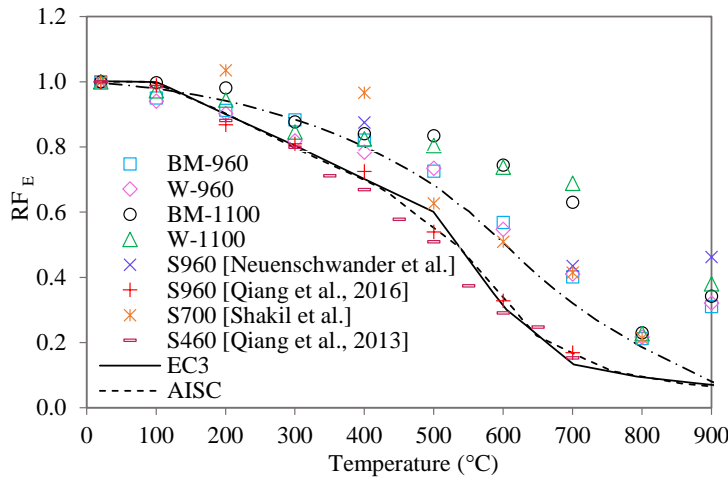


Figure 4.32: The elastic modulus reduction factors of the tested UHSSs at elevated temperatures in comparison with some design code models and datasets from the literature (*modified from Publication IV*).

As can be seen in Figure 4.32, the elastic modulus reduction factors of as-welded S960MC and S1100 demonstrate no significant changes compared to the as-received ones. In the prediction of the temperature-dependent elastic modulus reduction factors of BM/W-960, as well as most of the data presented for the sake of comparison, a bilinear curve is associated, one from RT–500 °C and the other from 500 °C–800 °C, the latter with a steeper gradient that indicates an abrupt loss of strain hardening at these temperatures compared to moderately-elevated temperatures. Although continuous degradation with increased temperatures is involved in the elastic modulus of S1100, the degeneration level is lower, and the trend is clearly slower than that of S960MC. S1100 maintains a more stable microstructure at elevated temperatures than S960, which results in less strength degradation (Amraei et al., 2019).

As shown in Figure 4.32, up to 300 °C, the elastic modulus reduction factors of BM/W-960 are fairly predicted by EC3, AISC, and AS4100. As the temperature increases, predictions of EC3 and AISC start to err on the safe side, and they become overly conservative when the temperature exceeds 600 °C. AS4100, however, provides safe but not overly conservative predictions regarding the elastic modulus reduction factors of BM/W-960 at temperatures above 300 °C. The calculated reduction factors for BM/W-1100 up to 300 °C demonstrate more agreement with the predictive models of EC3 and AISC than with that of AS4100 as it becomes slightly unsafe. When the temperature exceeds 400 °C, all the design code models lean toward over-conservatism, with AS4100 having a smaller degree of conservatism than EC3 and AISC.

### 4.5.2 Yield strength

The reduction factors related to 0.2% proof stress ( $f_{0.2}$ ), which is commonly referred to as yield strength, were chosen for the sake of comparison with leading design standard predictive models and several datasets from the literature, as plotted in Figure 4.33. It should be noted that in this comparison, the yield strength reduction factors for as-received and as-welded conditions were calculated as  $(f_{0.2BM_T} / f_{0.2BM_{RT}})$  and  $(f_{0.2W_T} / f_{0.2W_{RT}})$ , respectively.

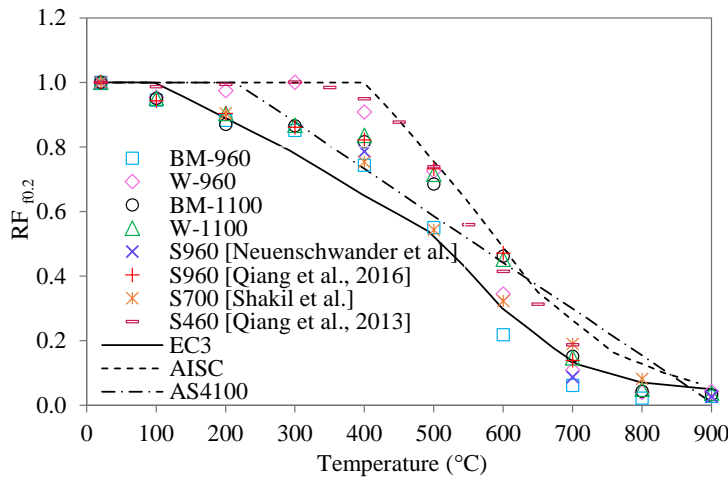


Figure 4.33: The yield strength reduction factors ( $f_{0.2}$ ) of the tested UHSSs at elevated temperatures in comparison with some design code models and datasets from the literature (*modified from Publication IV*).

As shown in Figure 4.33, continuous degradation of the yield strength occurs for BM-960 at all the testing temperatures, at a lower rate in the range RT–400 °C than in the following range, that is, 400 °C–800 °C, where a consequential strength decline happens. For BM-1100 a similar pattern is observable, albeit with a slower rate. In this regard, BM-1100 at 600 °C maintains approximately 50% of its original strength in contrast to the 20% maintained by BM-960. The yield strength absolute values of BM-960 are larger than those of W-960 in the temperature range RT–600 °C. For reduction factors, however, the scenario is different: yield strength reduction factors of W-960 take larger values than those of BM-960. That is, the strength degradation for as-received S960MC at elevated temperatures up to 600 °C occurs at a higher rate than for the as-welded joint, and the reason lies in the significant strength reduction due to welding of S960MC. With respect to S1100, both as-received and as-welded specimens demonstrate very close yield strength reduction patterns, which means the elevated-temperature yield strength of W-1100 can be considered identical to that of BM-1100.

With respect to  $f_{0.2}$  reduction factors, AICS provides less safe predictions for UHSSs than either EC3 and AS4100. Predictions of EC3 for BM-960 in the temperature range up to 200 °C are slightly nonconservative, while safe estimations are provided in the temperature range 200 °C–500 °C before they move into an unsafe region above 500 °C. Predictions of EC3 for W-960 in the temperature range RT–100 °C and above 700 °C fall in a slightly unsafe region. In the temperature range 100 °C–700 °C, reduction factors of W-960 are safely predicted by EC3, but these predictions are overly conservative in the range 200 °C–500 °C. Predictions of EC3 for BM/W-1100 are similar to those for BM-960, albeit with a higher degree of conservatism in the temperature range 300 °C–700 °C. Predictions of AS4100 regarding the reduction factors of BM-960 are unsafe, and those of W-960 are safely predicted solely in the temperature range 200 °C–500 °C, which makes it thus inapplicable for the prediction of yield strength reduction factors of S960MC. In the temperature range 300 °C–600 °C, the reduction factors of BM/W-1100 are safely predicted by AS4100, and predictions fall into the unsafe region at all other temperatures.

When comparing the yield strength reduction factors of BM-960 with the datasets related to S960 provided in the literature (Neuenschwander et al., 2017; Qiang et al., 2016), a similar trend of strength degradation up to 400 °C is observed. In the temperature range 300 °C–700 °C, strength deterioration is more pronounced in S960MC, which is used in this study, than in S960QL from the literature (Neuenschwander et al., 2017; Qiang et al., 2016). One reason can be that the quenched and tempered S960QL, due to solid solution strengthening, has a higher molybdenum content than the direct-quenched S960MC, which can contribute to increasing the creep resistance of the steel (Xiong et al., 2018).

#### 4.5.3 Ultimate tensile strength

The ultimate tensile strength reduction factors of the tested steels in as-received and as-welded conditions were calculated as  $(f_{uBM_T}/f_{uBM_{RT}})$  and  $(f_{uW_T}/f_{uW_{RT}})$ , as shown in Figure 4.34.

In terms of BM/W-960, the predictions of EC3 and the calculated reduction factors based on the experimental data up to 500 °C are in an acceptable agreement. Exceeding 500 °C, predictions of EC3 fall on the unsafe side. With respect to BM/W-1100, EC3 fails to safely predict the reduction factors in the temperature range 100 °C–350 °C. Above 350 °C and up to 700 °C, predictions of EC3 become safe and conservative. In the range 700 °C–900 °C, although predictions of EC3 become less conservative, they remain safe. The ultimate tensile strength deterioration trends related to BM/W-1100 are quite similar to those of S960QL, plotted in Figure 4.34, and EC3 thus similarly provides inaccurate estimations for their reduction factors in the temperature range 100 °C–350 °C.

AISC is shown to be inapplicable to predicting the reduction factors of all the datasets provided in Figure 4.34. Solely in the temperature range 500 °C–650 °C is an acceptable agreement reached between the calculated reduction factors of BM/W-1100 and S960QL from the literature and the estimations of AISC.

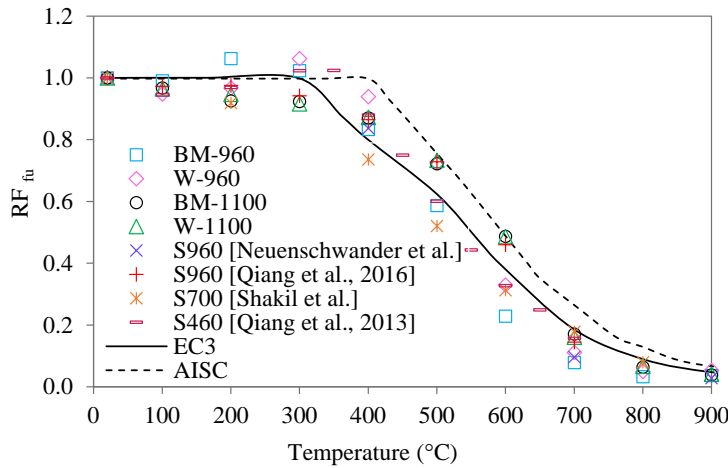


Figure 4.34: The ultimate tensile strength reduction factors ( $f_u$ ) of the tested UHSSs at elevated temperatures in comparison with some design code models and datasets from the literature (*modified from Publication IV*).

#### 4.5.4 Predictive equations

Based on the calculated reduction factors for the tested UHSSs in this study and the datasets related to S960QL from the literature, predictive equations as a function of temperature were developed to estimate the constitutive mechanical property reduction factors for UHSSs. Safe predictions in terms of UHSS reduction factors are provided by these equations; hence, they are useful in developing fire-resistance structural designs. Predictive equations were developed for elastic modulus, yield strength (0.2% proof strength), and ultimate tensile strength.

The datasets to derive the elastic modulus reduction factor predictive equations are plotted in Figure 4.35. As can be seen, when the temperature rises the data scatter increases. The main reason is the dramatic difference between the elastic modulus of the S960QL reported by (Qiang et al., 2016) and the rest of the datasets in the temperature range 300 °C–800 °C shown in Figure 4.35. For the sake of comparison, the predictive curves based on the Mean and Mean–2SD criteria including and excluding the datasets from (Qiang et al., 2016), are presented in Figure 4.35. The final predictive equation was derived based on the Mean–2SD criterion, where SD is the standard deviation of the data including the data reported by (Qiang et al., 2016).

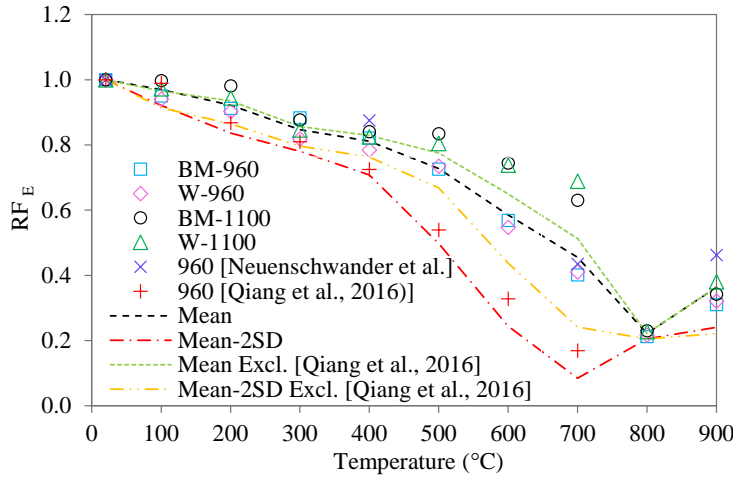


Figure 4.35: The datasets to derive the elastic modulus reduction factor predictive equations for UHSSs and the developed predictive curves (*modified from Publication IV*).

Elastic modulus reduction factors at elevated temperatures for UHSSs can be predicted using the following equation:

$$E_T/E_{RT} = \begin{cases} 3 \times 10^{-9}T^3 - 7 \times 10^{-8}T^2 - 0.001 \times T + 1.0203 & 20 \leq T < 300 \\ 2 \times 10^{-11}T^4 - 2 \times 10^{-8}T^3 - 5 \times 10^{-6}T^2 + 0.0057 \times T - 0.1604 & 300 \leq T < 700 \\ -4 \times 10^{-6}T^2 + 0.0076 \times T - 3.1406 & 700 \leq T \leq 900 \end{cases} \quad (4.1)$$

To make a comparison, Equation 4.1 is plotted against the design code predictive curves, as shown in Figure 4.36.

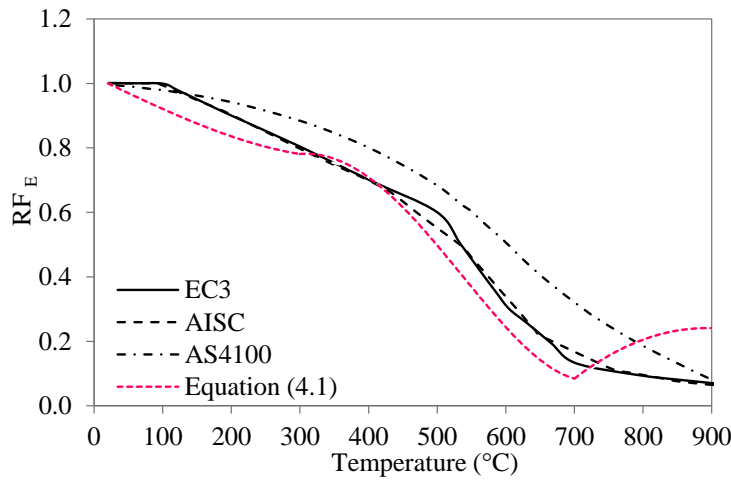


Figure 4.36: Equation 4.1 versus the predictive curves of some leading standards to estimate the elastic modulus reduction factors (*modified from Publication IV*).

As can be seen in Figure 4.36, compared to the predictive curve based on Equation 4.1, all the design code predictive models require modifications to deliver safe predictions for elastic modulus reduction factors in the temperature range RT–300 °C.

The predictive equation to estimate the yield strength reduction factors of UHSSs was derived based on the datasets plotted in Figure 4.37. To derive the predictive equation regarding the yield strength reduction factors, Mean–2SD criterion was used.

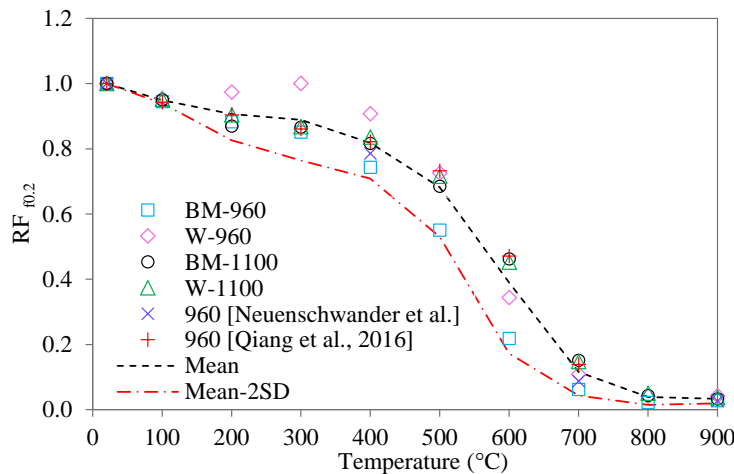


Figure 4.37: The datasets to derive the yield strength reduction factor predictive equations for UHSSs and the developed predictive curves (*modified from Publication IV*).



The yield strength reduction factors of the UHSSs used in this study at elevated temperatures can be estimated using the following equation:

$$f_{0.2,T}/f_{0.2,RT} = \begin{cases} -6 \times 10^{-11}T^4 + 5 \times 10^{-8}T^3 - 10^{-5}T^2 + 0.0004 \times T + 0.9972 & 20 \leq T < 400 \\ -9 \times 10^{-6}T^2 + 0.0063 \times T - 0.3729 & 400 \leq T < 600 \\ 3 \times 10^{-6}T^2 - 0.0055 \times T + 2.2698 & 600 \leq T \leq 900 \end{cases} \quad (4.2)$$

The graphical presentation of Equation 4.2 in comparison with the predictive curves of EC3, AISC and AS4100 is shown in Figure 4.38.

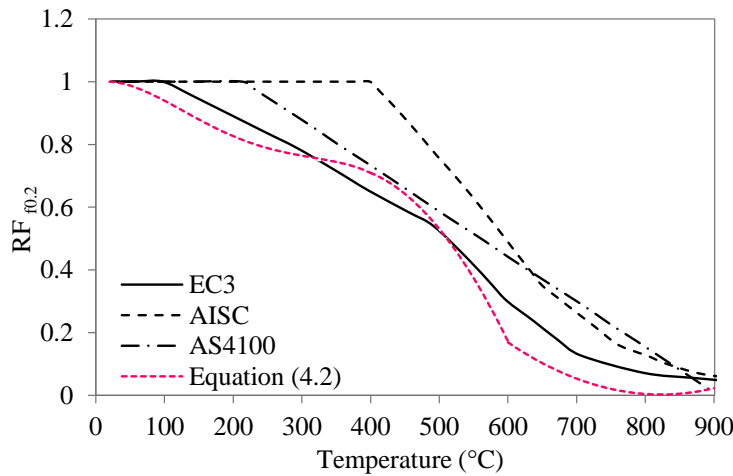


Figure 4.38: Equation 4.2 versus the predictive curves of some leading standards to estimate the yield strength reduction factors (*modified from Publication IV*).

As is observable, similar to the prediction of elastic modulus reduction factors, all the design codes fail to estimate the yield strength reduction factors safely. In this regard, EC3 maintains less deviation from the developed curve than AISC and AS4100 to obtain safe predictions.

The equation to predict the ultimate tensile strength reduction factors was obtained based on the datasets plotted in Figure 4.39.

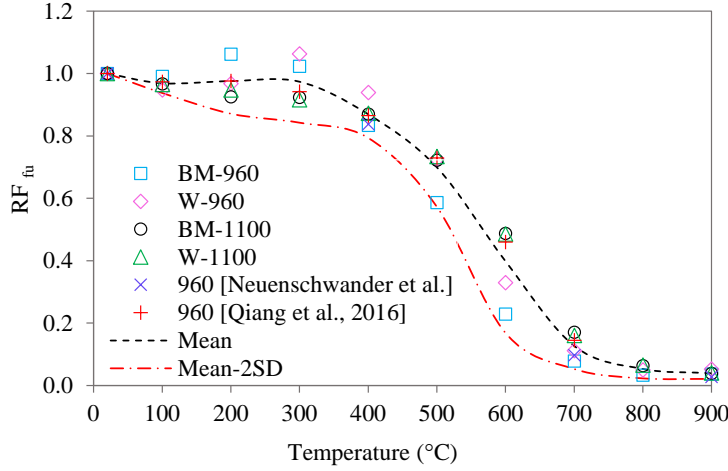


Figure 4.39: The datasets to derive the ultimate tensile strength reduction factor predictive equations for UHSSs and the developed predictive curves (*modified from Publication IV*).

Elevated-temperature reduction factors regarding the ultimate tensile strength of the UHSSs in this study can be estimated by the following equation:

$$f_{u,T}/f_{u,RT} = \begin{cases} \begin{aligned} &-4 \times 10^{-11}T^4 + 3 \times 10^{-8}T^3 - 5 \times 10^{-6}T^2 \\ &-0.0004 \times T + 1.0107 \\ &20 \leq T < 400 \end{aligned} \\ \begin{aligned} &-9 \times 10^{-6}T^2 + 0.0061 \times T - 0.1603 \\ &400 \leq T < 600 \end{aligned} \\ \begin{aligned} &3 \times 10^{-6}T^2 - 0.0047 \times T - 1.9841 \\ &600 \leq T \leq 900 \end{aligned} \end{cases} \quad (4.3)$$

A comparison is drawn in Figure 4.40 between the proposed equation to estimate the ultimate tensile strength reduction factors of the UHSSs used in this study, EC3, and AISC predictive curves.

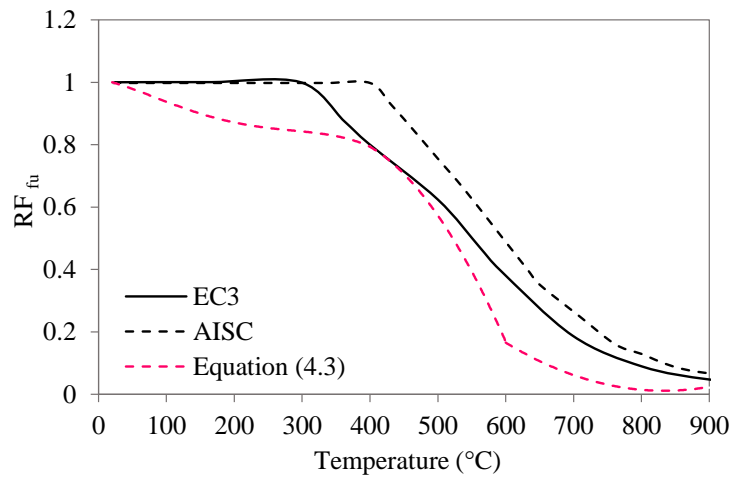


Figure 4.40: Equation 4.3 versus the predictive curves of some leading standards to estimate the ultimate tensile strength reduction factors (*modified from Publication IV*).

As can be seen, across all the testing temperatures both design code predictive models provide unsafe predictions and thus require modifications to be applicable for UHSSs. AISC retains more deviation from the developed curve than EC3 for safe estimations regarding the ultimate tensile strength reduction factors.

## 5 Conclusions

The full potential of HSSs/UHSSs can be realised if the phenomena contributing to the strength deterioration of these materials are identified and insight is sought into the prediction, assessment, alleviation, or negation of those effects. Welding thermal cycles, through non-uniform heating and cooling, have a significant effect on the load-bearing capacity of these materials by inducing softening effects. Another dramatic effect is the development of residual stresses and distortions. FE simulation of welding and the prediction of residual stress fields and welding distortions in different HSS/UHSS grades was investigated, and an experimental study of the mechanical behaviour of these materials at elevated temperatures was carried out. Based on **Publications I–III**, included in this research, the following conclusions with respect to thermomechanical welding simulation and prediction of welding-induced stresses and strains are drawn:

- Welding-induced residual stresses and distortions can be captured with reasonable accuracy as long as the thermal analysis is calibrated properly.
- Incorporation of solid-state phase transformation resulted in more accurate results with respect to capturing the angular and out-of-plane bending distortions.
- The configuration of external constraints (mechanical boundary conditions) has larger effects on the development of residual stress fields and distortions than the welding pass arrangement.
- In fillet welding with a single pass per side, the arrangement in which both passes are in the same direction resulted in slightly larger angular distortion and peak transverse stress than the arrangement in which the two passes are in the opposite directions.
- In continuous fillet welding over the length of the joint, transverse stresses are sensitive to the stiffness of external constraints. That is, increasing the stiffness degree can cause transverse stresses to rise. Removing or reducing the constraining stiffness, however, can release or ease transverse stresses. Longitudinal stresses are less affected by restraining stiffness than transverse stresses. In this context, using very rigid clamping at both ends in the transverse direction during welding and post welding removal can result in significant distortion prevention and releasing of the residual stresses.
- In non-continuous short fillet welds, although rigid clamping at both ends can result in distortion prevention, the effect is smaller than that on a long continuous fillet weld. In this respect, other distortion prevention methods, such as applying pre-deformations, might be considered for short fillet welds in addition to the application of rigid constraints.
- In short fillet welds, the stress field is local and has larger peak magnitudes than those in continuous long welds, and the peak magnitudes are considerably larger

than those for long welds. Peak stress can easily exceed the yield strength of the base material and is thus important to consider in real applications, as high tensile stresses might cause premature failures under dynamic loads.

In terms of the deterioration of constitutive mechanical response of UHSSs at elevated temperatures, based on the results of the **Publication IV** in this research the following conclusions are drawn:

- With an identical nominal strength grade, the elevated-temperature response of UHSSs highly depends on their manufacturing processes and chemical compositions.
- None of the design code models used for comparisons in this study can provide accurate predictions of the reduction factors of the constitutive mechanical properties of UHSSs. In this regard, the application of the predictive curves provided by the leading standards cannot practically be used for safe fire design of the structures and assemblies made of UHSSs. All the leading standards used for the sake of comparison require modifications in their predictive models for temperatures below 300 °C.
- EC3 shows better partial adoptability to the data packages related to UHSSs in this study than AS4100 and AISC.

## 6 References

ABAQUS, 2020. ABAQUS user's manual.

ABAQUS, 2017. ABAQUS user's manual.

Ahn, J., He, E., Chen, L., Pirling, T., Dear, J.P., Davies, C.M., 2018. Determination of residual stresses in fibre laser welded AA2024-T3 T-joints by numerical simulation and neutron diffraction. *Materials Science and Engineering A* 712, 685–703. <https://doi.org/10.1016/j.msea.2017.12.027>

Ahn, J., He, E., Chen, L., Wimpory, R.C., Dear, J.P., Davies, C.M., 2017. Prediction and measurement of residual stresses and distortions in fibre laser welded Ti-6Al-4V considering phase transformation. *Mater Des* 115, 441–457. <https://doi.org/10.1016/J.MATDES.2016.11.078>

AISC, 2005. AISC 360-05, Specification for Structural Steel Buildings. American Institute of Steel Construction. Inc: Chicago, IL.

Amraei, M., Ahola, A., Afkhami, S., Björk, T., Heidarpour, A., Zhao, X.L., 2019. Effects of heat input on the mechanical properties of butt-welded high and ultra-high strength steels. *Eng Struct* 198, 109460. <https://doi.org/10.1016/j.engstruct.2019.109460>

AS4100, 1998. Australian Standard AS 4100-1998: “Steel Structures” 1998.

ASTM, 2022. ASTM E8/E8M-22: Standard Test Methods for Tension Testing of Metallic Materials. ASTM International 1–31.

Azhari, F., Heidarpour, A., Zhao, X.L., Hutchinson, C.R., 2017. Post-fire mechanical response of ultra-high strength (Grade 1200) steel under high temperatures: Linking thermal stability and microstructure. *Thin-Walled Structures* 119, 114–125. <https://doi.org/10.1016/j.tws.2017.05.030>

Barsoum, Z., Lundbäck, A., 2009. Simplified FE welding simulation of fillet welds - 3D effects on the formation residual stresses. *Eng Fail Anal* 16, 2281–2289. <https://doi.org/10.1016/j.engfailanal.2009.03.018>

Bhatti, A.A., Barsoum, Z., Khurshid, M., 2014. Development of a finite element simulation framework for the prediction of residual stresses in large welded structures. *Comput Struct* 133, 1–11. <https://doi.org/10.1016/J.COMPSTRUC.2013.11.011>

- Bhatti, A.A., Barsoum, Z., Murakawa, H., Barsoum, I., 2015. Influence of thermo-mechanical material properties of different steel grades on welding residual stresses and angular distortion. *Mater Des* 65, 878–889. <https://doi.org/10.1016/j.matdes.2014.10.019>
- Björk, T., Toivonen, J., Nykänen, T., 2012. Capacity of fillet welded joints made of ultra high-strength steel. *Welding in the World* 56, 71–84. <https://doi.org/10.1007/BF03321337>
- Brickstad, B., Josefson, B.L., 1998. A parametric study of residual stresses in multi-pass butt-welded stainless steel pipes. *International Journal of Pressure Vessels and Piping* 75, 11–25. [https://doi.org/10.1016/S0308-0161\(97\)00117-8](https://doi.org/10.1016/S0308-0161(97)00117-8)
- Carvill, James., 1993. Mechanical engineer's data handbook. Butterworth-Heinemann.
- Chao, Y.J., 2005. Measuring welding-induced distortion. *Processes and Mechanisms of Welding Residual Stress and Distortion* 209–224. <https://doi.org/10.1533/9781845690939.2.209>
- Chen, C., Chiew, S.P., Zhao, M.S., Lee, C.K., Fung, T.C., 2020. Influence of cooling rate on tensile behaviour of S690Q high strength steel butt joint. *J Constr Steel Res* 173, 106258. <https://doi.org/10.1016/J.JCSR.2020.106258>
- Conejo, A.N., Birat, J.P., Dutta, A., 2020. A review of the current environmental challenges of the steel industry and its value chain. *J Environ Manage* 259, 109782. <https://doi.org/10.1016/J.JENVMAN.2019.109782>
- Cui, C., Zhang, Q., Bao, Y., Bu, Y., Luo, Y., 2019. Fatigue life evaluation of welded joints in steel bridge considering residual stress. *J Constr Steel Res* 153, 509–518. <https://doi.org/10.1016/J.JCSR.2018.11.003>
- Danis, Y., Lacoste, E., Arvieu, C., 2010. Numerical modeling of inconel 738LC deposition welding: Prediction of residual stress induced cracking. *J Mater Process Technol* 210, 2053–2061. <https://doi.org/10.1016/j.jmatprotec.2010.07.027>
- Deng, D., 2009. FEM prediction of welding residual stress and distortion in carbon steel considering phase transformation effects. *Mater Des* 30, 359–366. <https://doi.org/10.1016/j.matdes.2008.04.052>
- Deng, D., Liang, W., Murakawa, H., 2007a. Determination of welding deformation in fillet-welded joint by means of numerical simulation and comparison with experimental measurements. *J Mater Process Technol* 183, 219–225. <https://doi.org/10.1016/J.JMATPROTEC.2006.10.013>
- Deng, D., Murakawa, H., 2008. Finite element analysis of temperature field, microstructure and residual stress in multi-pass butt-welded 2.25Cr–1Mo steel pipes.

Comput Mater Sci 43, 681–695.  
<https://doi.org/10.1016/J.COMMATSCI.2008.01.025>

Deng, D., Murakawa, H., 2006. Numerical simulation of temperature field and residual stress in multi-pass welds in stainless steel pipe and comparison with experimental measurements. Comput Mater Sci 37, 269–277.  
<https://doi.org/10.1016/J.COMMATSCI.2005.07.007>

Deng, D., Murakawa, H., Liang, W., 2007b. Numerical simulation of welding distortion in large structures. Comput Methods Appl Mech Eng 196, 4613–4627.  
<https://doi.org/10.1016/J.CMA.2007.05.023>

Eurocode 3, 2005. EN 1993-1-2: Design of steel structures - Part 1-2: General rules - Structural fire design.

Fu, G., Lourenco, M.I., Duan, M., Estefen, S.F., 2014. Effect of boundary conditions on residual stress and distortion in T-joint welds. J Constr Steel Res 102, 121–135.  
<https://doi.org/10.1016/J.JCSR.2014.07.008>

Garlock, M., Paya-Zaforteza, I., Kodur, V., Gu, L., 2012. Fire hazard in bridges: Review, assessment and repair strategies. Eng Struct 35, 89–98.  
<https://doi.org/10.1016/j.engstruct.2011.11.002>

Goldak, J., Chakravarti, A., Bibby, M., 1984. A new finite element model for welding heat sources. Metallurgical Transactions B 15, 299–305.  
<https://doi.org/10.1007/BF02667333>

Goldak, J.A., Akhlaghi, M., 2005. Computational welding mechanics. Computational Welding Mechanics 1–321. <https://doi.org/10.1007/B101137/COVER>

Grong, Øystein., Institute of Metals, 2006. Metallurgical modelling of welding.

Guo, W., Li, L., Dong, S., Crowther, D., Thompson, A., 2017. Comparison of microstructure and mechanical properties of ultra-narrow gap laser and gas-metal-arc welded S960 high strength steel. Opt Lasers Eng 91, 1–15.  
<https://doi.org/10.1016/j.optlaseng.2016.11.011>

Heinze, C., Schwenk, C., Rethmeier, M., 2012a. Numerical calculation of residual stress development of multi-pass gas metal arc welding. J Constr Steel Res 72, 12–19.  
<https://doi.org/10.1016/j.jcsr.2011.08.011>

Heinze, C., Schwenk, C., Rethmeier, M., 2012b. Effect of heat source configuration on the result quality of numerical calculation of welding-induced distortion. Simul Model Pract Theory 20, 112–123. <https://doi.org/10.1016/J.SIMPAT.2011.09.004>

Hicks, John., 1999. Welded joint design, 3rd ed. Woodhead Publishing.



- Jiang, W., Xie, X., Wang, T., Zhang, X., Tu, S.T., Wang, J., Zhao, X., 2021. Fatigue life prediction of 316L stainless steel weld joint including the role of residual stress and its evolution: Experimental and modelling. *Int J Fatigue* 143, 105997. <https://doi.org/10.1016/J.IJFATIGUE.2020.105997>
- JMatPro Ver.8.0, 2014. Sente Software Ltd.
- Khedmati, M.R., Rastani, M., Ghavami, K., 2007. Numerical study on the permissible gap of intermittent fillet welds of longitudinally stiffened plates under in plane axial compression. *J Constr Steel Res* 63, 1415–1428. <https://doi.org/10.1016/J.JCSR.2006.11.016>
- Koistinen, D.P., Marburger, R.E., 1959. A general equation prescribing the extent of the austenite-martensite transformation in pure iron-carbon alloys and plain carbon steels. *Acta Metallurgica* 7, 59–60. [https://doi.org/10.1016/0001-6160\(59\)90170-1](https://doi.org/10.1016/0001-6160(59)90170-1)
- Kubiak, M., Piekarska, W., 2016. Comprehensive model of thermal phenomena and phase transformations in laser welding process. *Comput Struct* 172, 29–39. <https://doi.org/10.1016/j.compstruc.2016.05.014>
- Kumar, Dilip, Kumar, Deepak, 2015. Management of coking coal resources, *Management of Coking Coal Resources*. <https://doi.org/10.1016/c2014-0-01427-x>
- Lee, C.H., Chang, K.H., 2011. Prediction of residual stresses in high strength carbon steel pipe weld considering solid-state phase transformation effects. *Comput Struct* 89, 256–265. <https://doi.org/10.1016/j.compstruc.2010.10.005>
- Lee, C.H., Chang, K.H., 2009. Finite element simulation of the residual stresses in high strength carbon steel butt weld incorporating solid-state phase transformation. *Comput Mater Sci* 46, 1014–1022. <https://doi.org/10.1016/j.commatsci.2009.05.007>
- Lee, S.H., Kim, E.S., Park, J.Y., Choi, J., 2018. Numerical analysis of thermal deformation and residual stress in automotive muffler by MIG welding. *J Comput Des Eng* 5, 382–390. <https://doi.org/10.1016/J.JCDE.2018.05.001>
- Li, G.Q., Song, L.X., 2020. Mechanical properties of TMCP Q690 high strength structural steel at elevated temperatures. *Fire Saf J* 116, 103190. <https://doi.org/10.1016/j.firesaf.2020.103190>
- Li, H., Gai, K., He, L., Zhang, C., Cui, H., Li, M., 2016. Non-isothermal phase-transformation kinetics model for evaluating the austenization of 55CrMo steel based on Johnson–Mehl–Avrami equation. *Mater Des* 92, 731–741. <https://doi.org/10.1016/J.MATDES.2015.12.110>

- Li, X., Hu, L., Deng, D., 2022. Influence of contact behavior on welding distortion and residual stress in a thin-plate butt-welded joint performed by partial-length welding. *Thin-Walled Structures* 176, 109302. <https://doi.org/10.1016/J.TWS.2022.109302>
- Li, Y., Lu, H., Yu, C., Wu, Y., 2015. Accurate prediction of welding stress evolution by considering improved phase transformation model. *Mater Trans* 56, 715–719. <https://doi.org/10.2320/MATERTRANS.M2014344>
- Li, Y., Wang, M., Li, G., Jiang, B., 2021. Mechanical properties of hot-rolled structural steels at elevated Temperatures : A review. *Fire Saf J* 119, 103237. <https://doi.org/10.1016/j.firesaf.2020.103237>
- Liang, W., Deng, D., 2018. Influences of heat input, welding sequence and external restraint on twisting distortion in an asymmetrical curved stiffened panel. *Advances in Engineering Software* 115, 439–451. <https://doi.org/10.1016/J.ADVENGSOFT.2017.11.002>
- Liang, W., Hu, X., Zheng, Y., Deng, D., 2020. Determining inherent deformations of HSLA steel T-joint under structural constraint by means of thermal elastic plastic FEM. *Thin-Walled Structures* 147, 106568. <https://doi.org/10.1016/j.tws.2019.106568>
- Lindgren, L.-E., 2007. *Computational welding mechanics: thermomechanical and microstructural simulations*. Woodhead Publishing.
- Little, G.H., Kamtekar, A.G., 1998. The effect of thermal properties and weld efficiency on transient temperatures during welding. *Comput Struct* 68, 157–165. [https://doi.org/10.1016/S0045-7949\(98\)00040-6](https://doi.org/10.1016/S0045-7949(98)00040-6)
- Moshayedi, H., Sattari-Far, I., 2015. The effect of welding residual stresses on brittle fracture in an internal surface cracked pipe. *International Journal of Pressure Vessels and Piping* 126, 29–36. <https://doi.org/10.1016/j.ijpvp.2015.01.003>
- Neuenschwander, M., Scandella, C., Knobloch, M., Fontana, M., 2017. Modeling elevated-temperature mechanical behavior of high and ultra-high strength steels in structural fire design. *Mater Des* 136, 81–102. <https://doi.org/10.1016/j.matdes.2017.09.041>
- Piekarska, W., Kubiak, M., Saternus, Z., 2012. Numerical modelling of thermal and structural strain in laser welding process. *Archives of Metallurgy and Materials* 57, 1219–1227. <https://doi.org/10.2478/V10172-012-0136-Y>
- Qiang, X., Bijlaard, F.S.K., Kolstein, H., 2013. Elevated-temperature mechanical properties of high strength structural steel S460N: Experimental study and recommendations for fire-resistance design. *Fire Saf J* 55, 15–21. <https://doi.org/10.1016/j.firesaf.2012.10.008>

- Qiang, X., Bijlaard, F.S.K., Kolstein, H., 2012. Post-fire mechanical properties of high strength structural steels S460 and S690. *Eng Struct* 35, 1–10. <https://doi.org/10.1016/j.engstruct.2011.11.005>
- Qiang, X., Jiang, X., Bijlaard, F.S.K., Kolstein, H., 2016. Mechanical properties and design recommendations of very high strength steel S960 in fire. *Eng Struct* 112, 60–70. <https://doi.org/10.1016/j.engstruct.2016.01.008>
- Radaj, D., 1992. Heat Effects of Welding. *Heat Effects of Welding*. <https://doi.org/10.1007/978-3-642-48640-1>
- Ranawaka, T., Mahendran, M., 2009. Experimental study of the mechanical properties of light gauge cold-formed steels at elevated temperatures. *Fire Saf J* 44, 219–229. <https://doi.org/10.1016/j.firesaf.2008.06.006>
- Rikken, M., Pijpers, R., Slot, H., Maljaars, J., 2018. A combined experimental and numerical examination of welding residual stresses. *J Mater Process Technol* 261, 98–106. <https://doi.org/10.1016/j.jmatprotec.2018.06.004>
- Rosenfeld, P.E., Feng, L., 2011. Risks of Hazardous Wastes. *Risks of Hazardous Wastes*. <https://doi.org/10.1016/C2009-0-62341-2>
- Seleš, K., Perić, M., Tonković, Z., 2018. Numerical simulation of a welding process using a prescribed temperature approach. *J Constr Steel Res* 145, 49–57. <https://doi.org/10.1016/J.JCSR.2018.02.012>
- Serth, R.W., Lestina, T.G., 2014. Process Heat Transfer: Principles, Applications and Rules of Thumb: Second Edition. *Process Heat Transfer: Principles, Applications and Rules of Thumb: Second Edition* 1–609. <https://doi.org/10.1016/C2011-0-07242-3>
- Shakil, S., Lu, W., Puttonen, J., 2020. Experimental studies on mechanical properties of S700 MC steel at elevated temperatures. *Fire Saf J* 116, 103157. <https://doi.org/10.1016/j.firesaf.2020.103157>
- Shan, X., Davies, C.M., Wangsdan, T., O'Dowd, N.P., Nikbin, K.M., 2009. Thermo-mechanical modelling of a single-bead-on-plate weld using the finite element method. *International Journal of Pressure Vessels and Piping* 86, 110–121. <https://doi.org/10.1016/J.IJPVP.2008.11.005>
- Shen, J., Chen, Z., 2014. Welding simulation of fillet-welded joint using shell elements with section integration. *J Mater Process Technol* 214, 2529–2536. <https://doi.org/10.1016/J.JMATPROTEC.2014.04.034>

- Siltanen, J., Tihinen, S., Kömi, J., 2015. Laser and laser gas-metal-arc hybrid welding of 960 MPa direct-quenched structural steel in a butt joint configuration. *J Laser Appl* 27, S29007. <https://doi.org/10.2351/1.4906386>
- Skriko, T., Ghafouri, M., Björk, T., 2017. Fatigue strength of TIG-dressed ultra-high-strength steel fillet weld joints at high stress ratio. *Int J Fatigue* 94, 110–120. <https://doi.org/10.1016/j.ijfatigue.2016.09.018>
- Suikkanen, P.P., Kömi, J.I., 2014. Microstructure, properties and design of direct quenched structural steels. *Materials Science Forum* 783–786, 246–251. <https://doi.org/10.4028/WWW.SCIENTIFIC.NET/MSF.783-786.246>
- Sun, J., Liu, X., Tong, Y., Deng, D., 2014. A comparative study on welding temperature fields, residual stress distributions and deformations induced by laser beam welding and CO<sub>2</sub> gas arc welding. *Mater Des* 63, 519–530. <https://doi.org/10.1016/j.matdes.2014.06.057>
- Ueda, Y., Murakawa, H., Ma, N., 2012. Welding Deformation and Residual Stress Prevention. *Welding Deformation and Residual Stress Prevention*. <https://doi.org/10.1016/C2011-0-06199-9>
- Xiong, M.X., Richard Liew, J.Y., Du, Y., 2018. Effects of heat-treatment methods on mechanical performance of high-tensile strength steel subject to elevated temperatures. *Applications of Fire Engineering - Proceedings of the International Conference of Applications of Structural Fire Engineering, ASFE 2017* 1, 379–384. <https://doi.org/10.1201/9781315107202-40>
- Yaghi, A., Hyde, T.H., Becker, A.A., Sun, W., Williams, J.A., 2006. Residual stress simulation in thin and thick-walled stainless steel pipe welds including pipe diameter effects. *International Journal of Pressure Vessels and Piping* 83, 864–874. <https://doi.org/10.1016/j.ijpvp.2006.08.014>
- Yan, X.F., Yang, C., 2019. Experimental research and analysis on residual stress distribution of circular steel tubes with different processing techniques. *Thin-Walled Structures* 144, 106268. <https://doi.org/10.1016/J.TWS.2019.106268>
- Zhang, C., Sun, J., Li, Y., Deng, D., 2022. Numerical simulation of residual stress of butt-welded joint involved in complex column-beam welded structure. *J Manuf Process* 83, 458–470. <https://doi.org/10.1016/J.JMAPRO.2022.09.010>
- Zhu, X.K., Chao, Y.J., 2002. Effects of temperature-dependent material properties on welding simulation. *Comput Struct* 80, 967–976. [https://doi.org/10.1016/S0045-7949\(02\)00040-8](https://doi.org/10.1016/S0045-7949(02)00040-8)



## **Publication I**

Ghafouri, M., Ahn, J., Mourujärvi, J., Björk, T., and Larkiola, J.

**Finite element simulation of welding distortions in ultra-high strength steel S960  
MC including comprehensive thermal and solid-state phase transformation models**

Reprinted with permission from  
*Journal of Engineering Structures*  
Vol. 219, p. 110804, 2020  
© 2020, Elsevier





# Finite element simulation of welding distortions in ultra-high strength steel S960 MC including comprehensive thermal and solid-state phase transformation models



Mehran Ghafouri<sup>a,\*</sup>, Joseph Ahn<sup>b</sup>, Juho Mourujärvi<sup>c</sup>, Timo Björk<sup>a</sup>, Jari Larkiola<sup>c</sup>

<sup>a</sup> Laboratory of Steel Structures, School of Energy Systems, LUT University, P.O. Box 20, 53851 Lappeenranta, Finland

<sup>b</sup> Department of Mechanical Engineering, Imperial College London, South Kensington Campus, London SW7 2AZ, UK

<sup>c</sup> Materials and Production Engineering, Faculty of Technology, University of Oulu, P.O. Box 4200, 90570 Oulu, Finland

## ARTICLE INFO

### Keywords:

Welding simulation  
Solid-state phase transformation  
Finite element simulation  
Ultra-high strength steel  
Welding distortion

## ABSTRACT

The objective of this study is developing a thermo-metallurgical-mechanical finite element (FE) model incorporating the effect of solid-state phase transformation (SSPT) to accurately simulate deformations for single bead-on-plate welding of an ultra-high strength carbon steel. Comprehensive phase transformation modeling including both diffusive and diffusionless (displacive) transformation kinetics, was performed and the effect of SSPT on welding-induced deformations was investigated. Modelling the heat source and thermal boundary conditions were accomplished in the ABAQUS user subroutines, the former based on the Goldak's double ellipsoidal heat source model. An ABAQUS user subroutine was developed in which kinetics of diffusive and diffusionless transformations based on Machnienko model and Koistinen-Marburger formula, respectively, were implemented. Modification of strains due to volumetric change as a result of SSPT was accomplished using an ABAQUS user-defined subroutine. A comparison between the temperature histories from thermal simulations (with isotropic as well as anisotropic conductivities) and measurement with thermocouples shows that much better verification with experiments can be obtained when anisotropic conductivity is applied. From the results of the mechanical simulations (with and without considering the effect of SSPT) and comparison with measured deformations, it is observable that more accurate prediction of welding-induced angular and bending distortions is possible when the effect of SSPT is incorporated for the material under investigation.

## 1. Introduction

Indispensable demand of fast-growing technology for light-weight yet high-performance materials has led to advent and actuated the development of ultra-high strength steels (UHSS) as a member of high-strength low-alloy (HSLA) steels during the past decades. Together with high load-bearing capacity, HSLA steels have a superb combination of toughness, weldability and high strength-to-weight ratio making them highly applicable in a wide variety of manufacturing industries such as heavy lifting, oil and gas, automotive and ship-building industries as well as in industrial equipment manufacturing sector and offshore construction [1–3].

Cost-effectiveness, efficiency and reliability of fusion welding techniques and in particular, conventional arc welding processes such as gas metal arc welding (GMAW), make them the main and the most prevalent methods of making permanent joints in fabrication of components and structures made up of HSLA steels [1,4]. In this context,

dramatic effects of employing such joining techniques operating upon transporting a tremendous heat input into material should be meticulously contemplated. Due to high heat input of arc welding processes and slow cooling rates, HSLA steels in general, experience heat-affected zone (HAZ) softening [5]. The impacts of elevated temperatures on strength reduction of UHSSs, have also been reported [6]. More importantly, rapid non-uniform heating and cooling due to welding thermal cycles, lead to appearance of elasto-plastic thermal strains. SSPT which itself controls thermal and mechanical properties of material and causes localized volume changes, might also arise in the welding area and adjacent HAZ contributing to evolution of thermal strains [7–9]. In addition, inadvertent plastic deformation can degrade performance and quality of the welded connections, impose complexity to assembly of the structure, increase fabrication costs and delay the production and in extreme cases, might cause inapplicability of the entire structure [7,9,10].

Development of well-functioning methodologies and efficient

\* Corresponding author.

E-mail address: [mehran.ghafouri@lut.fi](mailto:mehran.ghafouri@lut.fi) (M. Ghafouri).

<https://doi.org/10.1016/j.engstruct.2020.110804>

Received 11 November 2019; Received in revised form 5 April 2020; Accepted 12 May 2020

Available online 17 June 2020

0141-0296/ © 2020 Elsevier Ltd. All rights reserved.



**Table 1**  
Chemical compositions of S960 MC and Böhler Union X96 (wt. %).

Material	C	Si	Mn	P	S	Al	Ti	Cu	Cr	Ni	Mo	N
S960 MC	0.097	0.20	1.09	0.008	0.001	0.034	0.02	0.033	1.13	0.38	0.191	0.005
Union X96	0.12	0.80	1.90	–	–	–	–	–	0.45	2.35	0.55	–

models to predict and analyze welding-induced stresses and strains accurately, become imperative in order to exploit the maximum load-bearing capacity of the joints made up of UHSSs and provide safety to their application. In this regard, FE method has proven its potential and reliability to solve a broad spectrum of linear and non-linear mathematical and engineering problems. In the field of heat transfer and welding simulations, over the past decades, computational welding mechanics (CWM) aiming at analyzing the temperature field, welding-induced stresses and strains along with microstructural evolution has been significantly developed [11–16]. Numerous studies have been hitherto conducted concerning welding simulation and prediction of residual stresses and distortions for different joint types [4,10,17–19], materials [4,10,18–25] and welding processes [4,10,19,24]. Although remarkable research has been devoted to welding simulation of steels, a few concentrated on comprehensive metallurgical modeling [26,27]. With respect to high strength steels (HSS) and UHSSs, some studies considered welding simulations including austenite–martensite transformation [25,28–30] and some neglected such effect [24]; however, less attention has been paid to comprehensive metallurgical modelling including both diffusive and displacive transformations for modern direct-quenched thermo-mechanically rolled UHSSs. Accurate prediction of welding deformations is essential in decreasing fabrication costs, increasing the quality and performance of the joint, service life of the component as well as efficiency of production processes such as digitalized robot welding. The objective of this research is developing a comprehensive thermo-metallurgical-mechanical (TMM) FE model to accurately predict welding-induced angular and out of plane bending distortions of direct-quenched thermo-mechanically rolled UHSS S960 MC. In this regard, a three-dimensional sequentially-coupled model for numerical simulation of a single pass bead-on-plate welding of the UHSS S960 MC specific to GMAW process is elaborated in ABAQUS software [31].

Accurate computational modeling of thermal and metallurgical phenomena which incorporates both diffusive and displacive SSPT kinetics models in FE simulation is accomplished. Subsequently, the effect of SSPT on mechanical analysis and prediction of out of plane angular and bending deformations are investigated. Thermal phenomena is modeled by applying a body heat flux upon implementation of Goldak's double ellipsoidal heat source model [32] in the user subroutine DFLUX and developing the user subroutine FILM to consider the combined convective and radiative heat transfer. Dilatometric tests are conducted and continuous cooling transformation (CCT) diagram of the material is determined experimentally. A linear relationship to consider incomplete austenite transformation during heating based on the previous researches [26,28,33] along with Machnienko kinetics for diffusional and Koistinen-Marburger equation for diffusionless transformations are implemented in the user subroutine USDFLD. Volume fractions of austenite during heating as well as arising phases upon austenite decomposition in cooling stage are accordingly calculated. The computed volume fractions together with experimentally obtained full volumetric change strains from dilatometric data are

formulated in the user subroutine UEXPAN to calculate volume changes due to phase transformation during both heating and cooling. Computer simulations in terms of prediction of temperature histories, present microconstituents in fusion zone (FZ) and HAZ as well as welding-induced distortions are verified by experimental measurements.

## 2. Experimental procedure

### 2.1. Material

The parent material used in this study is S960 MC manufactured by SSAB, which is an advanced low carbon ultra-high strength low alloy steel offering a minimum yield strength of 960 MPa. This UHSS is made by a modern thermo-mechanical rolling process integrated with direct quenching in which water quenching occurs forthwith after hot rolling. This process differs from the conventional method, which contains hot rolling, air-cooling, reheating and ultimately quenching [34,35].

The filler material utilized to deposit the weld bead is Böhler Union X96 solid wire with 1 mm diameter, which practically has the same strength as the parent material [36]. Chemical composition of the material under investigation based on the material certificate of the manufacturer and those of filler material from the literature [37] are presented in the table 1.

### 2.2. Welding procedure

A single rectangular block of S960 MC with dimensions of  $300 \times 300 \times 8$  mm was used as the base material upon its center line, a layer of filler material in a single pass GMAW process was deposited. It must be mentioned that base material was positioned in the way that welding torch travels in transverse direction (perpendicular to rolling direction) of the material. The convention for welding direction was assumed to be along the +Y-axis and +Z is normal to the top surface of the plate. Welding was carried out in ambient temperature of 20 °C without any application of preheat based on the recommendation of the manufacturer [38]. Due to softening effects on the material, heat input level should be optimized [36], thus, welding parameters were adjusted to meet the heat input requirements, as are presented in the table 2.

Adjusting the value of 0.8 as the welding efficiency for GMAW process, a total energy of 179.2 kJ corresponding to a net heat input value of 640 J/mm was supplied during the welding.

### 2.3. Temperature measurement

Temperature histories during welding were monitored by attaching several K-type thermocouples at different positions on top as well as bottom surfaces of the parent material. It is worthy of note that as long as the FE model is verifiable by experimental results, the choice of number and location of thermocouples are optional. Two thermocouples were detached during welding and failed to record the temperature. The positions at which six thermocouples were mounted are

**Table 2**  
Welding process parameters.

Voltage (V)	Current (A)	Travel speed (m/min)	Wire diameter (mm)	Wire feed rate (m/min)	Gas flow rate (L/min)	Tip distance (mm)	Shielding gas
28	200	0.42	1	10	19.3	18	92% Ar + 8% CO <sub>2</sub>

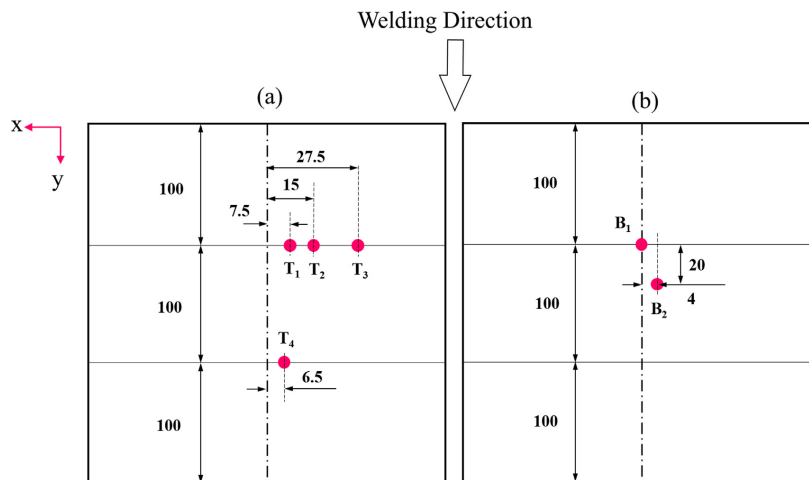


Fig. 1. Positions of thermocouples on top (a) and bottom (b) surfaces. (Units in mm).

schematically shown in Fig. 1. Thermocouples T<sub>1</sub> and T<sub>4</sub> attached in HAZ to capture higher temperatures while T<sub>2</sub> and T<sub>3</sub> mounted in base material, show lower temperatures. B<sub>1</sub> and B<sub>2</sub> provide more data regarding the temperature distribution through thickness. From FE point of view, six thermocouples can provide sufficient data to verify the nodal temperatures calculated by FE model.

#### 2.4. Deformation measurement

Out of plane angular and bending distortions on specified paths on top surface before and after welding were measured using the laser profile scanner Micro-Epsilon optoNCDT 1700–20 in order to compare with numerical simulation as are depicted in Fig. 2. Paths 1 & 2 (red solid lines) starting at the weld toe, demonstrate the paths along which angular distortion is measured. Path 3 (green dashed line) shows the measuring path for out of plane bending distortion.

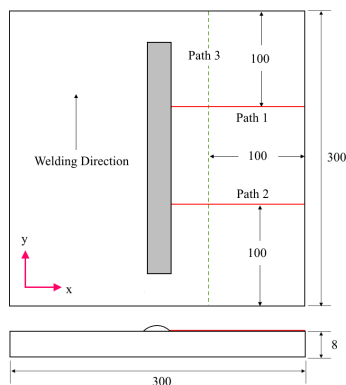


Fig. 2. Measurement paths for angular and bending distortions. (Units in mm).

### 3. Finite element simulation

Welding is a complex joining process which includes coupled interactions between heat and mass transfer, microstructural alterations and evolution of mechanical fields. Numerical procedures to accurately simulate such process, can be highly complicated and might not reach realistic solutions especially if capturing all the aspects is concerned. Not all the factors that impose complexity to welding simulation are consequential and thus, simplification of presumptions will result in elaborating an efficient yet precise model [20,28].

FE method is adopted to simulate the welding process and investigate the evolution of microstructure and development of distortions due to existence of a transient thermal field during welding in the current study. Capturing the temperature histories, simulation of phase transformation and prediction of welding distortions are accomplished developing a sequentially-coupled TMM formulation in ABAQUS FE code. Sequentially-coupled analysis is stated to have a favorable performance as dimensional changes during welding are insignificant and the effect of structural response on thermal field is inconsequential [4,25]. In thermal analysis, non-linear transient temperature field due to a moving heat source is determined upon solving constitutive heat conduction equation subject to defined boundary conditions. Metallurgical analysis is performed by calculating the volume fractions of austenite in heating and arising phases in cooling. In the subsequent mechanical analysis, the temperature histories obtained in the previous steps, are applied as thermal load. In addition, volume changes due to phase transformations are used to modify the thermal expansion coefficients and find the structural response and calculate the displacements at nodes.

#### 3.1. Model geometry and FE mesh

Modeling the as-welded geometry was carried out by extracting the curvature of the weld bead from the macrosection of the weld seam. Due to symmetry concerning the weld center line, only one-half of the geometry was considered as the analysis domain. Inasmuch as nodal temperatures captured in thermal analysis need transferring into the model for mechanical analysis, the same FE mesh with identical time steps as is shown in Fig. 3, albeit, with different element types were used in both analyses.

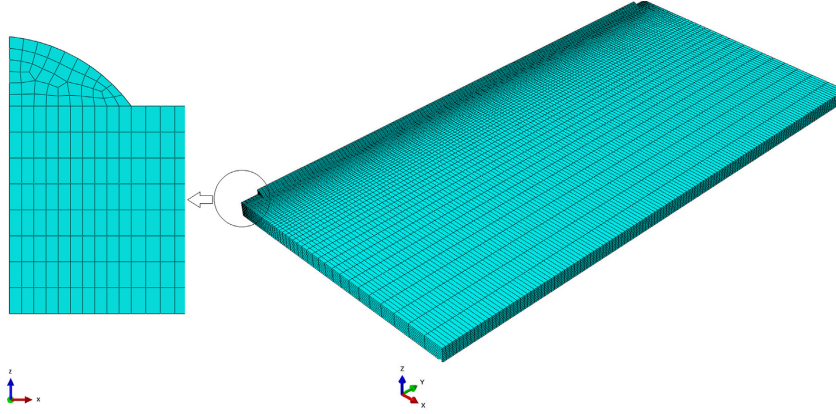


Fig. 3. Meshed symmetric geometry used in the analysis.

Respecting element types in welding simulation problems, employment of linear brick elements for both thermal and mechanical analyses by some authors [21,25] and application of quadratic brick elements in thermal as well as mechanical analyses [18] have been reported. Ahn et al. [19] on the other hand, used quadratic brick elements in thermal analysis and linear brick elements in the subsequent mechanical analysis. Thermal analysis in the present study, however, was performed by employing linear hexahedral eight-node three-dimensional continuum diffusive heat transfer elements (DC3D8) with temperature as the only degree of freedom at each node. Heat transfer analyses involving latent heat effects, as is incorporated in this study, are preferred to be solved using first order diffusive elements owing to their special integration approach [31]. First order reduced integration hexahedral three-dimensional continuum elements (C3D8R) with three translational degrees of freedom at each node were used in mechanical analysis. A better convergence is supposed to be achieved and excessive locking is prohibited during mechanical analysis using reduced integration elements [28].

A fine mesh grid in FZ and its close vicinity was applied, which becomes coarser as the distance towards the edges in transverse to welding direction increases. Fine mesh ensures accurate application of a heat flux introduced by a travelling torch which causes high temperatures and dramatic stress gradient in FZ and HAZ [19,28]. Mesh sensitivity was analyzed to study the effect of mesh density on the accuracy of the results. Mesh convergence was approached when no more accuracy was rendered by further mesh refinement. By taking into account the computational costs, a fine mesh with a total number of 64,808 elements and 71,398 nodes and the smallest element size of  $2.8 \times 0.5 \times 0.5$  mm was found sound enough to provide more than sufficient accuracy to the results.

### 3.2. Temperature-dependent material properties

Temperature-dependent thermo-physical properties of the base and filler materials namely density ( $\rho$ ), thermal conductivity ( $k$ ) and specific heat ( $c$ ) were obtained as a function of their chemical compositions from JMatPro [39]. In this study, due to very similar thermo-physical properties of the base and filler materials, they were defined as the same material and those of base metal was used for both materials as are shown in Fig. 4. It is worthy to mention that units are arranged so that all the properties can be shown in one single graph.

With respect to mechanical properties of material, temperature-dependent Poisson's ratio ( $\nu$ ) was taken from JMatPro [39].

Temperature-dependent yield strength and Young's modulus of base metal were experimentally obtained through conducting hot tensile tests from room temperature (RT) up to 1200 °C. True stress-strain curves of the base material at tested temperatures are shown in Fig. 5. Owing to difficulty finding those of filler material especially at high temperatures, mechanical properties of filler metal were assumed identical to those of base metal as are shown in Fig. 6.

### 3.3. Thermal analysis

Transient temperature field during welding is defined by constitutive heat conduction equation derived from Fourier's law of heat conduction and law of energy conservation with temperature-dependent material characteristics:

$$\rho(T)c_p(T)\frac{\partial T}{\partial t} = \frac{\partial}{\partial x}\left(k(T)\frac{\partial T}{\partial x}\right) + \frac{\partial}{\partial y}\left(k(T)\frac{\partial T}{\partial y}\right) + \frac{\partial}{\partial z}\left(k(T)\frac{\partial T}{\partial z}\right) + \dot{Q}_v \quad (1)$$

where  $\rho(T)$  [kg/m<sup>3</sup>],  $c_p(T)$  [J/kg°C] and  $k(T)$  [W/m°C] are temperature-dependent density, specific heat and thermal conductivity, respectively.  $T$  [°C] is temperature and  $t$  [s] represents time.  $\dot{Q}_v$  [W/m<sup>3</sup>] is known as volumetric heat source density or internal volumetric heat generation rate. In the present work, arc energy from a moving heat source transferred to the parent and weld metals, was applied as a volumetric heat flux implemented in the ABAQUS user subroutine DFLUX based on the model with double ellipsoidal distribution elaborated by Goldak et al. [32]. The model describes two heat flux distributions, one for the front half of the heat source:

$$q_f(x, y, z, t) = \frac{6\sqrt{3}f_r Q}{ab_r c \pi \sqrt{\pi}} e^{-3(\frac{x^2}{a^2} + \frac{(y-w)^2}{b_r^2} + \frac{z^2}{c^2})}, y \geq 0 \quad (2)$$

Similarly, for the rear half:

$$q_r(x, y, z, t) = \frac{6\sqrt{3}f_r Q}{ab_r c \pi \sqrt{\pi}} e^{-3(\frac{x^2}{a^2} + \frac{(y-w)^2}{b_r^2} + \frac{z^2}{c^2})}, y < 0 \quad (3)$$

where  $x, y, z$  are coordinates in the reference system.  $Q$  is power of the welding arc which is calculated using arc voltage, current and welding efficiency  $\eta$ , is assumed to be 0.8 for GMAW process [20]. The parameters  $a, b_r$  and  $c$  are Goldak's weld pool characteristics which can be initially adopted based on the photomicrograph of weld cross-section and weld pool boundaries dimensioning [11]. Via iteration, those parameters can be precisely adjusted to reach a favorable molten zone

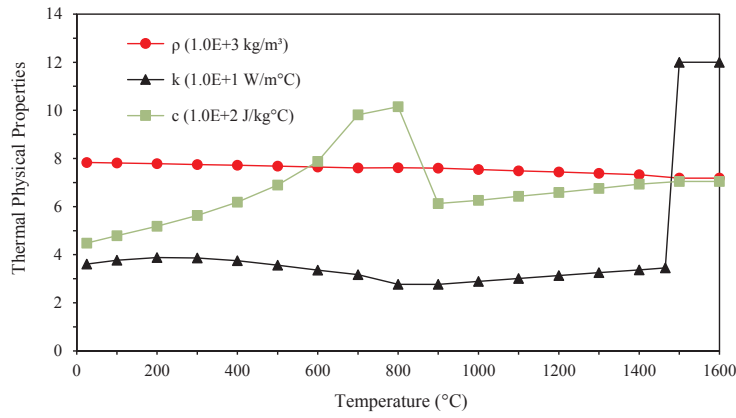


Fig. 4. Temperature-dependent thermo-physical properties of S960 MC.

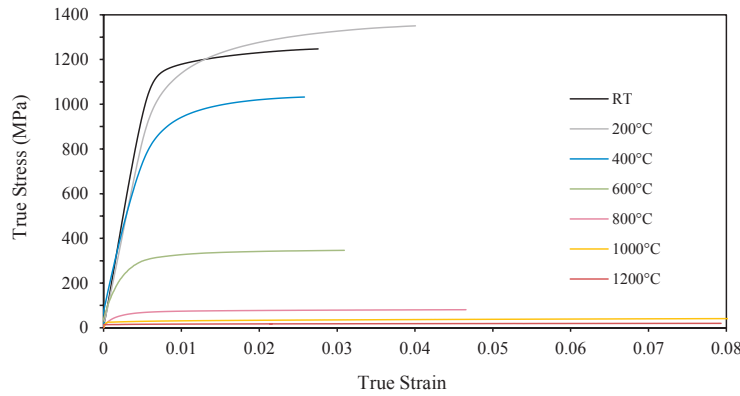
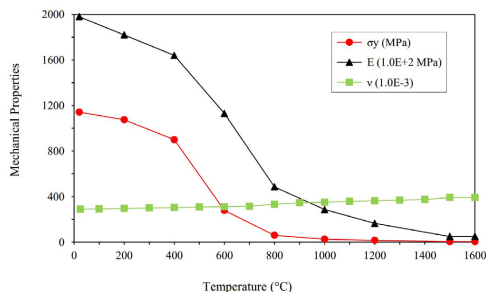


Fig. 5. True stress-strain curves of S960 MC at different temperatures.

Fig. 6. Temperature-dependent mechanical properties of S960 MC,  $\sigma_y$  (yield strength),  $E$  (modulus of elasticity) and  $\nu$  (Poisson's ratio).

and a close agreement between temperature histories from simulation and experiment.  $f_f$  and  $f_r$  are dimensionless fractions of the heat deposited in front and rear half of the heat source, respectively. Heat source parameters and their values used in the analysis, are

**Table 3**  
Parameters of Goldak's heat source model.

Parameter	$a$ (mm)	$b_f$ (mm)	$b_r$ (mm)	$c$ (mm)	$f_f$	$f_r$
Value	4.6	5	14	4	0.53	1.47

summarized in the table 3. The following mathematical relationships are observable by taking the continuity of the heat source into account:

$$\frac{f_r}{b_r} = \frac{f_f}{b_f} \quad (4)$$

$$f_f + f_r = 2 \quad (5)$$

Integration process will be involved in solving the Eq. (1) in which an arbitrary constant will be inserted. A unique solution will be found if the specific boundary conditions are defined. The most frequently applied boundary conditions in welding simulations are heat losses due to convection and radiation from free surfaces being defined based on the Newton's law of cooling and Stefan-Boltzmann's law, respectively. The involvement of the mentioned phenomena in this study was fulfilled by

considering the combined effect of convection and radiation, which is represented via the two mathematical expressions in the Eq. (6) as was practiced by several researchers [4,40,41]. The user subroutine FILM in ABAQUS was developed to model the combined thermal boundary conditions.

$$h = \begin{cases} 0.0668 \times T \left( \frac{W}{m^2 \cdot C} \right) & 0 \leq T \leq 500 \\ 0.231 \times T - 82.1 \left( \frac{W}{m^2 \cdot C} \right) & T \geq 500 \end{cases} \quad (6)$$

where  $h$  denotes the temperature-dependent heat transfer coefficient.

In the context of thermal simulation and calibration of model, convective stirring effect of fluid flow in molten zone was modeled using artificially increased thermal conductivity in temperature ranges higher than melting point termed as effective heat conductivity due to thermo-capillary flow, which is also known as Marangoni effect [4,28,40]. In this regard, thermal conductivity increased linearly between solidus and liquidus temperatures by a factor of three compared to the value of ambient temperature. Latent heat of fusion was taken into account to model the heat effects of solidification in weld pool by assuming the value  $260 \times 10^3$  J/kg between solidus temperature 1465 °C and liquidus temperature 1520 °C.

### 3.3.1. Incorporation of anisotropic heat conductivity in thermal analysis

As mentioned above, with regards to calibration of thermal model to reach an agreement between temperature histories from simulation and experiment, different parameters such as heat source parameters can be calibrated. As will be shown in the results section, further calibration of thermal model (in addition to calibration of Goldak's parameters) to reflect accurate temperature field comparable with experiment, was only possible when anisotropic temperature-dependent thermal conductivity was defined as a calibrating tool. Different phenomena might be involved whose effects were taken into account using anisotropic conductivity. One possible hypothesis is introduced based on the measurement of pre-austenite grain structure of the material and available literature connecting size of grains to anisotropic conductivity. Rolled steel sheets are believed to show orthotropic behavior [42]. Production process of steels can cause alteration in their spatial organizations and size of grains in different directions and anisotropy as a result. The mechanism is not discussed here but it is considered as a known priori. In a study by Jonšta et al. [43], effect of grain size on conductivity of steel samples was investigated. Improved heat transfer and higher thermal conductivity through the coarse-grained samples owing to a fewer number of grain boundaries implying less barrier and reduced resistance versus heat conduction, was reported. Austenite morphologies of the material under investigation in rolling (RD), transverse (TD) and normal (ND) directions is depicted in Fig. 7.

As can be seen in Fig. 7 in RD-ND section, grains are elongated in RD while considerably compressed in ND. A similar pattern is observable in section TD-ND. Size of grains in RD, TD and ND were measured approximately 60.9  $\mu$ m, 50.6  $\mu$ m and 11  $\mu$ m, respectively [44]. Based on this hypothesis, smaller grain size in ND might have an effect on weakening the thermal conductivity through thickness. In this regard, anisotropic material was defined in ABAQUS to which in thickness

**Table 4**

Anisotropic thermal conductivity values used in thermal analysis.

Temperature (°C)	25	200	400	600	800	1000	1200	1400	1500
Thermal conductivity (W/m°C)	RD 36 TD 36 ND 16	39 39 20	37 37 19	34 34 18	28 28 15	29 29 29	31 31 31	34 34 34	120 120 90

direction, decreased heat conductivity values compared to those of rolling and transverse directions, in the entire temperature ranges below the austenitization temperature, were assigned. Those values, then, were iterated to reach a close agreement between the temperature histories predicted by simulation and experiment as are summarized in the table 4.

### 3.4. Mechanical analysis

In a sequentially-coupled formulation, temperature histories predicted in thermal analysis are used as thermal load in mechanical analysis. Mechanical (structural) analysis is accomplished upon solving non-linear elasto-plastic governing partial differential equations. One of the equations is equilibrium equation [45]:

$$\nabla \cdot \sigma + F_b = 0 \quad (7)$$

where  $\nabla$  is divergence operator,  $\sigma$  shows Cauchy stress tensor and  $F_b$  implies body force vector. The other equation is thermal elasto-plastic constitutive equation through which the relation between stresses and strains is expressed [46]:

$$\{d\sigma\} = [D]\{d\epsilon\} - [C_{th}]\{dT\} \quad (8)$$

And  $[D] = [D^e] + [D^p]$  where  $d\sigma$ ,  $d\epsilon$  and  $dT$  show increments of stress, strain and temperature, respectively.  $C_{th}$  is matrix of thermal stiffness,  $[D^e]$  and  $[D^p]$ , respectively denote elastic and plastic stiffness matrices. Taking the effect of SSPT into account, the total strain rate component in this study, is decomposed by its constituents as is expressed by Eq. (9):

$$\dot{\epsilon}^{total} = \dot{\epsilon}^e + \dot{\epsilon}^p + \dot{\epsilon}^{th} + \dot{\epsilon}^{\Delta V} \quad (9)$$

where  $\dot{\epsilon}^{total}$  is total strain rate.  $\dot{\epsilon}^e$ ,  $\dot{\epsilon}^p$  and  $\dot{\epsilon}^{th}$  correspond to elastic, plastic and thermal strain rate components, respectively.  $\dot{\epsilon}^{\Delta V}$  is volumetric change strain due to phase transformation. Elastic strain is calculated using inverted generalized Hook's law in which temperature-dependent Poisson's ratio and Young's modulus are applied as below:

$$\epsilon_{ij}^e = \frac{1}{E} [(1 + \nu)\sigma_{ij} - \nu\sigma_{kk}\delta_{ij}] \quad (10)$$

where  $\delta_{ij}$  is Kronecker delta,  $E$  represents Young's modulus,  $\nu$  indicates Poisson's ratio and  $\sigma_{ij}$  is stress tensor. Plastic strain component is calculated upon employing a rate-independent plastic model as is demonstrated in Eq. (11), with temperature-dependent mechanical properties, Von Mises yield surface and isotropic hardening model [47]:

$$\dot{\epsilon}_{ij}^p = \lambda s_{ij} \quad (11)$$

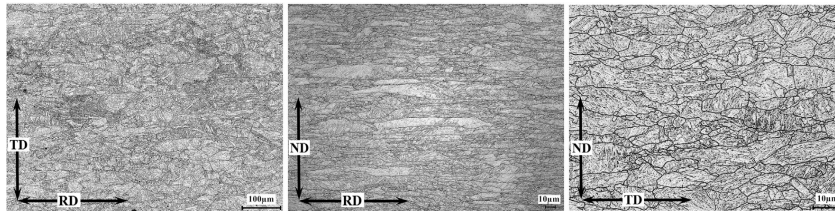


**Fig. 7.** Pre-austenite grain structure of S960 MC [44].

And  $s_{ij} = \sigma_{ij} - \frac{1}{3}\sigma_{kk}\delta_{ij}$  where  $\dot{\epsilon}_{ij}^p$  is plastic strain rate component,  $\lambda$  signifies the plastic flow factor and  $s_{ij}$  represents the deviatoric stress tensor, which is calculated by subtracting the hydrostatic tensor from the total stress tensor. The present study considers the effect of annealing on plastic behavior of material. When temperature of material rises and exceeds a specific temperature called annealing temperature, strain hardening memory is annihilated and the effect of prior work hardening for that node is removed. This matter is accomplished by ABAQUS through resetting the equivalent plastic strain to zero. On condition that a nodal temperature of material falls below the defined annealing temperature, it can work harden again [19,28]. The implementation in ABAQUS was performed via defining a sub-option in plastic properties of material which was set to a value of 900 °C in mechanical analysis. A cut-off temperature of 1500 °C was defined for material properties in mechanical analysis. If temperature exceeds 1500 °C, material properties are evaluated at cut-off temperature. In order to avoid convergence difficulties, yield strength and Young's modulus values at cut-off temperature were reduced to 5 MPa and 5 GPa, respectively. Inasmuch as no special clamping was used to constrain the work piece, in structural analysis, boundary conditions were defined to solely prevent rigid body motion [33]. That is, the symmetry plane is restricted in X-direction. Point A, the first node lying on welding centerline is constrained in Y and Z-directions and the last point on the welding centerline, point B, is restricted to move in Z-direction as is shown in Fig. 8.

### 3.5. Solid-state phase transformation

Involvement of volumetric change strain component in calculation of total strain increment was accomplished using the analysis of SSPT by applying kinetics of phase transformation and CCT diagram. Kinetics of SSPT was defined using applied mathematical models in which dilatometric data concerning the present phases during heating and cooling, transformation temperatures, linear thermal expansion coefficients of microconstituents as well as full volumetric change strains of present phases were mathematically correlated. All the data required to express transformation kinetics models in this study, were experimentally obtained by conducting dilatometric tests. An experimental graph regarding the heating rate 640 °C/s and cooling rate 50 °C/s is shown in Fig. 9. Thermal cycles during welding are addressed to as the particular contributor in occurrence of SSPT and associated volume change in steels. Volumetric change strains induced by transformations were derived from phase work hardening owing to the difference in thermal expansion coefficients of present phases [19].

#### 3.5.1. Austenitic transformation model

Prior to undergoing any thermal cycle, microstructure of the base material, based on Scanning electron microscopy (SEM) image, as is

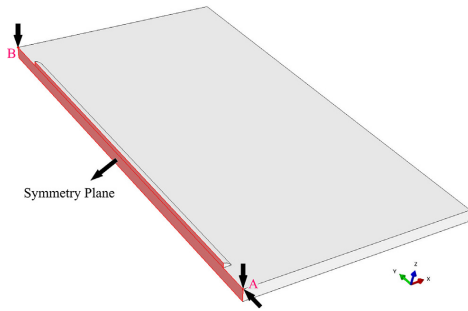


Fig. 8. Mechanical boundary condition.

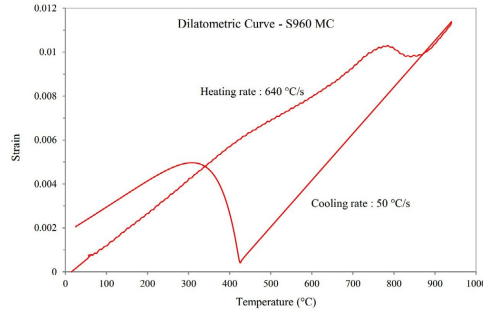


Fig. 9. Dilatometric curve of the investigated material for heating rate 640 °C/s and cooling rate 50 °C/s.

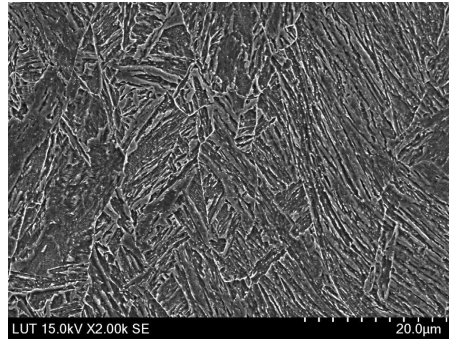


Fig. 10. Scanning electron micrograph of S960 MC with bainite and martensite as microconstituents.

shown in Fig. 10, is a mixture of bainite and martensite.

When material is heated up to  $A_1$  temperature, bainitic-martensitic microstructure of base metal starts to transform to austenite with a decrease in its net volume. It is assumed that increase in the volume fraction of austenite between  $A_1$  and  $A_3$  temperatures in heating, follows a linear rule as follows [26]:

$$f_a = \frac{T_{max} - A_1}{A_3 - A_1} \quad (12)$$

$$A_1 \leq T_{max} \leq A_3$$

where  $f_a$  denotes the volume fraction of austenite during austenitic transformation as a function of  $T_{max}$ , the maximum temperature a material point meets during heating.  $A_1$  and  $A_3$  which are lower and upper critical temperatures, respectively, were determined based on the analysis of the experimental dilatometric curve during heating and application of tangent-intersection method as was practiced by Li et al. [48]. The values of 775 °C and 863 °C were obtained for  $A_1$  and  $A_3$  temperatures, respectively.

#### 3.5.2. Diffusive transformation model

In diffusional transformation, might exist one or more nascent phases whose chemical compositions differ from the extant parent phase which requires long-distance diffusion. As the name indicates, the most substantial factor in this transformation is thermally activated atomic diffusion or movement of individual atoms. Inasmuch as diffusion is a time-dependent phenomenon, such transformations are not instantaneous and occur in the course of time [49]. Volume fractions of



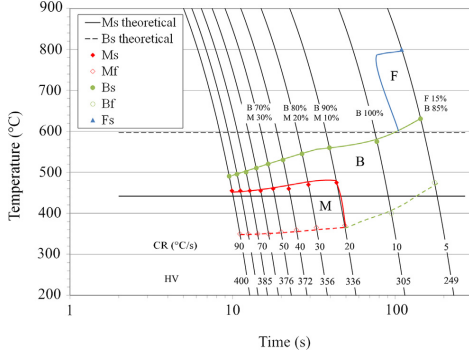


Fig. 11. CCT diagram of S960 MC.

phases whose transformations from austenite in cooling is diffusional, were defined using the final fraction of that specific microstructural constituent which depends on the cooling rate in the range 800–500 °C ( $v_{8/5}$ ) in addition to start and ending transformation temperatures. For the material under investigation, bainite is the only microconstituent whose formation is defined upon the kinetics of diffusive transformation based on the prevalent cooling rates in HAZ. Final fraction of bainite was calculated from the experimentally-determined CCT diagram. Kinetics model of Machnienko for diffusive transformation was applied as was previously practiced by Piekarska et al. [23] :

$$f_b(T, t) = f_b^{\infty} \left[ 1 - \exp\left(-k_a \frac{B_s - T}{B_s - B_f}\right) \right] \quad (13)$$

where  $f_b(T, t)$  denotes the volume fraction of bainite during diffusive transformation as a function of  $T$ , current temperature.  $f_a$  is the volume fraction of austenite formed during heating and  $f_b^{\infty}$  is the final fraction of bainite determined based on the CCT diagram which is shown in Fig. 11.  $k_a$  is a factor whose value was adjusted in the range 2.5–3. Bainite start temperature ( $B_s$ ) and bainite finish temperature ( $B_f$ ) were experimentally obtained from dilatometric tests being respectively 520 °C and 460 °C in both FZ and HAZ.

### 3.5.3. Martensitic transformation model

Diffusionless or displacive transformation refers to a transformation in which chemical composition of the nascent phase remains identical to extant parent phase. In steels, transformation of martensite from austenite has a diffusionless nature in which chemical composition of austenite is directly inherited by martensite [33,49]. Transformation of martensite from austenite, analogous to bainite transformation is followed by an increase in net volume. The amount of martensite transformed from austenite in cooling, depends highly on the martensite start temperature ( $M_s$ ), which is the onset of transformation of austenite into martensite. Martensite transformation is presumed to be completed when martensite finish temperature ( $M_f$ ) is met.  $M_f$  is the temperature at which austenite is fully transformed to martensite and below which, further cooling has no effect on amount of the formed martensite [25].  $M_s$  and  $M_f$  temperatures were identified experimentally based on the dilatometric curves during cooling which were set to 460 °C and 355 °C, respectively. Tracking the volume fraction of martensite during cooling in the temperature ranges below  $M_s$  were accomplished by employing Koistinen-Marburger kinetics model [23] as is expressed in the following formulation:

$$f_m = f_m^{\infty} \left[ 1 - \exp(-k_m (M_s - T)) \right] \quad (14)$$

where  $f_m$  denotes the volume fraction of martensite during martensitic transformation at  $T$ , current temperature.  $f_m^{\infty}$  is the final fraction of martensite obtained from the CCT diagram. Transformation evolution is characterized according to temperature by the factor  $k_m$  which was considered 0.05 in the present study based on the recommendations of Li et al. [30]. The sum of the strains due to thermal expansion and volume change in Eq. (9) is referred to as thermal dilatation which is calculated from the following expression [23]:

$$d\varepsilon^{th+\Delta V} = d\varepsilon^{th} + d\varepsilon^{\Delta V} = \sum_i \alpha_i f_i dT - \text{sign}(dT) \sum_i \varepsilon_i^{\Delta V} df_i \quad (15)$$

where  $f_i$  indicates the volume fraction of phase  $i$  calculated from Eqs. (12), (13) and (14) whereas,  $df_i$  shows the derivative of the mathematical expressions to calculate volume fraction of phase  $i$ .  $\alpha_i$  shows linear thermal expansion coefficient of phase  $i$ . The values of  $\alpha_a$ ,  $\alpha_b$  and  $\alpha_m$  corresponding to austenite, bainite and martensite in the present study, based on the dilatometric curves are  $2.02$ ,  $1.25$  and  $1.37 (\times 10^{-5}) [\frac{1}{^\circ\text{C}}]$ . The full volumetric change strain  $\varepsilon_i^{\Delta V}$  of phase  $i$  due to full austenitic, bainitic and martensitic transformations were determined based on dilatometric curves. The values  $1.51$ ,  $4.10$  and  $6.6 (\times 10^{-3})$  were respectively assigned to austenite, bainite and martensite.  $\text{sign}$  function depends on temperature change, i.e. provided that temperature difference is positive which happens during heating,  $\text{sign}$  is equal to +1 and during bainitic and martensitic transformations is equal to -1 [23].

### 3.5.4. Implementation of SSPT in ABAQUS

Simulation of phase transformation and modification of strains in mechanical analysis, were performed by implementation of SSPT kinetics in numerical subroutines in ABAQUS. User subroutine USDFLD is generally utilized to define material properties at each integration point of an element as a function of field variables. ABAQUS Utility routine GETVRM inside the USDFLD is used to access a material point data [31]. That is, temperature changes between the increments are saved inside a field variable. Based on the sign of temperature change (positive during heating and negative in cooling) and the maximum temperature of each integration point which was recorded by GETVRM, different scenarios are deemed and the decision is made whether or not the point has undergone transformation. For the material points underwent transformation, the relevant kinetics model is applied to obtain volume fraction of austenite during heating and arising phases upon the austenite decomposition in cooling [20,23,26]. In this context, to obtain volume fractions of microstructural constituents at each node and time increment, Eqs. (12), (13) and (14) were implemented in USDFLD subroutine. Solution-dependent state variables (SDVs) in USDFLD subroutine were employed in order to store the calculated volume fractions based on the above-mentioned mathematical relationships. SDV5, SDV7 and SDV8 are state variables in which calculated volume fractions of base material, bainite and martensite are respectively stored. A descriptive diagram regarding the implementation of the phase transformation kinetics in USDFLD is provided in Fig. 12. User subroutine UEXPAN is employed in applications where incremental thermal strains are defined as a function of temperature, field variables or state variables [31]. The output of USDFLD saved in field variables and state variables, are passed into the UEXPAN where incremental strains according to Eq. (15) are modified [23,26].

## 4. Results and discussion

### 4.1. Validation of thermal analysis

Distribution of temperature during welding based on the numerical simulation incorporating anisotropic temperature-dependent thermal conductivity is shown in Fig. 13. The Peak temperature calculated in the thermal analysis falls within the realistic temperature ranges (1800–2200 °C) based on the reported results by other researchers for

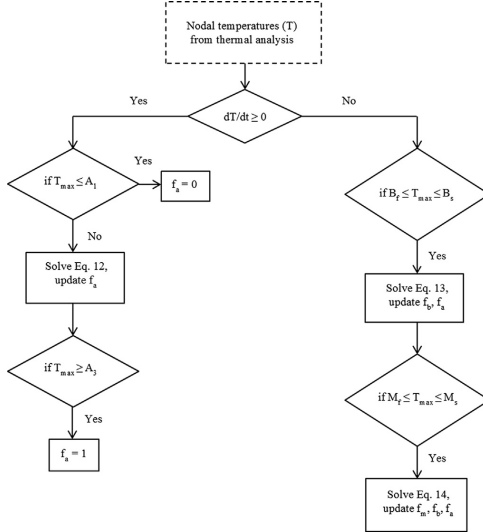


Fig. 12. The flow diagram of implanting SSPT kinetics in USDFLD.

similar welding process [4,25].

Prediction of the shape and size of the weld pool might act as an auxiliary index of correct thermal distribution in FZ and HAZ supplementary to temperature history records. Determining the precise weld pool shape and boundaries, requires modeling the fluid flow and dynamics of weld pool, which is not the concern of this study. In this regard, however, Goldak's parameters were adjusted in a realistic manner so that reinforcement width and depth of penetration are in close concurrence with the experimentally observed ones. A comparison has been drawn between the simulated and measured width and length of the fused reinforcement on top surface at the end of welding path in Fig. 14 (a). Depth of penetration and height of weld bead from simulation and cross-section of the welded specimen at mid-section are depicted in Fig. 14 (b).

In order to validate the thermal analysis and evaluate the accuracy of developed thermal model to predict nodal transient temperatures of welding, thermal cycles at various positions on both top and bottom surfaces were determined by thermocouples. Calibration of simulated curves versus recorded temperature histories includes variation of thermal boundary conditions to match the simulated and experimental temperature fields as close as possible. This study, nevertheless, shows that calibration of thermal conductivity in different directions of the investigated material has a significant role in verification of thermal analysis. The necessity of employing anisotropic thermal conductivity rather than isotropic one in thermal analysis of welding process for the material under investigation should be corroborated. To do so, a comparison is drawn between the simulated temperature histories at certain nodes corresponding to the positions of thermocouples by the two mentioned thermal models versus the experimentally determined ones as are shown in Fig. 15.

An excellent agreement between the FE simulation results considering anisotropic thermal conductivity and measurement of peak temperatures as well as heating and cooling rates at different thermocouple positions on both top and bottom surfaces is observable. Nevertheless, obvious discrepancies exist between temperature histories predicted by the model using isotropic temperature-dependent thermal conductivity and measurements. It is needed to mention that both models are calibrated in terms of the Goldak's parameters. That is, on top surface, for two thermocouple positions  $T_1$  and  $T_4$ , the latter located in HAZ and the former in the base metal adjacent to HAZ, as are shown in Fig. 15 (a) and (d), respectively, peak temperatures and cooling rates are predicted lower than the experiment. For two thermocouple positions far from HAZ, namely  $T_2$  and  $T_3$ , as are respectively presented in Fig. 15 (b) and (c), simulated curves by such model yet keep distance from the experimental curves with predicted peak temperatures higher than the measured ones. The reason can be attributed to the application of incorrect pattern of thermal conduction by such model in which the energy transported in all directions are assumed to be identical.

Fig. 15 (e) and (f) unequivocally demonstrate that even more dramatic differences exist between the predicted thermal field by the model runs upon isotropic conductivity assumption and observed reality on the bottom side. Serious errors are involved in reflecting the heating rates, cooling rates and more importantly, peak temperatures when this model is put into application for this material, which proves the inability of such model to represent acceptable results concerning prediction of the temperature histories especially at the bottom surface.

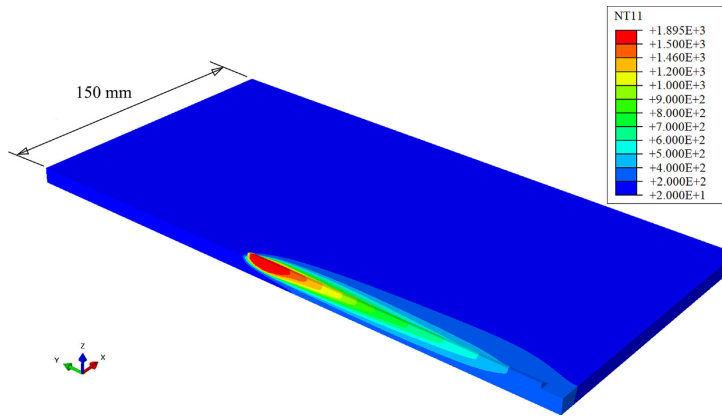


Fig. 13. Graphical presentation of thermal contours in symmetry plane during welding.



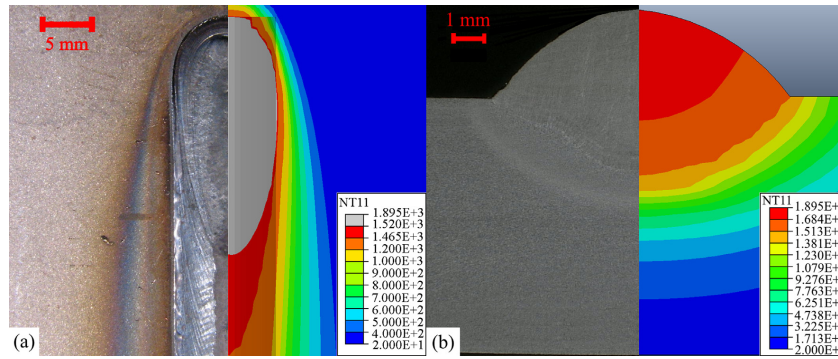


Fig. 14. Welding temperatures from simulation (NT11) and boundaries of the weld pool from simulation versus experiment on top surface (a), through thickness (b).

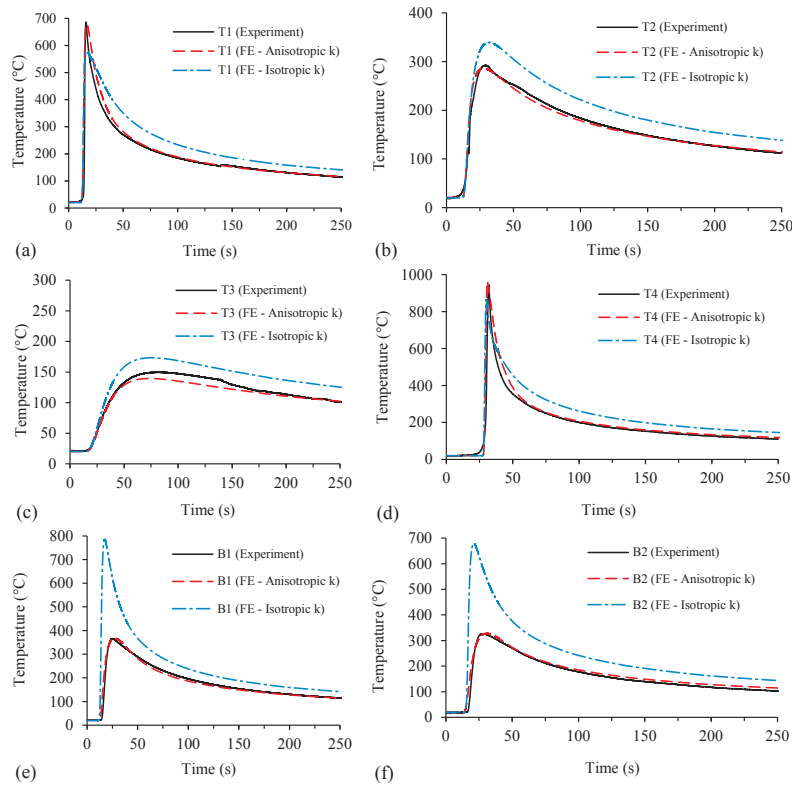


Fig. 15. Measured versus simulated (with anisotropic and isotropic thermal conductivities) temperature histories at thermocouple positions T<sub>1</sub> (a), T<sub>2</sub> (b), T<sub>3</sub> (c), T<sub>4</sub> (d), B<sub>1</sub> (e) and B<sub>2</sub> (f).

The importance of accuracy in determining the temperature histories is more highlighted as it pertains to prediction of microstructure in HAZ. A close attention to Fig. 15 (d) reveals that the thermocouple position T<sub>4</sub> experiences temperatures higher than A<sub>3</sub> temperature and is

fully austenitized, as is also predicted by anisotropic conductivity model, while such material point is predicted to undergo incomplete austenitic transformation by the isotropic conductivity model. Another relevant example in this regard is shown in Fig. 15 (e). Based on the

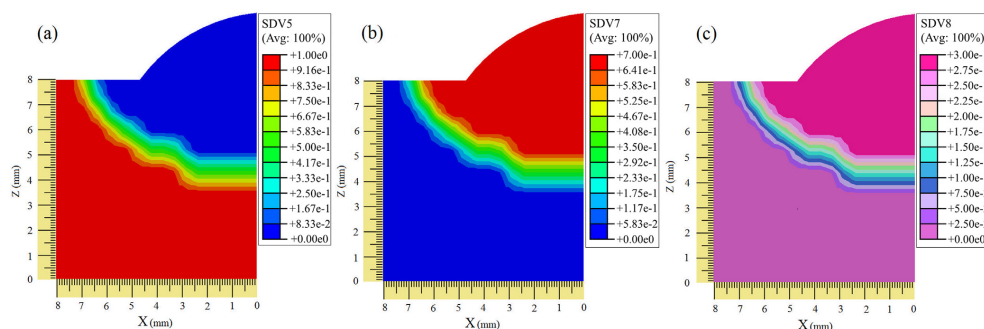


Fig. 16. Volume fractions of base metal (a), formed bainite (b) and martensite (c) in the middle section of the model.

isotropic model, thermocouple position B<sub>1</sub> undergoes austenitic transformation while in fact, the temperature experienced in that material point is far lower than A<sub>1</sub> temperature and thus, no phase transformation is anticipated to occur in the mentioned point. Such an analysis subsequently leads to an inaccurate evaluation of the fraction of phases arising during austenite decomposition. Therefore, the reliability of the thermal analysis based on the assumption of isotropic heat conductivity for the concerned material is questionable. Validation of temperature histories is the most prominent measure of correctness and accuracy of thermo-numerical model. Such validation is the bedrock of nodal temperature transfer for subsequent metallurgical and mechanical analyses, which are highly contingent upon correct distribution of heat in FZ and HAZ.

#### 4.2. Metallurgical analysis and prediction of microstructure

Kinetics of phase transformation as well as prediction of microstructure and boundaries of HAZ in regions whose temperatures exceeded A<sub>1</sub> temperature, were included in metallurgical analysis. Fig. 16 shows visual presentation of calculated volume fractions of bainite and martensite formed in HAZ and FZ upon decomposition of austenite as well as volume fraction of base material in which volume fractions of base material, bainite and martensite are presented by defined state variables SDV5, SDV7 and SDV8, respectively.

From Fig. 16 (a), for each node, volume fraction of parent material after welding and cooling can be obtained. Based on the presented figure, parent material might be untransformed (volume fraction is equal to 1 in presented contour bar), partially transformed or fully transformed (volume fraction is equal to 0 in the related contour bar). In the case of transformation of base material to austenite, in cooling stage, bainite and martensite will form whose simulated volume fractions are respectively shown in Fig. 16 (b) and (c). For an arbitrary node located 6.2 mm far from the weld center line in the mid-section of the FE model on top surface, simulated graphical presentation of welding thermal cycle and variations in volume fractions of austenite, bainite and martensite as a function of time are shown in Fig. 17.

Microstructural observation of the welded specimen in HAZ is in agreement with the results of the FE simulation with respect to the presence of a mixture of bainite and martensite, as is shown in Fig. 18. Grain growth in HAZ and prior-austenite grain boundaries with dashed lines are clearly shown in an SEM image in Fig. 18 (a). A mixture of bainite and martensite in the HAZ microstructure of the welded plate in which the volume fraction of bainite is greater than martensite volume fraction, is observable in Fig. 18 (b).

Similar to distribution of microstructure in HAZ, composition of structure in FZ, as is demonstrated in Fig. 19, consists of a bainitic microstructure in which martensite is scatteredly distributed.

Martensite islands are shown with dashed lines and the letter “M” refers to martensite. Bainite share, as can be clearly seen, is larger compared to that of martensite as is also observable from the calculated fractions of bainite and martensite presented in Fig. 16.

#### 4.3. Simulated mechanical analysis and the effect of SSPT on welding distortions

In order to elucidate the effect of SSPT on mechanical analysis and validation of the FE model to predict welding distortions, two simulation cases were considered. One case neglects the effect of volume change due to SSPT on mechanical analysis, while such effect was taken into account by the other model. Incorporation of SSPT in mechanical analysis was fulfilled by developing the user subroutine UEXPAN in ABAQUS in which strains were modified by including volume fractions of present phases and full volumetric change strain of each phase during heating and cooling.

In order to study the mesh sensitivity, four element sizes were chosen as are presented in the table 5 and mechanical analyses were performed to choose the efficient mesh to compare the results of FE models with experiment.

The effect of element size and mesh density on angular deformation simulated by FE model considering the effect of SSPT was investigated for the cases mentioned in the table 5 and the results are plotted in Fig. 20.

As can be observed in Fig. 20, reducing the size of elements, results in decreasing the angular distortion along the path 1 (specified in Fig. 2) predicted by the FE model. The deformation decreased by 18% when the meshing style was changed from case 1 to case 3. By taking into account the accuracy and computational costs, the meshing style in case 3 was applied to the FE models. Fig. 21 shows displacement contours in which U3 values are displacement values in Z-direction simulated by the FE model that considers SSPT.

A comparison has been made between the results of the FE models and experimental measurements concerning out of plane displacements, namely angular and bending distortions along the defined paths on top surface of the specimen. The results of measuring angular distortion along paths 1 & 2 specified in Fig. 2, versus simulated cases (with and without SSPT) are depicted in Fig. 22 (a) and (b), respectively.

Angular distortion as is observable from Fig. 21 is symmetrical with respect to the weld center line and rises as the distance from the weld line towards the outer edges increases. The results of simulations show an acceptable agreement with measurements. The model which incorporates the effect of SSPT, however, more accurately predicts angular distortion along path 1 & 2 specified in Fig. 2, and from magnitude point of view, keeps smaller distances from the experimental ones

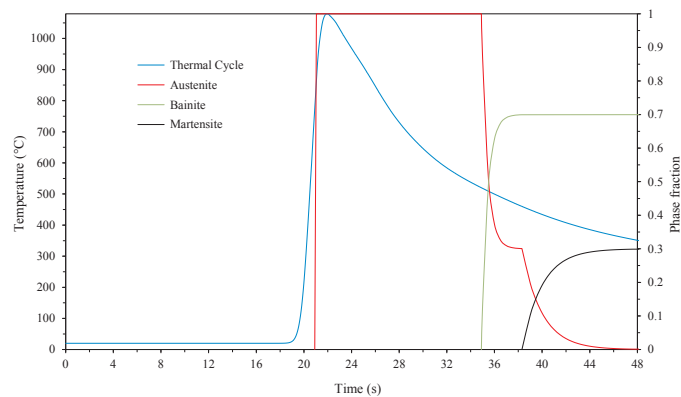


Fig. 17. Welding temperatures and volume fractions of microconstituents during the welding thermal cycle for a point in HAZ (6.2 mm from weld center line in mid-section) on top surface.

compared to the other FE model indicating the superiority of the SSPT model. The smaller values for angular displacement predicted by the SSPT model compared to the other FE model, originate from the volume increase during bainitic and martensitic transformations resulting in smaller distortion, which is in concurrent with the findings of a study by Deng [33]. The values of bending distortion which occurs along the path 3 specified in Fig. 2, predicted by the two models are plotted versus the experimentally measured ones in Fig. 23.

Magnitude of bending distortion compared to the angular deformation is smaller in this study and is limited to fraction of a millimeter. Both simulated cases overpredicted out of plane bending deformation, nonetheless, the resulted curve from the model ignoring SSPT holds a large distance from the experimental one, while the values predicted by the SSPT model, sustain smaller discrepancies from the measured values which proves the SSPT model is able to provide more accuracy to the results.

## 5. Conclusions and future work

In this paper, a FE model to simulate bead-on-plate GMAW of an ultra-high strength carbon steel in ABAQUS was developed. A comprehensive SSPT model considering both diffusive and displacive transformations was incorporated in numerical procedure, and its effect on welding distortion patterns was investigated. FE results regarding

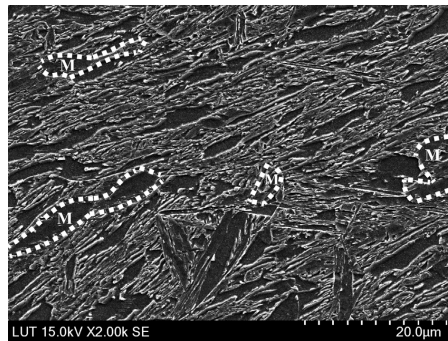


Fig. 19. SEM micrograph of FZ shows martensite with a smaller share is distributed in a bainitic microstructure.

thermal simulation and prediction of distortions were verified by experiments. The following conclusions from the simulation results and experimental measurements are drawn:

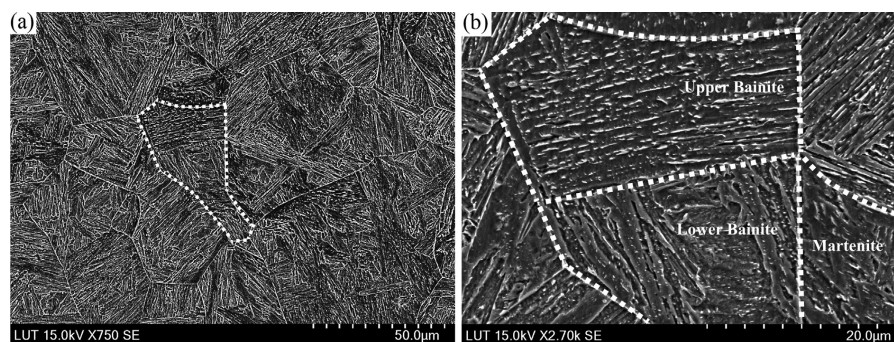


Fig. 18. SEM micrographs of HAZ, Prior austenite grain boundaries (a), a mixture of bainite and martensite (b).

**Table 5**  
Minimum element size and number of elements in each case.

Case	Min element size in weld region (length × width × thickness)	Number of meshing elements
1	$5.6 \times 1 \times 2$	7296
2	$2.8 \times 0.5 \times 1$	34,852
3	$2.8 \times 0.5 \times 0.5$	64,808
4	$1.4 \times 0.5 \times 0.5$	129,608

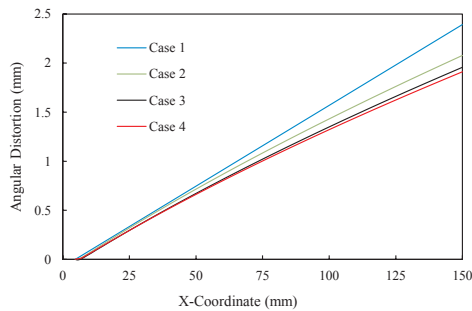


Fig. 20. Variation in angular distortion based on meshing cases.

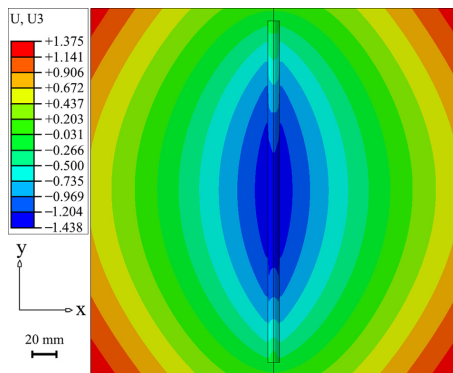
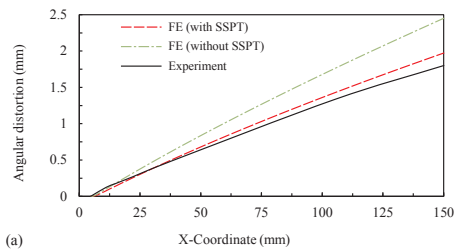
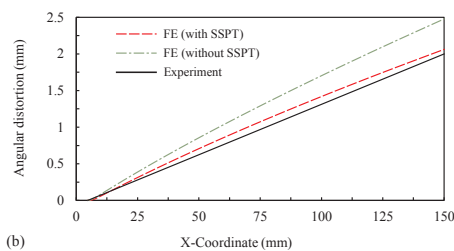


Fig. 21. Displacement contours (U3) after cooling and relaxation. (Units in mm).

- (1). The results of thermal model that uses isotropic conductivity show some differences with temperature measurement by means of thermocouples. Closer agreement between the results of thermal simulation and thermocouple measurements in terms of temperature distribution was observed when anisotropic conductivity as a calibrating tool was adopted. Based on austenite morphologies of the material and connection of grain size with heat conductivity from another research, one possible hypothesis is introduced in which reduced conductivity in thickness direction is correlated to smaller grain size through thickness.
- (2). Simulation predicts that welded material in HAZ and FZ has a bainitic-martensitic microstructure in which martensite share is smaller than that of bainite. This matter is also observable from microstructural observations of welded specimen in FZ and HAZ.
- (3). Prediction of welding-induced angular distortion and out of plane bending deformation with the SSPT model shows higher level of accuracy compared to the model that neglects such effect.



(a)



(b)

Fig. 22. Angular distortion along path 1 (a) and path 2 (b).

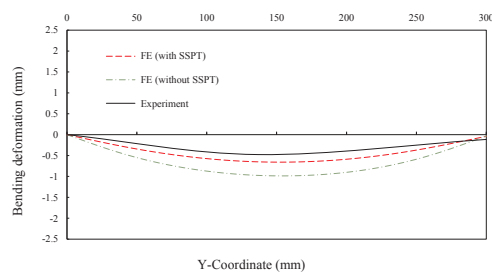


Fig. 23. Simulated bending distortion versus the experiment along the specified path.

- (4). In the present study, residual stresses are not studied. Design-wise, they are necessary to consider. Thus, in the upcoming research, numerical simulation and experimental measurement of longitudinal and transverse residual stresses will be considered.

#### CRedit authorship contribution statement

**Mehran Ghafouri:** Conceptualization, Methodology, Software, Validation, Writing - original draft, Visualization. **Joseph Ahn:** Methodology, Software, Writing - review & editing. **Juho Mourujärvi:** Validation, Writing - review & editing, Visualization. **Timo Björk:** Conceptualization, Writing - review & editing, Supervision, Funding acquisition. **Jari Larkiola:** Writing - review & editing, Supervision.

#### Declaration of Competing Interest

The authors declare that they have no known competing financial interests or personal relationships that could have appeared to influence the work reported in this paper.

## Acknowledgements

This research was funded by Business Finland (TEKES). The CSC - IT Center for Science Ltd. is acknowledged for providing the computational resources. The support of SSAB Europe is acknowledged.

## References

- [1] Guo W, Crowther D, Francis JA, Thompson A, Liu Z, Li L. Microstructure and mechanical properties of laser welded S960 high strength steel. *Mater Des* 2015;85:534–48.
- [2] Guo W, Li L, Dong S, Crowther D, Thompson A. Comparison of microstructure and mechanical properties of ultra-narrow gap laser and gas-metal-arc welded S960 high strength steel. *Opt Lasers Eng* 2017;91:1–15.
- [3] Dabiri M, Isakov M, Skriko T, Björk T. Experimental fatigue characterization and elasto-plastic finite element analysis of notched specimens made of direct-quenched ultra-high-strength steel. *Proceed Inst Mecha Eng, Part C: J Mech Eng Sci* 2016;231(22):4209–26.
- [4] Deng D, Murakawa H. Numerical simulation of temperature field and residual stress in multi-pass welds in stainless steel pipe and comparison with experimental measurements. *Comput Mater Sci* 2006;37(3):269–77.
- [5] Skriko T, Ghafouri M, Björk T. Fatigue strength of TIG-dressed ultra-high-strength steel fillet weld joints at high stress ratio. *Int J Fatigue* 2017;94:110–20.
- [6] Azhari F, Heidarpour A, Zhao X-L, Hutchinson CR. Mechanical properties of ultra-high strength (Grade 1200) steel tubes under cooling phase of a fire: An experimental investigation. *Constr Build Mater* 2015;93:841–50.
- [7] Anca A, Cardona A, Rizzo J, Fachinotti VD. Finite element modeling of welding processes. *Appl Math Model* 2011;35(2):688–707.
- [8] Goldak J, Bibby M, Moore J, House R, Patel B. Computer modeling of heat flow in welds. *Metall Trans B* 1986;17(3):587–600.
- [9] Heinze C, Schwenk C, Rethmeier M. Numerical calculation of residual stress development of multi-pass gas metal arc welding. *J Constr Steel Res* 2012;72:12–9.
- [10] Deng D, Murakawa H, Liang W. Numerical simulation of welding distortion in large structures. *Comput Methods Appl Mech Eng* 2007;196(45–48):4613–27.
- [11] Goldak J, Akhlaghi M. *Computational Welding Mechanics*. New York: Springer; 2005.
- [12] Lindgren L-E. *Computational Welding Mechanics*. Cambridge: Woodhead Publishing; 2007.
- [13] Lindgren L-E. Numerical modelling of welding. *Comput Methods Appl Mech Eng* 2006;195(48–49):6710–36.
- [14] Lindgren L-E. Finite element modeling and simulation of welding part 1: Increased complexity. *J Therm Stresses* 2001;24(2):141–92.
- [15] Lindgren L-E. Finite element modeling and simulation of welding. Part 2: Improved material modeling. *J Therm Stresses* 2001;24(3):195–231.
- [16] Lindgren L-E. Finite element modeling and simulation of welding. Part 3: Efficiency and integration. *J Therm Stresses* 2001;24(4):305–34.
- [17] Yaghi A, Hyde T, Becker A, Williams J, Sun W. Residual stress simulation in welded sections of P91 pipes. *J Mater Process Technol* 2005;167(2–3):480–7.
- [18] Shan X, Davies C, Wangsdan T, O'Dowd N, Nikbin K. Thermo-mechanical modelling of a single-bead-on-plate weld using the finite element method. *Int J Press Vessels Pip* 2009;86(1):110–21.
- [19] Ahn J, He E, Chen L, Wimpory R, Dear J, Davies C. Prediction and measurement of residual stresses and distortions in fibre laser welded Ti-6Al-4V considering phase transformation. *Mater Des* 2017;115:441–57.
- [20] Deng D, Murakawa H. Finite element analysis of temperature field, microstructure and residual stress in multi-pass butt-welded 2.25Cr-1Mo steel pipes. *Comput Mater Sci* 2008;43(4):681–95.
- [21] Danis Y, Lacoste E, Arvieu C. Numerical modeling of inconel 738LC deposition welding: Prediction of residual stress induced cracking. *J Mater Process Technol* 2010;210(14):2053–61.
- [22] Ahn J, He E, Chen L, Pirling T, Dear J, Davies C. Determination of residual stresses in fibre laser welded AA2024-T3 T-joints by numerical simulation and neutron diffraction. *Mater Sci Eng, A* 2018;712:685–703.
- [23] Piekarska W, Kubiak M, Saternus Z. Numerical Modelling of Thermal and Structural Strain in Laser Welding Process. *Arch Metall Mater* 2012;57(4):1219–27.
- [24] Bhatti AA, Barsoum Z, Murakawa H, Barsoum I. Influence of thermo-mechanical material properties of different steel grades on welding residual stresses and angular distortion. *Mater Des* 2015;65:878–89.
- [25] Lee C-H, Chang K-H. Finite element simulation of the residual stresses in high strength carbon steel butt weld incorporating solid-state phase transformation. *Comput Mater Sci* 2009;46(4):1014–22.
- [26] Kubiak M, Piekarska W. Comprehensive model of thermal phenomena and phase transformations in laser welding process. *Comput Struct* 2016;172:29–39.
- [27] Mi G, Xiong L, Wang C, Hu X, Wei Y. A thermal-metallurgical-mechanical model for laser welding Q235steel. *J Mater Process Technol* 2016;238:39–48.
- [28] Lee C-H, Chang K-H. Prediction of residual stresses in high strength carbon steel pipe weld considering solid-state phase transformation effects. *Comput Struct* 2011;89(1–2):256–65.
- [29] Taljat B, Radhakrishnan B, Zacharia T. Numerical analysis of GTA welding process with emphasis on post-solidification phase transformation effects on residual stresses. *Mater Sci Eng, A* 1998;246(1–2):45–54.
- [30] Li Y, Lu H, Yu C, Wu Y. Accurate Prediction of Welding Stress Evolution by Considering Improved Phase Transformation Model. *Mater Trans* 2015;56(5):715–9.
- [31] ABAQUS user's manual, Version 2017, Dassault Systèmes\*, 2017.
- [32] Goldak J, Chakravarti A, Bibby M. A new finite element model for welding heat sources. *Metall Trans B* 1984;15(2):299–305.
- [33] Deng D. FEM prediction of welding residual stress and distortion in carbon steel considering phase transformation effects. *Mater Des* 2009;30(2):359–66.
- [34] Suikkanen P, Kömi J. Microstructure, Properties and Design of Direct Quenched Structural. *Mater Sci Forum* 2014;783–786:246–51.
- [35] Siltanen J, Tihinen S, Kömi J. Laser and laser gas-metal-arc hybrid welding of 960 MPa direct-quenched structural steel in a butt joint configuration. *J Laser Appl* 2015;27(S2). pp. S29007–1–8.
- [36] Björk T, Toivonen J, Nykänen T. Capacity of Fillet Welded Joints Made of Ultra High-Strength Steel. *Weld World* 2012;56(3–4):71–84.
- [37] Amraei M, Skriko T, Björk T, Zhao X-L. Plastic strain characteristics of butt-welded ultra-high strength steel (UHSS). *Thin-Walled Struct* 2016;109:227–41.
- [38] SSAB, *Welding Handbook*, SSAB, Oxelösund, 2016.
- [39] JMatPro, Version 8.0, Sente Software Ltd.
- [40] Yaghi A, Hyde T, Becker A, Sun W, Williams J. Residual stress simulation in thin and thick-walled stainless steel pipe welds including pipe diameter effects. *Int J Press Vessels Pip* 2006;83(11–12):864–74.
- [41] Brickstad B, Josefson B. A parametric study of residual stresses in multi-pass butt-welded stainless steel pipes. *Int J Press Vessels Pip* 1998;75(1):11–25.
- [42] Lauwagie T, Sol H, Roebben G, Heylen W, Shi Y, Van der Biest O. Mixed Numerical-Experimental Identification of Elastic Properties of Orthotropic Metal Plates. *NDT E Int* 2003;36(7):487–95.
- [43] Jonšta P, Vlčková I, Křišťák L, Špička I, Jonšta Z. Contribution to the Thermal Properties of Selected Steels. *Metalurgija* 2015;54(1):187–90.
- [44] Dabiri M, Lindroos M, Andersson T, Afkhami S, Laukkanen A, Björk T. Utilizing the theory of critical distances in conjunction with crystal plasticity for low-cycle notch fatigue analysis of S960 MC high-strength steel. *Int J Fatigue* 2018;117:257–73.
- [45] Chiumenti M, Cervera M, Salmi A, Agelet de Saracibar C, Dialami N, Matsui K. Finite element modeling of multi-pass welding and shaped metal deposition processes. *Comput Methods Appl Mech Eng* 2010;199:2343–59.
- [46] Bhatti AA, Barsoum Z, Khurshid M. Development of a finite element simulation framework for the prediction of residual stresses in large welded structures. *Comput Struct* 2014;133:1–11.
- [47] Zhu X, Chao Y. Effects of temperature-dependent material properties on welding simulation. *Comput Struct* 2002;80(11):967–76.
- [48] Li H, Gai K, He L, Zhang C, Cui H, Li M. Non-Isothermal Phase-Transformation Kinetics Model for Evaluating the Austenization of 55CrMo Steel Based on Johnson-Mehl-Avrami Equation. *Mater Des* 2016;92:731–41.
- [49] Porter DA, Easterling KE, Sherif MY. *Phase Transformation in Metals and Alloys*. Boca Raton: CRC Press; 2009.

## **Publication II**

Ghafouri, M., Ahola, A., Ahn, J., and Björk, T.

**Welding-induced stresses and distortion in high-strength steel T-joints: Numerical and experimental study**

Reprinted with permission from  
*Journal of Constructional Steel Research*  
Vol. 189, p. 107088, 2022  
© 2022, Elsevier







Contents lists available at ScienceDirect

## Journal of Constructional Steel Research

journal homepage: [www.elsevier.com/locate/jcsr](http://www.elsevier.com/locate/jcsr)

# Welding-induced stresses and distortion in high-strength steel T-joints: Numerical and experimental study

Mehran Ghafouri<sup>a,\*</sup>, Antti Ahola<sup>a</sup>, Joseph Ahn<sup>b</sup>, Timo Björk<sup>a</sup><sup>a</sup> Laboratory of Steel Structures, School of Energy Systems, LUT University, P.O. Box 20, 53851 Lappeenranta, Finland<sup>b</sup> Department of Mechanical Engineering, Imperial College London, South Kensington Campus, London SW7 2AZ, UK

## ARTICLE INFO

## Keywords:

Welding simulation  
Residual stress  
Finite element simulation  
High strength steel  
Welding distortion

## ABSTRACT

The main objective of this study is to develop a computational approach based on the finite element (FE) method to efficiently predict welding deformations and residual stresses of fillet welded T-joints made of high strength steel (HSS), S700, using different welding sequences and external constraints. With this aim, thermo-elastic-plastic FE models were developed in ABAQUS FE code based on Goldak's double ellipsoidal heat source model, material non-linearity and geometrical non-linearity. The results of the FE models in terms of temperature fields, angular distortion and transverse residual stress were verified against measurements. The results showed that angular distortion and transverse residual stress were significantly impacted by configuration of the external constraints, while longitudinal stress were less affected. It was found that the welding sequences had a smaller effect on the sequential and cumulative welding distortions and final residual stresses than the configuration of the external constraints. The results of this study are meaningful for understanding of the calibration and accuracy of FE computational approaches to simulate welding processes. Additionally, from a practical point of view, the results are important to understand the distortions and residual stress control measures of structural members made from HSSs.

## 1. Introduction

Gas metal arc welding (GMAW) is widely used to make permanent joints between mechanical components and structural members, primarily due to its flexibility, practicality and high productivity [1]. However, localized and rapid heating due to heat input from the welding torch to the base material followed by non-uniform cooling in the weld zone give rise to residual stresses and distortions in the weld. The formation of residual stresses and deformations, which is a significant problem in welded structures, is affected by a number of factors, which fall mainly into three categories. Design-related factors include joint type and geometrical dimensions; and material-related factors comprise temperature-dependent thermal and mechanical properties of the base material and filler material. The third category encompasses process-related factors including the welding method, welding sequences, heat input and mechanical boundary conditions [2].

Some residual stresses, mainly compressive stresses, can be beneficial. Nevertheless, most residual stresses are detrimental to the service performance and integrity of the welded structure. Tensile residual stresses in the fusion zone (FZ) and heat-affected zone (HAZ) are known

to contribute to acceleration of a wide range of degradation phenomena in components and structures [3]. Reduced fatigue life of welded connections [4], decreased buckling strength [5], increased incidence of brittle fracture [6] and stress corrosion cracking [7,8] can all be attributed to residual stresses. Welding-induced distortion, another unwanted side-effect frequently found in GMAW welds, can cause undesirable secondary bending stresses, and it often results in loss of dimensional accuracy, which leads to extra costs for additional correction can cause schedule delays. Welding distortions can degrade joint quality, seriously impair fabrication and assembly of structural members, and, in extreme cases, might lead to the joint or component being unusable.

In the recent decades, HSSs have increasingly been used to reduce the weight of structures and improve their energy efficiency. The excellent strength-to weight ratio offered by HSSs may, however, be degraded when they experience HAZ softening and strength reduction from the applied welding heat input [9–11]. Fillet welds are commonly used in a wide range of steel structures such as plate girders and trusses. Structural members containing T-joints, are prone to different types of welding-induced distortions, of which angular distortion is a focus of

\* Corresponding author.

E-mail address: [mehran.ghafouri@lut.fi](mailto:mehran.ghafouri@lut.fi) (M. Ghafouri).<https://doi.org/10.1016/j.jcsr.2021.107088>

Received 17 October 2021; Received in revised form 3 December 2021; Accepted 4 December 2021

Available online 17 December 2021

0143-974X/© 2021 The Authors. Published by Elsevier Ltd. This is an open access article under the CC BY license (<http://creativecommons.org/licenses/by/4.0/>).



this work. Assessment of residual stresses after welding can be challenging because the use of destructive methods is impossible and non-destructive methods have their own restrictions. For example, the X-ray diffraction (XRD) method for measurement of residual stresses of T-joints has some limitations as, depending on the stiffener height, the measuring head often cannot reach regions near the weld toe.

In view of the damaging consequences of welding residual stresses and deformations, it is important to accurately predict and efficiently evaluate such stresses and distortions to be able to produce robust designs and ensure the safety of welded components and structures [1,3]. Thus, it is a meaningful task to develop a reliable computational approach based mainly on the FE method to predict welding thermal fields as well as welding stresses and distortions. In the past, there have been numerous studies on FE welding simulation for different materials [12–17], different joint types [18–22] and different welding processes [3,18,23]. FE simulation of welding of T-joints has been used in a number of research studies [12,18,24,25], however, there is still a lack of data in the literature regarding the effect of different welding sequences and external constraints on the welding distortions and residual stresses of HSSs.

The objective of the current research is to develop three-dimensional sequentially coupled thermo-mechanical models in ABAQUS FE software [26] to predict welding-induced distortions and residual stresses in T-joints made of HSS S700MC PLUS under different mechanical boundary conditions and for different welding sequences. Four fillet welding cases with two welding sequences and two specific mechanical boundary conditions are considered. Thermal fields are simulated by implementation of Goldak's double ellipsoidal heat source model [27] in the user-subroutine DFLUX. Thermal loss is modeled by applying the combined effects of radiation and convection, which are implemented in the user-subroutine FILM. Nodal temperatures calculated in the thermal analysis are mapped into a mechanical model to calculate stresses and strains for each welding case. The results of the simulations with respect to temperature fields, welding-induced residual stresses before and after release from the clamps, and sequential angular deformations due to each welding pass as well as final angular distortions are verified with experimental measurements.

## 2. Experimental setup

### 2.1. Materials

The base material in this study was HSS S700MC PLUS, which is a low carbon and low alloy HSS offering a minimum yield strength of 700 MPa. This HSS is manufactured using a modern hot strip rolling method integrated with direct quenching [28]. The filler material used in the welding process is ESAB OK AristoRod 13.29 solid wire with 1 mm diameter. This filler material has practically the same strength level as the base material. The chemical compositions of the base and filler materials based on the material certificates of the manufacturers are presented in Table 1.

### 2.2. Specimens and welding procedure

T-joint specimens with identical geometry were manufactured from 6 mm thick hot rolled strips of S700. The dimensions of the base plate and stiffener were  $460 \times 130$  mm and  $130 \times 25$  mm, respectively. The convention for the welding direction was adopted in the Y-direction, while Z is normal to the top surface of the base plate. Fig. 1 shows the

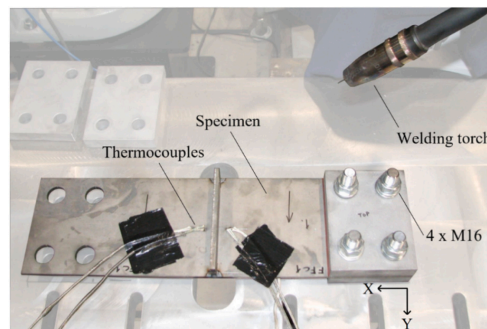


Fig. 1. Experimental set up for one of the specimens.

experimental set up for one of the specimens clamped from one side. The welding parameters presented in Table 2 were selected in order to achieve the designed leg size of 6 mm.

Based on a welding efficiency coefficient of 0.85 for GMAW [29], a net heat input value of 0.79 kJ/mm was applied to the specimens during fillet welding of the T-joints.

The fillet welding procedure consisted of deposition of filler material on both sides of the stiffener to make double-sided fillet welds. Four specimens in total were fillet welded using two welding sequences (see Fig. 2) and two different mechanical boundary conditions to consider the effects of external restraint on the residual stresses and distortions of fillet welded T-joints.

In the labelling of the specimens, the first letter shows the applied mechanical boundary conditions. C indicates the cases which were clamped at both ends and F signifies that the specimen was clamped at one end while the other end was free. S1 and S2 are welding sequences for fillet welding as illustrated in Fig. 2. In order to facilitate the drawing of conclusions for the different welding cases, the labels adopted for the specimens and the conditions the labels refer to are summarized in Table 3.

### 2.3. Temperature measurements

Temperature histories during the fillet welding were monitored using K-type thermocouples attached on the top and bottom surfaces of the specimens. For each specimen, four thermocouples (A–D) were used to record the temperature on the top surface, including the high temperature HAZ and regions with lower temperatures, to be able to verify the temperature field obtained from the corresponding FE model. For

Table 2  
Welding process parameters.

Voltage (V)	Current (A)	Travel speed (mm/s)	Wire diameter (mm)	Wire feed rate (m/min)	Tip distance (mm)	Shielding gas
25	260	7	1	12.5	16	Ar + 8% CO <sub>2</sub>

Table 1  
Chemical compositions of S700MC PLUS and ESAB OK AristoRod 13.29 (wt%).

Material	C	Si	Mn	P	S	Al	Ti	Cr	Ni	Mo	Nb	V
S700 MC	0.12	0.25	2.10	0.02	0.01	0.015	0.15	–	–	–	0.09	0.2
AristoRod 13.29	0.089	0.53	1.54	–	–	–	–	0.26	1.23	0.24	–	–

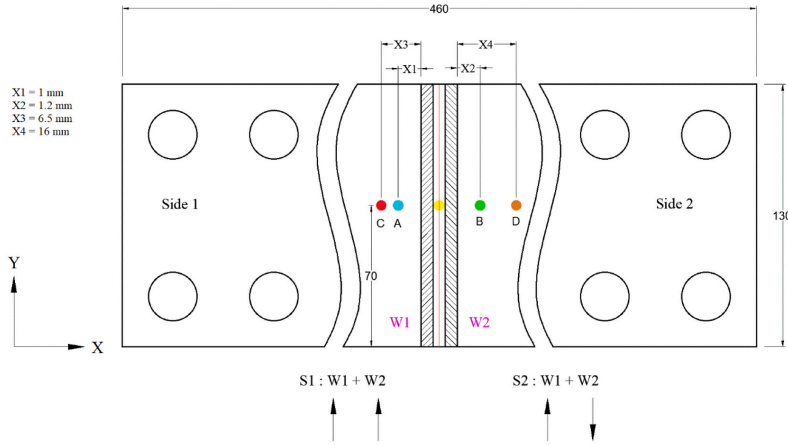


Fig. 2. Specimen configuration, positions of thermocouples and illustration of applied welding sequences. (Units in mm).

Table 3

Labels adopted for specimens in welding experiments.

Label	Condition
FS1	One Free end, welding Sequence 1
FS2	One Free end, welding Sequence 2
CS1	Both ends Clamped, welding Sequence 1
CS2	Both ends Clamped, welding Sequence 2

each welding case, one thermocouple was also used at the bottom side to facilitate verification of temperature distribution through the thickness of the specimen. The positions of the thermocouples are shown schematically in Fig. 2. It should be noted that the dimensions X1, X2, X3 and X4 refer to the distance between the weld toe and the thermocouples A, B, C and D, respectively. The real values were determined based on measurement data from a Hexagon 3D scanner.

### 3. Finite element model

From a complexity point of view, simulation of welding can become very complicated as the welding process includes coupled interactions between heat and mass transfer, material science, welding technology, microstructural evolution, computational sciences, and mechanics of materials. Capturing all the interactions involved in the welding process in a simulation is a highly demanding task and it is possible that convergence might not be reached. Thus, removing inconsequential aspects which only add complexity to a simulation and elaborating an efficient model with sufficient accuracy are of paramount importance.

In this research, evolution of stresses and strains of fillet welded specimens were studied by developing three-dimensional thermo-elastic-plastic FE models in ABAQUS FE Software. Since dimensional changes in welding are negligible and the effect of the mechanical field on the thermal field is insignificant, a sequentially coupled formulation was adopted [30]. For each case, the solution procedure consisted of two steps. In the first step, the non-linear transient temperature field was captured by solving the heat conduction equation in a thermal analysis. These nodal temperatures were later transferred and mapped into the subsequent mechanical analysis as a thermal load to find the structural response and calculate the residual stress field and nodal displacements.

#### 3.1. FE model geometry and mesh

Modeling of the deposited filler metal was carried out based on the experimentally measured weld leg and throat sizes. In each case, in order to facilitate transfer of the nodal temperature data from the thermal model to the mechanical model, the same FE mesh structure was used with an identical number of elements but different element types, as shown in Fig. 3. An 8-node linear heat transfer brick (DC3D8) with temperature as the only degree of freedom was used in the thermal analysis and a first order 8-node reduced integration brick element (C3D8R) with hourglass control was applied in the mechanical analysis. By using reduced integration elements, shear locking is prevented and less computational time as well as better convergence is achieved [31]. Convergence studies regarding the effect of mesh density on the accuracy of the simulation results were performed in a previous study [21]. A fine mesh grid with the smallest element size of  $3 \times 0.5 \times 1$  mm was applied in the FZ and adjacent HAZ for all the models. The size of the elements increased progressively from the weld toes towards the outer edges of the specimens. A fine mesh grid with a total number of 30,738 elements was able to represent stress and strain values in the weld regions with sufficient accuracy and acceptable computation time.

#### 3.2. Thermal analysis

In this study, a partial differential equation from Fourier's law of heat conduction and energy conservation, shown in Eq. (1), was applied to solve the transient temperature field during welding (T) in time (t) and space (x, y, z):

$$\rho(T)c_p(T)\frac{\partial T}{\partial t} = \frac{\partial}{\partial x}\left(k(T)\frac{\partial T}{\partial x}\right) + \frac{\partial}{\partial y}\left(k(T)\frac{\partial T}{\partial y}\right) + \frac{\partial}{\partial z}\left(k(T)\frac{\partial T}{\partial z}\right) + \dot{Q}, \quad (1)$$

where T is temperature and t represents time.  $\rho(T)$ ,  $c_p(T)$  and  $k(T)$  are temperature-dependent density, specific heat, and thermal conductivity, respectively. These temperature-dependent thermo-physical properties were obtained for the base material from the literature [18] and are shown in Fig. 4. It should be noted that the units are arranged so that all properties can be shown in a single graph.

As the filler material in this research shares the same matching strength configuration as the base material, the two metals were defined as identical materials and the same properties were assigned to both.  $\dot{Q}_v$  (W/m<sup>3</sup>) is the volumetric heat source density or internal heat generation

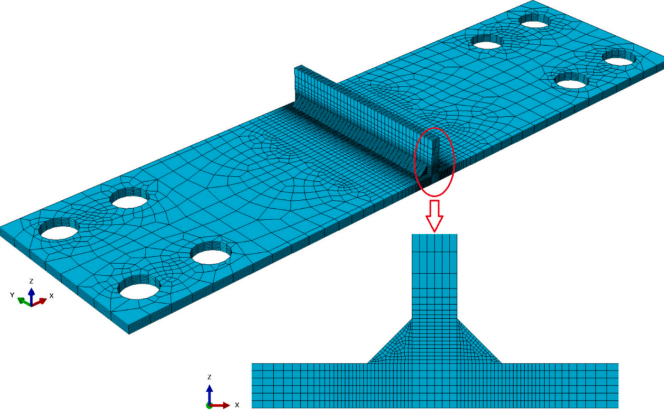


Fig. 3. Mesh details of the fillet welded T-joint.

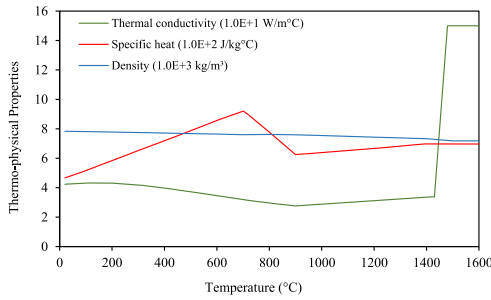


Fig. 4. Temperature-dependent thermo-physical properties of S700.

rate. Arc energy transferring from the moving heat source to the base and filler materials was modeled as a volumetric heat source with double ellipsoidal distribution proposed by Goldak et al. [27]. This model considers two heat flux distributions, one for the front half and one for the rear half of the heat source. The heat distributions are described by Eqs. (2) and (3), respectively:

$$q_f(x, y, z, t) = \frac{6\sqrt{5}\eta Q}{ab\sqrt{\pi}} e^{-3\left(\frac{x^2}{a^2} + \frac{(y-\eta t)^2}{b^2} + \frac{z^2}{c^2}\right)}, \quad y \geq 0 \quad (2)$$

$$q_r(x, y, z, t) = \frac{6\sqrt{5}\eta Q}{ab\sqrt{\pi}} e^{-3\left(\frac{x^2}{a^2} + \frac{(y+\eta t)^2}{b^2} + \frac{z^2}{c^2}\right)}, \quad y < 0 \quad (3)$$

where  $x$ ,  $y$  and  $z$  are coordinates in the reference system.  $Q$  is the power of the welding arc ( $Q = VI\eta$ ) calculated based on the welding current ( $I$ ), voltage ( $V$ ) and welding efficiency coefficient ( $\eta$ ).  $a$ ,  $b_f$ ,  $b_r$  and  $c$  are characteristics of the weld pool, while  $f_f$  and  $f_r$  are dimensionless fractions of heat deposited in the front and rear half of the heat source, respectively. Taking the continuity of the heat source into consideration, the following relationships are observable:

$$\frac{f_r}{b_r} = \frac{f_f}{b_f} \quad (4)$$

$$f_f + f_r = 2 \quad (5)$$

Representation of the applied heat source model was accomplished using the ABAQUS user subroutine DFLUX programmed in FORTRAN. To simulate the moving heat source for fillet welding of the T-joints, two translation and rotation matrices were defined to transform points in the global coordinate system into the local coordinate system at angles of  $-45^\circ$  and  $45^\circ$  for side 1 and side 2, respectively:

$$\begin{bmatrix} x \\ y \\ z \end{bmatrix} = \begin{bmatrix} \cos 45 & 0 & \sin 45 \\ 0 & 1 & 0 \\ -\sin 45 & 0 & \cos 45 \end{bmatrix} \begin{bmatrix} X - X_0 \\ Y - Y_0 \\ Z - Z_0 \end{bmatrix} \quad (6)$$

$$\begin{bmatrix} x \\ y \\ z \end{bmatrix} = \begin{bmatrix} \cos 45 & 0 & -\sin 45 \\ 0 & 1 & 0 \\ \sin 45 & 0 & \cos 45 \end{bmatrix} \begin{bmatrix} X - X_0 \\ Y - Y_0 \\ Z - Z_0 \end{bmatrix} \quad (7)$$

where  $x$ ,  $y$  and  $z$  are nodal coordinates in the local coordinate system and  $X$ ,  $Y$  and  $Z$  are nodal coordinates in the global coordinate system. The position of the heat source was calculated with respect to time, nodal coordinates, and welding speed in the subroutine DFLUX. At each integration point, non-uniform flux distribution was then calculated by DFLUX as a function of time, the coordinates of the heat source, and using the power of the welding arc. In order to predict welding residual stresses and distortions, the temperature field must be determined accurately, which necessitates calibration of the heat source model. Calibration of the heat source was performed by adjusting the heat source parameters in such a way that a close agreement was reached between the nodal temperatures captured by the thermocouples in the experimental measurements and the corresponding nodal temperatures obtained from the simulation. Further calibration was done by matching the boundaries of the FZ and HAZ from the FE model against the macrograph of the weld cross section. The heat source parameters and their values adjusted to perform thermal analysis are summarized in Table 4.

**Table 4**  
Adjusted heat source parameters.

Parameter	$a$ (mm)	$b_f$ (mm)	$b_r$ (mm)	$c$ (mm)	$f_f$	$f_r$
Value	7	4	10	10	0.57	1.43

Ambient as well as initial temperatures for all simulation cases were set to 20 °C. In terms of capturing the temperature field during welding, a unique solution will be reached when Eq. (1) is solved subject to specific boundary conditions. Thermal boundary conditions are generally applied in welding simulations to model the heat loss due to convection and radiation from free surfaces of the welded specimen, as shown schematically in Fig. 5. The distance between the clamps and heat source is large enough that temperature does not rise at the clamping areas, and, heat transfer between the base plate and clamps by means of conduction was hence ignored. The specimens are assumed to experience heat loss by means of convection and radiation. Heat loss during welding is generally modeled based on Newton's law of cooling and Stefan-Boltzmann's law to account for heat transfer due to convection and radiation, respectively. An alternative method in terms of heat loss during welding is to consider the combined effect of convection and radiation. In this study, the matter was addressed by defining a temperature-dependent heat transfer coefficient expressed in the form of two mathematical expressions as practiced by other researchers [32,33] and shown by Eq. (8):

$$h = \begin{cases} 0.0668 \times T \left( \frac{W}{m^2 \cdot ^\circ C} \right) & 0 \leq T \leq 500 \\ 0.231 \times T - 82.1 \left( \frac{W}{m^2 \cdot ^\circ C} \right) & T \geq 500 \end{cases} \quad (8)$$

where  $T$  (°C) is temperature and  $h$  denotes the temperature-dependent heat transfer coefficient. These mathematical expressions were implemented in the user subroutine FILM to model the combined thermal boundary conditions.

The coupled problem between the solid and liquid phases is not included in the ABAQUS package, and directly, modeling the fluid flow in the weld pool is thus not possible in such FE software. Fluid flow in the weld pool is, however, very important and has a significant effect on the temperature distribution in the weld pool. Artificially increased thermal conductivity was applied to account for the effect of fluid flow in the FZ. For temperatures higher than the liquidus temperature, thermal conductivity was considered to be four times as large as the value at room temperature, and increases linearly between the solidus and liquidus temperatures. The latent heat of fusion was considered to account for the thermal effects of solidification in the weld pool. The assumed value for latent heat was  $270 \times 10^3$  J/kg between the solidus temperature of 1430 °C and liquidus temperature of 1480 °C.

### 3.3. Mechanical analysis

Nodal temperatures computed for each time increment in the thermal analysis were transferred as a thermal load through predefined fields in the subsequent mechanical analysis. The structural response of the model was then calculated as the sum of individual strain rate components as expressed in Eq. (9):

$$\dot{\epsilon}^{total} = \dot{\epsilon}^e + \dot{\epsilon}^p + \dot{\epsilon}^{th} \quad (9)$$

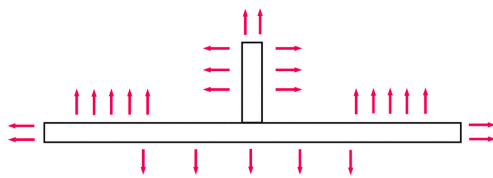


Fig. 5. Illustration of heat loss (convection and radiation) or thermal boundary conditions applied to the T-joints.

where  $\dot{\epsilon}^{total}$  is total strain rate.  $\dot{\epsilon}^e$ ,  $\dot{\epsilon}^p$  and  $\dot{\epsilon}^{th}$ , correspond, respectively, to elastic, plastic, and thermal strain increments. It should be noted that the strain rate component due to phase change was not considered in this study and the strain rate component due to creep was also neglected since the time period at high temperature was limited to a few seconds throughout the entire thermal cycle. Elastic strain was calculated using isotropic Hooke's law with temperature-dependent Young's modulus and Poisson's ratio. A rate-independent plastic model with temperature-dependent mechanical properties, isotropic hardening law and the Von Mises yield criterion were used to model the plastic behavior of the material. Thermal strain was calculated using a temperature-dependent thermal expansion coefficient. The required mechanical properties of the base and filler metals in the structural analysis, namely, temperature-dependent yield strength, Young's modulus, Poisson's ratio and the thermal expansion coefficient were taken from literature [18] and are shown in Fig. 6.

An annealing step was modeled by defining an annealing temperature. When the temperature of a material point exceeds the annealing temperature, strain hardening memory is annihilated by resetting the equivalent plastic strain to zero. Provided that the temperature of that material point falls below the annealing temperature during cooling, regeneration of work hardening happens if the material deforms plastically [12,19]. The annealing temperature was set to 900 °C in this study. In order to avoid convergence problems, the values of yield strength and Young's modulus were not considered to be zero for molten material, but they were reduced to 5 MPa and 5 GPa, respectively.

Prescription of external constraints is a common method to reduce welding deformations. This important task is, however, problematic since the application of mechanical constraints affects the residual stress field and welding distortions. Greater constraints give rise to a residual stress field and reduces welding deformations by increasing plastic strains and decreasing elastic strains, which are responsible for distortions after removing clamps. This implies that in an over-constraint situation, residual stresses might accumulate and result in welding-induced cracks, while deformations derived from an under-constraint situation might lead to dimensional instability, and, design of the welding fixtures must thus be done meticulously [12]. Two different clamping configurations were applied in the experiments and corresponding mechanical boundary conditions were considered in the FE models, as shown in Fig. 7. This approach makes it possible to analyze the development of residual stresses and distortions due to different mechanical boundary conditions and to optimize production procedures with the aim of obtaining smaller levels of distortions and welding residual stresses. One clamping set up was applied in which the related specimen was fixed rigidly at one end in a specified area, while the other end was free to experience angular distortion. Mechanical boundary conditions in the related FE model were set so that all the nodes in that area were restricted rotationally and translationally, as shown in Fig. 7 (a). The other clamping condition was set to rigidly fix both ends of the

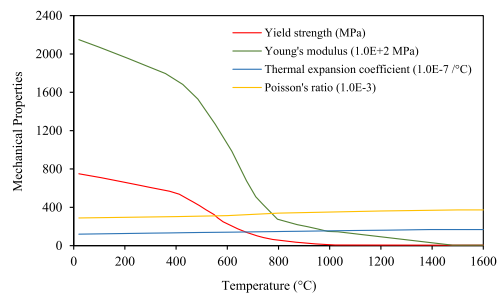


Fig. 6. Temperature-dependent mechanical properties of S700.

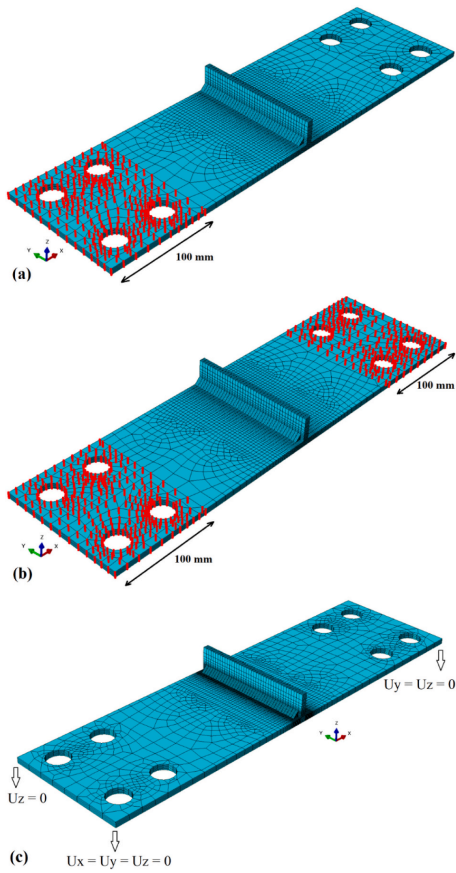


Fig. 7. Representation of different mechanical boundary conditions assigned to the FE models for mechanical analyses: (a) one end fixed and the other end free; (b) both ends fixed; and (c) after removal of the clamps.

related specimen in specified areas. As shown in Fig. 7(b), in the corresponding FE model, the boundary conditions were considered to prevent rotation and translation of all the nodes in the determined areas. After welding and reaching the ambient temperature, in all the cases, the mechanical boundary conditions corresponding to the removal of the clamps were set to prevent the rigid body motion, as shown in Fig. 7(c).

Modeling of the gradual deposition of filler material was performed, which is named element birth and death technique (model change) in ABAQUS [34]. In this modeling method, elements corresponding to the weld metal initially have inactivated status. As soon as the welding torch approaches and the filler material melts, the status of the heated element is changed from inactivated to reactivated and the specified temperature-dependent material properties are assigned.

#### 4. Results and discussion

##### 4.1. Results of thermal analysis

Obtaining accurate calculated welding-induced stresses and

distortions, necessitates accurate prediction of the welding temperature field. The temperature distribution obtained from FE simulation at half-way during welding of the S700 T-joint specimen SF2 is shown in Fig. 8. The FE model consisted of 2 regions of very fine mesh around the heat source in the FZ and HAZ where the temperature gradient is steep at both sides of the T-joint.

Correct prediction of weld pool geometry is an indicator of accurate temperature distribution in the FZ and HAZ. Calibration of welding temperature histories necessitates prediction of the shape and size of the weld pool and matching of the simulated weld pool geometry to the experimental macrograph obtained from the polished and etched weld cross section. The region of simulated molten metal or FZ, depicted in Fig. 8 in light gray, was determined based on the temperature contour above the liquidus temperature (1480 °C).

The cross section of the fillet weld at the mid-section of the specimen, which shows the depth of penetration, is compared with the simulation in Fig. 9(a). The dimensions of the FZ, i.e., the width and length of the weld pool at the end of the welding path, are compared with the simulation in Fig. 9(b).

As shown in Fig. 9(a) and (b), the FZ boundaries and finger-like penetration as well as the dimensions of the weld pool are well-captured by the simulation, which is a result of the realistic temperature distribution and correct calibration of the heat source model. However, small reinforcement, was not modeled as it was assumed to have a negligible effect on development of residual stresses and welding distortions [12].

Close agreement between the nodal temperatures recorded by the thermocouples and the corresponding nodal temperatures from the FE simulation is the main index of correct temperature distribution and welding thermal cycles [17]. Since the welding parameters and, consequently, heat input for all the cases are similar, only one of the cases (FS2) is used for comparison in terms of welding temperature distribution. However, all the cases were calibrated and verified against experimental measurements in the same manner. The results of the thermal analysis for the welding case FS2 for passes 1 and 2 are shown in Fig. 10(a) and (b), respectively.

Fig. 10(a) compares time-temperature curves at different distances from the weld toe for the first welding pass versus numerically calculated temperature histories calibrated using thermocouple measurements. Fig. 10(b), in the same manner, shows the experimental and numerical temperature histories for the second welding pass. It can be seen in Fig. 10(a) and (b) that the second pass was started almost 5550 s after beginning of the first pass, when the specimen reached ambient temperature. In Fig. 10(a) and (b), T1–T5 are thermocouples attached at various positions on both the top and bottom side of the T-joint specimen (FS2). X1–X4, are approximate distances from the weld toe (defined in Fig. 2), which were measured post welding with the Hexagon 3D scanner, and corresponding nodal distances from the weld toe in the FE model. A good agreement between the simulated temperature field and experimentally measured thermal histories in terms of heating rate, peak temperature and cooling rate is observable. Such agreement implies that calibration of the heat source parameters (Goldak's parameters) and thermal boundary conditions was performed correctly. Thus, the FE thermal model verified by means of thermocouples and FZ boundary matching, can be considered accurate enough for nodal mapping and data transfer to subsequent mechanical analyses.

##### 4.2. Results of simulated residual stresses and deformations

The effect of the welding sequence and mechanical boundary conditions on inhomogeneous stresses and distortions was investigated. Non-uniform heating and cooling during welding and subsequent expansion and contraction induce considerable tensile and compressive residual stresses in the weld region and adjacent HAZ. Variation in the distributions and magnitudes of the residual stresses and angular distortions due to change in the welding sequence and mechanical

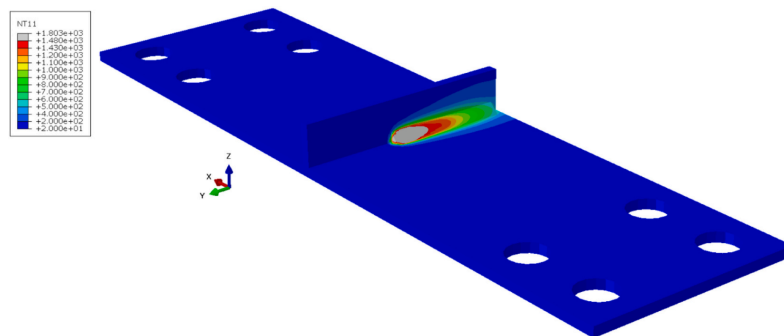


Fig. 8. Thermal contours obtained from thermal analysis of double-sided fillet welded S700 T-joint during welding.

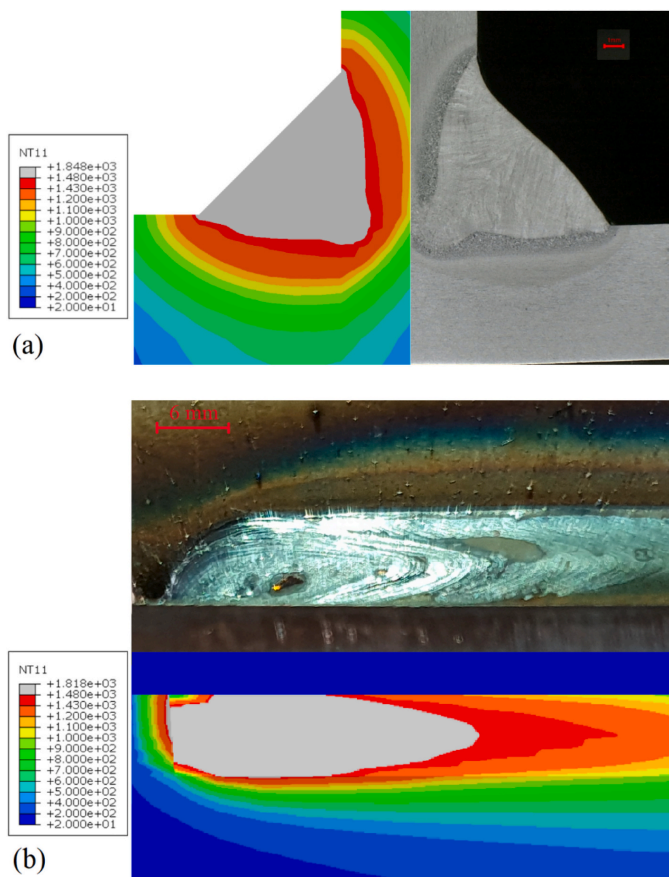


Fig. 9. Welding temperatures (NT11) and boundaries of the FZ from the experiment versus simulation: (a) through thickness; and (b) on the top surface of the specimen.



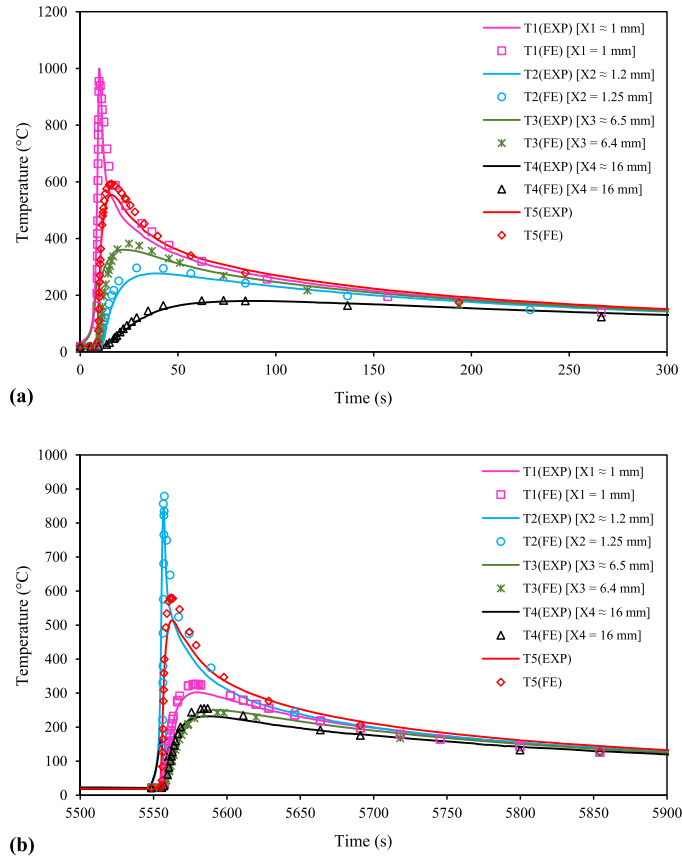


Fig. 10. Simulated temperature field versus experimentally measured temperature histories at various distances from the weld toe (Specimen FS2): (a) for the first welding pass; and (b) for the second welding pass.

boundary conditions were examined and compared with experimental measurements. It should be noted that transverse residual stresses were measured experimentally and compared with the simulation results in order to calibrate the FE models. The analysis of longitudinal stresses was performed numerically based on the validated FE model for each

case. In this regard, after thermal analyses and calibration of the FE thermal models, two mechanical boundary conditions corresponding to the utilized clamping configurations were applied in the mechanical analyses. In order to verify the results of the structural analyses, measurements were performed of residual stresses and distortions. For all

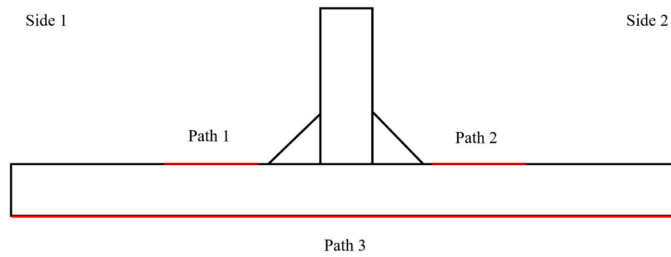


Fig. 11. Measurement paths for angular distortions and transverse residual stresses.

cases, the specimen was scanned for possible preliminary deformations prior to welding using a Hexagon ROMER Absolute Arm (resolution up to 63  $\mu\text{m}$ ) 3D Scanner. After each welding pass, after reaching the ambient temperature and after being released from the fixtures (specific to specimens CS1 & CS2), the specimen was scanned to be able to evaluate the sequential and cumulative angular distortions. The path in the mid-section of the specimens in the transverse direction (Path 3) along which angular distortions are measured at the bottom side of the specimens, is shown schematically in Fig. 11.

Transverse residual stresses on the top surface of the T-fillet specimens along the two specified paths (see Fig. 11) in the mid-section (Path 1 and Path 2) were measured using XRD by a Stresstech X3000 G3 device with a collimator diameter of 1 mm. It should be mentioned that for specimens CS1 and CS2, the stresses were also measured after completion of welding, but prior to release from the fixtures, in addition to measurement of the residual stresses after release from the fixtures.

#### 4.2.1. Angular distortion

The contours of final angular deformations for cases FS1 and FS2 are shown in Fig. 12(a) and (b), respectively. It can be seen that the patterns of angular distortion (U3) in the Z-direction for welding cases FS1 and FS2 with different welding sequences and the same mechanical boundary conditions are similar, albeit with a small difference in the magnitude of the maximum deformation. It should be noted that angular distortion through thickness does not change and the same pattern of deformation thus exists at the bottom side of each specimen. Figs. 13 and 14 depict contours of angular distortion for specimens CS1 and CS2, respectively. As is shown in Figs. 13(a) and 14(a), rigid clamping at both ends of the specimens results in very small angular distortion of less than 1 mm, which happens in the mid-length of the specimens in the transverse direction. After removing these constraints, as shown in Figs. 13(b) and 14(b), final angular distortions for both specimens amounts to less than 4 mm for each end. While the difference between the magnitudes of the final angular distortions caused by using the two different welding sequences is small (comparing FS1 and FS2 as well as CS1 and CS2), the utilized external constraints result in a considerable difference between the developed angular distortions (comparing FS1 and CS1 as well as FS2 and CS2).

In order to evaluate the accuracy of the developed FE model,

simulation results in terms of welding-induced angular distortions were compared with experimental measurements for all the cases. In Fig. 15 (a–d), simulated deflections (displacements in the Z-direction) along the transverse direction after cooling of each welding pass are plotted with solid lines for cases FS1, FS2, CS1 and CS2, respectively, while the experimental measurement data are shown with circular marks.

As is observable in Fig. 15(a) and (b), the FE models can predict welding distortions with reasonable accuracy for all the cases. For FS1 and FS2, percent errors calculated at the positions of maximum deflection after welding pass 2 are 9.3% and 10.9%, respectively. It can be seen in Fig. 15(a) and (b), that the angular distortions due to the chosen welding sequences remain very close and the maximum angular distortion produced in FS1 is only some fractions of a millimeter greater than FS2. This difference is 0.5 mm and 0.7 mm for the simulation and measurements, respectively. This implies that for T-joints which require 2 welding passes (one pass per side), adopting the opposite directions for the welding passes (on condition that one end of the specimen is free to deform) lead to smaller angular distortions compared to welding passes applied in the same direction. Although such difference compared to the size of specimens used in this study is negligible, in real applications and for structural members with larger dimensions, adopting S2 in contrast to S1 can result in considerably smaller deformation when the absolute magnitude of distortion is taken into account. With respect to the sequential angular distortions from the first and second welding passes, in both FS1 and FS2, the second welding pass produces greater deformation compared to the first pass. That is, based on the numerical results for FS1, pass 1 and pass 2, respectively, produce angular distortions of 6.57 and 7.43 mm, in which case the angular deformation due to the second pass is 13% greater than that of the first pass. For FS2, in the same vein, the angular distortions from the first and second welding passes are 6.56 and 6.94 mm, which shows pass 2 makes a greater contribution to total angular distortion (5.8% greater than pass 1). It should be noted that since the unrestrained ends deform freely in FS1 and FS2, the magnitudes and distributions of angular distortion, before and after release from the clamps remain unchanged. Thus, it was decided to show the angular distortion results for the condition in which the specimens are cooled down to the ambient temperature while still in the clamps.

With CS1 and CS2, shown in Fig. 15(c) and (d), the difference

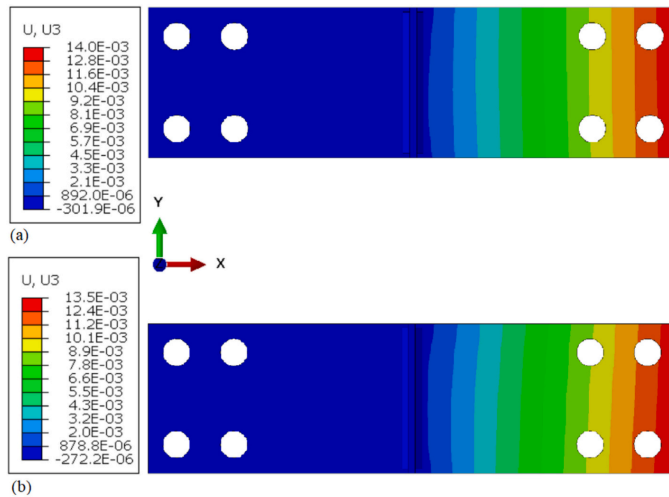


Fig. 12. Angular deformation distribution for: (a) FS1; and (b) FS2.



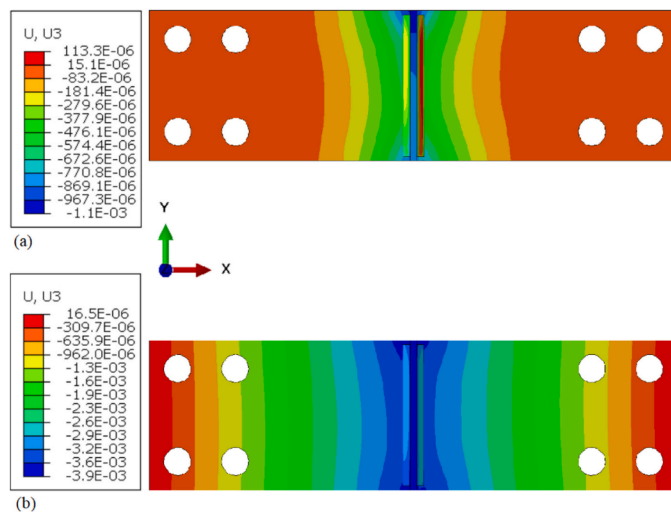


Fig. 13. Angular deformation distribution for specimen CS1: (a) after cooling and before removing the clamps; and (b) after releasing the clamps at both ends.

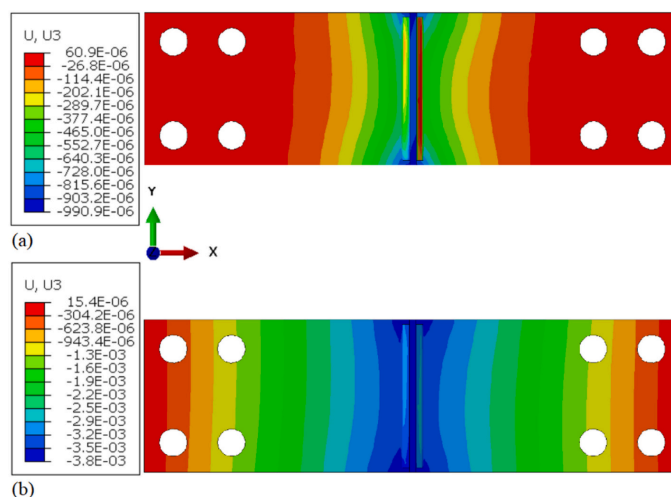


Fig. 14. Angular deformation distribution for specimen CS2: (a) after cooling and before removing the clamps; and (b) after releasing the clamps at both ends.

between the final angular distortions from the welding sequences is minor. As CS1 and CS2 are rigidly clamped at both ends, small deformations can be expected as they are in related fixtures. It should be noted that deformation data from simulations related to CS1 and CS2 were moved along the vertical axis (minimum deformation was set to zero) to be able to compare the simulation data with the measured data. The measured maximum angular distortion after cooling of the second welding pass before release from the welding fixture is almost 0.75 mm and the simulated distortion is 0.84 mm, which gives a maximum percent error of 10.7%. As can be seen from the experimental data,

although the distortion dimensions are in fractions of a millimeter, welding pass 1 produces greater angular distortion than welding pass 2, as is well predicted by the simulation. The size of the maximum simulated sequential angular distortions in CS1 and CS2 are approximately 0.7 mm and 0.14 mm for pass 1 and pass 2, respectively. Although these magnitudes are small, this issue can be very important in practical applications, such as construction of plate girders, when both ends are rigidly clamped, and the dimension of the specimen is large in the transverse direction. The sequential angular distortions can also be compensated by pre-alignment of the welded plate components. After

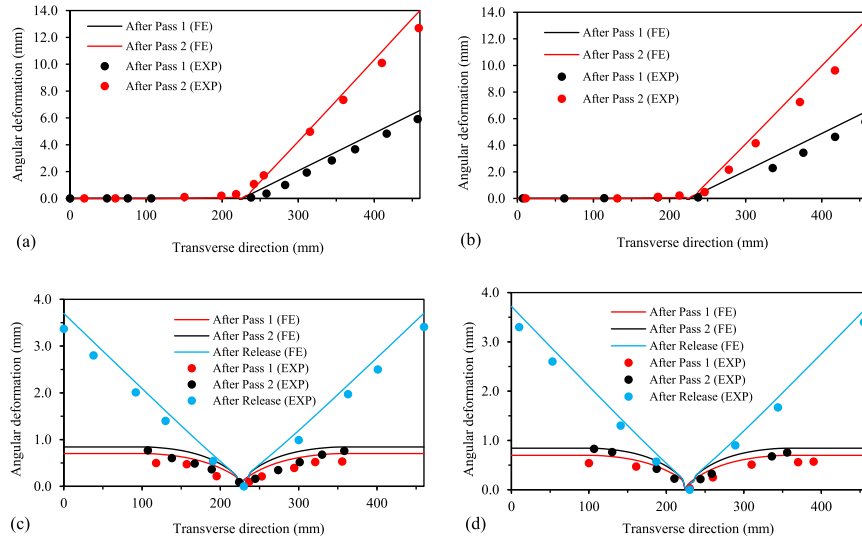


Fig. 15. Comparison of angular distortions between simulations and measurements for: (a) FS1, (b) FS2, (c) CS1, and (d) CS2 specimens.

release from the clamps, CS1 and CS2 experience angular distortion from the release of the residual stresses. The simulation results for angular distortions of CS1 and CS2 after release from the clamps are in good agreement with the measurement data. The percent error is approximately 8.4% for both cases. Total angular distortion after release experienced by specimens rigidly clamped at both ends is considerably smaller than that experienced by specimens rigidly clamped at one end. With respect to angular distortion, a comparison between FS1 and CS1, for example, shows that while FS1 experiences a total angular distortion of 14 mm (fixing one end and measuring the distortion at the other end), CS1 undergoes a total angular distortion of 7.2 mm (summation of the distortions at both ends, which is  $3.5 + 3.7$  mm (see Fig. 15(c)). This indicates that for the selected welding parameters and specimen size, the magnitude of the final angular distortion for the specimens clamped at one end is approximately twice as large as that for the specimens clamped at both ends. Comparison of the simulation results and measurement data shows the accuracy of the computational approach in capturing the mode and magnitude of the angular distortion.

#### 4.2.2. Transverse residual stresses

Simulated transverse residual stresses (S11) versus measurements for FS1, FS2, CS1, and CS2 along the 2 specified paths (see Fig. 11) are shown in Figs. 16, 17, 18, and 19, respectively. It should be noted that path 1 and path 2 on the top surfaces start at 1 mm from the weld toes and are extended towards the outer edges of the specimens (almost 25 mm in length) and zero on the X-axis is thus at the weld toe in the relevant graphs. Simulated and measured data for path 1 and path 2 are shown in the negative and positive directions of the X-axis, respectively, based on the conventions chosen for the coordinate system. As seen in Figs. 16 and 17, both welding cases experience a similar pattern of transverse residual stress distribution along the specified paths. In both cases, the magnitude of the tensile residual stresses increases and reaches an approximate peak of 241 MPa and 189 MPa for FS1 and FS2, respectively, in the HAZ at a distance of 3–4 mm from the weld toe. Moving through the HAZ, tensile residual stresses start to fall in magnitude. With regard to evaluating the accuracy of the developed FE models, it can be seen that the simulation predictions in terms of general trend as well as magnitude of the maximum tensile residual stress are in good agreement with the XRD measurements. It should be noted that

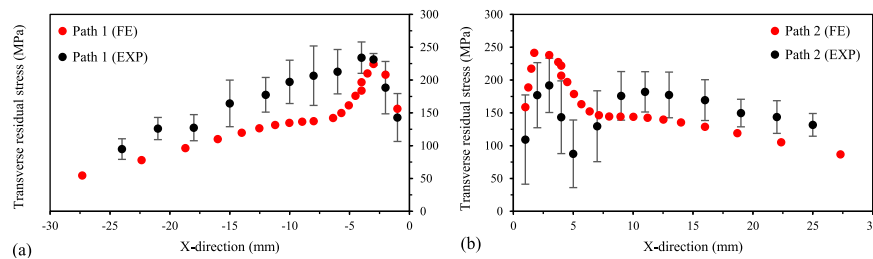


Fig. 16. Comparison of the simulated transverse residual stresses (S11) and measurements for FS1: (a) along path 1; and (b) along path 2.

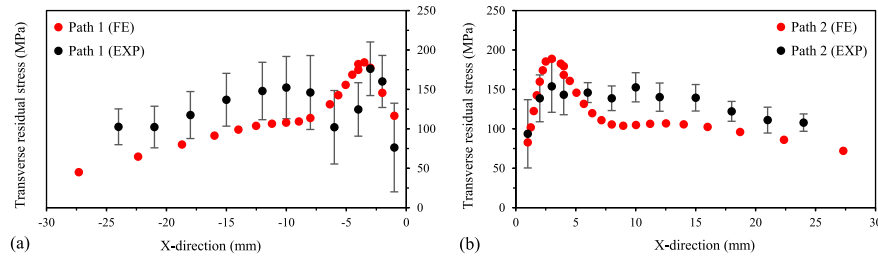


Fig. 17. Comparison of the simulated transverse residual stresses (S11) and measurements for FS2: (a) along path 1; and (b) along path 2.

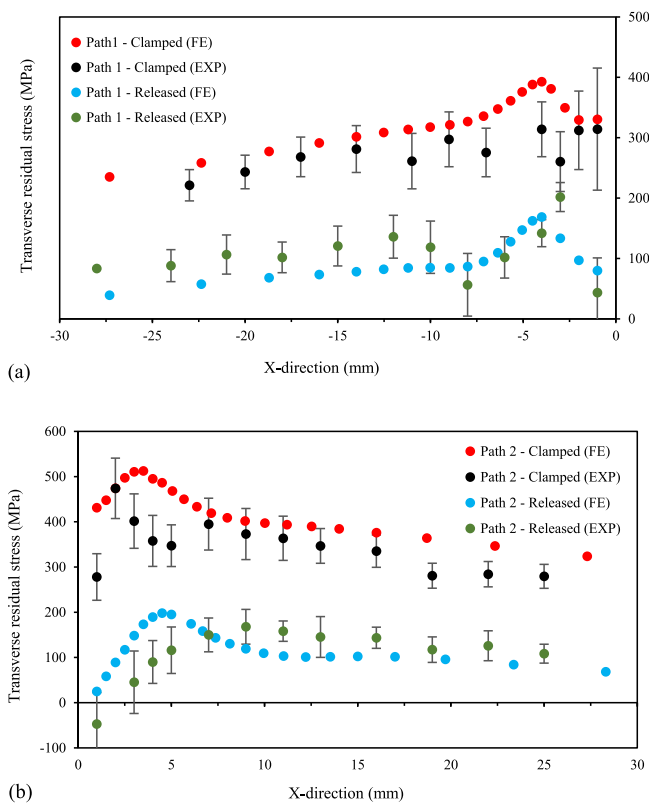


Fig. 18. Comparison of the simulated transverse residual stresses (S11) and measurements for CS1: (a) along path 1; and (b) along path 2.

XRD measurement data always falls within an error band, which should be taken into consideration when comparing FE results with experimental measurements. When comparing the simulation values and measurements for FS1, the maximum transverse tensile residual stresses predicted along path 1 and path 2 are 241 MPa and 224 MPa, in contrast to  $231 \pm 24$  MPa and  $192 \pm 41$  MPa from XRD measurements. In the

same vein for FS2, at the position of maximum tensile residual stress along path 1 and path 2, predictions are 174 MPa and 189 MPa, respectively, whereas the measured values are  $176 \pm 34$  MPa and  $153 \pm 25$  MPa. The maximum tensile residual stress calculated for FS1 is 52 MPa larger than that of FS2. For mechanical boundary conditions with one end rigidly clamped, the maximum transverse tensile residual stress

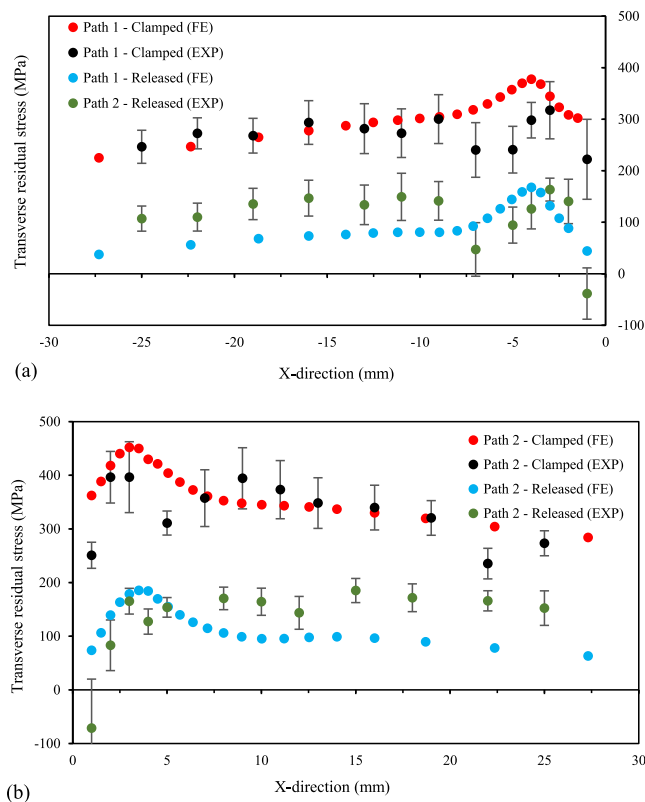


Fig. 19. Comparison of the simulated transverse residual stresses (S11) and measurements for CS2: (a) along path 1; and (b) along path 2.

reaches approximately 30% of the yield strength of the base material.

For CS1 and CS2, transverse residual stresses after welding and reaching ambient temperature while the specimens were still clamped, and residual stresses after removing the clamps are compared with corresponding data obtained from the experimental measurements. Fig. 18 compares the simulated transverse residual stresses distributions along path 1 and path 2 with measurement data for CS1. As is observable, the simulation results for CS1 are in acceptable agreement with the measurement data. As would be expected, the presence of rigid clamping with a higher degree of geometrical constraint (i.e., clamping at both ends of the specimen) prevents angular distortion to a large extent while giving rise to residual stresses. The pattern of simulated stress distribution along the two paths, before and after removing the welding fixtures, are similar, although with considerably different magnitude in the near-weld regions. That is, while the specimen is rigidly clamped, moving from the weld toe, the magnitude of the tensile residual stresses increases and reaches a peak stress of 393 MPa and 512 MPa for path 1 and path 2, respectively, at a distance of 3–4 mm from the weld toe. The high value of 512 MPa for tensile residual stress is almost 68% of the yield strength of the base material. Measurement data at the same position of maximum tensile residual stress along path 1 and 2 are  $314 \pm 49$  MPa and  $401 \pm 67$  MPa, respectively. Moving further towards the outer edges, tensile stresses gradually ease and fall in magnitude. The

patterns of the transverse residual stresses for the specimen after removing the clamps are similar to the situation before release from the constraints, however at very different levels. The calculated peak tensile residual stress along path 2 for the released specimen is 198 MPa, which is almost 39% of the peak stress calculated along the same measurement path for the specimen with strict geometrical constraints. The situation for CS2 (see Fig. 19) is very similar to that of CS1 with slight differences in the magnitude of the peak tensile stresses in the clamped condition, which are 378 MPa and 452 MPa calculated along path1 and path 2, respectively. After removing the constraints, the transverse residual stresses in the near-weld regions of CS1 and CS2 become close and comparable to those of FS1 and FS2, although slightly greater values obtained for FS1 and FS2. The maximum tensile transverse stresses calculated for CS1 are 60 MPa and 12 MPa larger than those of CS2, for the clamped and unclamped conditions, respectively.

In all the cases, comparison of the calculated peak tensile residual stresses, indicates that the magnitude of the tensile residual stresses developed on side 1 are smaller than those of side 2 (comparing Figs. 16(a), 17(a), 18(a) and 19(a) to 16(b), 17(b), 18(b) and 19(b), respectively). These differences are smaller in the case of FS1 and FS2 than for CS1 and CS2.

#### 4.2.3. Longitudinal residual stresses

In the current study, comparison of the longitudinal residual stresses (S22) was performed numerically based on the validated FE models for each welding case. Fig. 20 shows the longitudinal stresses calculated for FS1 and FS2 along path 1 and path 2. The curves related to FS1 are shown with solid lines and those for FS2 are plotted with dashed lines. As can be seen in the figure, for the specimens clamped at one end, the patterns and magnitudes of longitudinal stresses remain unchanged when the welding sequence is changed from S1 to S2. The pattern of longitudinal stresses are similar along both paths, however, with totally different peak tensile and compressive stresses. That is, near the weld toe, longitudinal stresses are in tensile mode for both paths, with peak stresses of approximately 380 MPa and 770 MPa for path 1 and path 2, respectively. Thermal effects may be a possible reason for this phenomenon. That is, the heat of pass 2, may modify and reduce the residual stresses developed on the weld area and HAZ of side 1 by redistribution of stresses. A similar phenomenon has been reported elsewhere [12]. Moving from the weld toe towards the outer edges, peak compressive stresses of 395 MPa and 266 MPa are found for path 1 and path 2 at approximately 7 mm from the weld toe, respectively.

Comparisons between the state of the longitudinal residual stresses before and after release from the external restraints for CS1 and CS2 are shown in Fig. 21(a) and (b), respectively. For the specimens clamped at both ends, changing the welding sequence from S1 to S2 had negligible effect on the state of the longitudinal stresses. With respect to the state of the longitudinal stresses before and after release, as can be seen in Fig. 21(a) and (b), the pattern of longitudinal stresses before and after release from the constraints remains almost identical in both cases, with, however, a shift towards the compressive side for the unclamped condition. That is, for the cases clamped at both ends, removal of the clamps had only a slight effect on the magnitudes of the tensile and compressive longitudinal stresses. The effect of unclamping is greater on transverse stresses than on longitudinal stresses for the cases clamped at both ends. The peak tensile and compressive longitudinal stresses for CS1 and CS2 are smaller in both the clamped and unclamped conditions than for FS1 and FS2. The peak tensile longitudinal stress for CS1 and CS2 is considerably smaller along path 1 than path 2, which is similar to the cases clamped at one end.

In order to investigate the sensitivity of transverse and longitudinal stresses to the external constraints, variations of these stresses during the welding of FS1 and CS1 for a unique node were plotted against time. The node is located on side 1 in the mid-section of the specimen in the welding direction at a distance of 1 mm from the weld toe. As can be seen in Fig. 22(a) and (b), both the transverse and longitudinal stresses become compressive due to expansion of the regions experienced a high temperature of 900 °C. As these areas start to cool down, residual stresses start to rise. The stresses are remarkable for longitudinal stresses

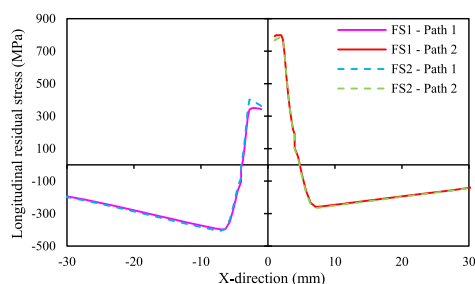


Fig. 20. Simulated longitudinal stresses (S22) for FS1 and FS2 along path 1 and path 2.

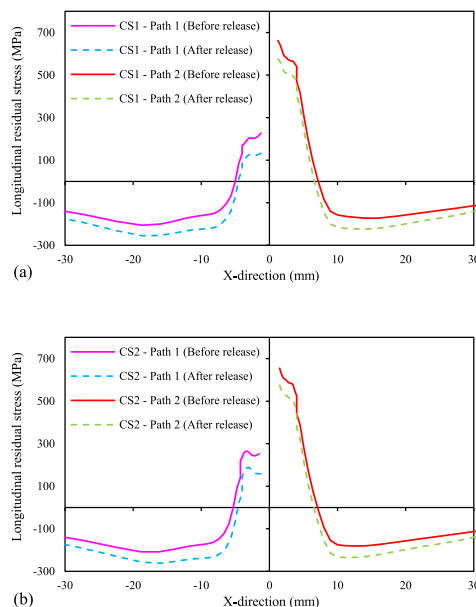


Fig. 21. The simulated longitudinal stresses (S22) along path 1 and path 2 before and after release for: (a) CS1; and (b) CS2.

and remain constant as the specimens reach the ambient temperature. When the second welding pass starts, the stresses become modified, redistributed, and start to fall as the heat reaches these areas. When the second welding pass ends and the specimens cool down to room temperature, residual stresses increase and reach constant levels. Regardless of the final magnitude of the residual stresses in the restrained condition, the change in the levels of the transverse and longitudinal stresses after removal of the clamps is interesting. As can be seen in Fig. 22(a), after unclamping of FS1, which was clamped at one end, the change in the transverse and longitudinal stresses is negligible. In Fig. 22(b), for CS1, which was clamped at both ends, when removing the clamps, the transverse residual stress falls dramatically, while a slight decrease is observable in the magnitude of the longitudinal stress. This implies that transverse stress is sensitive to the stiffness of external constraints and it can be released if the stiffness of the constraint decreases [35]. It should be noted that the fall in the magnitude of the transverse residual stress for this constraint configuration after unclamping depends on its distance from the heat source, i.e., the thermal cycles it experiences.

#### 5. Conclusions and future work

Thermo-elastic-plastic FE models were developed in ABAQUS code to simulate welding temperature fields, transverse residual stresses and angular distortions in T-fillet specimens made from a HSS for two different welding sequences and two mechanical boundary conditions. Supportive measurements in terms of welding temperatures, residual stresses and welding deformations were carried out to verify the developed computational approach. Based on the simulation and the experimental results, the following conclusions are drawn.

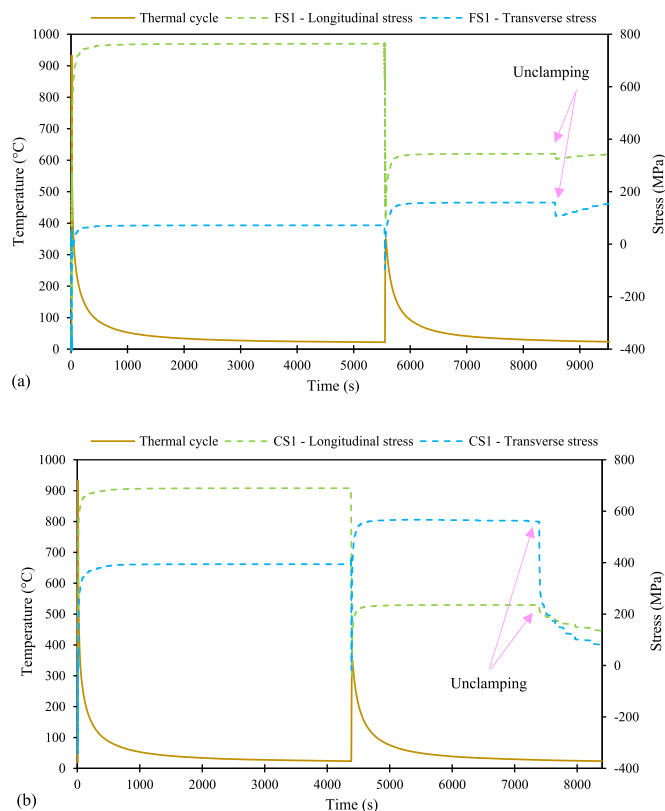


Fig. 22. Evolution of the transverse and longitudinal stresses for a node at a distance of 1 mm from the weld toe during the welding of: (a) FS1; and (b) CS1.

- (1) The results of the thermal and mechanical analyses are in good agreement with the experimental measurements. Consequently, it can be concluded that the developed numerical approach can accurately capture distributions of welding angular distortion and residual stresses.
- (2) The configuration of mechanical boundary conditions has larger effects on the development of angular distortion and transverse residual stress than welding sequence.
- (3) The welding sequence in which the two passes are in the same direction results in less angular distortion and lower peak transverse residual stress than the welding sequence where the welding passes are in the opposite directions. The difference between the peak longitudinal stresses in both the tensile and compressive modes, which developed due to a change in the welding sequence, is minor.
- (4) Transverse residual stresses are sensitive to the stiffness degree of the constraints, i.e., a higher degree of restraint can cause an increase in the transverse residual stresses. By removing or reducing the restraining stiffness, transverse stresses can be released or eased. Longitudinal residual stresses are less sensitive to the restraining stiffness of the external constraints.
- (5) Using rigid clamping at both ends during the welding and its removal post welding can significantly reduce the angular distortion and lower the levels of the induced residual stresses, especially transverse stresses.
- (6) Non-continuous fillet welds are common in practical applications either temporarily (as tack welds) or permanently (as intermittent fillet welds). It is thus of interest to investigate the effect of external constraints and welding sequence on the development of welding angular distortions and residual stresses in non-continuously fillet welded joints made of HSSs.

#### Declaration of Competing Interest

Hereby, authors of this paper declare no conflict of interest.

#### Acknowledgements

This research was funded by Business Finland (formerly TEKES) in the DigRob research project. The support of SSAB Europe is acknowledged.

## Appendix A. Residual stress components

For structural integrity assessment purposes, the distribution of residual stresses can be discussed based on certain invariant characteristics. Once a through thickness distribution of the residual stress is available, based on the results of an FE model, for example, it can be decomposed into three parts, namely, membrane, bending and self-equilibrating components, which are described by Eqs. (A.1), (A.2), and (A.3), respectively:

$$\sigma_{res,m} = \frac{1}{t} \int_0^t \sigma_{res,x}(z) dz \quad (A.1)$$

$$\sigma_{res,b} = \frac{6}{t^2} \int_0^t [\sigma_{res,x}(z) - \sigma_{res,m}] \left( \frac{t}{2} - z \right) dz \quad (A.2)$$

$$\sigma_{res,se} = \sigma_{res,x} - \sigma_{res,m} - \sigma_{res,b} \left( 1 - \frac{2z}{t} \right) \quad (A.3)$$

where  $\sigma_{res,m}$ ,  $\sigma_{res,b}$  and  $\sigma_{res,se}$  are membrane, bending and self-equilibrating components, respectively.  $t$  is material thickness and  $\sigma_{res,x}(z)$  is the transverse residual stress (S11 in this study), which was read from the FE model in the Z-direction (through thickness). By applying this decomposition technique for CS1 on side 1 at the weld toe and performing integration over the weld length (by intervals of approximately 3 mm), where  $z = 0$  is on the top surface and  $z = t$  is on the bottom surface, the following results for the membrane and bending components are observed regarding the clamped and unclamped conditions for the specimen CS1.

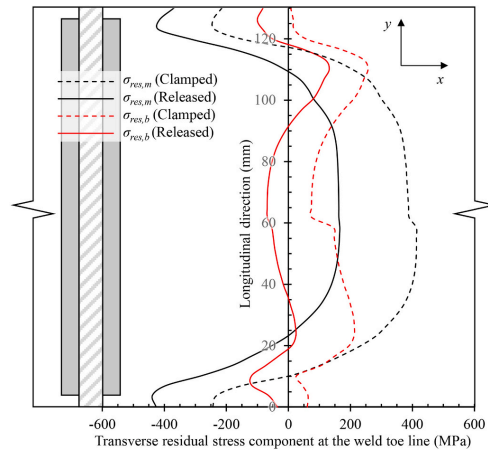


Fig. A.1. Membrane and bending components calculated for CS1 on side 1 at the weld toe in the clamped and released conditions.

As can be seen in Fig. A.1, when the specimen is clamped, the bending and normal components of the residual stresses are considerable and have magnitudes of +238 and +136 MPa calculated based on Eqs. (A.1) and (A.2), respectively. When removing the external constraints, the membrane and bending components reduce in magnitude and tend to reach a zero level and get the magnitudes of -7 and -17 MPa. After unclamping, the residual stresses are self-balanced, although, unequally distributed in the welding direction. It should be noted that the through-thickness residual stresses were not measured, for example by neutron diffraction method, to validate the stress components. However, the distribution of the membrane residual stress component is similar to the conventionally accepted distribution presented in [36]. The stress decomposition technique presented in this section, which uses the results of the FE welding simulation, is applicable to assessment of the stability of plate components and study of the behavior of crack growth under the influence of an unequal residual stress field, and it can help to estimate the stress intensity factor due to residual stresses [37,38].

## References

- [1] J. Sun, X. Liu, Y. Tong, D. Deng, A comparative study on welding temperature fields, residual stress distributions and deformations induced by laser beam welding and CO2 gas arc welding, *Mater. Des.* 63 (2014) 519–530, <https://doi.org/10.1016/j.matdes.2014.06.057>.
- [2] D. Deng, Y. Zhou, T. Bi, X. Liu, Experimental and numerical investigations of welding distortion induced by CO2 gas arc welding in thin-plate bead-on joints, *Mater. Des.* 52 (2013) 720–729, <https://doi.org/10.1016/j.matdes.2013.06.013>.
- [3] C.H. Lee, K.H. Chang, Finite element simulation of the residual stresses in high strength carbon steel butt weld incorporating solid-state phase transformation, *Comput. Mater. Sci.* 46 (2009) 1014–1022, <https://doi.org/10.1016/j.commatsci.2009.05.007>.
- [4] Z. Barsoum, I. Barsoum, Residual stress effects on fatigue life of welded structures using LEFM, *Eng. Fail. Anal.* 16 (2009) 449–467, <https://doi.org/10.1016/j.engfailanal.2008.06.017>.
- [5] D. Deng, FEM prediction of welding residual stress and distortion in carbon steel considering phase transformation effects, *Mater. Des.* 30 (2009) 359–366, <https://doi.org/10.1016/j.matdes.2008.04.052>.

- [6] H. Moshayedi, I. Sattari-Far, The effect of welding residual stresses on brittle fracture in an internal surface cracked pipe, *Int. J. Press. Vessel. Pip.* 126 (2015) 29–36, <https://doi.org/10.1016/j.ijpvp.2015.01.003>.
- [7] C. Heinze, C. Schwenk, M. Rethmeier, Numerical calculation of residual stress development of multi-pass gas metal arc welding, *J. Constr. Steel Res.* 72 (2012) 12–19, <https://doi.org/10.1016/j.jcsr.2011.08.011>.
- [8] X.F. Yan, C. Yang, Experimental research and analysis on residual stress distribution of circular steel tubes with different processing techniques, *Thin-Walled Struct.* 144 (2019) 106268, <https://doi.org/10.1016/j.tws.2019.106268>.
- [9] T. Skriko, M. Ghafouri, T. Björk, Fatigue strength of TIG-dressed ultra-high-strength steel fillet weld joints at high stress ratio, *Int. J. Fatigue* 94 (2017) 110–120, <https://doi.org/10.1016/j.ijfatigue.2016.09.018>.
- [10] M. Amraei, A. Ahola, S. Afkhami, T. Björk, A. Heidarpour, X.L. Zhao, Effects of heat input on the mechanical properties of butt-welded high and ultra-high strength steels, *Eng. Struct.* 198 (2019) 109460, <https://doi.org/10.1016/j.engstruct.2019.109460>.
- [11] T. Björk, A. Ahola, N. Tuominen, On the design of fillet welds made of ultra-high-strength steel, *Weld. World* 62 (2018) 985–995, <https://doi.org/10.1007/s40194-018-0624-4>.
- [12] J. Ahn, E. He, L. Chen, T. Pirling, J.P. Dear, C.M. Davies, Determination of residual stresses in fibre laser welded AA2024-T3 T-joints by numerical simulation and neutron diffraction, *Mater. Sci. Eng. A* 712 (2018) 685–703, <https://doi.org/10.1016/j.msea.2017.12.027>.
- [13] M. Rikken, R. Pijpers, H. Slot, J. Maljaars, A combined experimental and numerical examination of welding residual stresses, *J. Mater. Process. Technol.* 261 (2018) 98–106, <https://doi.org/10.1016/j.jmatprotec.2018.06.004>.
- [14] Y. Denis, E. Lacoste, C. Arvieu, Numerical modeling of Inconel 738LC deposition welding: Prediction of residual stress induced cracking, *J. Mater. Process. Technol.* 210 (2010) 2053–2061, <https://doi.org/10.1016/j.jmatprotec.2010.07.027>.
- [15] B.Q. Chen, C. Guedes Soares, Experimental and numerical investigation on welding simulation of long stiffened steel plate specimen, *Mar. Struct.* 75 (2021) 102824, <https://doi.org/10.1016/j.marstruct.2020.102824>.
- [16] A. Evdokimov, N. Doyunov, R. Ossenbrink, A. Obrosoy, S. Weiß, V. Michailov, Thermomechanical laser welding simulation of dissimilar steel-aluminum overlap joints, *Int. J. Mech. Sci.* 190 (2021) 106019, <https://doi.org/10.1016/j.jlmeccs.2020.106019>.
- [17] C. Chen, S.P. Chiew, M.S. Zhao, C.K. Lee, T.C. Fung, Influence of cooling rate on tensile behaviour of S690Q high strength steel butt joint, *J. Constr. Steel Res.* 173 (2020) 106258, <https://doi.org/10.1016/j.jcsr.2020.106258>.
- [18] A.A. Bhatti, Z. Barsoum, H. Murakawa, I. Barsoum, Influence of thermo-mechanical material properties of different steel grades on welding residual stresses and angular distortion, *Mater. Des.* 65 (2015) 878–889, <https://doi.org/10.1016/j.matdes.2014.10.019>.
- [19] X. Hu, G. Feng, Y. Wang, C. Zhang, D. Deng, Influence of jumping passes on calculation accuracy and efficiency of welding residual stress of thick-plate butt joint in boiling water reactor, *Eng. Struct.* 222 (2020) 111136, <https://doi.org/10.1016/j.engstruct.2020.111136>.
- [20] P. Dai, Y. Wang, S. Li, S. Lu, G. Feng, D. Deng, FEM analysis of residual stress induced by repair welding in SUS304 stainless steel pipe butt-welded joint, *J. Manuf. Process.* 58 (2020) 975–983, <https://doi.org/10.1016/j.jmapro.2020.09.006>.
- [21] M. Ghafouri, J. Ahn, J. Mourujärvi, T. Björk, J. Larkiola, Finite element simulation of welding distortions in ultra-high strength steel S960 MC including comprehensive thermal and solid-state phase transformation models, *Eng. Struct.* 219 (2020) 110804, <https://doi.org/10.1016/j.engstruct.2020.110804>.
- [22] Q. Zhang, Y. Ma, C. Cui, X. Chai, S. Han, Experimental investigation and numerical simulation on welding residual stress of innovative double-side welded rib-to-deck joints of orthotropic steel decks, *J. Constr. Steel Res.* 179 (2021) 106544, <https://doi.org/10.1016/j.jcsr.2021.106544>.
- [23] M. Kubiak, W. Piekarska, Comprehensive model of thermal phenomena and phase transformations in laser welding process, *Comput. Struct.* 172 (2016) 29–39, <https://doi.org/10.1016/j.compstruc.2016.05.014>.
- [24] Z. Barsoum, A. Lundbäck, Simplified FE welding simulation of fillet welds - 3D effects on the formation residual stresses, *Eng. Fail. Anal.* 16 (2009) 2281–2289, <https://doi.org/10.1016/j.engfailanal.2009.03.018>.
- [25] W. Liang, X. Hu, Y. Zheng, D. Deng, Determining inherent deformations of HSLA steel T-joint under structural constraint by means of thermal elastic plastic FEM, *Thin-Walled Struct.* 147 (2020) 106568, <https://doi.org/10.1016/j.tws.2019.106568>.
- [26] ABAQUS user's manual, Version 2020, 2020.
- [27] J. Goldak, A. Chakravarti, M. Bibby, A new finite element model for welding heat sources, *Metall. Trans. B* 15 (1984) 299–305, <https://doi.org/10.1007/BF02667333>.
- [28] J. Siltanen, S. Tihinen, J. Kömi, Laser and laser gas-metal-arc hybrid welding of 960 MPa direct-quenched structural steel in a butt joint configuration, *J. Laser Appl.* 27 (2015), S29007, <https://doi.org/10.2351/1.4906386>.
- [29] D. Deng, H. Murakawa, W. Liang, Numerical simulation of welding distortion in large structures, *Comput. Methods Appl. Mech. Eng.* 196 (2007) 4613–4627, <https://doi.org/10.1016/j.cma.2007.05.023>.
- [30] D. Deng, H. Murakawa, Numerical simulation of temperature field and residual stress in multi-pass welds in stainless steel pipe and comparison with experimental measurements, *Comput. Mater. Sci.* 37 (2006) 269–277, <https://doi.org/10.1016/j.commatsci.2005.07.007>.
- [31] C.H. Lee, K.H. Chang, Prediction of residual stresses in high strength carbon steel pipe weld considering solid-state phase transformation effects, *Comput. Struct.* 89 (2011) 256–265, <https://doi.org/10.1016/j.compstruc.2010.10.005>.
- [32] A. Yaghi, T.H. Hyde, A.A. Becker, W. Sun, J.A. Williams, Residual stress simulation in thin and thick-walled stainless steel pipe welds including pipe diameter effects, *Int. J. Press. Vessel. Pip.* 83 (2006) 864–874, <https://doi.org/10.1016/j.jipvp.2006.08.014>.
- [33] B. Brickstad, B.L. Josefson, A parametric study of residual stresses in multi-pass butt-welded stainless steel pipes, *Int. J. Press. Vessel. Pip.* 75 (1998) 11–25, [https://doi.org/10.1016/S0308-0161\(97\)00117-8](https://doi.org/10.1016/S0308-0161(97)00117-8).
- [34] K. Seleš, M. Perić, Z. Tonković, Numerical simulation of a welding process using a prescribed temperature approach, *J. Constr. Steel Res.* 145 (2018) 49–57, <https://doi.org/10.1016/j.jcsr.2018.02.012>.
- [35] G. Fu, M.I. Lourenco, M. Duan, S.F. Estefen, Effect of boundary conditions on residual stress and distortion in T-joint welds, *J. Constr. Steel Res.* 102 (2014) 121–135, <https://doi.org/10.1016/j.jcsr.2014.07.008>.
- [36] K. Masubuchi, *Analysis of Welded Structures: Residual Stresses, Distortion, and their Consequences*, Pergamon Press, 1980.
- [37] S. Bhardwaj, R.M. Chandima Ratnayake, Residual stress estimation in defect assessment procedures at weld toe and away locations on girth welds: Review of key parameters, *Theor. Appl. Fract. Mech.* 111 (2021) 102848, <https://doi.org/10.1016/j.tafmec.2020.102848>.
- [38] P. Dong, Length scale of secondary stresses in fracture and fatigue, *Int. J. Press. Vessel. Pip.* 85 (2008) 128–143, <https://doi.org/10.1016/j.jipvp.2007.10.005>.





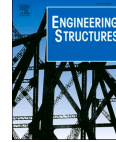
## **Publication III**

Ghafouri, M., Ahola, A., Ahn, J., and Björk, T.

**Numerical and experimental investigations on the welding residual stresses and distortions of the short fillet welds in high strength steel plates**

Reprinted with permission from  
*Journal of Engineering Structures*  
Vol. 260, p. 114269, 2022  
© 2022, Elsevier





# Numerical and experimental investigations on the welding residual stresses and distortions of the short fillet welds in high strength steel plates

Mehran Ghafouri<sup>a,\*</sup>, Antti Ahola<sup>a</sup>, Joseph Ahn<sup>b</sup>, Timo Björk<sup>a</sup>

<sup>a</sup> Laboratory of Steel Structures, School of Energy Systems, LUT University, P.O. Box 20, 53851 Lappeenranta, Finland

<sup>b</sup> Department of Mechanical Engineering, Imperial College London, South Kensington Campus, London SW7 2AZ, UK

## ARTICLE INFO

### Keywords:

Welding simulation  
Welding residual stress  
High strength steel  
Welding distortion  
Finite element simulation

## ABSTRACT

The current study investigates the influence of different welding sequences and external constraints on development of welding-induced angular distortion and residual stresses in the short fillet welds made of the high strength steel (HSS), S700, using the finite element (FE) method. Three-dimensional thermo-elastic-plastic FE modeling was performed in the ABAQUS FE software based on the double-ellipsoidal heat source model, temperature-dependent material properties, and considering geometrical non-linearity. The accuracy of the FE models were verified by comparing the simulation results and experimentally measured data. Both the numerical method and measurements show that external constraint has relatively larger influence than welding sequence on the development of angular distortion and the peak magnitude of residual stresses. To determine the significance of short fillet welds in terms of induced distortion and residual stress fields, the results captured by simulation and validated by measurements were compared to those of continuous fillet welds. From a numerical point of view, the results of this study are meaningful to understand the reasonable accuracy required to capture the necessary details of the welding process. From an engineering prospect, the results of this study can be important as they indicate that transverse residual stress fields due to short fillet welds are localized with considerably larger peak magnitudes compared to continuous fillet welds. With respect to the angular distortion, the results of this study show that stiffness of external constraint has a greater impact on prevention of angular distortion in continuous fillet welds than in short fillet welds. In the case of fillet welds with small lengths, beside proper clamping, other deformation control techniques such as pre-alignment of the welded members need to be considered.

## 1. Introduction

In the world of construction and manufacturing, steel is one of the main construction materials. Steel production is claimed to be the largest energy consumer among the industrial sectors. The process is highly energy intensive with consequential environmental impacts [1]. It is of paramount importance to make balance between the environmental impacts from one side and huge demands for such materials from the other side. In this respect, one environmental energy solution is to increase the strength level of steels, which has contributed to the advent of lightweight and high-performance materials. This insight has triggered the development of high and ultra-high strength steels (HSS/UHSS). Remarkable features of these materials such as high strength to weight ratio, desirable weldability and toughness, makes them highly applicable in a wide variety of industrial applications, such as the oil and

gas industries, offshore construction, automotive and shipbuilding industries [2].

Due to its advantages over mechanical joining methods, the fusion welding process has been widely used in the construction and manufacturing industries to fabricate large structures and assemblies. Weight reduction, enhanced structural performance and flexibility in design, and cost-effectiveness can be named among the advantages attributed to the fusion welding technology [3]. Arc welding processes and among them gas metal arc welding (GMAW), which is categorized as a fusion welding technique, has been extensively utilized to permanently join structural members and components made from HSSs [2]. Fusion welding, however, is a complex thermal process, which transports highly concentrated and tremendous heat input to the welded joint. This uneven temperature field followed by a non-linear cooling in the weld zone, can cause serious strength problems such as heat-affected

\* Corresponding author.

E-mail address: [mehran.ghafouri@lut.fi](mailto:mehran.ghafouri@lut.fi) (M. Ghafouri).

<https://doi.org/10.1016/j.engstruct.2022.114269>

Received 7 December 2021; Received in revised form 15 March 2022; Accepted 10 April 2022

Available online 19 April 2022

0141-0296/© 2022 The Authors. Published by Elsevier Ltd. This is an open access article under the CC BY license (<http://creativecommons.org/licenses/by/4.0/>).

**Table 1**  
The chemical compositions of S700MC PLUS and ESAB OK AristoRod 13.29 (wt. %).

Material	C	Si	Mn	P	S	Al	Ti	Cr	Ni	Mo	Nb	V
S700 MC	0.12	0.25	2.10	0.02	0.01	0.015	0.15	–	–	–	0.09	0.2
AristoRod 13.29	0.089	0.53	1.54	–	–	–	–	0.26	1.23	0.24	–	–

zone (HAZ) softening [4] and rise of residual stresses and distortions [5]. Welding residual stresses can be detrimental or beneficial depending on magnitude, distribution or sign of stresses [6]. Tensile residual stresses are harmful and directly affect fatigue performance and service life of welded connections [7–9]. Stress corrosion cracking [10], which contributes to degradation of the structural integrity of welded joints, and decreased buckling strength [11] are attributed to the presence of tensile residual stresses. Welding deformation is a technical challenge resulting in dimensional inaccuracy and leads to decrease the quality of the welded joint. By imposing correction work, welding deformation can cause fabrication delays, incur financial cost, and decrease productivity. Excessive deformation might seriously impair fabrication, and, in extreme cases, lead to failure [12].

Reliable design of steel structures and ensuring safety to their applications necessitates evaluation of welding residual stresses and distortions. Measurement of residual stress in the literature has been reported by means of different destructive and non-destructive techniques such as hole-drilling [13,14], crack compliance [15], XRD [6,16], and Neutron diffraction techniques [17–20]. Assessment of residual stresses by means of experimental methods post welding is available. However, those methods in general have their own challenges. Destructive methods, such as the hole drilling technique, are inapplicable and non-destructive methods have their own limitations in terms of accessibility, such as the X-ray diffraction (XRD) method.

The privilege of the numerical methods over the experimental methods is the ability of computational techniques in prediction of residual stress state and welding deformation patterns before the real welds are applied. Although development of welding residual stresses and distortions can hardly be avoided, accurate prediction makes it possible to adopt engineering measures to reduce welding deformations and stresses. This matter, especially in terms of HSSs where rapid heating and cooling inherent to welding can seriously degenerate their high load bearing capacity, is of particular importance.

During the past decades, a number of studies have been done concerning elaboration of the computational methods to predict welding residual stresses and deformations. As a numerical approach, the FE method has proven its ability to solve a broad spectrum of engineering and scientific problems and is frequently used in the field of welding simulation. FE simulation of different welding processes [6,16,17,21–23] for a wide range of materials [13,15,24–28] have been accomplished.

Fillet weld is known to be one of the most prevalent weld types used in the fabrication of a broad range of steel structures such as plate girders and stiffened panels. Fillet welded joints either single or double sided, may suffer from different welding deformation types, such as transverse and longitudinal shrinkages, and angular distortion [29]. Depending on the design and applied load, in order to reduce the labor cost and weight of the stiffened panels, an alternative method of attaching the stiffener to the base plate is non-continuous welding, which is also known as intermittent welding [30]. During the fabrication of steel structures in the assembly stage, making temporary connections between the structural members is performed through tack welds, which can also be considered as short welds. From the tack welding viewpoints, it is also important to understand the formation of welding distortions under different tack welding sequences and boundary conditions, as they might be considered in manufacturing, for example, by pre-alignments or changing the welding sequence. Although there has been several research on welding simulation of T-fillet welded steel joints [29,31–34], till present there is lack of data regarding the welding

**Table 2**  
The nominal mechanical properties of S700MC PLUS and ESAB OK AristoRod 13.29.

Material	Yield strength $\sigma_y$ [MPa]	Ultimate tensile strength $\sigma_u$ [MPa]	Elongation %
S700 MC PLUS	700	750–950	13
AristoRod 13.29	700	800	19

distortions and residual stresses developed due to short fillet welds in HSSs under the influence of different external restraints and welding sequences.

The aim of this research is prediction and evaluation of welding stresses and angular distortion developed in the T-joints made of HSS S700MC PLUS due to short fillet welds under different external constraints and welding sequences. The matter is accomplished by developing three-dimensional sequentially coupled thermal-structural FE models in ABAQUS code [35]. The temperature field is simulated by considering a moving heat source based on the model proposed by Goldak et al. [36] being implemented in the user-subroutine DFLUX. The combined effects of convection and radiation are considered in modeling the heat loss. Subsequent to capturing the temperature distribution in thermal analysis, the predicted nodal temperatures are transferred into a mechanical model to calculate the welding stresses and angular distortion. The distributions of residual stresses, sequential and final angular distortions due to the external constraints and welding sequences are verified with the experimental measurements, and comparisons are made between the results of the short and continuous fillet welds in terms of thermal and mechanical fields.

## 2. Experimental setup

### 2.1. Materials

HSS S700MC PLUS, which is a high strength low carbon and low alloy steel with a minimum yield strength of 700 MPa was used in this study. This material is manufactured by modern hot strip rolling and direct quenching, which differs from the conventional quenching procedures [37]. The filler material for joining the stiffeners to the base plates in this study was ESAB OK AristoRod 13.29 solid wire with 1 mm diameter. This filler material falls in the matching strength level with the base material. Table 1 presents the chemical compositions of the base and filler materials based on the material certificates of the manufacturers. The nominal mechanical properties of the base and filler materials are shown in Table 2.

### 2.2. Specimens and welding procedure

To investigate the effect of welding sequence and mechanical boundary conditions on deformation characteristics and residual stresses in T-joints connected by short fillet welds, four identical T-joint specimens were fabricated. The dimensions of the base plates and stiffeners being cut from 6 mm hot rolled strips of S700, were  $460 \times 130$  mm and  $130 \times 25$  mm, respectively. Laser cutting of the material was accomplished in such a way that the welding direction was perpendicular to the rolling direction of the base plate. The convention for the welding direction was assumed along the +Y-axis, while Z-axis was normal to the top surface of the base plate. A GMAW robotized arm was

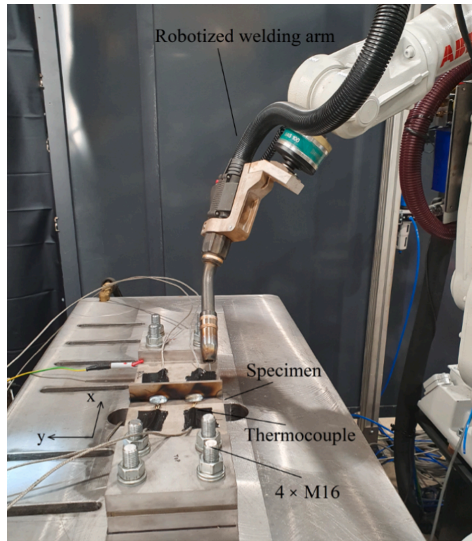


Fig. 1. The experimental set-up of the T-joint specimen.

**Table 3**  
Welding process parameters.

Voltage (V)	Current (A)	Travel speed (mm/s)	Wire diameter (mm)	Wire feed rate (m/min)	Tip distance (mm)	Shielding gas
25	260	7	1	12.5	16	Ar + 8% CO <sub>2</sub>

used for welding, as shown in Fig. 1. The torch angle was considered 45° for all the welding cases. Selecting the welding parameters presented in Table 3, the welding leg size of 6 mm was achieved. The net heat input value transported to the joint, amounts to 0.79 kJ/mm by applying a welding efficiency coefficient of 0.85 for GMAW process [38].

The fillet welding procedure included deposition of four weld layers with an approximate length of 20 mm each, on both sides of the specimens. Two different welding sequences were considered to investigate the effect of the welding sequence on the residual stress and deformation patterns, as shown schematically in Fig. 2. The effect of external constraints on welding stresses and deformations were investigated by applying two different clamping set-ups. One configuration was performed so that the specimens were rigidly clamped at both ends (see Fig. 1), while the other clamping restrained the specimens only at one end. Considering the two different welding sequences and external restraints, in total four experimental welding cases were fabricated.

In order to facilitate the discussion and drawing comparisons between the welding cases, to each welding case a label was assigned. In the labelling of specimens, the first letter shows the applied mechanical boundary conditions. That is, F indicates the welding cases being clamped at one end, while C is used for the cases clamped at both ends. S1 and S2 are used to show the welding sequences 1 and 2, respectively. The labels assigned to the welding cases are summarized in Table 4.

### 2.3. Temperature measurements

Thermal cycles during welding were measured by attaching several K-type thermocouples at different locations on the top surface of each specimen. The positions of thermocouples were arranged so that the high temperature HAZ, and the lower temperature fields far from the

**Table 4**  
Labels assigned to the specimens in welding experiments.

Label	Condition
FS1	One Free end, Sequence 1
FS2	One Free end, Sequence 2
CS1	Both ends Clamped, Sequence 1
CS2	Both ends Clamped, Sequence 2

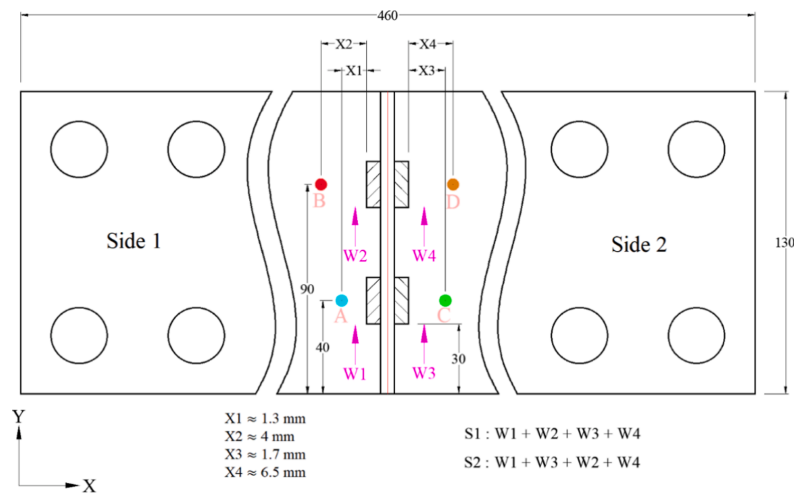


Fig. 2. Illustration of the welding sequences S1 and S2, and the positions of thermocouples. (Units in mm).

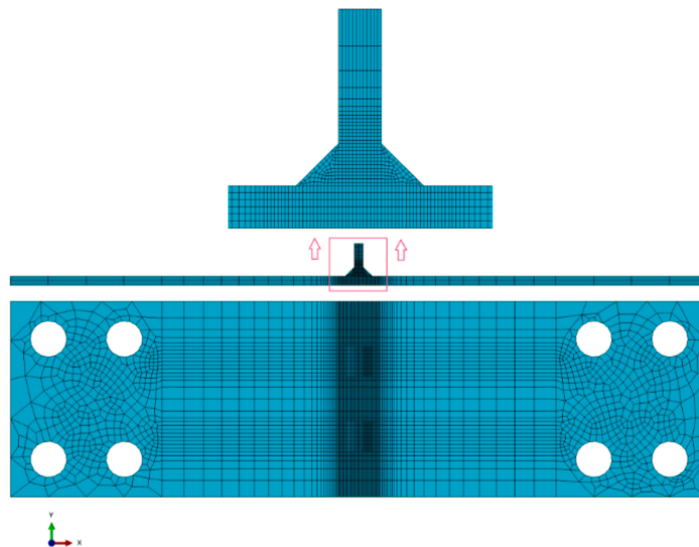


Fig. 3. Mesh details of the fillet welded T-joint.

weld zone can be captured in order to verify the temperature histories obtained from the corresponding FE models. The locations of thermocouples are shown schematically in Fig. 2. As can be seen, four weldments, namely W1–W4, two on each side were produced. The distances of thermocouples A, B, C, and D from the weld toes are shown with X1, X2, X3, and X4, respectively. The accurate values of X1–X4 were determined post welding based on the measurements by a Hexagon 3D scanner in order to make comparisons with the corresponding nodal temperatures from the FE simulations.

### 3. Finite element simulation

Temperature distribution and evolution of welding deformations and stresses of T-joints due to short fillet welds were investigated by means of the FE method. In this context, three-dimensional thermo-elastic-plastic FE models were developed in ABAQUS FE code. Since the mechanical work performed compared to the thermal energy of the welding arc is negligible, and the structural response under the thermal load has insignificant influence on the temperature field, a sequentially coupled formulation was adopted [39]. In this solution procedure, the heat conduction equation is solved independently from the stress and strain problems. The effect of a non-linear transient temperature field on the mechanical response is considered through the thermal expansion and temperature-dependent mechanical properties of the material. This formulation consists of two steps. In the first step, temperature distribution due to a moving heat source is captured by performing a thermal analysis and solving heat conduction equation. In the next step, the captured nodal temperatures are transferred into a mechanical model and applied as a thermal load to find the mechanical response and compute the developed residual stresses and strains.

#### 3.1. FE model geometry and mesh

All the experimental welding specimens and the amounts of the deposited filler material were identical, however, with different welding sequences and external constraints. In this regard, a 3D FE model with

the same mesh structure (see Fig. 3) was developed for all the cases. Nevertheless, the order of element activation varied, which corresponds to the applied welding sequence, and the mechanical boundary conditions applied in accordance with the external restraints. In the thermal analysis, a 1st order 3D 8-node linear diffusive heat transfer brick hexahedron element (DC3D8) with temperature as the only degree of freedom was employed. In order to facilitate the data mapping between the thermal and mechanical models, the same FE mesh with identical number of elements, however different element types were used. In the structural analysis, a 1st order 3D 8-node linear hexahedron reduced integration elements (C3D8R) was used. Shear locking is avoided, better convergence is achieved, and less computational time is required when the reduced integration elements are used [22]. The convergence study on mesh density was carried out in a previous investigation [16] to ensure that the employed mesh structure is sufficiently refined to yield accurate simulation results. Mesh convergence was completed when further refinement of the mesh structure had inconsequential effect on the results. A fine mesh grid with a total number of 28,988 elements was found to be sufficiently accurate to represent the stress and strain results. The smallest element size was  $0.5 \times 2.5 \times 1$  mm (in the X, Y, and Z directions), which was applied in the FZ and HAZ, where high tensile residual stresses are expected to be built up. The size of elements increased progressively as the distance from the weld toe towards the outer edges of the specimen increased. Gradual addition of the filler material was simulated using the element birth and death technique, also known as model change in ABAQUS [40]. In this method, the weld metal is divided into several segments. All the elements representing the filler metal are initially inactivated. Based on the assigned step time, when the heat approaches and the relevant segment is heated up, its status is changed from inactive to active to which temperature-dependent thermo-physical properties in the thermal analysis and temperature-deponent mechanical properties in the structural analysis are allocated.

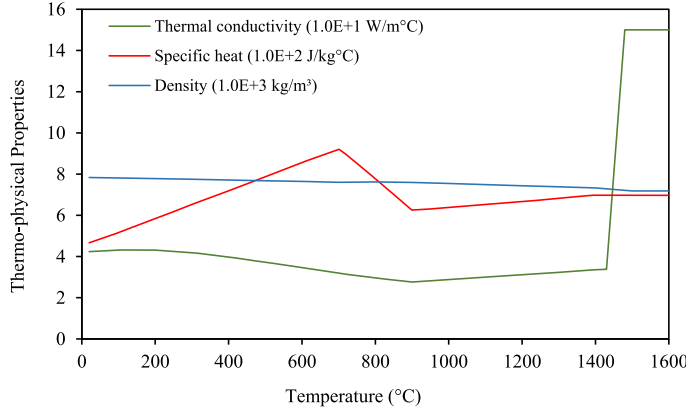


Fig. 4. Temperature-dependent thermo-physical properties of S700.

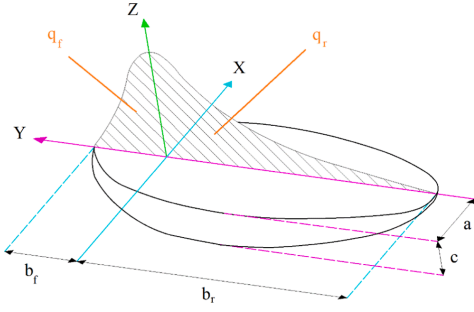


Fig. 5. Schematic of Goldak's volumetric heat source shape.

### 3.2. Thermal analysis

Transient temperature field during welding ( $T$ ) in time ( $t$ ) and space ( $x, y, z$ ) was solved using a non-linear isotropic partial differential equation derived from Fourier's law of heat conduction and law of energy conservation, as shown in Eq. (1):

$$\rho(T)c_p(T)\frac{\partial T}{\partial t} = \frac{\partial}{\partial x}\left(k(T)\frac{\partial T}{\partial x}\right) + \frac{\partial}{\partial y}\left(k(T)\frac{\partial T}{\partial y}\right) + \frac{\partial}{\partial z}\left(k(T)\frac{\partial T}{\partial z}\right) + q \quad (1)$$

where  $\rho(T)$ ,  $c_p(T)$  and  $k(T)$  are temperature-dependent density, specific heat, and thermal conductivity, respectively. These temperature-dependent thermo-physical properties for S700 were obtained from the literature [41], as shown in Fig. 4. It must be noted that the units are arranged so that all properties can be shown in a single graph. The parent and filler materials share almost the same strength level and thus, in the FE models were defined as identical materials to both the same material properties were assigned.

In Eq. (1),  $q$  ( $W/m^3$ ) is known as the volumetric heat source density or internal heat generation rate. A volumetric heat source with double ellipsoidal distribution proposed by Goldak et al. [36] was considered to represent the energy transferred from the welding arc to the base and weld materials, as shown schematically in Fig. 5. Two heat flux distributions are defined by this model, one for the front half and the other for the rear half of the heat source, as expressed by Eq. (2) and Eq. (3),

respectively:

$$q_f(x, y, z, t) = \frac{6\sqrt{3}f_f Q}{ab_f c \pi \sqrt{\pi}} e^{-3\left(\frac{x^2}{a^2} + \frac{(y-y_0)^2}{b_f^2} + \frac{z^2}{c^2}\right)}, \quad y \geq 0 \quad (2)$$

$$q_r(x, y, z, t) = \frac{6\sqrt{3}f_r Q}{ab_r c \pi \sqrt{\pi}} e^{-3\left(\frac{x^2}{a^2} + \frac{(y-y_0)^2}{b_r^2} + \frac{z^2}{c^2}\right)}, \quad y < 0 \quad (3)$$

$q_f$  and  $q_r$  are the heat flux distributions accumulated in the front half and rear half of the heat source, respectively.  $Q$  is the power of the welding arc, which can be calculated based on the welding current ( $I$ ), voltage ( $V$ ) and welding efficiency coefficient ( $\eta$ ). The parameters  $a$ ,  $b_f$ ,  $b_r$  and  $c$  are characteristics of the welding heat source.  $f_f$  and  $f_r$  are dimensionless parameters, and account for the fractions of heat deposited in the front and rear half of the heat source, respectively. Taking the continuity of the heat source into consideration the following relationships are observable:

$$\frac{f_r}{b_r} = \frac{f_f}{b_f} \quad (4)$$

$$f_f + f_r = 2 \quad (5)$$

The welding torch in the experiments had a work angle of  $45^\circ$ . Simulation of the moving heat source at a specified angle necessitates transformation of points from the global coordinate system into a local coordinate system by means of rotation and translation. Considering the defined convention for the welding direction, rotations of  $-45^\circ$  and  $45^\circ$  were performed for side 1 and side 2, respectively:

$$\begin{bmatrix} x \\ y \\ z \end{bmatrix} = \begin{bmatrix} \cos 45 & 0 & \sin 45 \\ 0 & 1 & 0 \\ -\sin 45 & 0 & \cos 45 \end{bmatrix} \begin{bmatrix} X - X_0 \\ Y - Y_0 \\ Z - Z_0 \end{bmatrix} \quad (6)$$

$$\begin{bmatrix} x \\ y \\ z \end{bmatrix} = \begin{bmatrix} \cos 45 & 0 & -\sin 45 \\ 0 & 1 & 0 \\ \sin 45 & 0 & \cos 45 \end{bmatrix} \begin{bmatrix} X - X_0 \\ Y - Y_0 \\ Z - Z_0 \end{bmatrix} \quad (7)$$

where  $x, y$  and  $z$  represent nodal coordinates in the local coordinate system and  $X, Y$  and  $Z$  are nodal coordinates in the global coordinate system. Mathematical equations representing the moving heat source were implemented in the ABAQUS user-subroutine DFLUX programmed in FORTRAN. The user-subroutine DFLUX calculated the position of the heat source with respect to time, travel speed of the torch and nodal coordinates. It then, calculated the non-uniform volumetric flux distri-



**Table 5**  
Adjusted heat source parameters.

Parameter	$a$ (mm)	$b_f$ (mm)	$b_r$ (mm)	$c$ (mm)	$f_f$	$f_r$
Value	7	3	10	7	0.46	1.54

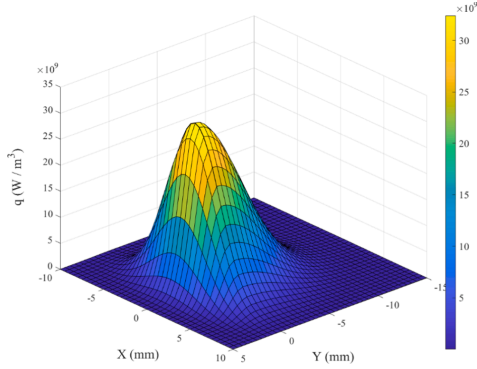


**Fig. 6.** Power distribution of the double-ellipsoidal heat source using the parameters in Table 5.

bution at each integration point as a function of time, the position of the heat source and using the heat source power.

Temperature histories during the welding must be precisely predicted to be able to have an acceptable accuracy in prediction of residual stresses and strains. To do so, calibration of the heat source is required, which was accomplished by iteration of the Goldak's characteristics of the weld pool so that a close agreement was reached between the nodal temperatures from the simulation and measurements. Matching the boundaries of the FZ and HAZ captured by simulation against the macrograph of the weld cross section was performed as the further calibration of the heat source. Table 5 summarizes the heat source parameters and their adjusted values to calibrate the thermal model. Using the calibrated Goldak's heat source parameters in Table 5, power distribution of the double-ellipsoidal heat source for the front half and rear half of the energy source on the top surface is shown in Fig. 6.

In all the simulation cases, ambient temperature was set to 20 °C. To reach a unique solution for Eq. (1), it should be solved subject to specific boundary conditions. In welding simulation problems, the most widely applied thermal boundary conditions are the heat loss due to convection and radiation from free surfaces of the specimen to the surroundings, as depicted schematically in Fig. 7. Heat loss by convection during welding is generally taken into account using Newton's law of cooling and heat loss by radiation is modeled by applying Stefan-Boltzmann's law. An

alternative method to model the heat loss during welding is to account for the combined effect of convection and radiation, which is generally performed by defining a temperature-dependent heat transfer coefficient [42,43], as is expressed by the following equation:

$$h = \begin{cases} 0.0668 \times T \left( \frac{W}{m^2 \cdot C} \right) & 0 \leq T \leq 500 \\ 0.231 \times T - 82.1 \left( \frac{W}{m^2 \cdot C} \right) & T \geq 500 \end{cases} \quad (8)$$

where  $T(^{\circ}C)$  is temperature and  $h$  denotes the temperature-dependent heat transfer coefficient. The mathematical expressions presented in Eq. (8) were implemented in the user-subroutine FILM to model the combined thermal boundary conditions. It should be noted that heat transfer by means of conduction between the specimen and clamping are ignored since the distance between the heat source and clamped areas are large enough so that the temperature rise at those regions are negligible.

The interaction between solid and liquid phases is not included in the ABAQUS package and modeling the fluid flow is not directly possible when using this FE software. However, since this phenomenon has consequential influence on the temperature distribution of the weld pool, it was accounted for using artificially increased thermal conductivity at temperatures higher than the melting point, i.e., thermal conductivity at temperatures higher than the liquidus temperature was considered almost 4 times as large as that value at room temperature. To account for the thermal effects of solidification in the weld pool, the latent heat of fusion was considered with a value of  $270 \times 10^3$  J/kg between the solidus temperature of 1430 °C and liquidus temperature of 1480 °C.

### 3.3. Mechanical analysis

In each mechanical analysis, the temperature histories predicted by the corresponding thermal analysis were transferred and applied as an input (thermal load) in a non-linear elastic-plastic analysis to calculate the residual stresses and distortions. In the current study, the strain rate due creep was not taken into account in the mechanical analysis since in the entire thermal cycle, the time period with high temperature was limited to a few seconds and the effect of creep on the total strain was insignificant [21,25]. Phase transformation in solid state is one of the phenomena which may have significant effect on welding-induced stresses and strains depending on the type of material. Austenitic stainless steels are known not to experience phase transformation [9] while carbon steels are more prone to phase transformation. In this regard, welding-induced residual stress and distortion in medium and high carbon steels are stated to be more significantly affected by phase transformation than low carbon steels [11,13]. Ferro et al. [44], however, found that including solid state phase transformation in mechanical analysis in low carbon steels results in more accurate and reliable values for residual notch stress intensity factors. In this study, due to lack

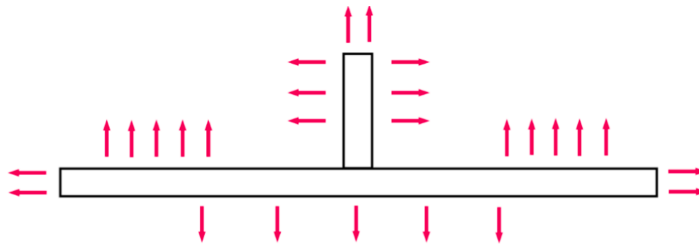


**Fig. 7.** Illustration of the heat loss by means of convection and radiation from the free surfaces of the T-joints.

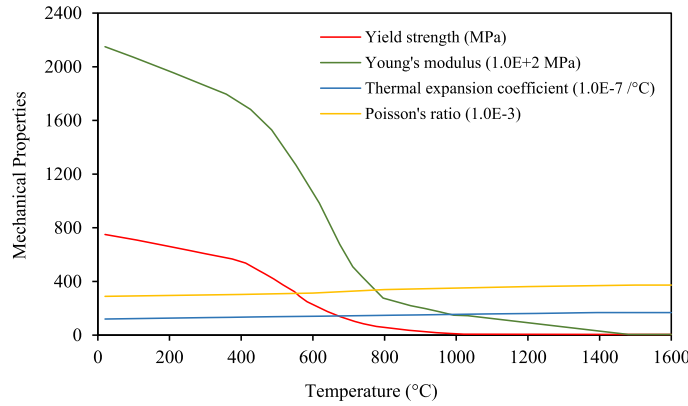


Fig. 8. Temperature-dependent mechanical properties of S700.

of experimental data being essential to include phase transformation, strain rate due to phase change was not included in the mechanical analysis. Nevertheless, the influence of phase change on formation of residual stresses and strains in HSSs is of interest and a further study would include such effect. Excluding the strain rate components due to phase transformation and creep, the total strain rate is decomposed by its constituents as follows:

$$\{de^{total}\} = \{de^e\} + \{de^p\} + \{de^{th}\} \quad (9)$$

where  $de^{total}$  is the increment of total strain.  $de^e$ ,  $de^p$  and  $de^{th}$  correspond to elastic, plastic, and thermal strain increments, respectively. Elastic strain was modeled based on the isotropic Hooke's law using temperature-dependent modulus of elasticity and Poisson's ratio. Modeling the plastic strain component was accomplished using a rate-independent plastic model including the following features: Von Mises yield criterion, isotropic strain hardening law and temperature-dependent mechanical properties. A temperature-dependent thermal expansion coefficient was used in modeling of the thermal strain. Temperature-dependent mechanical properties used in calculation of the structural response were taken from the literature [41], as presented in Fig. 8.

In the mechanical analysis, the effect of annealing on strain hardening was considered by defining an annealing temperature. If the temperature of any material point rises above the annealing temperature, strain hardening memory is lost by resetting the equivalent plastic strain to zero at that material point. On condition that the temperature of a material point falls below the defined annealing temperature during cooling, material retrieves its work hardening memory at that point. In this study, the annealing temperature was set to 900 °C [16].

In welded joints, application of welding fixtures or clamps is one of the major techniques to control the induced distortions. Using fixtures in over-restraint conditions, can reduce the welding deformation, it can, however, negatively affect residual stress fields where stresses can build up and cause cracking problems. In welding of under-constrained components, the development of distortions can increase dimensional instability. Although in the case of short fillet welds, smaller levels of distortion are expected compared to the continuous welding, the residual stress field should be considered carefully. In this regard, correct application of external restraints contributes to optimization of welding-induced stresses and strains. Regarding tack welds (temporary non-continuous welds), although by applying the main weld layer, stress fields due to applying the tack welds are mainly annihilated, welding deformations caused by those tack welds will remain and must thus be

thoroughly taken into consideration. This matter, in real applications such as robotized welding is of particular importance where the accuracy and productivity of such technologies may decline if the previous deformations due to tack welds are not accounted for. In the experimental part of the study, two clamping conditions were tested; In one case, the external constraints were applied in such a way that the related specimen was restrained at one end in a specified area. In the corresponding FE model, the mechanical boundary conditions were applied to simulate the clamping condition, and all the nodes in the specified area were restricted to move translationally and rotationally, as shown in Fig. 9 (a). The other clamping configuration was considered to fix the specimen rigidly at both ends in the two defined areas. In the related FE model, all the nodes in those areas were prevented from rotation and translation, as shown in Fig. 9 (b). It should be noted that the length of the clamping in the X-direction was 100 mm. After welding and reaching the ambient temperature, the mechanical boundary conditions were defined in the FE models corresponding to the removal of the clamps. That is, after the cooling stage, all the mechanical boundary conditions were deactivated and those to prevent the rigid body motion only were defined, as shown in Fig. 9 (c).

## 4. Results and discussion

### 4.1. Results of thermal simulation

The temperature distribution and peak temperature captured by the FE thermal simulation of short fillet welds in T-joints made of S700 are shown in Fig. 10. It should be noted that due to the identical welding parameters and heat source model for all the cases, the thermal analysis results are presented only for one of the cases (FS1). As can be seen in Fig. 10, the maximum temperature of the weld pool is approximately 1800 °C. In the same figure, the FZ, i.e., the regions with peak temperatures higher than the liquidus temperature (1480 °C) are shown in light gray. To achieve reasonable results for mechanical response, an accurate prediction of temperature distribution during the welding is a requirement.

Matching the shape and size of the weld pool from the simulation and experimental measurements is one of the indices to evaluate the correctness of temperature distribution during the welding. Fig. 11 represents the depth of penetration captured from the macrograph of the weld cross section versus the simulation at a distance of 5 mm from the start of the segment. As shown in Fig. 11, the depth of penetration is well-captured by simulation and boundaries of the FZ from the simulation

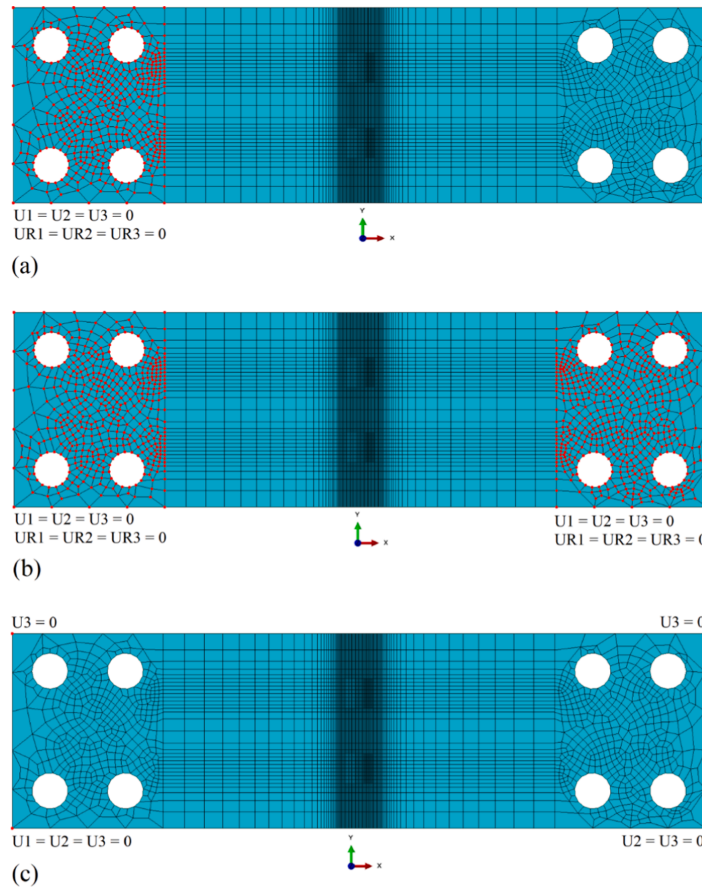


**Fig. 9.** Representation of the mechanical boundary conditions assigned to the FE models for: (a) clamping at one end; (b) clamping at both ends; and (c) removal of the clamps.

reasonably match the macrograph of the weld cross section. Matching the experimental and simulated temperature histories, which was carried out by adjusting the heat source parameters and calibration of the heat loss model, is another index of the accuracy of thermal analysis. In this respect, the experimental time-temperature curves obtained through the thermocouple measurements at several locations and the simulation results for the corresponding nodes are presented in Fig. 12. As mentioned before, the applied heat input and specimen configuration for all the cases were identical and hence, only one of the specimens (FS1) was chosen for the sake of comparison in terms of the experimental and simulated thermal cycles.

For a better clarity regarding the features of time-temperature curves, the entire temperature histories obtained from the simulation and those captured by the thermocouple measurements for FS1 are divided into four parts (a–d), as shown in Fig. 12. That is, Fig. 12 (a–d), refers to the welding thermal cycles of segments W1–W4, respectively. In Fig. 12, T1–T4 are the thermocouples attached on the top surface of the specimen (specified in Fig. 2), and X1–X4 refer to the distances of those thermocouples from the weld toes and the corresponding nodal

distances in the FE model. X1–X4, were measured from the 3D scan image of the specimen post welding and after detaching the thermocouples. It can be seen that the simulated curves are in close concurrence with the experimental ones in terms of the heating and cooling rates, and the peak temperatures. Such agreement implies that the heat source parameters (Goldak's characteristics) were adjusted reasonably, and the heat loss model was calibrated correctly. Comparing the numerical results of T1 in Fig. 12 (a) to T2 in Fig. 12 (b), with the specified distances of 1.25 and 4 mm from the heat source, respectively, shows that the regions close to the weld, experienced considerably higher peak temperatures compared to the areas farther from the heat source, while reasonably maintained the heating rates similar to those areas. Based on the results of thermal analysis, it was assumed that the thermal FE model validated through the transient temperature histories and the weld pool dimensions, was accurate enough in order to transfer the nodal temperatures from the thermal to the mechanical model.

It is expected that welds with shorter lengths experience faster cooling rates. In this regard, a comparison is drawn to clarify how the cooling rate changes for the fillet welds with considerably shorter

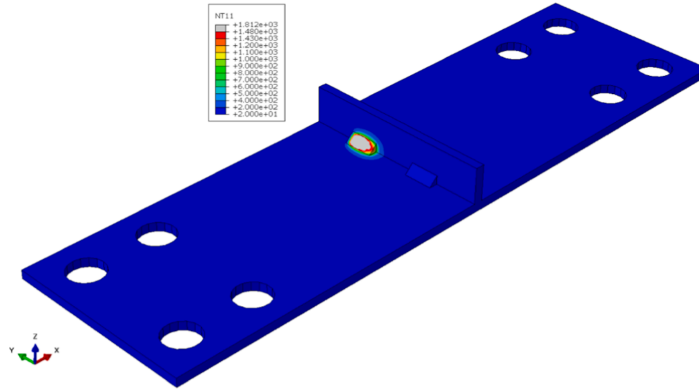


Fig. 10. Temperature contours captured during the welding of W2 on FS1.

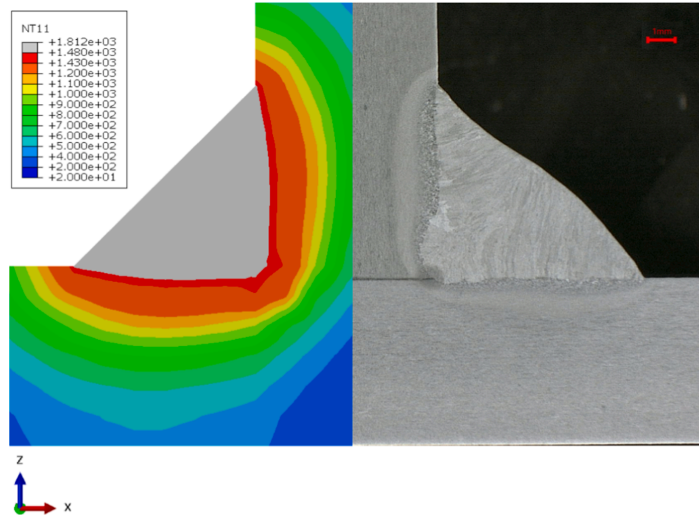


Fig. 11. Welding temperatures (NT11) and Boundaries of the weld pool from the simulation versus the experiment through the thickness.

lengths compared to the continuous ones. In addition to the FE simulation of short fillet welds with a specified length of 20 mm, an FE thermal simulation for a double-sided fillet weld with an approximate length of 122 mm on each side, was performed. It should be noted that identical heat inputs for both cases were used. Fig. 13 shows the time-temperature curves captured from the simulation for a node positioned at a distance of  $X = 0.5$  mm from the weld toe at half-length of the weld in each case. As can be seen, while both welds experienced almost the same peak temperature and heating rate, a considerable difference was obtained for the cooling rate. From Fig. 13, cooling times ( $t_{8/5} = t_{500} - t_{800}$ ), for the continuous and short welds, are 11.45 and 3.86 s, respectively. The calculated cooling rates ( $v_{8/5} = 300/(t_{8/5})$ ) are 26.2 and 77.7 °C/s, for the continuous and short welds, respectively.

This heating and very fast cooling due to the short length of the weld can produce localized residual stress fields with large magnitudes. In

addition,  $t_{8/5}$  is known to have a significant effect on the final microstructure of the HAZ in welded structures since most microstructural changes occur at temperatures above 500 °C. As  $t_{8/5}$  decreases, the tendency to form martensite increases, and, consequently, the hardness of the HAZ rises. In direct-quenched HSSs and UHSSs, the maximum limit of  $t_{8/5}$  should not be exceeded to avoid detrimental softening in the HAZ [45,46]. Microstructural investigation is out of the scope of the current study, it is, however, important to note that the FE thermal simulation can contribute to conduct comparative studies on the effect of cooling rate due to the different weld lengths or heat inputs on the microstructure and mechanical properties of the advanced HSSs.

#### 4.2. The simulated residual stresses and angular distortion

The effect of external constraints and welding sequence on

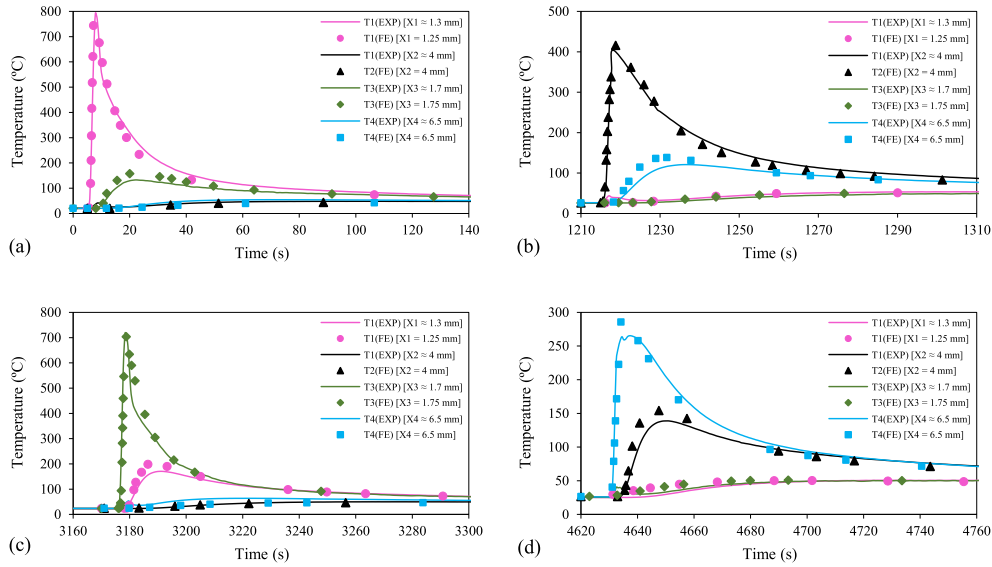


Fig. 12. The experimental versus simulated thermal cycles for FS1 during the welding of segments: (a) W1; (b) W2; (c) W3; and (d) W4.

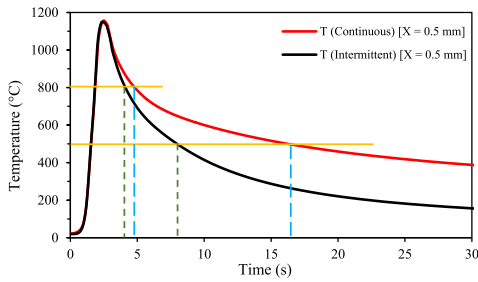


Fig. 13. Comparison of the simulated thermal cycles for a short fillet weld with a length of 20 mm, and a continuous fillet weld with a length of 122 mm.

development of residual stresses and angular distortion, which is induced by non-uniform heating and cooling during the welding, was investigated. Experimental measurements were conducted to verify the results of the simulated residual stresses and angular distortion regarding the distribution patterns and magnitudes due to change in the mechanical boundary conditions and welding sequence.

Measurement of angular distortion was fulfilled by using a 3D scanner before welding (for possible small deformation), and after the deposition of each fillet weld and reaching the ambient temperature for each case. Angular distortion was measured in the mid-section (half-way along the weld line) and in the transverse direction (perpendicular to the weld line) at the bottom side of the specimen (Path 5), as shown schematically in Fig. 14.

Transverse surface residual stresses on the top surface of FS1 and CS1 were measured at the mid-length of W1 (Path 1) and W4 (Path 4) to validate the simulation results using XRD by a Stresstech X3000 G3 device with a collimator diameter of 1 mm. The developed residual stresses for the other cases, and residual stresses along path 2 and path 3,

were studied from the results of the validated simulations.

#### 4.2.1. Angular distortion

Contours of angular distortion for FS1 and FS2 after removal of the clamps are shown in Fig. 15 (a) and 15 (b), respectively. Those for CS1 and CS2 after release from the external constraints are depicted in Fig. 16 (a) and 16 (b). As can be observed, the patterns of angular distortion (deflection in the Z-direction) for all the welding cases are similar. Through the comparison between Fig. 15 (a) and 16 (a), and Fig. 15 (b) and 16 (b), it can be understood that the external constraints at both ends slightly better prevented angular distortion compared to the clamping at one end after these constraints were removed.

In order to evaluate the accuracy of the FE simulations with regard to the effect of welding sequence and external restraints on angular distortion quantitatively, the sequential and cumulative angular distortions for FS1 and FS2 from the simulations and measurements (See Fig. 14 for the measurement path) are compared. For CS1 and CS2, due to the very small sequential distortions expected after each short weld (W1–W4), only the final angular distortions (after removal of the clamps) were measured experimentally, and the sequential distortions are discussed based on the numerical results. The results of the sequential angular distortions for FS1 and FS2 are shown in Fig. 17 (a) and (b), respectively. The simulated data are plotted with solid lines, while the measurement data are shown with circular marks. The simulated sequential angular distortions for CS1 and CS2, before release from the clamps are shown in Fig. 18 (a) and (b), respectively.

As can be seen in Fig. 17 (a) and (b), the distortion predictions by FE simulations are in reasonable agreements with the measurements. In almost all the cases, simulation overpredicts the angular distortion when compared to the experimental measurements. Both the simulation and measurement demonstrate that the final angular distortion produced in FS1 is slightly greater than that induced in FS2. For FS1, the experimental and simulated values are 3.95 and 4.61 mm, respectively, which makes a percent error of 16.7 %. In the same vein, the experimental and numerical values obtained for FS2 are 3.76 and 4.34 mm with a percent

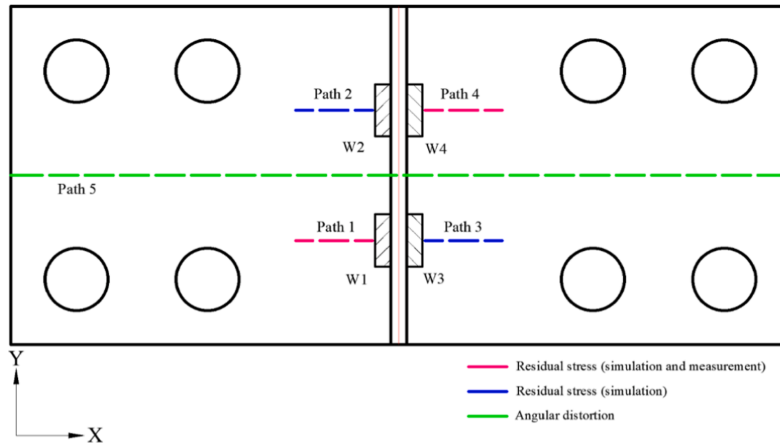


Fig. 14. Illustration of the measurement paths for angular distortion at the bottom surface, and residual stresses on the top surface.

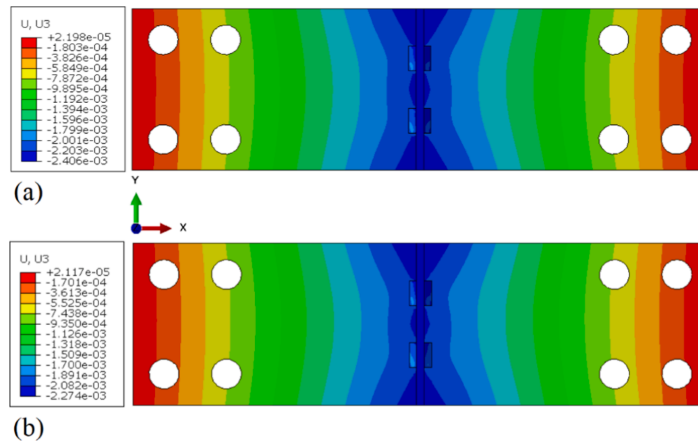


Fig. 15. Contours of the final angular distortion for: (a) FS1; and (b) FS2 (Units are in m).

error of 15.4 %. The final angular distortion in FS1 is approximately 6 % (from both the simulation and measurements) greater than that of FS2. Compared to the size of the specimen and final angular distortion, the difference is minor. Nevertheless, in practice where a large number of short fillet welds are required (based on the design), the difference due to a change in the welding sequence can be considerable. The same trend, i.e., a slightly greater angular distortion due to the welding sequence S1 compared to S2, can be seen in Fig. 18 (a) and (b). The simulated angular distortions for CS1 and CS2 in the clamped conditions are 0.51 and 0.48 mm, respectively. The angular distortion specific to each fillet weld (W1–W4) from the simulation and measurements for FS1 and FS2 are compared in Fig. 19 (a). The simulated angular distortions due to the deposition of the fillet welds (W1–W4) for CS1 and CS2 are shown in Fig. 19 (b). It should be noted that the values in Fig. 19 (b) refer to the situation when CS1 and CS2 were still in clamps. It can be seen in Fig. 19 (a), as was predicted by simulation and measurements, in both FS1 or FS2, W2 and W3, have the largest and the smallest shares in

the final angular distortion, respectively. The same trend respecting the shares of W2 and W3 in the total angular distortion, can be observed for CS1 and CS2 in the restrained conditions in Fig. 19 (b).

The effect of external constraints on the angular distortions induced in the studied cases, are evaluated by plotting the simulated angular distortions after removal of the clamps, as shown in Fig. 20. As was expected, clamping the specimen at one end permitted the development of angular distortion freely during the welding, and, therefore, releasing the related specimens after reaching the ambient temperature had no effect on the magnitude of the maximum angular distortion. For a higher degree of geometrical constraints, as experienced by CS1 and CS2, deformation is prevented during the welding by increasing plastic strains and reducing elastic strains. Elastic strains or locked-in stresses are responsible for the deformations after unclamping [17]. As the external constraints were removed, the remaining elastic strains were released partially as the specimen started to deform. As can be seen in Fig. 20, the smallest deformation obtained for the specimen which was

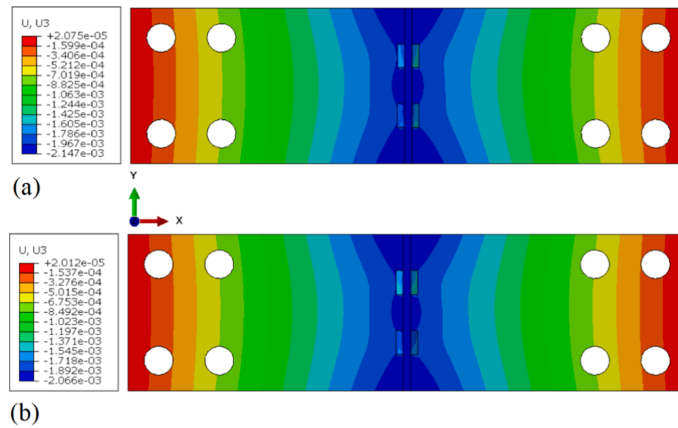


Fig. 16. Contours of the final angular distortion for: (a) CS1; and (b) CS2 (Units are in m).

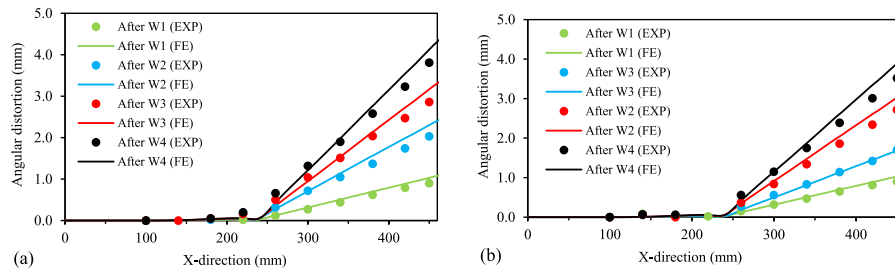


Fig. 17. The simulated versus the measured sequential angular distortions for: (a) FS1; and (b) FS2.

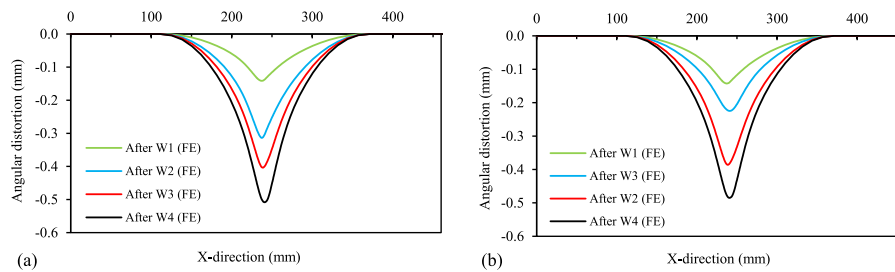


Fig. 18. The simulated sequential angular distortions in the restrained condition for: (a) CS1; and (b) CS2.

welded using sequence S2 and was clamped at both ends, while the largest angular distortion captured for the specimen being clamped only at one end and was welded using sequence S1. The results of simulations show that the angular distortion for FS1 is 9.2 % greater than that of CS1. In the same manner, the angular distortion for FS2 is 7.1 % larger than that for CS2. Based on the distortions due to the different welding sequences and external restraints, it can be understood that for this specimen configuration with a specified number of short fillet welds with a length of 20 mm each, the effect of the welding sequence is slightly smaller than that of the external constraints.

In order to compare the effect of clamping on angular distortion when short fillet weld changes to continuous fillet weld, for a similar specimen, a thermal simulation was performed. The simulation included deposition of the weld metal on both sides of the T-joint specimen in the same direction and with the same heat input being applied to the other cases in this study. The weld length on each side was approximately 122 mm. In the subsequent mechanical analyses, the two boundary conditions, which were previously used for the other welding cases, were applied. The results of the angular distortion after reaching the ambient temperature, before and after unclamping for the continuous and short



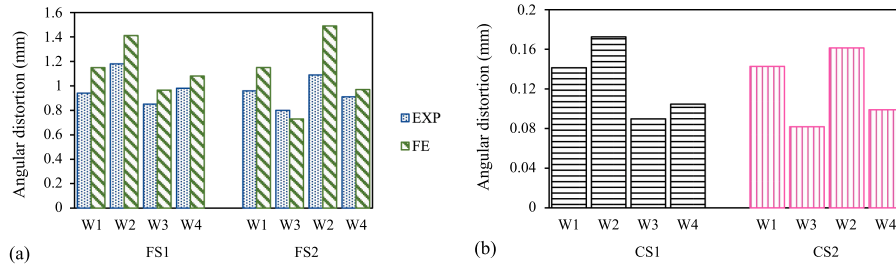


Fig. 19. The angular distortions developed due to each fillet weld: (a) from the simulation and measurements for FS1 and FS2; (b) from the simulation for CS1 and CS2.

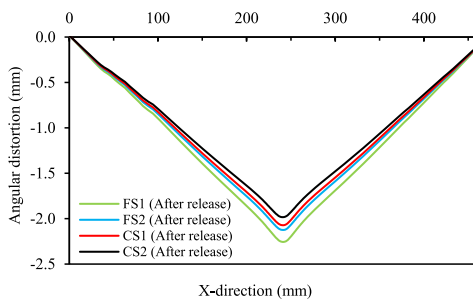


Fig. 20. The final angular distortions after unclamping of the specimens.

welds are shown in Fig. 21.

As can be seen in Fig. 21, in the case of continuous fillet welds, using higher degree external constraints could considerably reduce the final distortion by increasing plastic strain and reducing the remaining elastic strains. In the case of short fillet welds, however, adding more restraints, only slightly improved the distortion prevention. It can be understood that in the case of short fillet welds, adding more rigidity does not considerably reduce the angular distortion, and other distortion control techniques, such as applying pre-deformation can thus be considered.

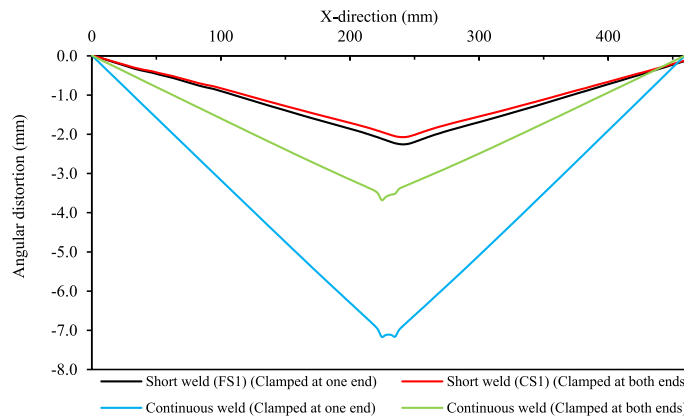


Fig. 21. The simulated final angular distortions for the cases with continuous welds and short fillet welds (FS1 and CS1).

#### 4.2.2. Transverse residual stress

In the current study, transverse residual stresses for FS1 and CS1 along the specified paths (see Fig. 14) were measured to validate the corresponding simulation results. The rest of the comparisons are drawn based on the validated FE models. The stress measurement paths on the top surface start at approximately 1 mm from the weld toe and are extended in the X-direction (almost 25 mm in length). It should be noted that in comparisons of residual stresses, path 1 and path 2 are considered in the negative direction of the X-axis, while path 3 and path 4 are shown in the positive direction of the X-axis. Fig. 22 shows the measured and simulated transverse stresses for FS1 after cooling down to ambient temperature. As can be seen in Fig. 22, the simulation results are in a relatively good agreement with the measurement data. It should be noted that XRD measurement data always fall within an error band which can be considerable in the FZ and HAZ and hence, the issue should be taken into account when comparing with simulation results. As moving from the weld toe in the X-direction, there exist regions of maximum tensile residual stress in the HAZ at 3–4 mm from the weld toes predicted by experimental measurements and simulation. Passing through the HAZ, the tensile residual stresses fall in magnitude rapidly. As clearly shown in Fig. 22, based on both the simulation and measurements, the peak tensile transverse stress due to the welding of W4 is considerably greater than that of W1. The measurement data demonstrate that the maximum tensile transverse stress due to W4 almost reaches the yield strength of the base material, while the peak residual stress predicted by simulation exceeds the yield strength of the base



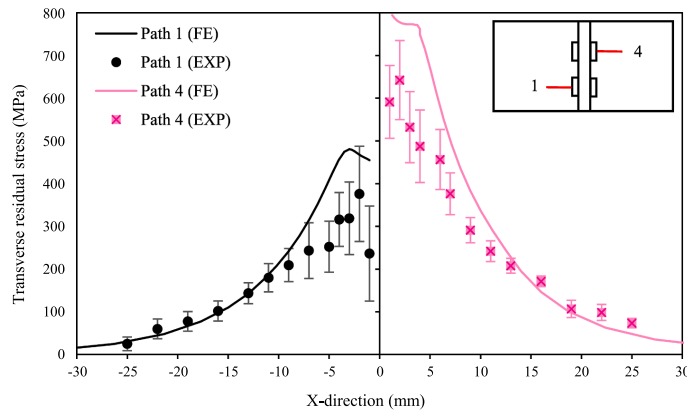


Fig. 22. Comparison of the measured and simulated transverse residual stresses for FS1 along path 1 and path 4.

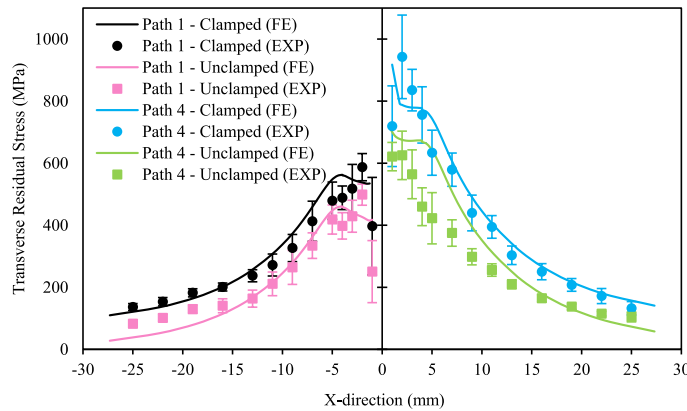


Fig. 23. Comparison of the measured and simulated transverse residual stresses for CS1 along path 1 and path 4, before and after unclamping.

plate slightly. For W1, the maximum tensile residual stress from both the simulation and measurement is approximately 480 MPa, which is almost 65 % of the yield strength of the base material.

In order to validate the results of the simulation regarding the effect of external constraints on the residual stress fields, the transverse residual stresses before and after removal of the external restraints for CS1 were measured and compared with those of the corresponding simulation, as shown in Fig. 23. As is observable in Fig. 23, the simulation results are in a relatively good agreement with the experimental data in terms of both the trend and peak magnitudes, before and after removal of the constraints. Along both paths, after removal of the constraints, tensile transverse stress fell in value. That is, the approximate peak tensile stress of 560 MPa in the clamped condition decreased to 480 MPa after unclamping for path 1. Along path 4, before removal of the constraints, the maximum tensile transverse stress can exceed 1000 MPa, which is considerably greater than the yield strength of the material. This matter is very important in practice such as intermittently fillet welded connections, where the joint must be welded in strict restraints and perform its service in the permanent external constraints. After removal of the clamps, however, the peak value decreased to yield

strength of the material. In this case, similar to FS1, the peak stress along path 4 is considerably greater than that of path 1, both before and after removal of the clamps.

The simulated transverse residual stresses along paths 1–4 for FS1 and FS2 are plotted in Fig. 24 to evaluate the residual stresses induced in the specimens due to each of the fillet welds W1–W4. The simulated transverse stresses for CS1 and CS2 in the clamped and unclamped conditions are shown in Fig. 25 (a) and Fig. 25 (b), respectively. As can be observed in Fig. 24, the residual stress field developed due to W1, has the lowest peak magnitude amongst the others, while the stress field resulting from the deposition of W4 experienced the greatest peak stress for both FS1 and FS2. In FS2, where W3 was deposited on side 2 before W2 on side 1, the peak magnitude in the stress field due to W3 is almost 55 MPa smaller than that in FS1. The peak value in the stress field due to W2 is approximately 75 MPa larger than that in FS1. The maximum tensile transverse stresses in FS2 along path 2 and path 3 are 529 and 680 MPa, respectively.

As can be seen in Fig. 25 (a) and (b), unclamping lowered the levels of transverse stress in an approximate range of 100–120 MPa for both CS1 and CS2, while it retained the distribution patterns similar to the

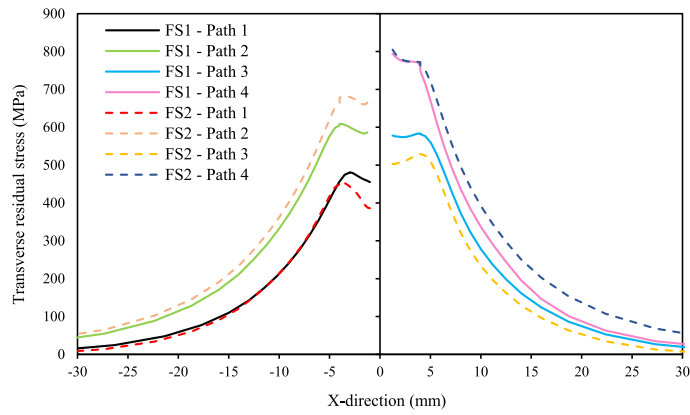
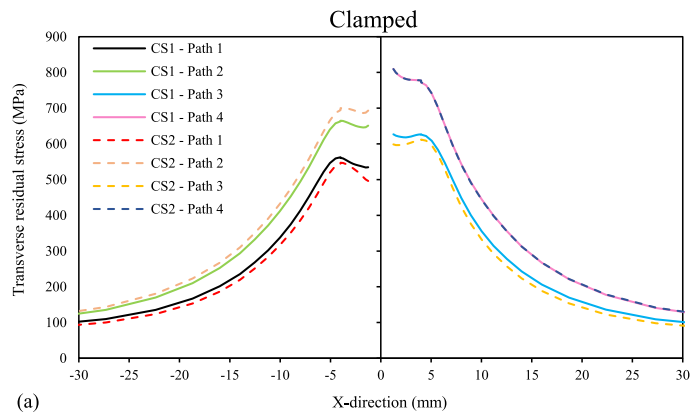
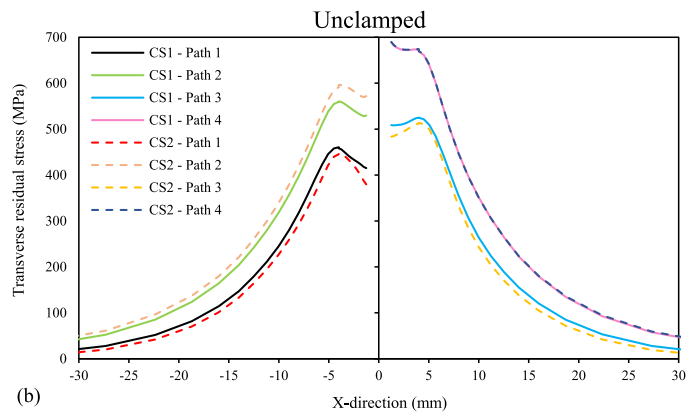


Fig. 24. The simulated transverse residual stresses for FS1 and FS2 along paths 1–4.



(a)



(b)

Fig. 25. The simulated transverse residual stresses for CS1 and CS2 along paths 1–4 for: (a) clamped; and (b) unclamped conditions.

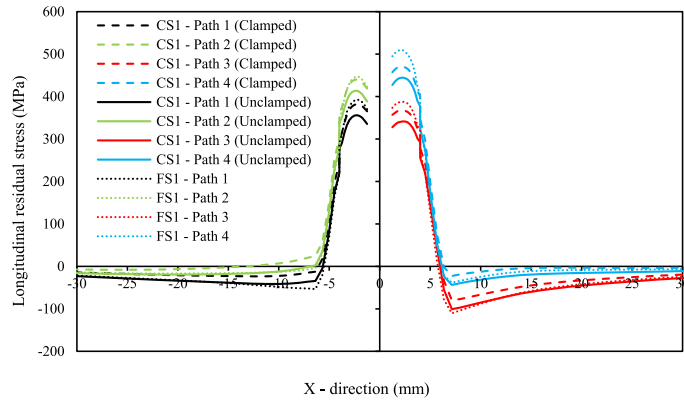


Fig. 26. The simulated longitudinal residual stresses for FS1 and CS1 starting at 1 mm from the weld toe along paths 1–4.

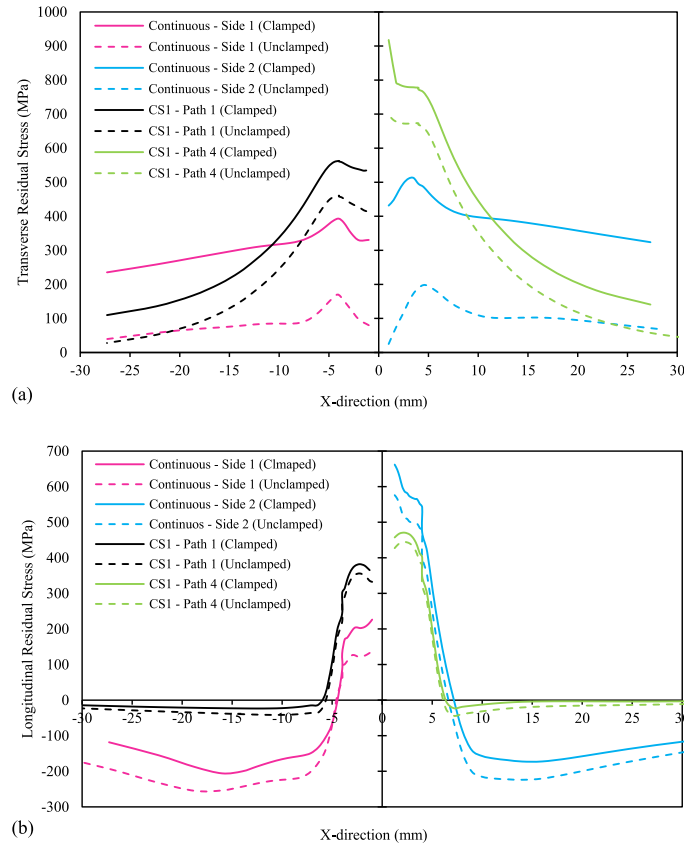


Fig. 27. Comparison between the cases with short and continuous fillet welds (rigidly clamped at both ends) in terms of: (a) Transverse stresses; and (b) longitudinal stresses.

clamped condition. In a comparison between CS1 and CS2, as can be seen, in CS1, the distribution of stress along path 1 has a slightly larger peak magnitude compared to that of CS2. In contrast to S1, when S2 was used, the peak stress along path 3 dropped from 525 to 511 MPa, while the peak magnitude along path 2, rose from 560 to 595 MPa. The distribution of transverse stress along path 4 for both CS1 and CS2 are almost identical.

#### 4.2.3. Longitudinal residual stress

The effect of clamping configuration on longitudinal residual stress was investigated by comparing the simulated longitudinal stress distributions for FS1 and CS1. As shown in Fig. 26, the maximum tensile longitudinal stress, which developed along path 4, is smaller than the maximum transverse stress (see Figs. 24 and 25 (a)) developed along the same path for both FS1 and CS1. As can be seen in Fig. 26, the rigid clamping at both ends produced stresses which were 35–60 MPa smaller compared to the clamping at one end when the specimen was released. The peak longitudinal stresses developed in FS1 along paths 1 and 2 are almost identical to those developed in the clamped CS1 along the same paths. Along path 3 and path 4, the stresses in FS1 were slightly greater than those in CS1 along the same paths. A comparison between the results plotted in Figs. 24 and 25 (a) with those in Fig. 26, indicates that in contrast to the longitudinal stress, the transverse one is more sensitive to the stiffness of the external constraints.

The simulated transverse and longitudinal stresses in one of the cases, CS1 as an example, are compared with those in a double-sided fillet welded T-joint with the similar welding parameters and mechanical boundary conditions. The length of the deposited filler material on each side of the continuous fillet weld case was approximately 122 mm. For CS1, the transverse residual stresses are plotted along paths 1 and 4, and for the continuous case, the stresses are plotted along the two paths perpendicular to the welding direction in the mid-section of the specimen on the top surface on side 1 and side 2, as shown in Fig. 27 (a). In the same vein, the longitudinal stresses are plotted in Fig. 27 (b). Regarding the rigid clamping at both ends, which implies a high restraining stiffness, as can be seen in Fig. 27 (a), transverse residual stresses being induced in the continuous fillet weld case are more sensitive to unclamping than those in the short fillet weld case. That is, after removal of the clamps, release of the transverse residual stresses in the continuous fillet weld case are more considerable than the other case. The peak magnitudes of tensile transverse stresses and the gradient of decrease as moving away from the weld toe, in both the clamped and unclamped conditions, for the short fillet welds are significantly greater than those for the continuous case, which indicates the localized stress fields with larger peak magnitudes near the short fillet welds.

As can be seen in Fig. 27 (b), with using high degree mechanical boundary conditions, longitudinal stress of the continuous fillet weld case is more sensitive to the removal of the clamps compared to the short fillet weld case. Longitudinal stress, however, is less sensitive to the removal of the rigid clamps at both ends, compared to transverse stress. The fall of the longitudinal stresses as moving away from the HAZ, for both the continuous and short fillet welds occurs approximately with the same slope, however, the case with continuous welds experienced greater peak magnitudes of compressive longitudinal stresses than the case with short welds.

## 5. Conclusions and future work

Simulations of the temperature field, residual stress and angular distortion for the short fillet welds made from S700 were performed by developing three-dimensional FE models in ABAQUS FE code. Two welding sequences and two mechanical boundary conditions were considered in the simulations to study the effect of external restraints and welding sequence on development of angular distortion and residual stresses. The numerical approach was validated through conducting experimental measurements of temperature field, angular distortion and

transverse residual stress. A series of comparisons were also made between the cases of continuous and short fillet welds with respect to the temperature field, residual stress and angular distortion. Based on the experimental measurements and numerical results, the following conclusions are made:

- (1) The experimental measurement data are in a relatively good agreement with the results of the simulations for temperature fields, angular distortion and transverse residual stresses. It can be concluded that the developed computational approach is able to capture the distributions of the welding residual stresses and angular distortion with acceptable accuracy.
- (2) Both the measurement and simulation show that the welding sequence S2 resulted in slightly smaller angular distortion compared to S1 for both of the clamping configurations.
- (3) In this study, the external constraints had more influence on the angular distortion than the welding sequence. Using rigid clamping at both ends can significantly prevent angular distortion in continuous fillet welds. For the short fillet welds, using rigid clamping at both ends had a smaller effect on controlling of angular distortion compared to the continuous fillet welds. This matter shows that in practice, controlling of angular distortion due to short fillet welds, apart from using a rigid clamping requires other techniques, such as applying pre-deformations.
- (4) The peak stress can easily exceed the yield strength of the material for some of the short fillet welds, especially when clamps with high restraining stiffness are used. In practical applications, this issue should be considered for intermittently fillet welded joints and avoid producing short welds where dynamic loads are introduced, as the high tensile residual stresses can contribute to premature failures, such as fatigue failure.
- (5) In short fillet welds, longitudinal residual stress is less sensitive to removal of the rigid clamps than transverse stress. Transverse stress in short fillet welds compared to continuous welds, is less sensitive to the removal of the rigid clamps with high restraining stiffness.
- (6) In the stress fields due to each short fillet weld, the differences between peak longitudinal stress magnitudes are smaller than those related to transverse stress. Passing through the HAZ, the gradient of decrease in the longitudinal stress for the short and continuous welds are very similar. Transverse stresses in the short fillet welds, however, have considerably sharper gradients of fall than the continuous fillet welds as moving from the weld toe towards the outer edges.

It was observed in the results that, as the length of the weld decreases, the cooling rate increases. This matter, depending on the steel type, can have a significant impact on the microstructure of the near-weld regions. It is of interest to investigate the effects of the weld length and leg size and consequently cooling rate on the microstructure and deformation patterns of different ultra-high strength steel grades being manufactured with different processes. The aim of this work was to investigate HSSs, and thus the findings of the study are principally limited to these steel grades. However, a future study might also investigate the effect of material strength level on development of residual stresses and distortions in short fillet welds.

#### CRediT authorship contribution statement

**Mehran Ghafouri:** Conceptualization, Methodology, Software, Validation, Writing – original draft, Visualization. **Antti Ahola:** Methodology, Writing – review & editing. **Joseph Ahn:** Methodology, Software, Writing – review & editing. **Timo Björk:** Conceptualization, Writing – review & editing, Supervision, Funding acquisition.

### Declaration of Competing Interest

The authors declare that they have no known competing financial interests or personal relationships that could have appeared to influence the work reported in this paper.

### Acknowledgements

This research was funded by "Finnish Foundation for Technology Promotion" and "Business Finland" (formerly TEKES) in the DigRob research project. The support of SSAB Europe is acknowledged.

## Appendix A

### A.1. Residual stress components

Distribution of residual stress, in general, comprises both tensile and compressive stresses whose magnitude might reach the yield strength of the material. Distribution, peak magnitude and location of residual stresses, to a great extent, depend on the welding process, external restraints, material properties and geometry of the joint. In the fields of fatigue and fracture mechanics evaluation of welded joints, which are vital topics in structural integrity assessment, the knowledge of residual stress distribution is required. For structural integrity assessment, residual stresses can be generalized based on some invariant features. One technique also known as stress decomposition technique, is used to decompose residual stresses through the thickness. Once distribution of transverse residual stresses over the thickness is available, based on either experimental measurements or FE simulation, residual stress is decomposed into membrane, bending and self-equilibrating stress components, which are described by Eq. (A.1), Eq. (A.2), and Eq. (A.3), respectively:

$$\sigma_{res,m} = \frac{1}{t} \int_0^t \sigma_{res,x}(z) dz \quad (A.1)$$

$$\sigma_{res,b} = \frac{6}{t^2} \int_0^t [\sigma_{res,x}(z) - \sigma_{res,m}] \left( \frac{t}{2} - z \right) dz \quad (A.2)$$

$$\sigma_{res,se} = \sigma_{res,x} - \sigma_{res,m} - \sigma_{res,b} \left( 1 - \frac{2z}{t} \right) \quad (A.3)$$

where  $\sigma_{res,m}$ ,  $\sigma_{res,b}$ , and  $\sigma_{res,se}$  are membrane, bending and self-equilibrating components, respectively.  $t$  is material thickness and  $\sigma_{res,x}(z)$  is the transverse residual stress in the Z-direction (through thickness). This decomposition technique was applied to CS1 on both sides at the weld toe, and performing integration over the weld length, where  $z = 0$  is on the top surface and  $z = t$  is on the bottom surface of the specimen. The results regarding the membrane and bending stress components for the clamped and unclamped conditions are shown in Fig. A.1. In addition, Fig. A.1 includes the results of residual stress components for a similar joint being welded continuously over the length of the joint on both sides, where both weld passes were in the same directions.

As can be seen in Fig. A.1, in the case of short welds, and in the clamped conditions, both membrane and bending stress components are high tensile stresses in the location of welds which tend to become compressive in the regions where no welding was performed. The peak tensile stresses of membrane and bending components in short welds are comparably higher than those in continuous welds, which implies that in the case short fillet welds residual stress field is highly localized and dimensionally smaller than those in continuous fillet welds, while the peak magnitudes are comparably larger than those of continuous welds. For example, on side 1 and in the clamped condition, based on Eq. (A.1) and Eq. (A.2), the

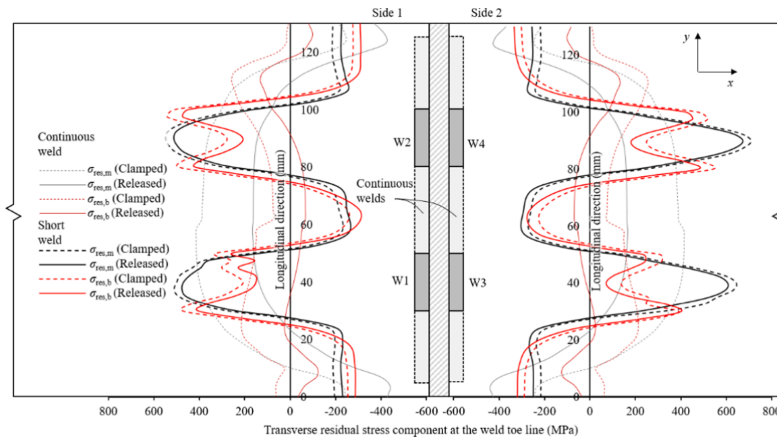


Fig. A1. Membrane and bending components calculated for CS1 at the weld toe in the clamped and released conditions.

membrane and bending stress components of short welds have the peak magnitudes of +547 MPa and +541 MPa, respectively, while these magnitudes for continuous case are +495 MPa and +195 MPa. Provided that the average value over the length of the joint is considered, the membrane and bending stress components for short and continuous welds become +162 MPa, +158 MPa, +238 MPa and +136 MPa, respectively. After removal of the clamps, as can be seen in Fig. A.1, release of both membrane and bending residual stresses in short fillet welds has been done in a smaller extent compared to the continuous fillet welds. The averaged values of membrane and bending components over the length of the joint after release from the clamping in short and continuous welds are +125 MPa, +99 MPa, −7 MPa and −17 MPa, respectively. As can be seen, removal of the clamps had a smaller effect on the residual stress field in short fillet welds than in continuous fillet welds.

The stress decomposition technique presented in this section, which uses the results of the FE welding simulation, is applicable in assessment of the stability of plate components and study of the behavior of crack growth under the influence of an unequal residual stress field, and it can help to estimate the stress intensity factor due to residual stresses [47,48].

## References

- [1] Conejo AN, Birat J-P, Dutta A. A review of the current environmental challenges of the steel industry and its value chain. *J Environ Manage* 2020;259:109782.
- [2] Guo W, Crowther D, Francis JA, Thompson A, Liu Z, Li L. Microstructure and mechanical properties of laser welded S960 high strength steel. *Mater Des* 2015;85:534–48. <https://doi.org/10.1016/j.matdes.2015.07.037>.
- [3] Liang W, Deng D. Influences of heat input, welding sequence and external restraint on twisting distortion in an asymmetrical curved stiffened panel. *Adv Eng Softw* 2018;115:439–51. <https://doi.org/10.1016/j.advengsoft.2017.11.002>.
- [4] Skriko T, Ghafouri M, Björk T. Fatigue strength of TIG-dressed ultra-high-strength steel fillet weld joints at high stress ratio. *Int J Fatigue* 2017;94:110–20. <https://doi.org/10.1016/j.jfatigue.2016.09.018>.
- [5] Deng D, Liu X, He J, Liang W. Investigating the influence of external restraint on welding distortion in thin-plate bead-on joint by means of numerical simulation and experiment. *Int J Adv Manuf Technol* 2016;82(5–8):1049–62.
- [6] Barsoum Z, Lundback A. Simplified FE welding simulation of fillet welds - 3D effects on the formation residual stresses. *Eng Fail Anal* 2009;16(7):2281–9. <https://doi.org/10.1016/j.engfailanal.2009.03.018>.
- [7] Barsoum Z, Barsoum I. Residual stress effects on fatigue life of welded structures using LEM. *Eng Fail Anal* 2009;16(1):449–67. <https://doi.org/10.1016/j.engfailanal.2008.06.017>.
- [8] Cui C, Zhang Q, Bao Y, Bu Y, Luo Y. Fatigue life evaluation of welded joints in steel bridge considering residual stress. *J Constr Steel Res* 2019;153:509–18. <https://doi.org/10.1016/j.jcsr.2018.11.003>.
- [9] Jiang W, Xie X, Wang T, Zhang X, Tu S-T, Wang J, et al. Fatigue life prediction of 316L stainless steel weld joint including the role of residual stress and its evolution: Experimental and modelling. *Int J Fatigue* 2021;143:105997.
- [10] Heinze C, Schwenk C, Rethmeier M. Numerical calculation of residual stress development of multi-pass gas metal arc welding. *J Constr Steel Res* 2012;72:12–9. <https://doi.org/10.1016/j.jcsr.2011.08.011>.
- [11] Deng D. FEM prediction of welding residual stress and distortion in carbon steel considering phase transformation effects. *Mater Des* 2009;30(2):359–66. <https://doi.org/10.1016/j.matdes.2008.04.052>.
- [12] Liang W, Hu X, Zheng Y, Deng D. Determining inherent deformations of HSLA steel T-joint under structural constraint by means of thermal elastic plastic FEM. *Thin-Walled Struct* 2020;147:106568. <https://doi.org/10.1016/j.tws.2019.106568>.
- [13] Ma N, Cai Z, Huang H, Deng D, Murakawa H, Pan J. Investigation of welding residual stress in flash-butt joint of U71Mn rail steel by numerical simulation and experiment. *Mater Des* 2015;88:1296–309. <https://doi.org/10.1016/j.matdes.2015.08.124>.
- [14] Wu J, Qiang B, Liao X, Kang L, Yao C, Li Y. Experimental investigation and numerical simulation of welding residual stress in orthotropic steel deck with diaphragm considering solid-state phase transformation. *Eng Struct* 2022;250:113415.
- [15] Rikken M, Pijpers R, Slot H, Maljaars J. A combined experimental and numerical examination of welding residual stresses. *J Mater Process Technol* 2018;261:98–106. <https://doi.org/10.1016/j.jmatprotec.2018.06.004>.
- [16] Ghafouri M, Ahn J, Mounirjari J, Björk T, Larkola J. Finite element simulation of welding distortions in ultra-high strength steel S960 MC including comprehensive thermal and solid-state phase transformation models. *Eng Struct* 2020;219:110804. <https://doi.org/10.1016/j.engstruct.2020.110804>.
- [17] Ahn J, He E, Chen L, Pirling T, Dear JP, Davies CM. Determination of residual stresses in fibre laser welded AA2024-T3 T-joints by numerical simulation and neutron diffraction. *Mater Sci Eng, A* 2018;712:685–703. <https://doi.org/10.1016/j.msea.2017.12.027>.
- [18] Hemmes K, Farajian M, Boin M. Numerical studies of welding residual stresses in tubular joints and experimental validations by means of x-ray and neutron diffraction analysis. *Mater Des* 2017;126:339–50. <https://doi.org/10.1016/j.matdes.2017.03.088>.
- [19] Jiang W, Chen W, Woo W, Tu ST, Zhang XC, Em V. Effects of low-temperature transformation and transformation-induced plasticity on weld residual stresses: Numerical study and neutron diffraction measurement. *Mater Des* 2018;147:65–79. <https://doi.org/10.1016/j.matdes.2018.03.032>.
- [20] Wan Yu, Jiang W, Song M, Huang Y, Li J, Sun G, et al. Distribution and formation mechanism of residual stress in duplex stainless steel weld joint by neutron diffraction and electron backscatter diffraction. *Mater Des* 2019;181:108086.
- [21] Sun J, Liu X, Tong Y, Deng D. A comparative study on welding temperature fields, residual stress distributions and deformations induced by laser beam welding and CO2 gas arc welding. *Mater Des* 2014;63:519–30. <https://doi.org/10.1016/j.matdes.2014.06.057>.
- [22] Lee C-H, Chang K-H. Prediction of residual stresses in high strength carbon steel pipe weld considering solid-state phase transformation effects. *Comput Struct* 2011;89(1–2):256–65. <https://doi.org/10.1016/j.compstruc.2010.10.005>.
- [23] Jin D, Hou C, Shen L. Effect of welding residual stress on the performance of CFSF tubular joints. *J Constr Steel Res* 2021;184:106827.
- [24] Evdokimov A, Doynov N, Ossenbrink R, Obrosova A, Weiß S, Michailov V. Thermomechanical laser welding simulation of dissimilar steel-aluminum overlap joints. *Int J Mech Sci* 2021;190:106019.
- [25] Ahn J, He E, Chen L, Wimpory RC, Dear JP, Davies CM. Prediction and measurement of residual stresses and distortions in fibre laser welded Ti-6Al-4V considering phase transformation. *Mater Des* 2017;115:441–57. <https://doi.org/10.1016/j.matdes.2016.11.078>.
- [26] Danis V, Lacoste E, Arvieu C. Numerical modeling of inconel 738LC deposition welding: Prediction of residual stress induced cracking. *J Mater Process Technol* 2010;210(14):2053–61. <https://doi.org/10.1016/j.jmatprotec.2010.07.027>.
- [27] Yaghi AH, Hyde TH, Becker AA, Sun W, Wen Wu, Hilson G, et al. Comparison of measured and modelled residual stresses in a welded P91 steel pipe undergoing post weld heat treatment. *Int J Press Vessel Pip* 2020;181:104076.
- [28] Hu X, Feng G, Wang Y, Zhang C, Deng D. Influence of lumping passes on calculation accuracy and efficiency of welding residual stress of thick-plate butt joint in boiling water reactor. *Eng Struct* 2020;222:111136. <https://doi.org/10.1016/j.engstruct.2020.111136>.
- [29] Deng D, Liang W, Murakawa H. Determination of welding deformation in fillet-welded joint by means of numerical simulation and comparison with experimental measurements. *J Mater Process Technol* 2007;183(2–3):219–25.
- [30] Khedmati MR, Rastani M, Ghavami K. Numerical study on the permissible gap of intermittent fillet welds of longitudinally stiffened plates under in plane axial compression. *J Constr Steel Res* 2007;63(10):1415–28.
- [31] Perić M, Tonković Z, Rodić A, Surjak M, Garašić I, Boras I, et al. Numerical analysis and experimental investigation of welding residual stresses and distortions in a T-joint fillet weld. *Mater Des* 2014;53:1052–63.
- [32] Zhang Y, Wang Y. The influence of welding mechanical boundary condition on the residual stress and distortion of a stiffened-panel. *Mar struct* 2019;65:259–70. <https://doi.org/10.1016/j.marstruc.2019.02.007>.
- [33] Fu G, Lourenco MI, Duan M, Estefen SF. Effect of boundary conditions on residual stress and distortion in T-joint welds. *J Constr Steel Res* 2014;102:121–35. <https://doi.org/10.1016/j.jcsr.2014.07.008>.
- [34] Ghafouri M, Ahola A, Ahn J, Björk T. Welding-induced stresses and distortion in high-strength steel T-joints: Numerical and experimental study. *J Constr Steel Res* 2022;189:107088.
- [35] ABAQUS user's manual, Version; 2020.
- [36] Goldak J, Chakravarti A, Bibby M. A new finite element model for welding heat sources. *Metall Trans B* 1984;15(2):299–305. <https://doi.org/10.1007/BF02667333>.
- [37] Siltanen J, Tihinen S, Kömi J. Laser and laser gas-metal-arc hybrid welding of 960 MPa direct-quenched structural steel in a butt joint configuration. *J Laser Appl* 2015;27:S29007. <https://doi.org/10.2351/1.4906386>.
- [38] Deng D, Murakawa H, Liang W. Numerical simulation of welding distortion in large structures. *Comput Methods Appl Mech Eng* 2007;196(45–48):4613–27.
- [39] Shen J, Chen Z. Welding simulation of fillet-welded joint using shell elements with section integration. *J Mater Process Technol* 2014;214(11):2529–36.
- [40] Seles K, Perić M, Tonković Z. Numerical simulation of a welding process using a prescribed temperature approach. *J Constr Steel Res* 2018;145:49–57. <https://doi.org/10.1016/j.jcsr.2018.02.012>.
- [41] Bhatti AA, Barsoum Z, Murakawa H, Barsoum I. Influence of thermo-mechanical material properties of different steel grades on welding residual stresses and angular distortion. *Mater Des* 2015;65:878–89. <https://doi.org/10.1016/j.matdes.2014.10.019>.
- [42] Brickstad B, Josefson BL. A parametric study of residual stresses in multi-pass butt-welded stainless steel pipes. *Int J Press Vessel Pip* 1998;75(1):11–25. [https://doi.org/10.1016/S0308-0161\(97\)00117-8](https://doi.org/10.1016/S0308-0161(97)00117-8).
- [43] Yaghi A, Hyde TH, Becker AA, Sun W, Williams JA. Residual stress simulation in thin and thick-walled stainless steel pipe welds including pipe diameter effects. *Int J Press Vessel Pip* 2006;83(11–12):864–74. <https://doi.org/10.1016/j.ijpvp.2006.08.014>.
- [44] Ferro P, Berto F, Bonollo F, Tang K. Does metallurgy affect the residual notch stress intensity factor value induced by welding operations? A comprehensive study via a 3D numerical model. *Int J Fatigue* 2021;149:106261.

- [45] Björk T, Ahola A, Tuominen N. On the design of fillet welds made of ultra-high-strength steel. *Weld World* 2018;62(5):985–95.
- [46] Amraei M, Ahola A, Afkhami S, Björk T, Heidarpour A, Zhao X-L. Effects of heat input on the mechanical properties of butt-welded high and ultra-high strength steels. *Eng Struct* 2019;198:109460. <https://doi.org/10.1016/j.engstruct.2019.109460>.
- [47] Bhardwaj S, Chandima Ratnayake RM. Residual stress estimation in defect assessment procedures at weld toe and away locations on girth welds: Review of key parameters. *Theor Appl Fract Mech* 2021;111:102848.
- [48] Dong P. Length scale of secondary stresses in fracture and fatigue. *Int J Press Vessel Pip* 2008;85(3):128–43.

## **Publication IV**

Ghafouri, M., Amraei, M., Pokka, A. P., Björk, T., Larkiola., J., Piili, H., and Zhao, X. L.

**Mechanical properties of butt-welded ultra-high strength steels at elevated temperatures**

Reprinted with permission from  
*Journal of Constructional Steel Research*  
Vol. 198, p. 107499, 2022  
© 2022, Elsevier







Contents lists available at ScienceDirect

## Journal of Constructional Steel Research

journal homepage: [www.elsevier.com/locate/jcsr](http://www.elsevier.com/locate/jcsr)

## Mechanical properties of butt-welded ultra-high strength steels at elevated temperatures

Mehran Ghafouri<sup>a</sup>, Mohsen Amraei<sup>b,\*</sup>, Aki-Petteri Pokka<sup>c</sup>, Timo Björk<sup>a</sup>, Jari Larkiola<sup>c</sup>, Heidi Piili<sup>b</sup>, Xiao-Lin Zhao<sup>d</sup><sup>a</sup> Laboratory of Steel Structures, School of Energy Systems, LUT University, P.O. Box 20, 53851 Lappeenranta, Finland<sup>b</sup> Department of Mechanical and Materials Engineering, University of Turku, Turku 20520, Finland<sup>c</sup> Materials and Production Engineering, Faculty of Technology, University of Oulu, P.O. Box 4200, 90570 Oulu, Finland<sup>d</sup> Department of Civil and Environmental Engineering, The Hong Kong Polytechnic University, Hong Kong, China

## ARTICLE INFO

## Keywords:

Ultra-high strength steel  
Welded joints  
GMAW  
Mechanical properties  
Elevated temperature  
Fire-resistance design

## ABSTRACT

Variety of ultra-high strength steels (UHSS) with different microstructural characteristics is becoming available with continuous development of the manufacturing process in the steel industries. In order to effectively design structures made of such steel grades, a detailed knowledge of the mechanical properties is vital. Fire safety design is one of the areas in which such knowledge is essential. Welding process is indispensable in construction of steel structures with inevitable welding-induced degradation of mechanical properties of UHSSs. Thus, conducting experimental research on elevated-temperature constitutive mechanical behavior of welded joints made of UHSSs is of paramount importance. This study addresses elevated-temperature mechanical properties of as-received and as-welded S960 (manufactured via direct quenching technique) and S1100 (quenched and tempered) steel grades. A fully automated gas metal arc welding (GMAW) process with low heat input value was utilized to join the steel plates. Next, steady-state uniaxial tensile tests in the temperature range between room temperature (RT) and 900 °C were carried out. Accordingly, reduction factor-temperature relations for each tested steel in both as-received and as-welded forms are discussed and compared with several design standards, as well as with previous studies in the literature. Finally, predictive equations are proposed to estimate the elevated-temperature mechanical properties reduction factors of the tested UHSSs in as-received and as-welded forms.

## 1. Introduction

Steels with different degrees of strength have been used during the past decades in various applications, such as the automotive industry, construction of large-span bridges, and skyscrapers all around the globe. Less exploitation of natural resources and energy-saving trends in recent years from one side and demand of fast-growing technology from the other side have triggered the invention and development of high and ultra-high strength steels (HSS/UHSS). These materials offer a superb combination of load-bearing capacity and high strength-to-weight ratio combined with good weldability, which makes them highly useful in a variety of industrial applications [1–5]. In the field of construction and structural engineering, application of HSS and UHSS can lead to environmental and socioeconomic benefits: decreasing material consumption via obtaining smaller cross-sectional size in design, saving labor and

costs related to fabrication and transportation, as well as reducing carbon emission [3,6].

In the field of construction, fusion welding processes and particularly conventional arc welding techniques have been frequently applied to make permanent joints between structural members and components made of UHSSs due to their cost-effectiveness, versatility and reliability [7–9]. However, since UHSS is manufactured in a controlled heating and cooling process resulting in a certain microstructural characteristic, the welding thermal cycles can deteriorate the desired microstructure [10]. The research on welded UHSS is mainly focused on GMAW [11,12] and laser welding (LW) [10,13]. Some detrimental phenomena are attributed to tremendous heat input from the welding processes (GMAW for example has higher level of heat input compared to LW), such as strength reduction (under fatigue and tensile loads) due to the softened heat-affected zone (HAZ). Skriko et al. [14] found that TIG-dressing of T-

\* Corresponding author.

E-mail address: [Mohsen.amraei@utu.fi](mailto:Mohsen.amraei@utu.fi) (M. Amraei).<https://doi.org/10.1016/j.jcsr.2022.107499>

Received 19 May 2022; Received in revised form 6 August 2022; Accepted 9 August 2022

Available online 9 September 2022

0143-974X/© 2022 The Authors. Published by Elsevier Ltd. This is an open access article under the CC BY license (<http://creativecommons.org/licenses/by/4.0/>).

joints made of S960 causes significant softening in the fusion line and HAZ, which has negative effects on fatigue strength of the joint. According to the literature, the tensile strength reduction at the softened HAZ can reach as high as 60% [10,13,15,16]. Hence, great attention should be paid to the design of welded connections made of UHSSs.

Fire can be mentioned as among the most, if not the most, prominent catastrophic incidents to which structures are vulnerable, which can result in structural failure, followed by extreme consequences such as human fatalities, economic loss and environmental pollution [4,6,17–20]. Fire-safe designs and assessing the performance of steel structures made of HSSs and UHSSs exposed to fire conditions necessitate a profound understanding of constitutive behavior of such materials at elevated temperatures. Numerous research efforts have been hitherto conducted to investigate the mechanical properties of steels at elevated temperatures and post-fire mainly on mild steels [21,22].

Existing models in leading design standards such as Eurocode 3 (EC3) [23] for constitutive behavior of steels at elevated temperatures are generally based on reduction factors for mechanical properties including elastic modulus, yield strength and ultimate tensile strength. These models, however, have been developed based on the results for mild steels, and adoption of those code models for estimating the mechanical properties of HSSs and UHSSs at elevated temperatures is still questionable. Due to lack of recommendations for HSSs and UHSSs in the current design codes and urgent need for assessing the degradation of mechanical properties of HSSs and UHSSs in fire and post-fire conditions, several research studies have been conducted [4,6,17,24–28]. Qiang et al. [26] studied mechanical properties of S960QL (manufactured via quenched and tempered process) in fire conditions by conducting steady and transient hot tensile tests in the temperature range 20–700 °C. Characteristic strengths obtained from their tests were compared with different leading design standards. Their results revealed that none of the proposed models by design codes can be used for accurate prediction of mechanical properties of their UHSS at elevated temperatures. They concluded that degradation of mechanical properties of HSSs and UHSSs at elevated temperatures is contingent upon steel grade and manufacturing process. Neuenchwander et al. [4] conducted extensive comparative research on deterioration of mechanical properties of S690QL and S960QL at different strain rates under steady-state and transient conditions at temperatures 20 °C–900 °C. Comparing their results in the case of HSSs with grades below S700 with EC3, they showed that the Eurocode predictive model for elastic modulus and effective yield strength at 2% total strain at elevated temperatures is overconservative and nonconservative, respectively. For UHSSs with grades above S700, they noted the necessity of more experimental research to conclusively assess the adoptability of the EC3 model for prediction of mechanical properties at elevated temperatures.

Although there has been some research on deterioration of mechanical properties of HSSs and UHSSs at elevated temperatures in the context of fire-safe designs, only a few studies focused on steel grades above 900 MPa [4,26,29,30]. These researchers, however, conducted their experiments on quenched and tempered UHSSs; direct-quenched steels were not included in their investigations. As has been reflected in the literature [17], mechanical properties of UHSSs at elevated temperatures are highly dependent on chemical composition, especially carbon content and manufacturing process, which necessitates conducting research on UHSSs with different manufacturing processes. More importantly, elevated-temperature mechanical properties of welded joints made of UHSSs have not been investigated thus far. Inasmuch as welding is indispensable in construction of steel structures, and degradation of mechanical properties of UHSSs is inevitable due to welding [10], conducting experimental research on elevated-temperature constitutive mechanical behavior of welded joints made of UHSSs is of paramount importance. Such research contributes to provide scientific background to improve code models and scrutinize the suitability of adopting those predictive models for UHSSs.

This study fills the knowledge gap in understanding elevated-

temperature mechanical properties of as-received and as-welded ultra-high strength steel by including two UHSSs not covered in the literature, namely S960MC (manufactured via direct quenching technique) and S1100 (quenched and tempered) steel grades. In this regard, four sets of specimens were prepared, and steady-state tensile tests in the temperature range RT–900 °C were carried out. For each specimen elastic modulus, effective yield strength at 0.2% strain level and ultimate tensile strength are obtained from stress-strain curve at corresponding temperature. Accordingly, reduction factor-temperature relations for each tested steel in both as-received and as-welded forms are discussed and compared with some leading design standard predictive models, such as the EC3, the American Institute of Steel Construction (AISC) [31], and the Australian Standard AS4100 [32]. Moreover, comparison of the results with the existing literature for different grades of HSS/UHSSs, such as S460N (normalized rolled delivery condition) [33], S700MC (thermomechanically rolled delivery condition) [17] and S960QL [4,26] is also performed. Finally, this paper further extends the knowledge through establishing predictive equations to safely estimate the elevated-temperature elastic modulus, 0.2% proof stress, and ultimate tensile strength reduction factors of the tested steels in both as-received and as-welded forms. In addition, comparisons between the proposed equations and the above-mentioned design code models are drawn.

## 2. Materials and experimental procedure

### 2.1. Materials

The base materials (BMs) considered for this study were S960MC and S1100 UHSS alloys with low carbon contents. As-received S960MC was manufactured by modern hot rolling and direct quenching processes [34], while the S1100 grade was manufactured by the quenching and tempering process [16]. Both steel alloys were received from 8 mm thick hot rolled strips. The chemical compositions (wt%) of the two steel grades according to the manufacturer's certificates are listed in Table 1.

The carbon equivalent (CEV) in Table 1 is calculated using the following equation:

$$CEV = C + \frac{Mn}{6} + \frac{Cr + Mo + V}{5} + \frac{Ni + Cu}{15} \quad (1)$$

The nominal mechanical properties of the studied steels are presented in Table 2.

The effects of elevated temperatures on the constitutive mechanical properties (i.e. elastic modulus, 0.2% proof and ultimate tensile stress) of butt-welded UHSSs were studied in this paper. The GMAW process which is commonly used to join UHSSs, was applied to achieve this aim [10,35]. Due to softening effect at the weld HAZ, especially in direct-quenched (DQ) UHSSs, welding parameters were chosen so that heat input (HI) level falls in an optimum range as recommended in the literature [10,36]. The specimens were allowed to cool down to room temperature between each weld pass. Similar welding parameters were utilized for both steel alloys as shown in Table 3. In order to achieve high quality and consistency in welding, a fully automated process using a robot arm was used.

The applied HI due to the welding was calculated according to Eq. (2):

$$Q = U \times I \times \eta / (\nu \times 1000) \text{ (kJ/mm)} \quad (2)$$

where  $Q$  is heat input,  $U$  voltage,  $I$  electric current,  $\eta$  welding efficiency coefficient, and  $\nu$  travel speed of the welding torch. Considering a welding efficiency coefficient of 0.8 for the GMAW process, a net HI value of 0.7 kJ/mm was calculated, which lies in the permitted range for the two steel grades.

The filler material used in the GMAW process was Böhler Union X96 solid wire. The nominal yield and ultimate tensile strength of the filler

**Table 1**

The nominal chemical composition of BMs (wt%).

Steel	C	Si	Mn	P	S	V	Cu	Cr	Ni	Mo	CEV
S960	0.088	0.2	1.11	0.008	0.000	0.010	0.009	1.09	0.06	0.125	0.52
S1100	0.129	0.18	1.48	0.006	0.002	–	0.439	1.29	0.99	0.371	0.83

**Table 2**

Nominal mechanical properties of the parent materials.

Steel	Min 0.2% proof strength (MPa)	Ultimate tensile strength (MPa)	Elongation $A_5$ (%)
S960	1028	1126	9
S1100	1126	1153	11

**Table 3**

Welding parameters used in the experiment.

Voltage (V)	Current (A)	Travel speed (mm/s)	Wire feed rate (m/min)	Wire diameter (mm)	Gas flow (L/min)	Shielding gas
25.1	216	6.2	10	1.0	20	92% Ar + 8% CO <sub>2</sub>

material are slightly lower than those of parent materials. However, previous studies prove the strength of the welded joints made from both steels falls in the matching strength level with the BMs [10]. Table 4 lists chemical composition (wt%) as well as the mechanical properties of the filler material used in this study.

The microstructure of both steel grades is a mixture of bainite (B), martensite (M), islands of martensite/austenite (M/A) and tempered martensite as shown in Fig. 1. The details of the microstructure of the BM studied in this paper can be found at [10,16]. The low carbon content makes these steel grades suitable for welding, hence their potential for construction applications. However, the martensitic microstructure of these steel grades is more sensitive to the welding HI, hence softening at the weld HAZ may occur [37]. In order to overcome this issue, the welding HI should be kept as low as possible [10].

## 2.2. Test specimens

Two sets of specimens for each steel grade (i.e. as-received and as-welded) were manufactured according to the specifications of ASTM E8M [38]. Due to thickness limitations, sub-sized specimens were made. At first, 8 mm thick steel plates were laser cut in rolling direction. Then, the cut pieces were machined to form cylindrical specimens as shown in Fig. 2. Due to the limitation in fixtures at elevated temperatures, cylindrical shape was chosen.

In order to manufacture as-welded specimens, two laser-cut base plates were butt-welded using a robot arm from which the samples were cut. Hence, all specimens were taken from the welded block as shown schematically in Fig. 3. Prior to groove preparation, edges at the weld area were removed mechanically for 2 mm to eliminate possible HAZ from the laser cutting process. The double V-shape groove was then prepared by machining. The schematic of the joint is shown in Fig. 3(a). After welding, specimens were laser cut from the welded workpiece

**Table 4**

Chemical composition (wt%) and nominal mechanical properties of Union X96.

	C	Si	Mn	Cr	Mo	Ni
Union X96	0.12	0.8	1.90	0.45	0.55	2.35
	Yield Strength (MPa)		Ultimate tensile strength (MPa)		Elongation (%)	
	930		980		14	

perpendicular to welding direction (parallel to rolling direction) as shown schematically in Fig. 3(b). Sectioned specimens were machined to produce cylindrical specimens identical to those from BM in accordance to the specification of ASTM E8M [38].

## 2.3. Experimental setup and procedure

A series of steady-state (isothermal) hot tensile tests were conducted. Tensile tests were carried out using a Zwick/Roell Z100 testing machine (Fig. 4) with maximum load capacity of 100 kN equipped with two separate heating chambers. A three-zone resistance heating furnace, also called high-temperature furnace suitable for testing temperatures from 300 °C to 1300 °C, at a heating rate of ~20 °C/min was used. In this chamber, continuous temperature monitoring was facilitated by means of three N-type thermocouples attached on the upper, central and lower parts of the sample. An environmental chamber was used for temperatures below 300 °C. In this chamber, temperature was measured by one K-type thermocouple attached either on the upper part or lower part of the specimen. Strain measurement of the specimen during tensile testing was accomplished using contact-type extensometers. In environmental chamber, Zwick's "makroXtens" extensometer with extended arms was used while a high-temperature MayTec extensometer with ceramic sensor arms in the three-zone resistance furnace was utilized. Seven different target temperatures were considered: RT, 100 °C, 200 °C, 300 °C, 400 °C, 500 °C, 600 °C, 700 °C, 800 °C and 900 °C. As a testing procedure, the sample was first heated up to its target temperature at a constant heating rate of 20 °C/min after it was mounted and gripped inside the chamber. Prior to loading, the sample was held at the target temperature for 5 min in order to eliminate thermal gradient and ensure uniform temperature. Strain-controlled tensile tests were then conducted with a constant strain rate of 0.0001 s<sup>-1</sup> until rupture. The testing procedure was similar to those in the literature [6,26,27,33].

## 3. Results and discussion

In order to study the fire behavior of UHSSs, mechanical properties such as modulus of elasticity, proof stress at different strain levels, ultimate tensile strength and total strain at ultimate tensile strength were determined. Inasmuch as a pronounced yield point is absent in stress-strain curves, assessment of yield strengths at different strain levels has been practiced especially for elevated temperatures as the stress-strain curve becomes highly nonlinear. In this context, EN 1993-1-2 [23] defines the effective yield strength as the strength at 0.2% total strain level ( $f_{0.2}$ ). Other methods for determining effective yield strengths include defining proof stresses at 0.5%, 1.5% and 2% total strain levels, as practiced commonly by researchers [3,4,17,26]. Determining the values of characteristics strengths and strains are illustrated schematically on a typical stress-strain curve in Fig. 5.

As shown in Fig. 5, elastic modulus at the corresponding temperature is calculated based on the tangent of initial linear part of the stress-strain curve in elastic region. The  $f_{0.2}$  being used to define yield strength was determined as the intersection point of stress-strain curve with proportional line offset by 0.2% strain level. The strain corresponding to the 0.2% proof stress is termed as proof strain ( $\epsilon_y$ ). The same approach has been used to determine  $f_{0.5}$  by the means of proportional line from the 0.5% strain level. Yield strengths at 1.5% and 2% strain levels, i.e.  $f_{1.5}$  and  $f_2$ , were determined from the intersection points of stress-strain curves with vertical lines starting at the given strain values. In the same vein, maximum stress level for each temperature at related stress-

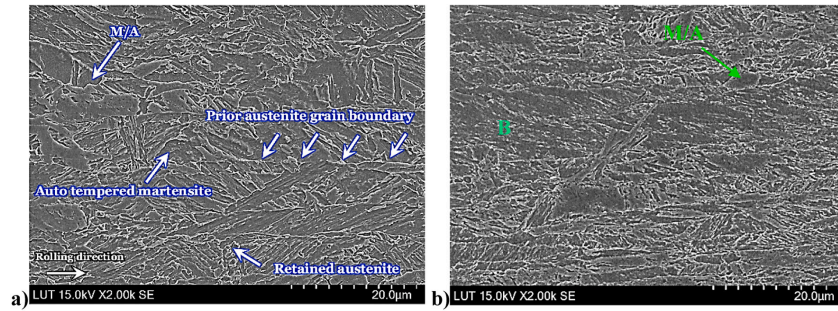


Fig. 1. Scanning electron microscopy of the studied steels, a) S960 [16], b) S1100 [10].

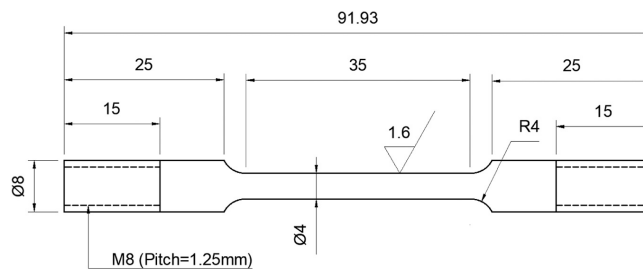


Fig. 2. Schematic of cylindrical specimen used in the study (Dimensions are in mm, not to scale).

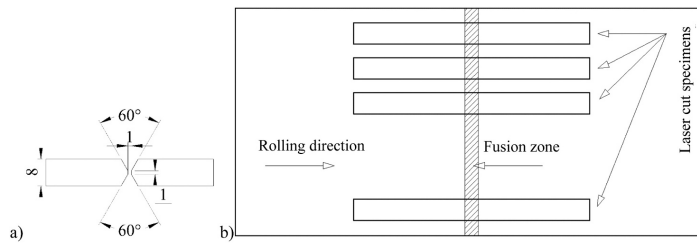


Fig. 3. Specimen preparation, (a) the butt-welded configuration (b) schematic of the butt-welded workpiece and the laser-cut sections. (Dimensions are in mm, not to scale).

strain curve denotes the ultimate tensile strength ( $f_u$ ), and the corresponding strain level is ultimate total strain or uniform elongation ( $\epsilon_u$ ).

### 3.1. Visual observations and failure mode

During the elevated temperature tensile tests, as a general phenomenon, the surface color of the test specimens would change. As can be seen in Fig. 6 (a-d) for both as-received and as-welded specimens made from S960 and S1100, the surface color remains almost silver/white at RT up to 200 °C. When the temperature exceeds 200 °C, the surface color changes slightly to light yellow, and at 300 °C, the color turns to dark blue. From 400 °C to 600 °C, the surface color changes from light gray to almost black. Exceeding 700 °C, the surface color changes to blackish gray due to severe oxidation at those high temperatures and formation of oxide layers [18].

Typical failure mode of tensile test specimens made from as-received and as-welded S960 and S1100 at elevated temperatures are shown in Fig. 6 (a-d). As shown in Fig. 6 (a) and Fig. 6 (c), for all the specimens, both as-received and as-welded, necking occurs before failure, which becomes more obvious as temperature increases. The as-welded S960 specimens fail at the HAZ from RT to 500 °C, as shown in Fig. 6 (b). However, for the same temperature range, all the welded S1100 specimens failed from the BM. Both steel grades revealed a weld failure at 600 °C, followed by irregular failures at higher temperatures.

### 3.2. Stress-strain curves

The stress-strain curves of as-received and as-welded specimens at RT, as well as various elevated temperatures obtained from steady-state hot tensile tests for S960 and S1100, are plotted in Figs. 7 and 8,

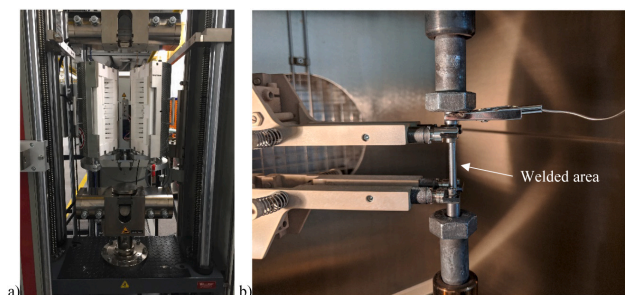


Fig. 4. Tensile testing equipment at elevated temperatures, (a) chamber, (b) round bar specimen.

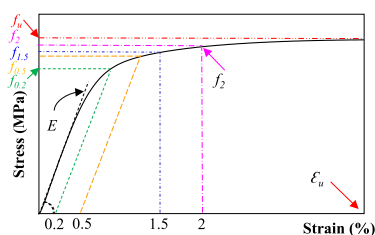


Fig. 5. Schematic of a typical UHSS stress-strain curve up to the ultimate stress and the definition of its characteristics.

respectively. The values corresponding to the characteristic strengths and strains for the examined steel alloys are presented in Tables 5 and 6. It should be mentioned that the abbreviations BM and W corresponds to as-received base material and as-welded conditions, respectively. The numbering in specimen labels 96 and 11 represents the steel grades S960 and S1100, respectively. The testing temperature is added at the end of labeling. For instance, W-96-400 is the butt-welded S960 specimen tested at 400 °C. As can be seen in Figs. 7 and 8, in all the tested cases, as-welded specimen shows smaller ductility compared to the corresponding as-received specimen at the same elevated temperature. Both steel alloys show relatively similar mechanical properties ( $E$ ,  $f_{0.2}$  and  $f_u$ ) at room temperature. However, the welded joints significantly show different performances. While S960MC shows 35% reduction of its proof stress after being welded, the S1100 reveals no reduction, as shown in Fig. 9. As mentioned earlier, softening is attributed to the HAZ of weldments made of UHSSs, which contributes to strength reduction of the joint. A comparison is drawn between the hardness values of the butt-welded joints from S1100 and S960MC. As presented in Fig. 10, both joints in the weld area show comparable hardness with slightly higher values for weldments made of S1100. As moving towards HAZ, while the hardness of welded S1100 reveals no reduction but a fluctuation, there is significant hardness reduction (softening effect) associated with S960MC weldment. Such an effect is correlated to strength reduction of the joints made from S960MC (approximately 35% strength reduction due to welding) as is clear from stress-strain curves in Fig. 9. The hardness reduction at the softened weld HAZ in S960 compared to S1100 is the formation of softer microstructure such as ferrite during the cooling cycle of welding [10].

### 3.3. Modulus of elasticity

Service performance and load-bearing capacity of steel structures are significantly affected by decrease in elastic modulus at elevated

temperatures. A robust fire-resistance design and providing safety to the application of structures made of UHSSs necessitate quantitative evaluation of deterioration of elastic modulus at fire or elevated temperature conditions. In order to discuss the deterioration of elastic modulus with increasing temperature, generally a reduction factor at corresponding temperature is presented. The reduction factor of elastic modulus at a specific elevated temperature is determined as the ratio of elastic modulus at that given temperature to that of RT. Temperature-dependent mechanical properties of steels on the basis of the reduction factor concept is commonly practiced by different design standards, such as Eurocode for fire-resistance design of steel structures [23]. In this study, reduction factors corresponding to elastic modulus at given tested temperatures were obtained from experimental stress-strain curves. A comparison between reduction factors related to elastic modulus ( $E_T/E_{RT}$ ) for the studied steels (BM and weldment), respective prediction models of design standards (i.e. EC3, AISC and AS4100), and from literature [4,17,26,33] is drawn as shown in Fig. 11. It is essential to mention that reduction factors of elastic modulus for BM-960/1100 in Fig. 11 are calculated as  $E_{BM_T}/E_{BM_{RT}}$ . In the same vein, reduction factors corresponding to W-960/1100 are  $E_{W_T}/E_{W_{RT}}$ .

As shown in Fig. 11, the welded joints of both steel alloys show no major reduction in temperature-dependent elastic modulus compared to their BMs. A bilinear curve can be associated with the decrease of elastic modulus for most the data from literature provided for comparison, including BM/W-960, one RT–500 °C, and the other 500 °C–800 °C. The latter has a sharper slope for temperature-induced degradation which is rooted in the elimination of strain hardening at higher temperatures compared to the moderately elevated temperature range RT–500 °C. Elastic modulus of BM/W-1100, although experiencing continuous reduction, compared to BM/W-960, there is lower degradation, and the trend is clearly slower. For example, at 600 °C, while BM/W-960 keeps only 60% of its original elastic modulus, BM/W-1100 retains almost 80% of its elastic modulus at RT. At the same temperature, S460 [33] and S960 [26] lose almost 70% of their elastic modulus at RT. The studied S1100 seems to have a more stable microstructure under temperature gradients resulting less degradation of the mechanical properties. Similar behavior is reported when welded S960 was compared to S1100 at room temperature and after welding [10].

Fig. 11 also indicates that design codes such as EC3, AISC and AS4100 models fairly predict the results of present tests for BM/W-960 in the temperature range RT–300 °C. Predictions of EC3 and AISC in the same manner, start to move on the conservative side as temperature exceeds 300 °C and becomes overly conservative in the temperature range 600 °C–900 °C. The result of the current study up to a temperature of 300 °C agrees with the literature on similar UHSS grades [4,26]. The results of this study in terms of elastic modulus reduction factor values, however, surpass the findings of Qiang et al. [26] and stays below the results of Neuenschwander et al. [4] as temperature increases up to



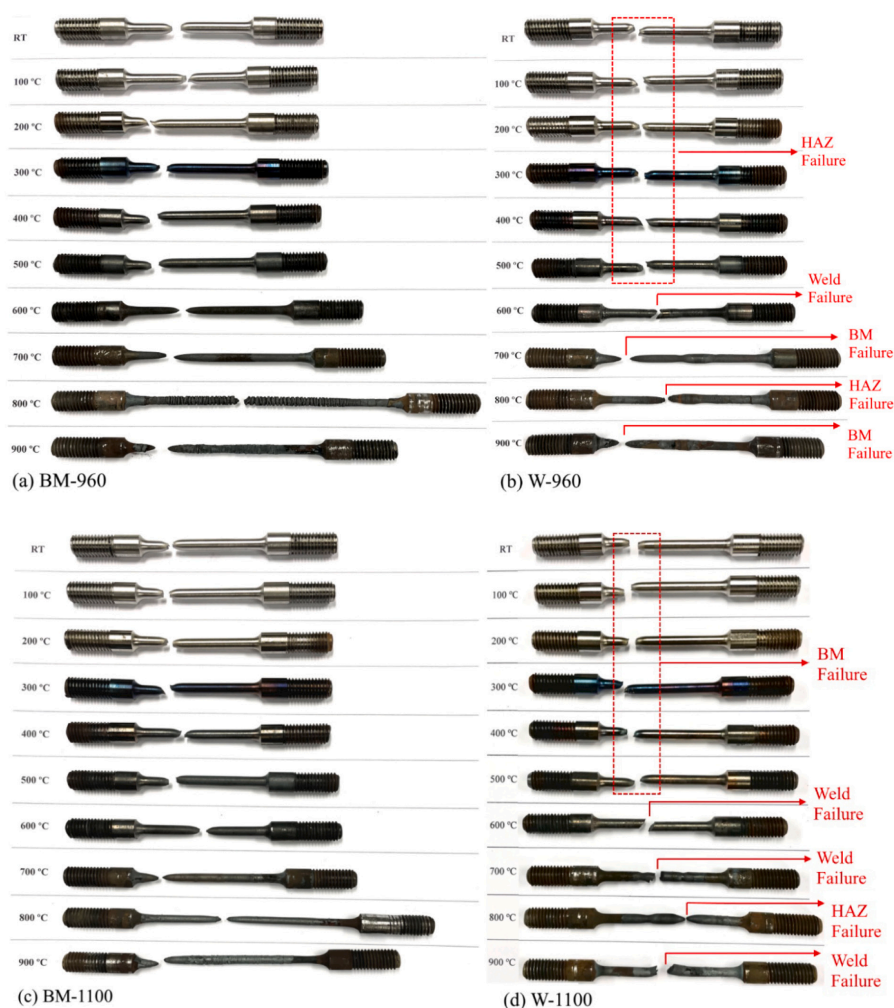


Fig. 6. Visual observation and failure mode of the tested specimen at elevated temperatures, (a) BM-960, (b) W-960, (c) BM-1100, and (d) W-1100.

900 °C. The investigated S960 steel grade in the two mentioned studies was quenched and tempered, while the delivery condition of the S960 in this study was directly quenched. The behavior of S460 is not accurately predicted by EC3 and AISC at temperatures above 300 °C as they become nonconservative and only in the temperature range above 600 °C can reasonably predict the behavior of the material. AS4100 is unsafe for prediction of elastic modulus of S460 at all tested temperatures. All the mentioned design codes are overly conservative regarding the elastic modulus reduction factors of S700 at temperatures 200 °C–400 °C. At temperatures above 400 °C, although the degree of conservativity decreases, EC3 and AISC remain conservative. AS4100 exhibits unsafe prediction at 500 °C for S700 and reasonable predictions in the temperature range 600 °C–800 °C.

The experimental results on the studied BM/W-1100 show a better

match with EC3 and AISC models compared to AS4100 for temperatures up to 300 °C as AS4100 leans slightly on the unsafe side. At higher temperatures, all the mentioned design codes are overly conservative for predicting the results of the present test series, with a smaller degree of conservativity for AS4100. Moreover, predications of all the design codes for S1100, compared to S960MC, show more pronounced degrees of conservativity. The results of this study, in terms of elastic modulus of S1100, completely match the data set from the study by Neuenschwander et al. [4], as depicted in Fig. 11.

### 3.4. Yield strength

Temperature-dependent effective yield strengths of the two tested steels in as-received and as-welded forms based on the reduction factor

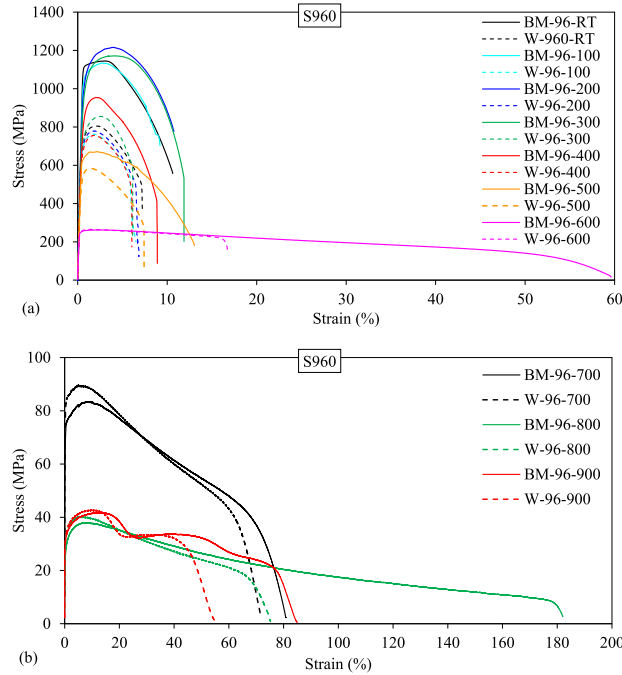


Fig. 7. Engineering stress-strain results of S960 specimens, (a) RT-600 °C, and (b) 700 °C-900 °C.

concept were considered. Effective yield strength reduction factors ( $f_{0.2}$ ,  $\tau/f_{0.2, RT}$ ), ( $f_{0.5}$ ,  $\tau/f_{0.5, RT}$ ), ( $f_{1.5}$ ,  $\tau/f_{1.5, RT}$ ) and ( $f_2$ ,  $\tau/f_2, RT$ ) corresponding to strain levels 0.2, 0.5, 1.5 and 2, respectively, were calculated as presented in Tables 5 and 6. Reduction factors related to  $f_{0.2}$ , which is commonly used to define yield strength of the material, are compared with the predictive models from design codes EC3 [23], AISC and AS4100 [32] as well as the literature in Fig. 12. It should be mentioned that reduction factors in Fig. 12 for BM and W are calculated as  $f_{0.2BM}/f_{0.2BM, RT}$  and  $f_{0.2W}/f_{0.2W, RT}$ , respectively.

As is shown in Fig. 12, for BM-960, yield strength decreases continuously up to 400 °C, at a lower rate compared to the subsequent temperature range 400 °C-800 °C where significant strength degradation occurs. As is observable in Fig. 12, the same trend of strength reduction is experienced by BM-1100 up to the onset of rapid strength fall at 400 °C. However, compared to BM-960, strength degeneration of BM-1100 at temperatures above 400 °C happens at a slower rate, reaching a reduction factor of almost 0.5 in contrast to 0.2 for BM-960 at 600 °C. Degeneration of  $f_{0.2}$  for both BMs continuously continues in a similar manner in the temperature range 700 °C-900 °C.

The absolute 0.2% proof stress of W-960 compared to BM-960 is smaller in the temperature range of RT-600 °C. However, when the reduction factors are compared, the welded S960 shows a better performance. The reason is the significant strength reduction for as-welded joints made of S960 compared to as-received material, as shown in Fig. 9. The strength degradation of BM-960 compared to W-960 at elevated temperatures happens at a greater level and higher rate. Reaching the temperature of 500 °C, W-960 retains 75% of its strength at RT, while such value for BM-960 remains 55%. Significant degradation occurs for both BM/W-960 at 600 °C. The reduction factor for W-960, calculated based on the  $f_{0.2}$  at 600 °C to the reference  $f_{0.2}$  at RT, takes the

value of 0.34, while for the comparable scenario with respect to BM-960, the reduction factor reaches the value of 0.21. Exceeding 600 °C, the values of  $f_{0.2}$  for both BM/W-960 becomes quite similar accompanied by significant degradation of strength.

BM-1100 and W-1100 exhibit the same degeneration trend with respect to  $f_{0.2}$ , such deviation as demonstrated for S960 is not observed. That is, mechanical properties of W-1100 in terms of yield strength can be considered identical to that of BM-1100.

In terms of comparison with design codes, AISC presents the most unsafe predictive model and is inapplicable for HSS/UHSS with respect to  $f_{0.2}$ . Prediction of reduction factors with respect to  $f_{0.2}$  by AISC for S460 is considerably better compared to the rest of the data sets, although in such a scenario, predictions for temperatures above 500 °C remain on the unsafe side. EC3 predictions for BM-960 in the temperature range RT-200 °C is slightly nonconservative, as shown in Fig. 11. Predictions of EC3, however, deviate moderately from experimental data and lean on the conservative side for temperatures up to 500 °C before starting to move into the unsafe region again. For BM-1100, similar overestimation of the yield strength values by EC3 in the temperature range RT-200 °C is demonstrated in Fig. 11. For the rest of the temperature range up to 700 °C, however, EC3 predicts the experimental data with a higher degree of conservativity compared to the data set related to S960. With respect to predictions of EC3 for W-1100, since the experimental data exhibit no significant deviation from the BM-1100 data, predictions of EC3 for W-1100 are similar to predictions for BM-1100. For W-960, the degree of conservativity regarding the predictions of EC3 increases compared to estimations for BM-960. That is, for temperatures RT-100 °C, predictions fall in the unsafe region, while conservative predictions are provided for the entire tested temperatures up to 700 °C before it leans slightly on the unsafe region. Predictions of



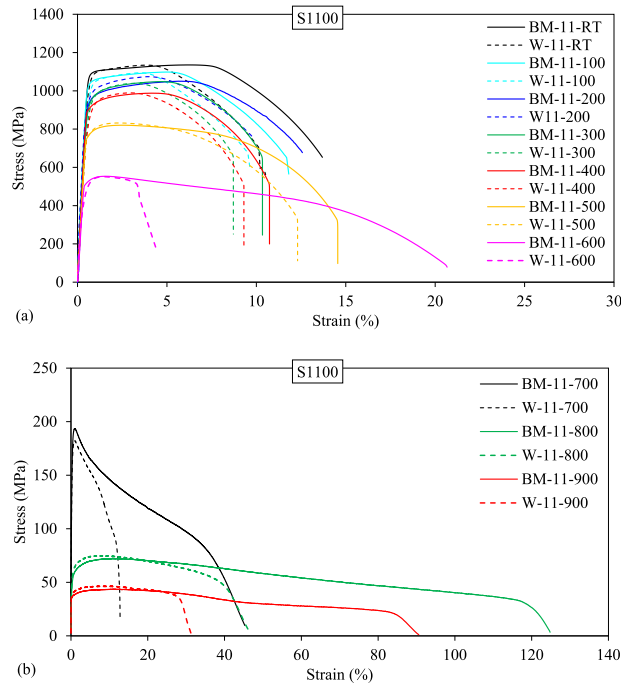


Fig. 8. Engineering stress-strain results of S1100 specimens, (a) RT-600 °C, and (b) 700 °C-900 °C.

Table 5

Mechanical properties of S960 in as-received and as-welded forms at elevated temperatures.

T (°C)	Label	E (GPa)	$f_{0.2}$ (MPa)	$f_{0.5}$ (MPa)	$f_{1.5}$ (MPa)	$f_2$ (MPa)	$f_u$ (MPa)	$\epsilon_{0.2}$	$\epsilon_u$
RT	BM	199.7	1115.5	1126.9	1133.2	1139.4	1144.6	0.755	3.03
	W	195.4	721.6	764.7	797.5	804.6	804.8	0.574	2.08
100	BM	189.8 (0.95)	1053.5 (0.94)	1083.4 (0.96)	1105.9 (0.97)	1121.5 (0.98)	1134.0 (0.99)	0.752	2.73
	W	183.7 (0.94)	688.5 (0.95)	728.8 (0.95)	759.8 (0.95)	760.6 (0.94)	762.5 (0.95)	0.574	1.77
200	BM	182.1 (0.91)	985.2 (0.88)	1076.3 (0.95)	1143.2 (1.008)	1177.0 (1.033)	1215.7 (1.062)	0.657	3.92
	W	176.4 (0.88)	703.0 (0.97)	747.5 (0.98)	775.9 (0.97)	777.5 (0.97)	778.9 (0.97)	0.602	1.83
300	BM	176.4 (0.88)	949.3 (0.85)	1040.8 (0.92)	1109.4 (0.98)	1140.1 (1.00)	1171.5 (1.02)	0.693	4.13
	W	160.0 (0.82)	721.7 (1.00)	780.7 (1.02)	830.8 (1.04)	849.0 (1.06)	855.3 (1.06)	0.607	2.56
400	BM	164.0 (0.82)	829.3 (0.74)	898.6 (0.80)	941.5 (0.83)	953.3 (0.84)	954.0 (0.83)	0.687	2.18
	W	153.2 (0.78)	655.5 (0.91)	713.5 (0.93)	751.8 (0.94)	755.0 (0.94)	755.8 (0.94)	0.531	1.85
500	BM	144.9 (0.73)	614.0 (0.55)	641.9 (0.57)	668.5 (0.59)	669.6 (0.59)	671.3 (0.59)	0.458	2.20
	W	143.6 (0.73)	523.6 (0.73)	568.0 (0.74)	583.4 (0.73)	577.7 (0.72)	583.6 (0.73)	0.518	1.43
600	BM	113.6 (0.57)	243.8 (0.22)	255.3 (0.23)	261.1 (0.23)	261.7 (0.23)	262.2 (0.23)	0.219	2.63
	W	107.0 (0.55)	248.3 (0.34)	259.8 (0.34)	264.9 (0.33)	264.1 (0.33)	265.0 (0.33)	0.260	2.60
700	BM	80.1 (0.4)	68.7 (0.06)	83.1 (0.07)	85.8 (0.08)	86.3 (0.08)	89.7 (0.08)	0.270	9.17
	W	80.1 (0.41)	78.1 (0.11)	83.1 (0.11)	85.8 (0.11)	86.4 (0.11)	89.7 (0.11)	0.282	5.06
800	BM	42.4 (0.21)	24.1 (0.02)	28.2 (0.03)	32.9 (0.03)	34.1 (0.03)	38.0 (0.03)	0.247	7.32
	W	42.4 (0.22)	29.0 (0.04)	32.7 (0.04)	36.7 (0.05)	37.7 (0.05)	40.1 (0.05)	0.246	6.08
900	BM	62.5 (0.31)	30.4 (0.03)	32.5 (0.03)	35.7 (0.03)	36.6 (0.03)	41.8 (0.04)	0.221	12.16
	W	62.8 (0.32)	30.8 (0.04)	32.9 (0.04)	37.1 (0.05)	38.0 (0.05)	42.7 (0.05)	0.240	9.58

EC3 for W-960 in the temperature range 200 °C – 500 °C are overly conservative. AS4100, on the other hand, fails to render accurate predictions for reduction factors of BM/W-1100 up to 300 °C. For the rest of the temperatures, however, this design code provides better agreement with experimental data up to 600 °C. Above 600 °C up to 900 °C, the predictions of AS4100 for BM/W-1100 fall in the unsafe region. With respect to BM-960, AS4100 fails to safely predict reduction factors. For

W-960, although the whole prediction package presented by AS4100 is questionable, for temperatures above 200 °C up to 500 °C, safe predictions are provided by such a model. In another comparison between the results of the current study and data sets from the literature [4,26], where BM-960 is concerned, a similar strength degradation trend is observable up to 400 °C. However, between 400 °C and 700 °C, the results of this study show higher strength degradation compared with

**Table 6**  
Mechanical properties of S1100 in as-received and as-welded forms at elevated temperatures.

T (°C)	Label	E (GPa)	$f_{0.2}$ (MPa)	$f_{0.5}$ (MPa)	$f_{1.5}$ (MPa)	$f_2$ (MPa)	$f_u$ (MPa)	$\epsilon_{0.2}$	$\epsilon_u$
RT	BM	193.1	1088.9	1102.7	1109.0	1112.8	1135.5	0.759	6.28
	W	192.6	1035.9	1092.9	1108.8	1117.0	1134.3	0.696	3.83
100	BM	192.6 (1.00)	1034.7 (0.95)	1057.5 (0.96)	1069.8 (0.96)	1076.4 (0.97)	1098.3 (0.97)	0.675	5.08
	W	187.2 (0.97)	985.7 (0.95)	1047.6 (0.96)	1067.2 (0.96)	1077.7 (0.96)	1094.4 (0.96)	0.693	3.55
200	BM	189.4 (0.98)	947.1 (0.87)	979.6 (0.89)	999.2 (0.90)	1011.4 (0.91)	1050.5 (0.93)	0.714	5.64
	W	181.9 (0.94)	936.8 (0.90)	997.7 (0.91)	1032.0 (0.93)	1048.1 (0.94)	1074.2 (0.95)	0.599	3.89
300	BM	169.3 (0.88)	942.8 (0.87)	982.6 (0.89)	1007.4 (0.91)	1021.2 (0.92)	1048.5 (0.92)	0.736	4.74
	W	162.9 (0.85)	898.6 (0.87)	971.4 (0.89)	1008.6 (0.91)	1024.2 (0.92)	1039.3 (0.92)	0.684	3.21
400	BM	162.3 (0.84)	889.0 (0.82)	924.4 (0.84)	958.2 (0.86)	969.8 (0.87)	987.9 (0.87)	0.524	4.14
	W	158.9 (0.83)	866.1 (0.84)	937.3 (0.86)	967.2 (0.87)	980.0 (0.88)	989.5 (0.87)	0.703	3.00
500	BM	161.1 (0.83)	745.9 (0.69)	784.2 (0.71)	813.8 (0.73)	819 (0.74)	820.4 (0.72)	0.488	2.47
	W	155.0 (0.80)	741.6 (0.72)	788.1 (0.72)	825.2 (0.74)	831.3 (0.74)	832.2 (0.73)	0.482	2.36
600	BM	143.7 (0.74)	503.0 (0.46)	532.4 (0.48)	553.4 (0.50)	551.8 (0.50)	553.5 (0.49)	0.381	1.59
	W	142.2 (0.74)	468.5 (0.45)	529.5 (0.48)	551.2 (0.50)	545.0 (0.49)	551.3 (0.49)	0.473	1.49
700	BM	121.7 (0.63)	164.6 (0.15)	183.1 (0.17)	190.3 (0.17)	185.7 (0.17)	193.5 (0.17)	0.325	0.92
	W	132.6 (0.69)	152.4 (0.15)	172.5 (0.16)	178.6 (0.16)	174.3 (0.16)	182.1 (0.16)	0.305	0.97
800	BM	44.4 (0.23)	47.1 (0.04)	54.2 (0.05)	62.3 (0.06)	64.3 (0.06)	72.2 (0.06)	0.290	12.15
	W	43.8 (0.23)	51.6 (0.05)	58.6 (0.05)	67.5 (0.06)	69.0 (0.06)	74.8 (0.07)	0.302	8.05
900	BM	66.1 (0.34)	35.9 (0.03)	37.3 (0.03)	39.7 (0.04)	40.3 (0.04)	43.6 (0.04)	0.257	11.21
	W	73.2 (0.38)	38.2 (0.04)	39.9 (0.04)	42.9 (0.04)	43.7 (0.04)	46.4 (0.04)	0.247	7.92

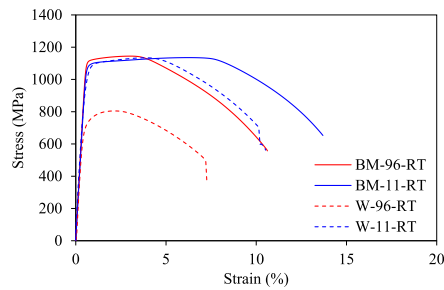


**Fig. 9.** Engineering stress-strain curves of the base materials and their butt-welds.

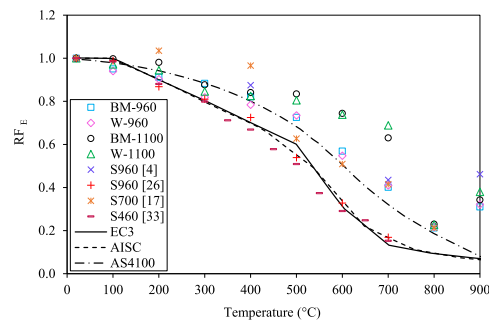


**Fig. 11.** Elastic modulus reduction factors at elevated temperatures.

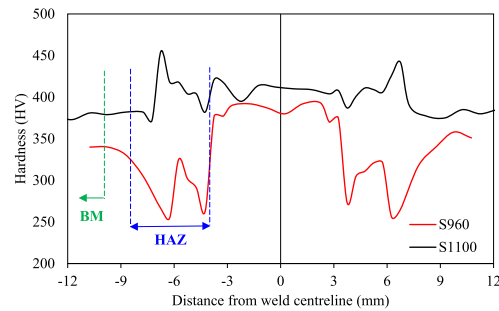


**Fig. 10.** Vickers hardness distribution along the weldments. (Measurement is performed at the through-thickness 1 mm below surface, modified from [10].)

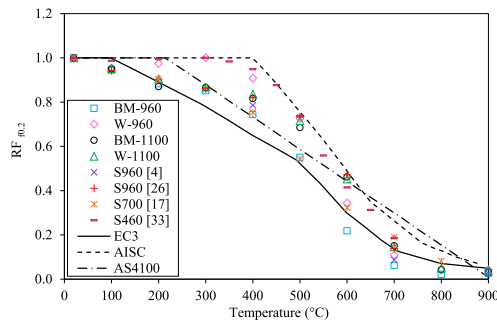


**Fig. 12.** Reduction factors of 0.2% proof stress at elevated temperatures.

the two studies for S960QL. The reason can be attributed to the higher molybdenum content of S960QL compared to S960MC in this study, almost 0.5% [4] versus 0.125%, respectively, which is believed to increase creep resistance of steels by solid solution strengthening [39]. Compared to S700 from the literature [17], BM-960 keeps the same strength reduction up to around 500 °C before it experiences a more pronounced decline in its strength up to 800 °C. For BM/W-1100,

nonetheless, predictions of this study completely match the results of the studies [4,26] in the entire tested temperature range. Experiencing lower deterioration in strength level, the values of reduction factors corresponding to W-960 stand above the reduction factor values of BM/W-1100 and grades above S700 from literature in the temperature range 200 °C–500 °C. Exceeding 500 °C and up to 700 °C, the reduction factor

values of W-960 fall below the corresponding values of BM/W-1100.

### 3.5. Ultimate tensile strength

The ultimate tensile strength reduction factors of the tested steels as the ratio of ultimate tensile strength at that particular temperature ( $f_u, T$ ) to the ultimate tensile strength at RT ( $f_{u, RT}$ ) were calculated, and the results corresponding to BM/W-960 and BM/W-1100 are plotted in Fig. 13. For the purpose of comparison, the predictive models by EC3 and AISC as well data from previous studies related to several HSS/UHSSs are presented.

As depicted in Fig. 13, degeneration of the ultimate tensile strengths of BM/W-960 and BM/W-1100 at elevated temperatures follows the trends which are very close to what was observed for their yield strengths. In this regard, larger reduction factor values at a corresponding temperature for W-960 compared to that of BM-960 is observed for the same reason explained in Section 3.3. For instance, 0.23 versus 0.33, respectively for BM-960 and W-960 at 600 °C. The decline in the ultimate tensile strength of BM-1100 at each corresponding elevated temperature proves to be almost identical to that of W-1100.

Comparing with design codes, the results of ultimate tensile strength reduction factors with respect to BM-960 are an acceptable match with the EC3 predictive model at temperatures up to 500 °C. Prediction of  $f_u$  in the range 600 °C–900 °C, however, leans on the unsafe side. Reduction factors of W-960, similar to BM-960, are predicted safely by EC3 in the range RT–500 °C, while between 600 °C and 900 °C estimations tend to be in the unsafe region. At intermediate elevated temperatures, 100 °C–300 °C, stress anomaly is exhibited in the behavior of BM/W-960, with a peak at 200 °C, as was reported in previous studies [7]. While results of this study for S960MC in the temperature range 100 °C–350 °C agree with the EC3 model due to anomaly associated, findings of Neuenchwander et al. [4], and Qiang et al. [26] related to S960QL show a continuous decrease, which makes the EC3 model quite unsafe in the mentioned temperature range for those steels. EC3 is inapplicable to predict the ultimate tensile behavior of S700, while it partially (i.e., temperature range 250 °C–450 °C) can safely predict the ultimate tensile behavior of S460. Having the identical degradation trend, the ultimate tensile behavior of BM/W-1100 at moderately elevated temperatures, 100 °C–350 °C, is inaccurately predicted by the EC3 model. As is revealed, compared to BM/W-960, no stress anomaly is exhibited in the ultimate tensile behavior of BM/W-1100. EC3, however,

conservatively estimates the calculated reduction factors for BM/W-1100 at temperatures above 350 °C. Reduction factors of BM/W-1100 predicted by EC3 in the range 700 °C–900 °C tends to match the experimental data. The trend of reduction in the ultimate tensile strength of BM/W-1100 in this study completely matches the findings of the two mentioned studies for S960QL [4,26], which identifies the EC3 model as an unsafe model for the moderately elevated temperature range 100 °C–350 °C.

AISC, on the other hand, predicts reduction factors of BM/W-960 as well as S700 and S460 quite inaccurately, and the degree of safety decreases as temperature rises. Reduction factors related to BM/W-1100 as well as S960QL from a previous study [26] estimated by AISC are in agreement with experimental data only at temperatures above 500 °C and below 650 °C, while the model is inapplicable to safely predict the ultimate tensile behavior of the mentioned steels at temperatures below 500 °C and temperatures above 650 °C.

## 4. Predictive equations for UHSS

Based on the experimental results of this study for the tested UHSSs including as-received and as-welded, as well as the dataset from the literature for the UHSS grade 960 [4,26] predictive equations are developed as a function of temperature to describe the degradation of the mechanical properties of UHSSs at elevated temperatures. These equations can safely predict mechanical properties reduction factors at elevated temperatures and be thus useful in the field of structural engineering to conduct fire-safe designs for the tested UHSSs.

### 4.1. Modulus of elasticity

The datasets used to derive the predictive equation for elastic modulus reduction factors of S960 and S1100 are shown in Fig. 14. As can be seen, data scatter increases as temperature rises mainly due to the difference of the elastic modulus values of S960 reported by reference [26]. As is observable, on condition that the data of reference [26] is excluded, the prediction curve may be less conservative in the temperature range 300 °C–800 °C. Mean–2SD was chosen as the criterion to derive the predictive equation, where SD is the standard deviation of the data including the data of the reference [26].

Deterioration of the elastic modulus in the form of reduction factors are presented by Eq. (3).

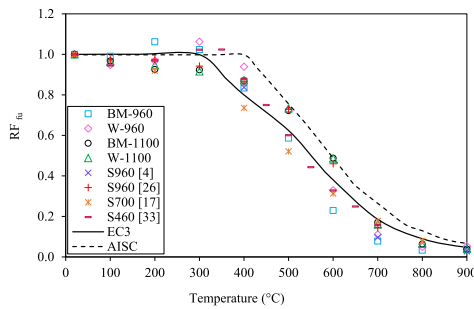


Fig. 13. Reduction factors of  $f_u$  at elevated temperatures.

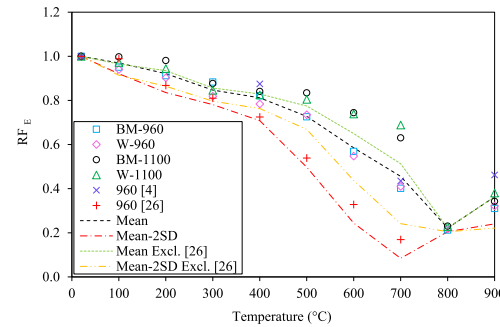


Fig. 14. The dataset used in order to derive the predictive equation for elastic modulus reduction factors of UHSSs.

$$E_T/E_{RT} = \begin{cases} 3 \times 10^{-9}T^3 - 7 \times 10^{-8}T^2 - 0.001 \times T + 1.0203 & 20 \leq T < 300 \\ 2 \times 10^{-11}T^4 - 2 \times 10^{-8}T^3 - 5 \times 10^{-6}T^2 + 0.0057 \times T - 0.1604 & 300 \leq T < 700 \\ -4 \times 10^{-6}T^2 + 0.0076 \times T - 3.1406 & 700 \leq T \leq 900 \end{cases} \quad (3)$$

Fig. 15 compares the derived equation for prediction of the elastic modulus reduction factors of UHSSs with some of the design code models.

As is observable in Fig. 15, all the design codes, as it pertains to UHSSs, need to be modified for safer predictions in the temperature range RT–300 °C. In the temperatures range 300 °C–700 °C, the predictive curve becomes close to EC3 and AISC models, albeit with safe predictions of elastic modulus reduction factors for the entire UHSS envelopes used in this study.

#### 4.2. Yield strength

The datasets to derive the yield strength reduction factor relationships of S960 and S1100 are shown in Fig. 16. The same criterion, namely Mean–2SD was used to establish the predictive equation to safely predict the yield strength reduction factors.

The elevated-temperature yield strength reduction factors of UHSSs can be expressed using the following equation:

$$f_{0.2,T}/f_{0.2,RT} = \begin{cases} -6 \times 10^{-11}T^4 + 5 \times 10^{-8}T^3 - 10^{-5}T^2 + 0.0004 \times T + 0.9972 & 20 \leq T < 400 \\ -9 \times 10^{-6}T^2 + 0.0063 \times T - 0.3729 & 400 \leq T < 600 \\ 3 \times 10^{-6}T^2 - 0.0055 \times T + 2.2698 & 600 \leq T \leq 900 \end{cases} \quad (4)$$

A comparison is drawn in Fig. 17 between the predictive equation for the yield strength reduction factors of UHSSs 960 and 1100 and some of the design code models.

As can be observed in Fig. 17, among the design code models, EC3 is closer to the predictive curve developed in this study than other models

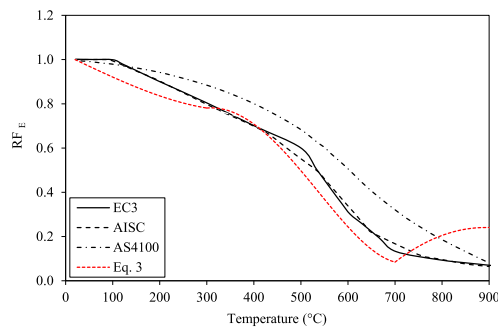


Fig. 15. Comparison between Eq. (3) and design code models.

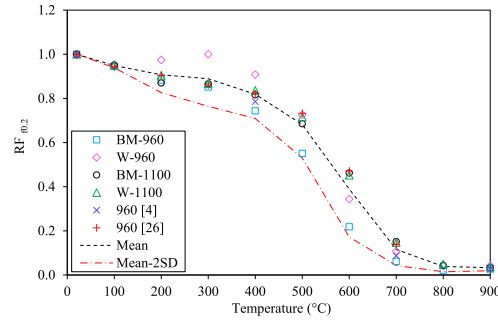


Fig. 16. The dataset used in order to derive the predictive equation for the yield strength reduction factors of UHSSs.

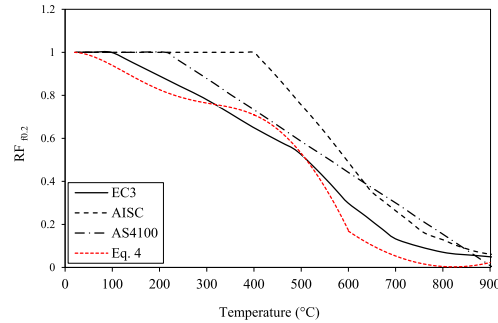


Fig. 17. Comparison between Eq. (4) and design codes models.

considering some modifications in the range RT–300 °C and above 600 °C. However, one should consider that EC3 uses mean-2SD value, while the other codes use mean itself in their reliability predictions.

#### 4.3. Ultimate tensile strength

In order to derive the equation to predict the ultimate tensile strength reduction factors of UHSSs, the datasets are shown in Fig. 18. As

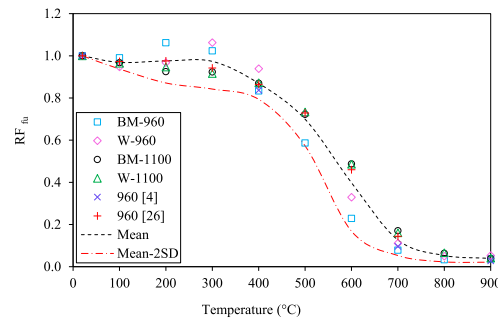


Fig. 18. The dataset used in order to derive the predictive equation for the ultimate tensile strength reduction factors of UHSSs.

is shown, the curve which represents the criterion to derive the equation, namely Mean-2SD can provide safe predictions for the entire UHSS package used in this study.

Degradation of the ultimate tensile strength of the UHSS data envelopes used in this study at elevated temperatures is expressed by the following equation:

$$f_{u,T}/f_{u,RT} = \begin{cases} -4 \times 10^{-11}T^4 + 3 \times 10^{-8}T^3 - 5 \times 10^{-6}T^2 - 0.0004 \times T + 1.0107 & 20 \leq T < 400 \\ -9 \times 10^{-6}T^2 + 0.0061 \times T - 0.1603 & 400 \leq T < 600 \\ 3 \times 10^{-6}T^2 - 0.0047 \times T - 1.9841 & 600 \leq T \leq 900 \end{cases} \quad (5)$$

The proposed equation to estimate the ultimate tensile strength reduction factors of UHSSs in this study is compared with the design code models, as shown in Fig. 19.

As can be seen, in order to predict the ultimate tensile strength reduction factors of UHSSs safely in the entire temperature range RT-900 °C, the predictive model is more conservative than the existing design code models such as EC3 and AISC. Both design code models have obvious unsafe regions between RT and 300 °C, which should be modified in the case of UHSSs.

## 5. Conclusions

In this study, elevated-temperature mechanical properties of UHSSs grades 960MC and 1100 in both as-received and as-welded forms were examined. Elevated-temperature steady-state tensile tests up to 900 °C were conducted and stress-strain curves, temperature-dependent elastic modulus, 0.2% proof and ultimate tensile strengths were determined. Elastic modulus of as-received S960/1100 with their as-welded forms at all tested temperatures remains almost identical. In terms of 0.2% proof and ultimate tensile strengths, although there is significant welding-induced strength reduction associated with S960MC, elevated-temperature strength reduction with respect to as-welded form surprisingly occurs at a lower level and rate compared to as-received form. S1100 shows no noticeable variation in strength degradation trends for as-received and as-welded forms.

In terms of comparison with several design codes, it can be stated that none of them can be used for accurate prediction of constitutive mechanical behavior of HSS/UHSSs at elevated temperatures and accordingly safe fire-resistance design. All the design codes used in this paper for the sake of comparison, proved to need reconsideration in their predictive models for temperatures below 300 °C for HSS/UHSSs, as they partially but not safely predicted elevated-temperature mechanical properties.

In terms of elastic modulus, for the temperature range above 300 °C, EC3 shows more adaptability to the entire UHSS data package used in this study, while the two other design code models largely underestimate temperature-dependent elastic modulus, and this conservativity increases as temperature and strength level of the material rises. For 0.2% proof strength, AISC is inapplicable for UHSSs, and EC3 surpasses AS4100 in terms of partial adaptability to HSS/UHSSs. In terms of ultimate tensile strength, although applicability of design code models for HSS/UHSSs is questionable, in the temperature range above 300 °C, as steel strength increases, the possibility to adopt EC3 for prediction of mechanical properties increases. Further investigation should be conducted to study in detail the effect of manufacturing process on strength degradation of different grades of UHSSs and their weldments at elevated temperatures. It is also worth including the effect of strain rate

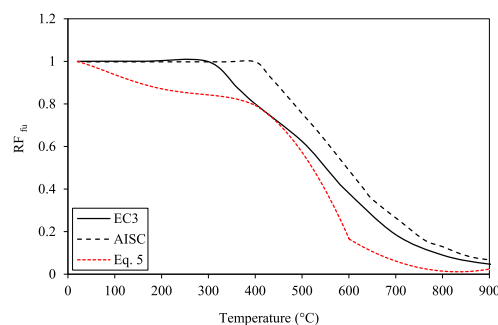


Fig. 19. Comparison between the proposed equation for prediction of the ultimate tensile strength reduction factors and some design code models.

on elevated-temperature mechanical properties of UHSSs at higher temperatures, as can happen in real fire situations.

## CRedit authorship contribution statement

**Mehran Ghafouri:** Conceptualization, Methodology, Validation, Investigation, Resources, Writing – original draft, Writing – review & editing, Visualization. **Mohsen Amraei:** Conceptualization, Methodology, Validation, Investigation, Resources, Writing – original draft, Writing – review & editing, Visualization. **Aki-Petteri Pokka:** Methodology, Validation, Investigation, Writing – review & editing. **Timo Björk:** Resources, Supervision, Funding acquisition, Writing – review & editing. **Jari Larkiola:** Resources, Supervision, Writing – review & editing. **Heidi Piili:** Funding acquisition, Writing – review & editing. **Xiao-Lin Zhao:** Conceptualization, Methodology, Supervision, Writing – review & editing.

## Declaration of Competing Interest

The authors declare that they have no known competing financial interests or personal relationships that could have appeared to influence the work reported in this paper.

## Data availability

No data was used for the research described in the article.

## Acknowledgements

The financial support of this research from “Finnish Foundation for Technology Promotion”, and “Business Finland” (BF) through the ISA-LUT project is highly appreciated. The support of SSAB Europe in providing the steel materials for this research is acknowledged. The authors also wish to thank the staff members of the Steel Structures research group at LUT University, and Material Production Engineering of Oulu University for assisting in conducting the experiments.

## References

- [1] M. Dabiri, M. Isakov, T. Skriko, T. Björk, Experimental fatigue characterization and elasto-plastic finite element analysis of notched specimens made of direct-quenched ultra-high-strength steel, *Proc. Inst. Mech. Eng. Part C J. Mech. Eng. Sci.* 231 (22) (Nov. 2017) 4209–4226, <https://doi.org/10.1177/0954406216661210>.
- [2] M. Ghafouri, A. Ahola, J. Ahn, T. Björk, Welding-induced stresses and distortion in high-strength steel T-joints: numerical and experimental study, *J. Constr. Steel Res.* 189 (Feb. 2022), 107088, <https://doi.org/10.1016/j.jcsr.2021.107088>.
- [3] F. Azhari, A. Heidarpour, X.L. Zhao, C.R. Hutchinson, Post-fire mechanical response of ultra-high strength (grade 1200) steel under high temperatures: linking

- thermal stability and microstructure, *Thin-Walled Struct.* 119 (Oct. 2017) 114–125, <https://doi.org/10.1016/j.tws.2017.05.030>.
- [4] M. Neuenschwander, C. Scandella, M. Knobloch, M. Fontana, Modeling elevated-temperature mechanical behavior of high and ultra-high strength steels in structural fire design, *Mater. Des.* 136 (Dec. 2017) 81–102, <https://doi.org/10.1016/j.matdes.2017.09.041>.
- [5] M. Ghafouri, A. Ahola, J. Ahn, T. Björk, Numerical and experimental investigations on the welding residual stresses and distortions of the short fillet welds in high strength steel plates, *Eng. Struct.* 260 (Jun. 2022), 114269, <https://doi.org/10.1016/j.engstruct.2022.114269>.
- [6] G.Q. Li, L.X. Song, Mechanical properties of TMCP Q690 high strength structural steel at elevated temperatures, *Fire Saf. J.* 116 (Sep. 2020), 103190, <https://doi.org/10.1016/j.firesaf.2020.103190>.
- [7] M. Ghafouri, J. Ahn, J. Mourujärvi, T. Björk, J. Larkiola, Finite element simulation of welding distortions in ultra-high strength steel S960 MC including comprehensive thermal and solid-state phase transformation models, *Eng. Struct.* 219 (May) (2020) 110804, <https://doi.org/10.1016/j.engstruct.2020.110804>.
- [8] W. Guo, D. Crowther, J.A. Francis, A. Thompson, Z. Liu, L. Li, Microstructure and mechanical properties of laser welded S960 high strength steel, *Mater. Des.* 85 (Nov. 2015) 534–548, <https://doi.org/10.1016/j.matdes.2015.07.037>.
- [9] S.P. Chiew, C. Cheng, M.S. Zhao, C.K. Lee, T.C. Fung, Experimental study of welding effect on S690Q high strength steel butt joints, *ce/papers 3* (3–4) (Sep. 2019) 701–706, <https://doi.org/10.1002/cepa.1124>.
- [10] M. Amraei, A. Ahola, S. Afkhami, T. Björk, A. Heidarpour, X.L. Zhao, Effects of heat input on the mechanical properties of butt-welded high and ultra-high strength steels, *Eng. Struct.* 198 (Nov. 2019), 109460, <https://doi.org/10.1016/j.engstruct.2019.109460>.
- [11] W. Guo, L. Li, S. Dong, D. Crowther, A. Thompson, Comparison of microstructure and mechanical properties of ultra-narrow gap laser and gas-metal-arc welded S960 high strength steel, *Opt. Lasers Eng.* 91 (Apr. 2017) 1–15, <https://doi.org/10.1016/j.optlaseng.2016.11.011>.
- [12] M. Amraei, T. Skrikko, T. Björk, X.L. Zhao, Plastic strain characteristics of butt-welded ultra-high strength steel (UHSS), *Thin-Walled Struct.* 109 (Dec. 2016) 227–241, <https://doi.org/10.1016/j.tws.2016.09.024>.
- [13] F. Farrokhi, J. Siltanen, A. Salminen, Fiber laser welding of direct-quenched ultrahigh strength steels: evaluation of hardness, tensile strength, and toughness properties at subzero temperatures, *J. Manuf. Sci. Eng. Trans. ASME* 137 (6) (Dec. 2015), <https://doi.org/10.1115/1.4030177>.
- [14] T. Skrikko, M. Ghafouri, T. Björk, Fatigue strength of TIG-dressed ultra-high-strength steel fillet weld joints at high stress ratio, *Int. J. Fatigue* 94 (Jan. 2017) 110–120, <https://doi.org/10.1016/j.ijfatigue.2016.09.018>.
- [15] H. Jiao, X.L. Zhao, A. Lau, Hardness and compressive capacity of longitudinally welded very high strength steel tubes, *J. Constr. Steel Res.* 114 (Nov. 2015) 405–416, <https://doi.org/10.1016/j.jcsr.2015.09.008>.
- [16] M. Amraei, et al., Mechanical properties and microstructural evaluation of the heat-affected zone in ultra-high strength steels, *Thin-Walled Struct.* 157 (Dec. 2020), 107072, <https://doi.org/10.1016/j.tws.2020.107072>.
- [17] S. Shakil, W. Lu, J. Puttonen, Experimental studies on mechanical properties of S700 MC steel at elevated temperatures, *Fire Saf. J.* 116 (Sep. 2020), 103157, <https://doi.org/10.1016/j.firesaf.2020.103157>.
- [18] Y. Li, M. Wang, G. Li, B. Jiang, Mechanical properties of hot-rolled structural steels at elevated temperatures: a review, *Fire Saf. J.* (Oct. 13, 2020) 103237, <https://doi.org/10.1016/j.firesaf.2020.103237>. Elsevier Ltd.
- [19] M. Garlock, I. Paya-Zaforteza, V. Kodur, L. Gu, Fire hazard in bridges: review, assessment and repair strategies, *Eng. Struct.* 35 (Feb. 2012) 89–98, <https://doi.org/10.1016/j.engstruct.2011.11.002>.
- [20] F. Azhari, A. Heidarpour, X.L. Zhao, On the use of Bernstein-Bézier functions for modelling the post-fire stress-strain relationship of ultra-high strength steel (grade 1200), *Eng. Struct.* 175 (Nov. 2018) 605–616, <https://doi.org/10.1016/j.engstruct.2018.08.088>.
- [21] J. Outinen, J. Kesti, P. Mäkeläinen, Fire design model for structural steel S355 based upon transient state tensile test results, *J. Constr. Steel Res.* 42 (3) (Jun. 1997) 161–169, [https://doi.org/10.1016/S0143-974X\(97\)00018-7](https://doi.org/10.1016/S0143-974X(97)00018-7).
- [22] P. Mäkeläinen, J. Outinen, J. Kesti, Fire design model for structural steel S420M based upon transient-state tensile test results, *J. Constr. Steel Res.* 48 (1) (Oct. 1998) 47–57, [https://doi.org/10.1016/S0143-974X\(98\)00005-4](https://doi.org/10.1016/S0143-974X(98)00005-4).
- [23] EN 1993-1-2, Eurocode 3: Design of Steel Structures - Part 1-2: General Rules - Structural Fire Design, CEN, Brussels, 2005.
- [24] T. Ranawaka, M. Mahendran, Experimental study of the mechanical properties of light gauge cold-formed steels at elevated temperatures, *Fire Saf. J.* 44 (2) (Feb. 2009) 219–229, <https://doi.org/10.1016/j.firesaf.2008.06.006>.
- [25] F. Azhari, A. Heidarpour, X.L. Zhao, C.R. Hutchinson, Mechanical properties of ultra-high strength (grade 1200) steel tubes under cooling phase of a fire: an experimental investigation, *Constr. Build. Mater.* 93 (Jul. 2015) 841–850, <https://doi.org/10.1016/j.conbuildmat.2015.05.082>.
- [26] X. Qiang, X. Jiang, F.S.K. Bijlaard, H. Kolstein, Mechanical properties and design recommendations of very high strength steel S960 in fire, *Eng. Struct.* 112 (Apr. 2016) 60–70, <https://doi.org/10.1016/j.engstruct.2016.01.008>.
- [27] X. Qiang, F.S.K. Bijlaard, H. Kolstein, Post-fire mechanical properties of high strength structural steels S460 and S690, *Eng. Struct.* 35 (Feb. 2012) 1–10, <https://doi.org/10.1016/j.engstruct.2011.11.005>.
- [28] A. Heidarpour, S. Cevro, Q.Y. Song, X.L. Zhao, Behaviour of stub columns utilising mild-steel plates and VHS tubes under fire, *J. Constr. Steel Res.* 95 (Apr. 2014) 220–229, <https://doi.org/10.1016/j.jcsr.2013.12.007>.
- [29] W. Wang, Y. Zhang, L. Xu, X. Li, Mechanical properties of high-strength Q960 steel at elevated temperature, *Fire Saf. J.* 114 (Jun. 2020) 103010, <https://doi.org/10.1016/j.firesaf.2020.103010>.
- [30] L. Keränen, M. Kangaspuoskari, J. Niskanen, Ultrahigh-strength steels at elevated temperatures, *J. Constr. Steel Res.* 183 (Aug. 2021) 106739, <https://doi.org/10.1016/j.jcsr.2021.106739>.
- [31] Specification for Structural Steel Buildings, ANSI/AISC 360-05, American Institute of Steel Construction, Chicago, 2005.
- [32] Steel Structures, AS 4100-1998, Australian Standards, Sydney, 1998.
- [33] X. Qiang, F.S.K. Bijlaard, H. Kolstein, Elevated-temperature mechanical properties of high strength structural steel S460N: experimental study and recommendations for fire-resistance design, *Fire Saf. J.* 55 (Jan. 2013) 15–21, <https://doi.org/10.1016/j.firesaf.2012.10.008>.
- [34] J. Siltanen, S. Tihinen, J. Kömi, Laser and laser gas-metal-arc hybrid welding of 960 MPa direct-quenched structural steel in a butt joint configuration, *J. Laser Appl.* 27 (S2) (Feb. 2015) S29007, <https://doi.org/10.2351/1.4906386>.
- [35] F. Javidan, A. Heidarpour, X.L. Zhao, C.R. Hutchinson, J. Minkinen, Effect of weld on the mechanical properties of high strength and ultra-high strength steel tubes in fabricated hybrid sections, *Eng. Struct.* 118 (Jul. 2016) 16–27, <https://doi.org/10.1016/j.engstruct.2016.03.046>.
- [36] T. Björk, J. Toivonen, T. Nykänen, Capacity of fillet welded joints made of ultra high-strength steel, *Weld. World* 56 (3–4) (2012) 71–84, <https://doi.org/10.1007/BF03321337>.
- [37] M. Amraei, H. Jiao, X.L. Zhao, L.W. Tong, Fatigue testing of butt-welded high strength square hollow sections strengthened with CFRP, *Thin-Walled Struct.* 120 (Nov. 2017) 260–268, <https://doi.org/10.1016/j.tws.2017.09.004>.
- [38] Standard Test Methods for Tension Testing of Metallic Materials, ASTM E8 / E8M, American Society for Testing and Materials, Conshohocken, 2013.
- [39] M.X. Xiong, J.Y. Richard Liew, Y. Du, Effects of heat-treatment methods on mechanical performance of high-tensile strength steel subject to elevated temperatures, *Appl. Fire Eng. - Proc. Int. Conf. Appl. Struct. Fire Eng. ASFE* 2017 1 (2–3) (Sep. 2018) 379–384, <https://doi.org/10.1201/9781315107202-40>.



## ACTA UNIVERSITATIS LAPPEENRANTAENSIS

- 1063. LUHAS, JUKKA. The interconnections of lock-in mechanisms in the forest-based bioeconomy transition towards sustainability. 2022. Diss.
- 1064. QIN, GUODONG. Research on key technologies of snake arm maintainers in extreme environments. 2022. Diss.
- 1065. TAMMINEN, JUSSI. Fast contact copper extraction. 2022. Diss.
- 1066. JANTUNEN, NIKLAS. Development of liquid–liquid extraction processes for concentrated hydrometallurgical solutions. 2023. Diss.
- 1067. GULAGI, ASHISH. South Asia's Energy [R]evolution – Transition towards defossilised power systems by 2050 with special focus on India. 2023. Diss.
- 1068. OBREZKOV LEONID. Development of continuum beam elements for the Achilles tendon modeling. 2023. Diss.
- 1069. KASEVA, JANNE. Assessing the climate resilience of plant-soil systems through response diversity. 2023. Diss.
- 1070. HYNINEN, TIMO. Development directions in software testing and quality assurance. 2023. Diss.
- 1071. AGHAHOSSEINI, ARMAN. Analyses and comparison of energy systems and scenarios for carbon neutrality - Focus on the Americas, the MENA region, and the role of geo-technologies. 2023. Diss.
- 1072. LAKANEN, LAURA. Developing handprints to enhance the environmental performance of other actors. 2023. Diss.
- 1073. ABRAMENKO, VALERII. Synchronous reluctance motor with an axially laminated anisotropic rotor in high-speed applications. 2023. Diss.
- 1074. GUTIERREZ ROJAS, DANIEL. Anomaly detection in cyber-physical applications. 2023. Diss.
- 1075. ESANOV, BAKHTIYOR. Adaptive user-controlled personalization for virtual journey applications. 2023. Diss.
- 1076. SILTANEN, JUKKA. Laser and hybrid welding of high-strength structural steels. 2023. Diss.
- 1077. NOUSIAINEN, JALO. Model-based reinforcement learning and inverse problems in extreme adaptive optics control. 2023. Diss.
- 1078. USTINOV, STANISLAV. Fast and accurate simulation of fluid power circuits in the presence of small volumes using advanced methods and models for numerical stiffness elimination. 2023. Diss.
- 1079. HUSSAIN, HAFIZ MAJID. Heuristic-based packetized energy management for residential electricity demand. 2023. Diss.
- 1080. HÄMÄLÄINEN, MINNA. Principals managing entrepreneurship education in schools. 2023. Diss.
- 1081. WANG, ZHAO. Photocatalytic degradation of pharmaceutical and person care products (PPCPs) by commercial and synthesized catalysts under UV irradiation. 2023. Diss.



- 1082.** LOHRMANN, ALENA. The water footprint of the global power sector: Status quo, challenges, and opportunities for tackling the global water crisis. 2023. Diss.
- 1083.** PONOMAREV, NIKOLAI. A salt and alkali synergy for synthesising active carbons from lignin: porosity development and techno-economic assessment. 2023. Diss.
- 1084.** AFANASYEVA, SVETLANA. Wind farm layout optimization: project economics and risk. 2023. Diss.
- 1085.** VOSTROV, KONSTANTIN. Reduction of non-circulating bearing currents by electrical machine design. 2023. Diss.
- 1086.** CARILLO MELGAREJO, DICK. Improving the design of cellular networks beyond 5G for smart grids. 2023. Diss.
- 1087.** MALACINA, IRYNA. Zooming in and out: The strategic management of innovation across multiple levels of complex supply networks. 2023. Diss.
- 1088.** SORE, SARISEELIA. Impact of information system capabilities on business value creation: Aspects of IT-producing and IT-consuming companies. 2023. Diss.
- 1089.** IMMONEN, EERO. Advances in optimal design of shapes and processes by computational fluid dynamics. 2023. Diss.
- 1090.** LAVOYE, VIRGINIE. Augmented reality in consumer retail: a presence theory approach. 2023. Diss.
- 1091.** HÄRKÖNEN, KALEVI. Smart buildings in the green energy transition. 2023. Diss.
- 1092.** TSYTSYNA, EVGENIYA. Motives, uncertainties, and imbalances in the evolution of a sustainable business ecosystem. 2023. Diss.
- 1093.** JÄÄSKELÄINEN, ATTE. Business model innovation opportunities when news has become a public good. 2023. Diss.
- 1094.** ADEDIPE, TAIWO. Atmospheric boundary-layer characteristics and their significance in wind energy and urban air quality assessment. 2023. Diss.
- 1095.** SOSUNOVA, INNA. Model and guidelines for designing Internet-of-Things-enabled smart waste management system in smart cities. 2023. Diss.
- 1096.** VUORELA, JYRI. Operative business development through system model and changing business structures. 2023. Diss.
- 1097.** TRIAPITCIN, ILIA. Knowledge injection method for real-time decision support. 2023. Diss.
- 1098.** RÄISÄNEN, OTTO. Open data in distribution network asset management. 2023. Diss.
- 1099.** MATELA, MIKA. Procurement improvement in the public agency. 2023. Diss.
- 1100.** SHAH, DIPAL. Quantification of synchronization. 2023. Diss.





ISBN 978-952-335-995-6  
ISBN 978-952-335-996-3 (PDF)  
ISSN 1456-4491 (Print)  
ISSN 2814-5518 (Online)  
Lappeenranta 2023